LA-9312-PR

Progress Report

C. 2

National Laboratory is operated by the University of California for the United States Department of Energy under contract W-7405-ENG-36.

Inertial Fusion Program

January—December 1981

Los Alamos

Los Alamos National Laboratory
Los Alamos, New Mexico 87545

The four most recent reports in this series, unclassified, are LA-7755-PR, LA-8114-PR, LA-8511-PR, and LA-9086-PR.

Compiled by Frederick Skoberne

Inertial Fusion Program

January—December 1981

The Inertial Fusion Program Staff
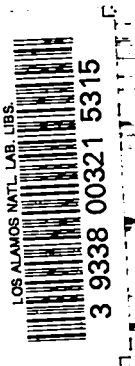
Los Alamos Los Alamos National Laboratory
Los Alamos, New Mexico 87545

CONTENTS

ACRONYMS

ACN	Antares control system computer network
AGP	alignment gimbal positioner
ANL	Argonne National Laboratory
CVD	chemical vapor deposition
DVS	detector and visible source
EMI	electromagnetic interference
GMB	glass microballoon
HEGLF	High Energy Gas Laser Facility
HIF	Heavy-Ion Fusion
HW	half wave
ICF	Inertial Confinement Fusion
LLNL	Lawrence Livermore National Laboratory
LPP	low-pressure-plasma polymerization
MHD	magnetohydrodynamic
MI	machine interface
MIRAS	microradiographic analysis system
NBS	National Bureau of Standards
NRC	National Research Council
OCLI	Optical Coating Laboratory, Inc.
OEL	Optical Evaluation Laboratory
OTB	optical test bed
PAM	power amplifier module
PDM	Pittsburgh-Des Moines Steel Company
PVD	physical vapor deposition
RFQ	radio-frequency quadrupole
RSS	root sum of squares
SCC	subsystem-control computer
S/D	sorption/diffusion
SEM	scanning electron micrograph (miscroscope)
SH	second harmonic
SNL	Sandia National Laboratories
TVS	target vacuum system
VPP	vapor phase pyrolysis
XRD	x-ray diode

INERTIAL FUSION PROGRAM
January—December 1981

by

The Inertial Fusion Program Staff

ABSTRACT

This report describes progress in the development of high-energy, short-pulse CO_2 laser systems for fusion research. Improvements in the Helios and Gemini lasers led to increased shot rates, higher output energies, and greater reliability. All buildings for Antares, the next generation CO_2 laser, have been completed, and installation of front-end, power amplifier, and target-system components is on schedule.

Target experiments (1) investigated the partition of absorbed energy into fast ions and backscattered light, (2) measured the energy and transport of electrons produced in the interaction, and (3) developed a vacuum insulation technique to inhibit high-energy, hot-electron transport (preheat) into the target.

The theory effort analyzed generation of high harmonics of incident laser light in the plasma, studied the effects of electric field saturation on resonance absorption, and developed models for electron transport that explain the apparent anomalous flux-limiting phenomena. Using the implicit-moment method, a new code, VENUS, performs two-dimensional plasma simulations.

Diagnostic development continued to emphasize x-ray spectral measurements and imaging systems because they provide information on hot-electron generation and transport. Mass spectroscopy techniques were extended to characterize the plasma's ion spectra; ion calorimetry was developed to measure the total ion energy in the plasma.

Target fabrication addressed special processes to fabricate microsphere targets and to develop nondestructive methods of target parameter characterization.

The advanced laser technology development program produced and characterized high-damage-threshold optical materials for the ultraviolet. Saturable-absorber mechanisms in this wavelength region were analyzed and several candidates were identified. Nonlinear phase conjugation at 248 nm was demonstrated.

Progress in investigations of accelerators, magnetic focusing systems, and target design for ion-beam drivers is summarized, and various phenomena expected in modified wetted-wall, magnetically protected, and fusion-fission hybrid inertial confinement reactors are discussed.

INTRODUCTION

The goal of the Inertial Confinement Fusion (ICF) program at Los Alamos is to determine the feasibility of using CO_2 lasers as fusion drivers, that is, whether energy at a 10.6-μm wavelength can be coupled to a target, transported, and converted to useful hydrodynamic energy for compressing and heating a fusion fuel pellet.

We use two very reliable and well-characterized high-energy, short-pulse CO_2 lasers, Helios and Gemini, for our laser/plasma interaction studies. Generating high-energy, hot electrons in this interaction has the detrimental effect of preheating the fuel and thus increasing the energy requirement to compress and heat the target to the desired conditions. In experimental and theoretical efforts we have therefore concentrated on these problems and have significantly advanced our understanding of the complex phenomena involved. We have developed a wide array of diagnostic techniques for these experiments. Our target fabrication effort, in addition to producing targets of specific design, has improved the techniques for assessing the quality of the targets.

Significant progress has been made on Antares, the next generation high-power laser system. Antares is expected to become operational in 1983 and will greatly extend our capability to investigate the problems of target physics at significantly increased energy levels.

OPERATING CO_2 LASER SYSTEMS

Helios

Helios, the eight-beam CO_2 laser, operated at an increased shot rate, output energy, and reliability in support of our ICF program. The system was fired 673 times in support of target experiments. Important accomplishments include

- improvement of the operating schedule to increase the target shot rate,
- installation and use of the movable Hartmann target-alignment sphere, and
- successful demonstration of 4-GHz data-channel recording in the control room area.

Gemini

Gemini was operated in support of ICF target experiments that required 632 target shots. Noteworthy accomplishments include

- installation and use of a new front-end oscillator and preamplifier system, and
- installation and use of machine modifications that increased the energy on target.

ANTARES—HIGH ENERGY GAS LASER FACILITY

The Antares front end is in place and operational. Electron-gun testing and preliminary power amplifier test data compare favorably with calculations. We installed and checked the target vacuum and optical support system. Alignment systems have been tested in the Optical Evaluation Laboratory (OEL), and the second power amplifier module (PAM) was used as an optical test bed (OTB). Calorimeters critical to beam characterization are in production, and controls for the energy storage and power amplifier systems have been implemented.

Front End

The Antares front-end system is in its final location; all hardware, including two driver amplifiers, is on site. We have measured 90-J, 1-ns output pulses and solved all postpulse problems.

Power Amplifier

The first power amplifier has been installed completely and has passed its initial mechanical and electrical shakedown tests. Electrical performance, measured at reduced operating voltage, was as expected. The amplifier had to be tested at less than design voltage because of electrical breakdown problems in the electron-beam gun. A considerable effort has been made to improve electron-beam gun operation.

The second power amplifier was installed without its electrical components; it will serve as a test-bed to check optical components and automatic alignment systems.

Target System

The target vacuum system (TVS) has been installed and successfully checked out. The large space frame on which all optical components and target diagnostic instrumentation are mounted in the vacuum chamber has been completed and installed.

Alignment and Diagnostics

The alignment and diagnostics systems have been prototyped, improved, and installed into the OTB amplifier.

Controls

The control systems for the energy storage and power amplifier systems are operational. Automatic alignment controls, a critical feature, are being installed and will be completed in 1982.

TARGET EXPERIMENTS

Target experiments in 1981 significantly improved our understanding of CO_2 laser/target interactions and the subsequent transport of energy within targets. From experiments at Helios we learned that hot-electron temperatures produced by the interaction of 10.6-μm light with matter are considerably higher than we expected—as high as 300-400 keV in high-intensity experiments. These hot electrons appear to be produced throughout the laser pulse. On Gemini, absorption measurements were extended to an incident energy of nearly 1 kJ, and measurements of direct backscatter at Helios (with limited solid angle) indicate roughly constant absorption throughout the laser pulse.

We studied the promising technique for controlling preheat by vacuum insulation in which hot electrons are constrained from crossing a vacuum gap by space-charge effects. After an extensive series of experiments, analysis of the data clearly demonstrates the desired effect of vacuum insulation and indicates that it may be significantly more effective for high-Z target materials than we had thought.

PLASMA PHYSICS AND TARGET DESIGN

Our theoretical effort continues to address primarily laser/target coupling with CO_2 light. The absence of equally good lasers at shorter wavelengths makes it imperative that we accurately assess this problem and its effect on target designs. Recent work has examined in detail the generation and transport of hot electrons.

Harmonics generated during resonant absorption in a steep density change have been calculated. The observation of harmonics as high as the 46th in CO_2 experiments is further evidence that resonant absorption plays an important role. We used a Lagrangian warm-fluid model to study saturation of the critical electric field in wavebreaking and convectively stabilized regimes.

Calculations of electron transport show that the need for severe flux-limiters arises from deficiencies in classical diffusion modeling of heat flow. We developed a new Monte Carlo electron-transport code to perform these calculations correctly. Modeling of CO_2 experiments with LASNEX shows that we need electron source temperatures of 350 keV to generate measured x-ray temperatures of 200 keV.

Calculations of collisional electron thermal transport in the presence of a laser field show effects that might be interpreted as flux-limiting or reduced thermal conductivity. These calculations are relevant to short-wavelength lasers such as KrF. In addition, we wrote a new code, VENUS, that uses implicit techniques to extend significantly the range of particle simulation.

DIAGNOSTICS DEVELOPMENT

We continued to develop a wide range of diagnostics that meet the experimental requirements of the ICF program. The state of the art has been advanced in several areas. We deployed x-ray streak cameras with a time resolution of 15 ps to study plasma dynamics. We also emphasized the development of time-resolved hard x-ray detection systems because these instruments can provide information on the important problems of hot-electron characterization. A high-resolution, time-integrated, soft x-ray grazing-incidence spectrograph, which also provides spatial resolution, was developed and deployed for detailed investigation of the laser/plasma

3

interaction phenomena. Finally, we developed a technique based on the excitation by high-energy electrons of the K_α x rays in nickel detectors to provide information on the electron-transport process.

LASER FUSION TARGET FABRICATION

Target Fabrication

About two-thirds of our effort was devoted to fabricating targets for experiments. Because of this emphasis on target fabrication, we either reduced significantly or postponed development of advanced materials and technologies. Cryogenic fuel development has been postponed indefinitely, and the staff has been reassigned to target fabrication and characterization.

A state-of-the-art precision micromachining lathe for air/vacuum bearings was designed and built from commercially obtainable parts. This lathe will allow us to fabricate machined hemispheres with surface finishes of ≤ 0.025 µm and maintain sphericity to within 1 µm.

We have developed a technique to fabricate free-standing very thin-walled (~ 1-µm) shells of tungsten and gold.

Polymer Science

We can now fabricate very thin, uniformly thick (within $\pm 10\%$) high-oxygen-content films for use as x-ray fluorescent materials and filters. These films contain up to 54 wt% oxygen and have been fabricated in thicknesses of 0.32, 0.63, and 1.26 µm.

Target Characterization

We developed a method to measure the thickness of thin films by x-ray peak ratioing in a scanning electron microscope (SEM) to an estimated accuracy of 5% on submicrometer films.

ADVANCED LASER TECHNOLOGY

Optical damage studies on materials and coatings continued and were extended to the ultraviolet region to provide basic information for designing laser systems to operate at those wavelengths. We characterized various saturable-absorber processes and materials for use at short wavelengths and identified one promising material.

We successfully extended to the uv region nonlinear phase-conjugation techniques that had been demonstrated previously at 10.6-µm wavelength.

HEAVY-ION FUSION DRIVER DEVELOPMENT

An inertial fusion driver for commercial and power production must be durable, reliable, and efficient; it also must be capable of performing at high average power. High-energy ion accelerator technology can meet these requirements and therefore holds high promise as a commercial ICF driver. Los Alamos has the lead role for developing heavy-ion fusion (HIF) accelerator technology and conducts important research in accelerator development, design of magnetic focusing systems, and target design.

Production of very intense ion beams is critical to the success of ion-beam inertial fusion. The radio frequency quadrupole (RFQ) and octupole accelerator systems we are developing are particularly well suited to generating intense beams. These beams, emerging from the accelerator, must be focused onto the target; we are designing magnetic lens systems for this purpose. Finally, ICF targets must be especially suited for ion-beam drivers; therefore, we are studying target performance as a function of ion-beam parameters such as power, energy, ion range, and uniformity of illumination.

SYSTEMS AND APPLICATIONS STUDIES OF INERTIAL FUSION

Our systems and applications studies encompass conceptual designs of specific devices to realize ICF applications and construction of mathematical models to analyze the feasibility and performance of ICF systems. These analyses include both technical and economic aspects of different ICF applications. Specifically, we concentrated on
- the response of liquid lithium layers to neutron and x-ray pulses; our results show that these responses will not pose severe design problems for the modified wetted-wall ICF reactor cavity.
- plasma behavior in magnetically protected ICF reactor cavities; we did not find any fundamental physical obstacle to magnetic wall protection.

- cyclic temperature excursions and thermal-stress fluctuations in fusion reactors, including fusion-fission hybrids; our explicit results provide a quantitative basis for tradeoff studies of technical and economic performance characteristics.

In the past year we have seen significant progress in all areas of ICF investigations. In the future, we will concentrate on studies of hot-electron physics and target designs that make use of these phenomena.

I. OPERATING CO_2 LASER SYSTEMS
(J. P. Carpenter)

Two high-energy, short-pulse CO_2 laser systems are operating routinely at Los Alamos in support of the target experimental program: Helios, which first demonstrated a 10-kJ, 1-ns output in June 1978, operates at ~15 TW on target in a subnanosecond pulse; Gemini, a two-beam system that served as a prototype for Helios, operates at 1.4 kJ on target in a nanosecond pulse.

HELIOS LASER SYSTEM

Introduction (E. L. Jolly)

Helios, our eight-beam, high-energy, short-pulse laser system, is the most powerful and important CO_2 laser facility committed to ICF research. A movable target beam-alignment sphere was installed early in 1981 and is used to irradiate new types of targets. System operation was characterized by increased shot rates, higher output energies, and improved reliability. The Helios system has been described in detail.[1]

Fig. I-1. Helios operational record for 1981.

Operations (E. L. Jolly)

We tried different modes of system operation to identify one that combines maximum target shot rate with minimum stress on operating personnel. Such a mode schedules target-shooting operations on 4 or 5 days/week between 7:00 a.m. and 5:00 p.m.; preparation and installation of target diagnostics as well as target-chamber pumpdown are performed the preceding evening. This mode of operation began in April 1981; it increased the shot rate to a level limited only by the rate of target fabrication (Fig. I-1).

We fired a record 673 shots in support of the experimental program. The facility was operational 6 days/week during December 1980 and January and February 1981 to accommodate an accelerated test schedule.

Optical Alignment (E. L. Jolly, B. Kortegaard, D. Stahl)

We developed the ability to align each target beam independently to provide spherically symmetric target illumination and to vary the focus with regard to the target over a range of 1 mm with a resolution of ~50 μm.

This flexibility is made possible by the movable Hartmann alignment system that is now in routine operation.

The electromechanical Hartmann system accurately positions an alignment sphere at the center of the target chamber. Because our Hartmann alignment technique results in a beam that is pointed and focused at the center of the alignment sphere, we can, by moving the sphere, correspondingly move the beam focal points. Figure I-2 shows the movable alignment sphere, its translation stages, and its stepping motors. This assembly is transported into the target chamber and kinematically positioned by the same mechanism that transports and positions the target. The microprocessor-based control system accepts and stores position coordinates from a user's terminal. Simple commands can recall these positions and transport the sphere to the desired position.

Multigigahertz Diagnostics System (R. L. Carlson)

We installed a 4-GHz data-recording channel adjacent to the Helios control room to demonstrate the feasibility
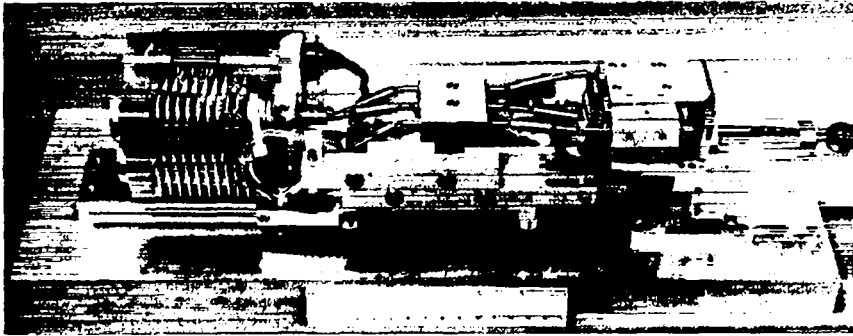
Fig. I-2. Electromechanical Hartmann target-alignment system.

of recording multigigahertz data at distances up to 38 m from the target chamber and beam-diagnostics area. Advantages of remote data recording include less severe x-ray and electromagnetic interference (EMI) environment, centralized operation, and easy access to recording instruments; it also releases valuable laser hall floor space that is presently occupied by our data-recording system. The demonstration channel successfully recorded a laser beam pulse shape (~700 ps FWHM).

This channel incorporated a 1- by 1-mm pyroelectric detector driving a 38-m foamflex coaxial cable, a passive microstrip equalization network, one 5-GHz B&H amplifier, and a Los Alamos Model 1776 oscilloscope. The oscilloscope reads with a digitizing camera that transmits data to the central computer system. The computer system, given the network transform for the detector, cable, equalizer, and oscilloscope, deconvolves the data to 4 GHz.

GEMINI LASER SYSTEM

Introduction (J. Hayden, V. Romero)

Gemini operations were performed mainly in support of laser/target interaction experiments; however, shots were also performed to test new target diagnostic instruments. A total of 632 shots were provided for experiments and an additional 151 shots were made for system tests and development.

New Front End (V. Romero)

We installed and placed in operation a new front end that consists of a multiline master oscillator and triple switchout similar to the one used in Helios. Its advantages over the old mode-locked front end include a multiline output, better time synchronization with external systems, shorter pulse width, and simplified operation.

Amplifier Optic Path (J. McLeod, V. Romero)

A major upgrade of the power amplifier optic path provides a saturable-absorber gas cell between passes 2 and 3 within the power amplifier, similar to the Helios system. When mounted in this position, the gas cell is much more effective in suppressing parasitic oscillations. This installation increased the maximum output beam energy from 400 to 700 J/beam.

REFERENCE

1. R. L. Carlson, J. P. Carpenter, D. E. Casperson, R. B. Gibson, R. P. Godwin, R. F. Haglund, Jr., J. A. Hanlon, E. L. Jolly, T. F. Stratton, IEEE J. Quantum Electron. QE-17, 1662-1678 (1981).

II. ANTARES—HIGH ENERGY GAS LASER FACILITY
(H. Jansen)

The Antares CO_2 laser system represents the next generation of CO_2 lasers needed to investigate the feasibility of laser-driven ICF. The Antares project was redirected in 1979 from a six-beam, 100-kJ system to the present Antares configuration of two 20-kJ power amplifiers that will deliver 40 TW on target in late 1983, 1 year earlier than the full design.

OVERVIEW AND STATUS (H. Jansen)

The Antares short-pulse CO_2 laser system was originally designed to deliver 100 kJ in a 1-ns pulse to a target using six large amplifiers. In 1979 we decided to reduce the initial system configuration from six to two amplifiers. The two-amplifier configuration, delivering 35-40 kJ to a target, would be completed in 1983 under present anticipated funding, 1 year earlier than the original date for the full system.

All building facilities have been completed (Fig. II-1). The complex consists of a main Laser Hall, a Target Building that houses the TVS, and an Office Support Facility. Hardware for the two amplifiers is in place (Fig. II-2). The first amplifier is used as an electrical checkout system, without the complexity of the optical train to check out the operation of the energy storage and associated control system, as well as for small-signal gain measurements. The second amplifier is used as an OTB to check out the optical alignment and controls system without the complexity of the electrical system. We expect to complete construction in late 1983.

FRONT-END SYSTEM (R. Gibson)

Introduction

The front end of the Antares system (Fig. II-3) will deliver 90 J in a 1-ns pulse to each of the two power
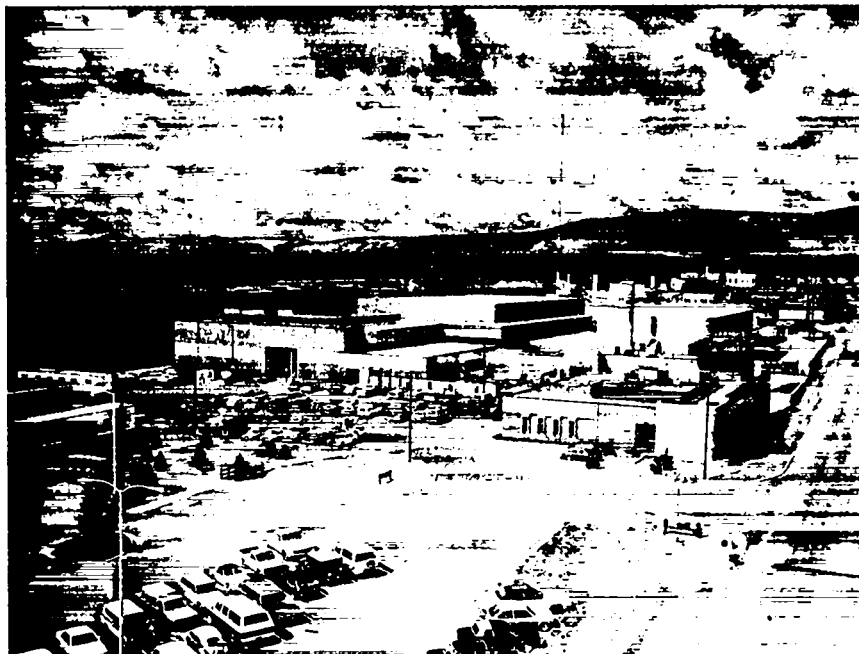
Fig. II-1. Antares main Laser Hall at left, Target Building in right background, and Office Support Facility foreground.
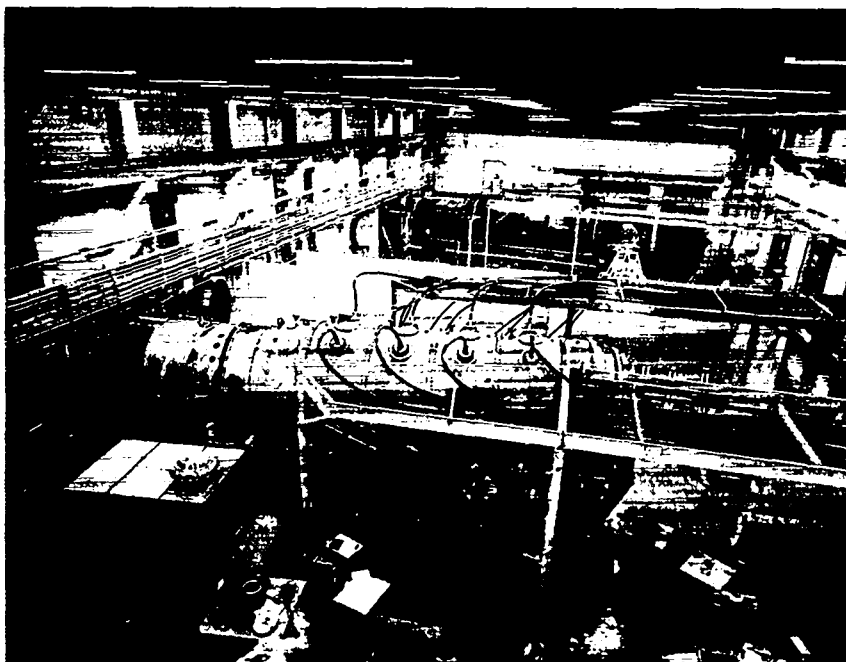
Fig. II-2. Antares Laser Hall with two amplifiers in place. The green amplifier is being used as a test bed for electrical checkout. The brown is used as a test bed for optical checkout.

amplifiers. (90 J is the required input to the power amplifiers for optimum energy extraction.) The short front-end pulse is generated in a single oscillator; the beam is then split into two and each is amplified to 90 J in separate driver amplifiers. The output to the amplifiers is an annular pulse of ~15-cm o.d. The front end has been prototyped in a final configuration and subsequently moved to its Antares location.

Description

We installed the prototype front-end beamline at its permanent location in the basement of the Laser Hall. The system is operational and will be used in initial energy-extraction experiments. An advanced multiline oscillator will be completed in later stages of the Antares project.

The front end is a three-stage assembly consisting of a tunable multiline oscillator, a preamplifier (triple-pass Lumonics 602), and two driver amplifiers (triple-pass 15- by 15- by 200-cm electron-beam-controlled discharge amplifier), one for each beamline.

Tests on the prototype beamline revealed a major problem that required the reconfiguration of some

parts—diffraction coupling occurred between passes through the optics of the Cassegrain telescopes that are used in both the preamplifier and driver amplifiers. This coupling generated postpulses of considerable magnitude in both amplifiers. The postpulses may not reduce the initial energy delivered to the target, but they do complicate the interpretation of experimental results; physical processes occur that are difficult to separate from those caused by the first pulse.

We changed the preamplifier optics to a simple nonexpanding triple-pass configuration that eliminates the coupling problem and still provides adequate drive for two beamlines. Diffraction coupling in the driver was suppressed by masking unused portions of the telescope mirrors and optimizing the gain and saturable-absorber pressure.

Results

With only one pulse from the driver amplifier, we can produce the required 90 J of energy in a 1-ns pulse with the driver Marx bank charged to only 55 kVdc, which is two-thirds of the maximum design voltage. Thus, we demonstrated that the front-end amplifiers can easily

9
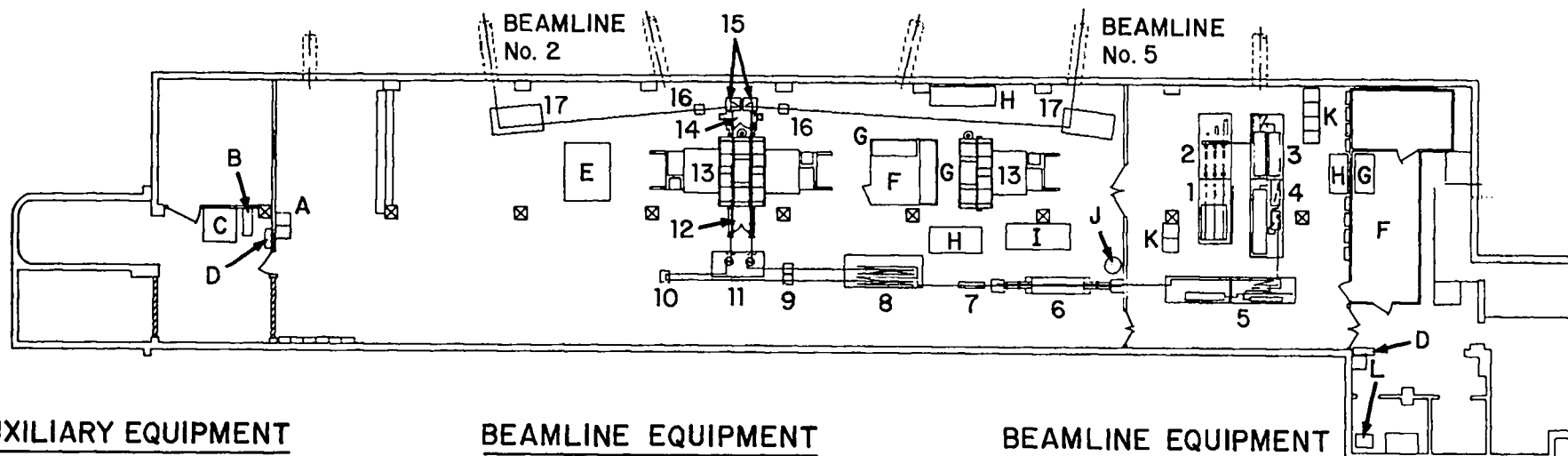
AUXILIARY EQUIPMENT

A. GAS-MIXING STATION
B. VACUUM PUMP (SF_6 SERVICE)
C. VACUUM PUMP (DRIVER SERVICE)
D. CLEAN ROOM CLOTHING SHELF
E. ELECTRON-GUN PULSER
F. SCREEN ROOM (DIAGNOSTICS)
G. DIAGNOSTICS TABLES
H. DIAGNOSTICS INPUT OPTICS TABLES
I. SMALL-SIGNAL GAIN PROBE LASER
J. PREAMPLIFIER POWER SUPPLY
K. INSTRUMENTION RACKS
L. VACUUM PUMP (OSCILLATOR SERVICE)

BEAMLINE EQUIPMENT

1. STABLE OSCILLATORS
2. ATTENUATORS
   POCKET CELLS
   PATH LENGTH ADJUSTERS
   BEAM COMBINERS
3. FOUR-PASS PREAMPLIFIER
   (LUMONICS 922)
   ONE-PASS PREAMPLIFIER
   (LUMONICS 922)
4. GEMINI OSCILLATOR
   SPATIAL FILTER No. 1
   SWITCH OUT
5. SPATIAL FILTER No. 2
   ALIGNMENT BEAM INJECTION STATION
6. TRIPLE-PASS PREAMPLIFIER
   (LUMONICS 602)

BEAMLINE EQUIPMENT

7. SATURABLE-ABSORBER CHAMBER
8. BEAM SPLITTER
   SPATIAL FILTER No. 3
9. ALIGNMENT TELESCOPE
10. PATH LENGTH ADJUSTER
11. DRIVER INPUT OPTICS TABLE
    BEAM STEERING MIRRORS
    PRIMARY CASSEGRAIN OPTIC
12. PARASITICS SUPPRESSION CHAMBER
13. DRIVER AMPLIFIER
14. SECONDARY CASSEGRAIN OPTIC
    DIAGNOSTIC PICK-OFF STATION
15. DRIVER OUTPUT TURN MIRRORS
16. BEAM BLOCK AND CALORIMETER
17. POWER AMPLIFIER
    ALIGNMENT STATION

Fig. II-3. Antares front-end layout.

deliver a single 1-ns 90-J pulse to each of the two power amplifiers.

ELECTRON-BEAM GUN (C. Mansfield, G. Allen)

Assembly and Testing

To control the discharge in the 48 chambers of the power amplifier, we need 48 large-area electron beams with an electron energy of ~500 keV and an intensity of ~50 mA/cm^2. These beams are produced by a broad-area coaxial electron gun. The electron gun for the first power amplifier has been assembled (Fig. II-4) and electrically tested in a dedicated test facility.

The facility consists of a main room with appropriate x-ray shielding, a control room, and an EMI-shielded data-acquisition room. All data links to a DEC 11/60 computer comprise electro-optical transmitters, fiber-optic cables, opto-electrical receivers, and transient digitizers. During testing of the gun, we gathered considerable experience that will be applied to the final Antares data-collection system.

We routinely monitored the major variables: cathode voltage, cathode current, grid voltage, grid current, total return current, Marx charge voltage, and return current via the electron-gun shell. Variables that were monitored occasionally were total Marx voltage and cathode-to-grid differential voltage.

Preliminary Test Results (C. Mansfield)

Operating Parameters. Major operational parameters of the electron gun with a grid resistance of 180 Ω are
peak cathode voltage (kV) 450
vacuum load impedance (Ω) ~15
length of time cathode remains above 350 kV (μs) ~2
output current density (mA/cm^2) ~ 60
variation of current density (%)
  window-to-window $<\pm 20$
  shot-to-shot $<\pm 20$.

High-Voltage Limitation. During the test program, it became rapidly apparent that the gun in its original configuration and assembly did not reliably reach the required operating voltage of ~500 keV. We believe electron energies of 500 keV or more are required to prevent streamer formation at the anode of the gas

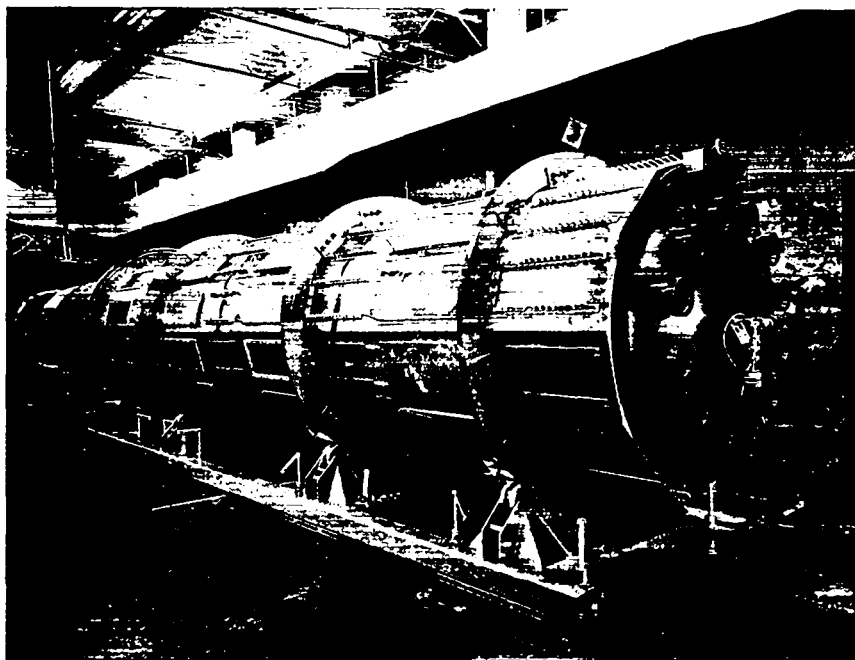Fig. II-4. Antares electron gun on fixture in test facility. The copper-colored sections are the foil apertures for the electron gun.

discharge (the electrons enter the discharge volume through the cathode foil window).

Vacuum arcs begin to form during the electron-gun high-voltage pulse. Their onset depends on voltage amplitude. These arcs are of no operational consequence if they occur after the maximum laser gain has been reached in the discharge, which is typically the case. The problem arises from the amount of destructive energy that the arcs can deposit in the electron foil window. The higher the number of arc shots, the shorter the mean time between failures of the gun.

Considering the design value of the average electric field (~30 kV/cm) between gun grid and anode or cathode and minimal field enhancement in areas other than the emitter blades, the reasons for arc formation include surface contamination, choice of materials, inductive arcing at strategically important points, local vacuum leaks, or the traveling-wave nature of the applied voltage.

We achieved dramatic improvements in preventing arc formation through cleanliness during assembly, especially by avoiding the formation of any hydrocarbon-based surface films. The fact that arcs tend to strike the bottom of the electron-gun shell is the primary indicator that cleanliness is critically important. We also found that dc conditioning is an important method to significantly increase the voltage.

In addition to cleaning and dc conditioning, we introduced a diverter spark gap in the Marx generator. This gap does not prevent arc formation, but it shunts the Marx energy, thus reducing the arc energy and increasing the mean time between failures of the gun. We are completing a detailed analysis of gun operation from an electrical circuit point of view. This analysis, coupled with future improved diagnostics, will help us decide whether the relatively complex transmission line of the gun may be at the heart of the problem.

Reliable gun operation at 450 kV is now possible (600 shots in one test sequence) and gives some indication that self-conditioning during operation may have moved this point closer to 500 kV.

Diagnostic Improvements. Initial diagnostics consisted only of current and voltage measurements in the Marx tank. Because a number of questions relating to gun operation imply that at least some gun problems are electrodynamic, that set of existing diagnostics was inadequate. Several new diagnostic tools have been developed to gain a more complete understanding of electron-gun operation.

Cerenkov Current Density Measurements. The intensity of the Cerenkov radiation emitted by electrons in the design energy range is nearly linear with current density. By placing 6-mm-thick lucite plates over the windows and photographing the light emitted when the beam of electrons hits the plate, we obtained a time-integrated high-spatial-resolution recording of current density.

Faraday Current Density Probes. Faraday cup current-density probes were developed to measure the time structure of the current density through the gun windows. Because these probes had to intercept a considerable (100-cm^2) area of beam to develop a usable signal, they provide only a limited measure of spatial resolution.

The probe design is very simple. A collecting plate is mounted perpendicularly to the electron-beam flux on ceramic standoffs from an aluminum base plate. The base plate, in turn, is mounted both electrically and mechanically to the outside of the electron-gun shell. A standard current-monitor transformer (dB/dt probe) measures the current. The output of the current transformer is connected directly to the transient digitizers in the screen room. Extreme caution in grounding the coaxial cables and avoiding ground loops prevented the pickup of unwanted noise by the data-acquisition system.

Through the use of collector probes and the Cerenkov detectors, we found that the current density along the opening in the gun was nearly constant. Current probes, in addition to the Faraday technique, were used successfully to characterize the gun.

Gun Pressure Measurements. An ionization vacuum gauge that senses pressure variations in the gun after a shot is one of the most important indicators of shot-to-shot gun performance. During a shot, electron and ion bombardment of interior gun walls results in a pressure pulse within the gun. A standard ionization vacuum gauge will not respond fast enough to follow the initial pressure surge; however, the response is proportional to the pressure surge. We use the pressure gauge mainly to indicate impending major arcing in the gun. When a major arc occurs, the pressure may surge by three orders of magnitude over those seen in normal operation.

The pressure recordings also explain why the gun may not be fired faster at a given rate. A finite time (several minutes) is required for the vacuum pumps to return the gun pressure to a level at which it can be fired without a gaseous arc developing.

Photometric Recording. A considerable amount of light is generated inside the electron gun during operation. We installed windows at the ends of the gun, each window located so that the emission blades can be seen through a hole in the grid. Photographs taken through these windows gave an early indication of the arc location. Later, mirrors were placed to provide a wide-angle view of the region between the grid and the shell.

A photomultiplier placed at the end windows provided information about the timing of major arcing occurrences. We found a definite correlation between visible arcs and the Marx current and voltage traces. By proper grounding and shielding, such a high-impedance device offers considerable promise for future use of high-speed spectroscopy as a diagnostic tool for understanding electron-gun behavior.

Vacuum Diagnostic Port. We built a vacuum diagnostic port that can be attached to the electron gun in place of an electron-beam window. This port has a 15.24-cm (6-in.) gate valve through which we can sample a relatively large area of the electron beam. Although we have only used this port to photograph emission sites on the emission blades, in the future we will also measure electron energy distributions and soft x-ray spectra.

Direct Current Conditioning. High-voltage conditioning is an important factor in obtaining proper operation of high-voltage equipment. Conditioning combines at least two phenomena: burning off potential emission sites and outgassing surfaces by heating. Our initial conditioning efforts in pulsed mode involved shorting the grid to the cathode and pulsing the gun at high voltage. Later, we found that better results can be obtained by connecting a dc (250-kV) supply to the cathode with a series-limiting resistor. After 1 to 2 h of operation with currents of 1-3 mA, this treatment resulted in drastically lowered gun pressures and increased hold-off voltages.

Diverter Gap (G. Allen). Gun arcing usually occurs at late times, 5-6 μs after the pulse begins and energy is deposited in the laser gas. Such arcs do not affect the laser operation; however, they ultimately (after several arcs in the same location) destroy electron-gun foil windows. The obvious protection against this damage is to divert the remaining energy stored in the Marx generator from the gun.

The two approaches we investigated were a nontriggered water gap and a triggered gas gap. The former had the advantage of being automatic. As soon as the Marx generator is erected, streamer formation begins in the water; gap closure is timed by the spacing of the gap. However, shock waves will eventually destroy the water gap, and residual arc resistance competes with the impedance of the arc in the gun. A triggered, pressurized gas gap does not exhibit these problems, but triggering such devices in the high-EMI environment of the Marx generator presents well-known difficulties. Fiber-optic decoupling overcame EMI-induced difficulties so that this approach was successful.

Vacuum Pump Studies (C. Winkelman)

The initial design of the electron-gun vacuum system incorporated a turbomolecular pump as the principal vacuum pump. This system was functionally tested and installed on the first electron gun for performance tests. The performance of this pumping system was considered satisfactory until the turbomolecular pump disintegrated during electron-gun testing. Other problems and less dramatic failures also occurred, and a tightened program schedule necessitated an alternative pumping system. As a result, we redesigned the electron-gun vacuum system and incorporated cryogenic pumps.

Hardware. The turbomolecular pumping system incorporated the TMP-3500 as the principal vacuum pump. The TMP-3500 is a 50-cm (20-in.) -diam throughput pump with a pumping speed for air (at 293 K) of 3500 L/s.

The cryogenic pumping system, on the other hand, incorporates the Cryo Torr 400 as the principal vacuum pump, which, at 40-cm (16-in.) throughput, has a pumping speed for air (at 293 K) of 5000 L/s and is a capture pump. A WS150 roots blower pumps the system from the 10^{-3}-torr roughing vacuum to the 10^{-5}-torr crossover at which the Cryo Torr pump is turned on. The D60A backs the blower, which is also used to regenerate the Cryo pump when it reaches its gas load limits.

Test Results. The electron gun is 1.52 m in diameter by 9.14 m long ($\sim$5 ft by 30 ft). The pumped volume is $\sim$20 000 L and the required pressure is $<2 \times 10^{-6}$ torr after 24 h of pumping from ambient.

Tests to date have covered a wide variety of electron-gun operational conditions. The Cryo Torr-based system's ultimate pressure was $\sim$4.0 $\times$ 10^{-7} torr, compared to the $\sim$5.0 $\times$ 10^{-6} of the turbopump vacuum system.

Two electron-gun foil window failures during cryopump testing did not damage the Cryo Torr 400 pump. The TMP-3500 pump could have failed as a result of the large inrush of 3-atm laser gas into the vacuum chamber through the punctured foil window.

A typical pumpdown of the electron gun with the turbomolecular pumping system is plotted in Fig. II-5; a similar curve for the Cryo pumping system is shown in Fig. II-6. The passive, safe, and satisfactory operation of the cryogenic pumps recommend their use in the electron gun.

TARGET SYSTEM (P. Wolfe)

Overview

The target system includes
- a mechanism for inserting and precisely holding a fusion target,
- 72 optical mirrors for directing and focusing the 12 laser beamlets from each of the two Antares power amplifiers onto the target,

Fig. II-6. Electron-gun pumpdown time with cryogenic pump.

- a vacuum enclosure and pumps to provide the 2×10^{-6}-torr environment required by the charged-particle diagnostics, and
- a building housing the system.

The system also requires massive, rigid support stands for the mirrors, the target positioner, and the orthogonal pair of telemicroscopes to aid in positioning targets and auxiliary optical alignment devices.

In 1981, we completed the vacuum system and the Target Building that houses it. In addition, the target-chamber space frame was erected and installed, and all other support stands were received. Mirrors and positioners are being fabricated within the Antares large-optics system and are scheduled for installation with their support structures in spring 1982. We held a final design review of the target-insertion mechanism late in 1981. The mechanism will be completed and installed with the mirrors in time for end-to-end tests of the laser system that are scheduled for summer 1983. Because of funding limitations, the telemicroscopes will not be fabricated until 1983. Our subcontractor, Questar Corporation, completed the optical design of this system,

Fig II-5. Electron-gun pumpdown time with turbomolecular pump.

and we are proceeding with the mechanical design. The physical arrangement of the 7-m-diam Antares target chamber will make these the world's largest microscopes.

Target Vacuum System (TVS)

To minimize costs and optical aberrations, there is only a single salt window in each beamlet path between the Antares power amplifier gain regions and the target. Thus, the vacuum system extends all the way from the Target Building to the power amplifier output windows in the Laser Hall, through a beam tube, which is 1.5 to 1.8 m in diameter and ~50 m in total length. Additionally, the vacuum enclosure must be large enough to house the reflective optics that illuminate the target. This consideration, rather than the space required for the experiments themselves, dictates the size of the target chamber, a cylindrical vessel, about 7 m in diameter and 7 m long. It is designed to accommodate the 72 plane folding and 72 f/6 parabolic focusing mirrors for the original 6-beam Antares. (Each Antares beam is actually an annular array of 12 beamlets, each of which has an independent set of optics.) In addition to the large target chamber, each beam tube has a 3-m-diam, 3-m-tall turning-mirror chamber that houses an array of 12 plane turning mirrors. These chambers are arranged in two groups in the Target Hall, at the two ends of the target chamber. They direct the Antares beams from their parallel configuration as they leave the Laser Hall to the two-ended arrangement required by the target-chamber optical layout.

Late in 1978, a contract was awarded to Pittsburgh-Des Moines Steel Company (PDM) to design, fabricate, erect, and start up the entire vacuum system. By the end of 1979, the six beam tubes connecting the power amplifiers in the Laser Hall with the turning chambers in the Target Building had been installed, and three of the six turning chambers were in place.

At that time, the Antares project plan changed to permit early target experiments with only two power amplifiers. This redirection simplified the TVS because only one beam tube and one turning chamber were needed at each end of the target chamber. However, most potential savings were offset by the need to redesign the target-chamber heads and relocate some of the pumps from unused beam tubes. In addition, almost all parts for the original six-beam arrangement had already been made, and some unneeded parts had been installed.

We completed construction of the system by the end of 1980, and vacuum tests began with good results. By mid-1981, almost all contracted tasks were completed, including (1) comprehensive leak testing; (2) finalizing plans; (3) carrying out the acceptance test program; (4) adding a port to the target chamber for one of the telemicroscopes; (5) extensive cleaning and painting of the system exterior and the Target Building interior; (6) installing additional lighting, power outlets, and signal conduits at the target chamber; and (7) training Antares personnel in system operation and handling. The completed system is shown in Fig. II-7.

Vacuum performance of the TVS is noteworthy, in view of its ~1000-m^2 interior surface of stainless steel and its 600-m^3 volume. The roughing-pump package, a 2400-L/s blower with two mechanical backers, takes the system from atmospheric pressure to 10^{-3} torr in less than 2 h. Six cryogenic pumps, each with a speed of ~15 000 L/s for room-air constituents, reduce pressure to the specified operating level, 2×10^{-6} torr, in less than 3 additional hours. Base pressures of 10^{-7} torr can be held in the empty system with only two of the cryogenic pumps operating. When the target-chamber space frame was first installed (in not particularly clean condition), a pressure of 5×10^{-7} torr was achieved in 8 h, starting from atmospheric pressure. This performance is well within system specification.

Target-Chamber Space Frame

This complex stainless steel structure (Fig. II-8) mounts the target-insertion system and all its precisely located optical components and experimental apparatus. The general design for the six-beam version of Antares was completed early in 1979 and was well on its way to implementation when we shifted to the two-beam version. Accordingly, our redesign of the two-beam system changed the space frame as little as possible.

Final design and fabrication of the space frame were done by PDM, who held the contract for TVS. Extensive cross checking of the Antares and PDM designs was required before beginning fabrication at PDM's plant in Provo, Utah, in mid-1980. The Antares optical-tooling team monitored the correct placement of critical mounting surfaces.

Final assembly of the space frame in the Target Hall was completed in June 1981. Airpads and a runout table will move the 11-ton space frame out of the target
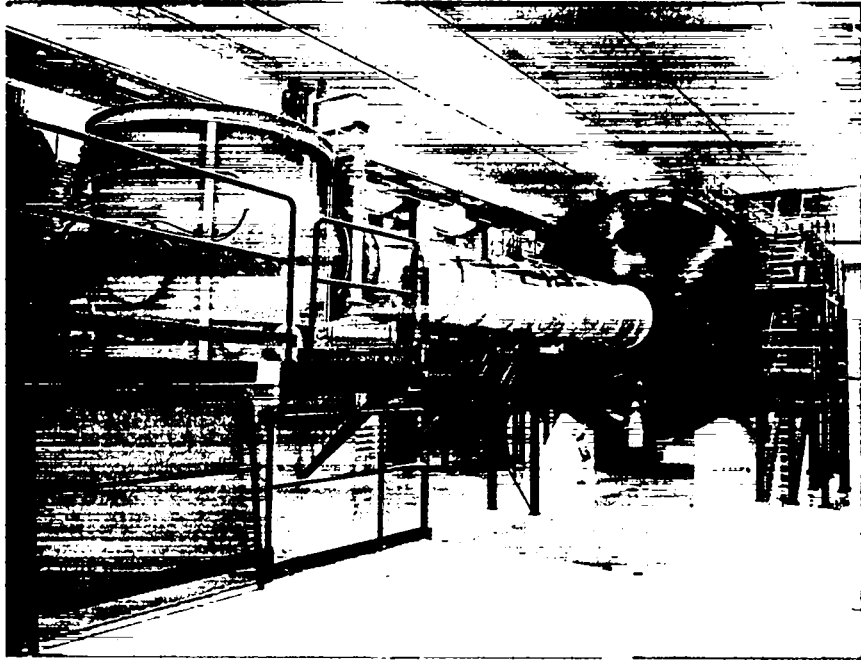
Fig. II-7. Antares Target Hall with the target chamber, connecting tube, and turning chamber. The turning-mirror chamber and the beam-transport tubes shown in beige conduct the beam to the target chamber.
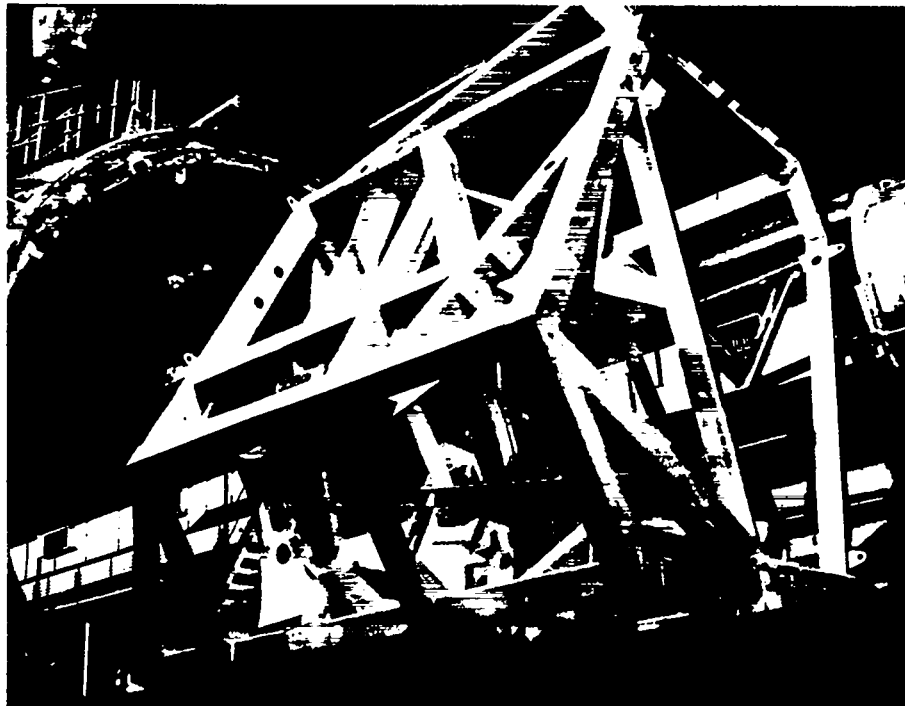

Fig. II-8. Antares target chamber and space frame.

chamber for component installation and service. We will install the major support structure and mirror in 1982.

OPTICAL BEAM MANAGEMENT (Q. Appert)

Beam Alignment

Most of the Antares automatic alignment system hardware and concepts were tested successfully on the prototype beamline in the OEL and the OTB. The prototype beamline has been in operation for more than a year and was fully instrumented for the tests. The OTB, in Power Amplifier 5, consisted of one sector of optics that was installed early in the fiscal year, and of the assembled and aligned alignment station.

Alignment System Description

Antares requires beam centering on mirrors with accuracies equivalent to ± 0.1 mm at a distance of 22 m (4.5×10^{-6} rad) and beam pointing at the target position within 45 μm (25×10^{-6} rad).

A single alignment station performs automatic alignment for each beamline. Intense, visible-point light sources are positioned at the desired beam centers along the beamline and are viewed by a telescope/TV camera from the alignment station (Fig. II-9). A video tracker determines the centroids of the light spots and generates error signals, which cause the computer control system to move appropriate mirrors in a closed-loop system. The video tracker overcomes diffraction limits when viewing down the beamline by resolving the diffraction spots to about 1 part in 10. We have achieved an accuracy of 0.03 mm at 22 m (1.5×10^{-6} rad) in 100 video frame samples (with a 3-s average). Averaging removes errors caused by scintillation and vibration.

Final alignment at the ultimate target position is accomplished with a CO_2 laser located at the alignment station and an aperture/detector combination. The detector aperture (or, equivalently, the pointing mirrors) is (are) moved under computer control to maximize the energy through the aperture. This final alignment removes error that results from dispersion in salt windows between visible and 10.6-μm light.

Prototype Beamline and Alignment System

The system (Fig. II-10) provided the first test of the overall alignment concept in the OEL. The prototype beamline substitutes a 17.8-cm (7-in.) -diam Questar telescope for the actual telescope that is being fabricated. An LSI-11 computer was used for control, and prototype stepper motor drives were used to drive the mirror positioner and telescope focus. Antares 1-mm fiber optics and light-source boxes were used for the point-light source.

Because the entire beamline was installed in ambient air, scintillation effects were pronounced, resulting in large excursions (5 to 10 TV lines) of the diffraction-limited light-source spots on the TV camera. This effect was overcome by taking large (100 to 1000) TV frame centroid samples and calculating the mean. Using this technique, the system automatically focused the telescope on each light source and corrected by a calculated amount each mirror that had been previously displaced.

Accuracies for beam centering and alignment were well within requirements. We determined the beam position at the target and tested algorithms to align coupled mirror sets on the OTB.

Beam Pointing at Target Position. We analyzed, prototyped, and tested a concept for beam alignment at the target position. The device, a detector and visible source (DVS), can be mounted on the alignment gimbal positioner (AGP), which points the DVS at each sector. The AGP also accepts a point diffraction interferometer for beam focus quality determination and analysis.

The DVS, as originally configured, consisted of a ZnSe imaging lens, germanium beam splitter, pyroelectric (CO_2) detector, and peak sense and hold circuitry (Fig. II-11). These elements were mounted in a package designed to replace a segment of the Smartt interferometer relay optics that are located in the aft portion of the AGP. All our testing has been accomplished in this configuration to date.

The ZnSe lens images on a 100-μm pinhole through the germanium beam splitter onto the pyroelectric detector. The germanium beam splitter also folds a visible fiber-optic light source into the optical path. The ZnSe lens then images this fiber-optic source onto the 100-μm pinhole. When the light source is illuminating the pinhole, the alignment telescope and video tracker may be used to locate the position of the DVS.
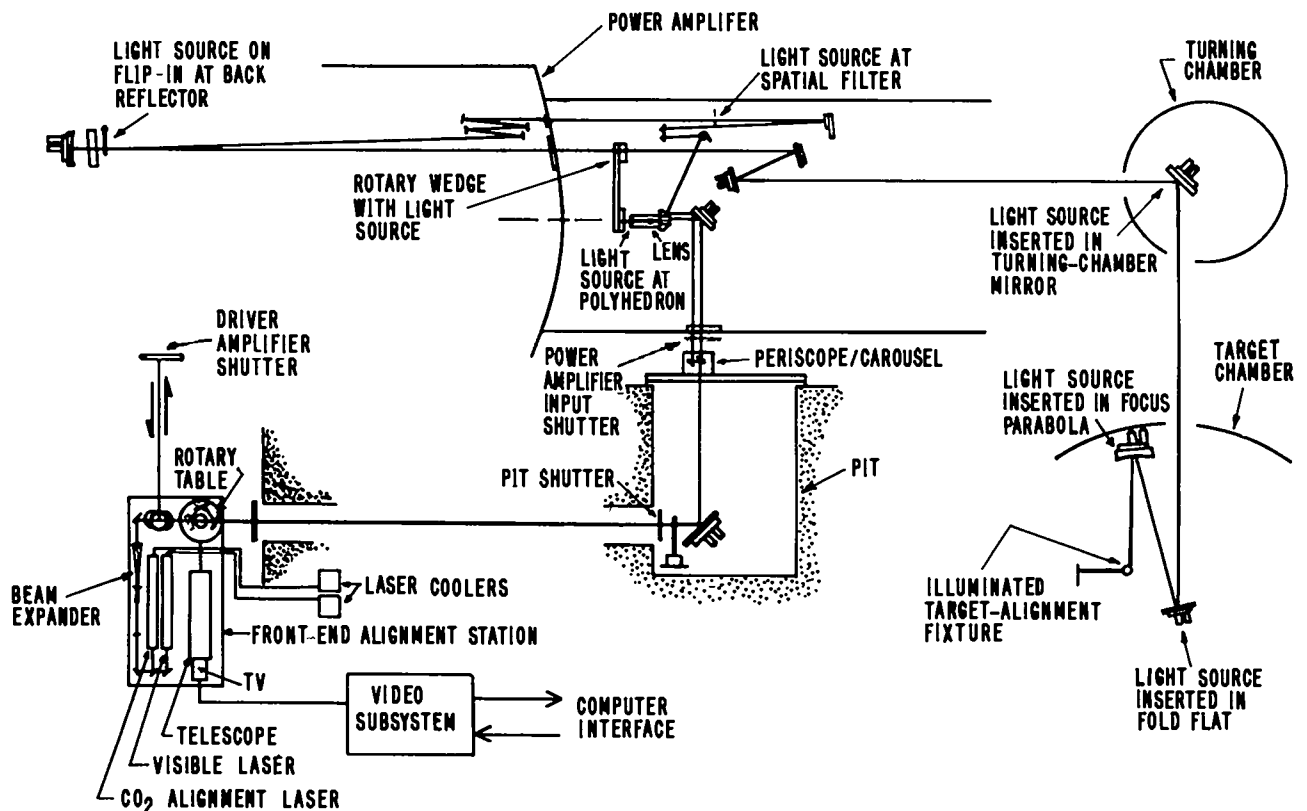
Fig. II-9. Antares automatic alignment schematic. The optical alignment path extends from the front-end room through the power amplifier and TVS onto the target position.

We have developed a simpler DVS design that eliminates the ZnSe lens. The new configuration retains the same concept but is smaller, requires no optics, and will be mounted on the AGP gimbal. The detector, pinhole, and germanium beam splitter are all mounted in a unit. Because the detector is only 5 mm from the pinhole, we eliminated the need for imaging optics. The design is 90% complete; fabrication will begin in January 1982.

When we examined the DVS in the OEL, we took into account two distinct considerations: the fundamental sensitivity of the device and the suitability of the software for beam alignment.

We plotted the laser beam profile as it swept across the DVS/pinhole system. The amplitude of the laser energy was attenuated to approximate the level anticipated in the operational system. These tests showed that the detector, electronics, and pinhole combination had sufficient sensitivity to locate the peak of the laser to the required accuracy of ± 15 μm.

Alignment software was written for and exercised on the interim LSI-11 computer. With the aid of the video tracker, we evaluated the ability of the software and DVS system to align the laser to the required accuracy. We compared the DVS position as determined by the tracker before system alignment was disturbed and after the software had realigned the system. Results indicated that the system was aligned to within ± 12 μm.

Alignment Gimbal Positioner (AGP). The AGP positions and points either the DVS or an interferometer, depending upon the type of alignment information needed. We will have the capability to focus each laser beam independently anywhere within a 1-cm³ space surrounding the target center. To align the beams, the AGP will (1) hold a variety of detectors; (2) point a detector at each laser beam to within ± 0.5 mm from a reference location in the x, y, and z axes; and (3) know the detector position relative to the reference throughout the travel of each motion to within a maximum root sum of squares (RSS) error of 15 μm.

18
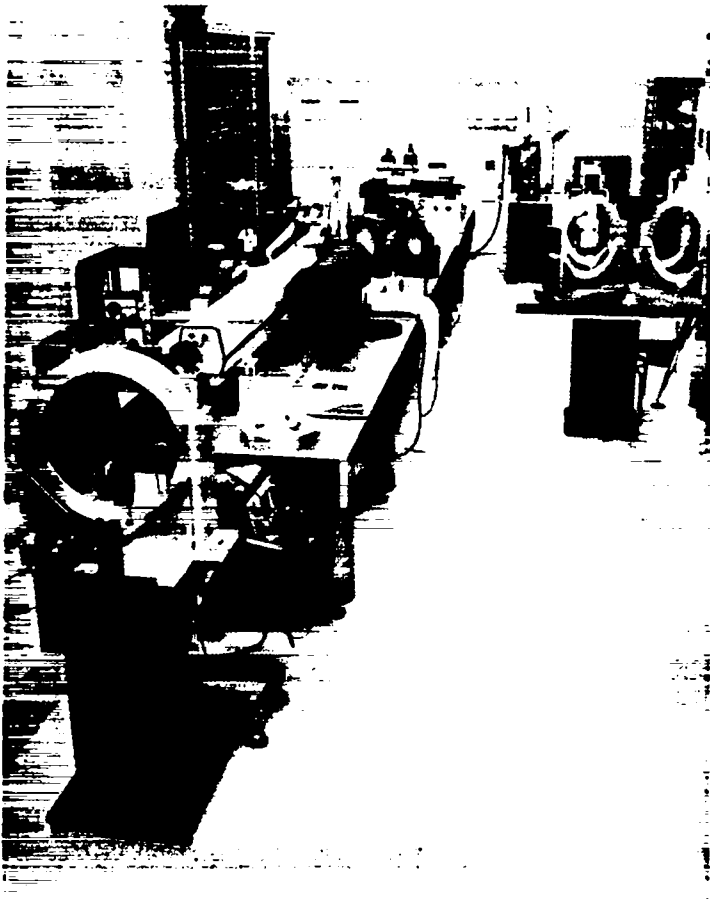
Fig. II-10. The Antares prototype beamline in the OEL simulates the actual beamline configuration from the front-end alignment station to the target.
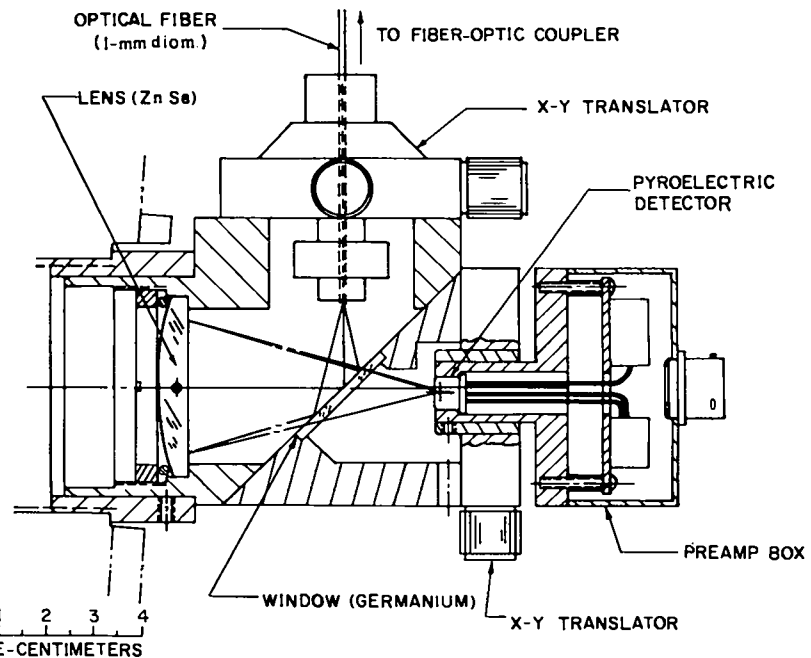
Fig. II-11. The DVS projects visible light from the target position to the alignment station telescope and detects CO_2 laser light from the alignment station.

OPTICAL FIBER
(1-mm diam.)

TO FIBER-OPTIC COUPLER

LENS (ZnSe)

X-Y TRANSLATOR

PYROELECTRIC
DETECTOR

PREAMP BOX

WINDOW (GERMANIUM)

X-Y TRANSLATOR

0 1 2 3 4
SCALE-CENTIMETERS

19

The AGP consists of a gimbal mounted to an x, y, z micropositioner and a set of optics or electrical connections that relay the detector information outside the target chamber. The detector center is located precisely at the intersection of the two gimbal axes. This arrangement allows us to point the detector toward any position in space and translate it to within the limits of the micropositioner. Figure II-12 shows the AGP with the interferometer (detector).

Until recently, it was difficult to reliably position a detector with an accuracy of better than 20 μm by using a linear bearing system. Experience with an earlier instrument revealed that most of the difficulty could be attributed to Abbe offset error. This error is associated with measuring the position of a point offset from the measurement of the axis, as illustrated in Fig. II-13. This figure also dramatizes the effect of linear bearing straightness on Abbe offset error. The linear bearings used on the earlier instrument were crossed roller bearings that were lubricated with vacuum-compatible grease and had an a:b ratio (Fig. II-14) of ~6:1. For the AGP, the a:b ratio should be reduced as much as possible to obtain the linear bearing system that will give the best predictability for the detector position.

Six configurations were tested; data for each are given in Table II-I. Those with solid circular rails were superior to the others whether we used wet or dry lubricant. Configuration 5 had the lowest error for a polynomial fit of less than 1.5 μm (at 99% confidence) for all dial
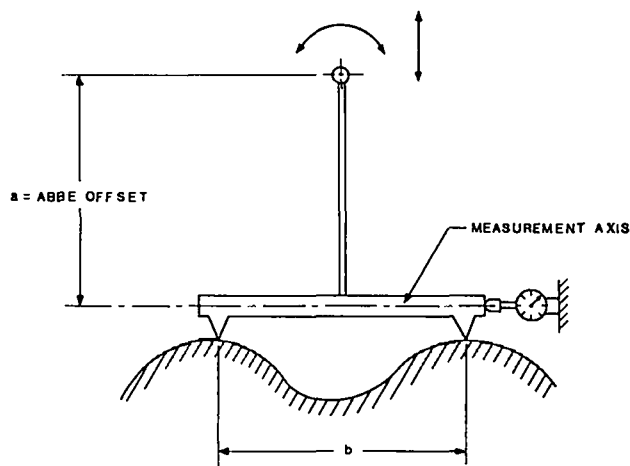
Fig. II-13. Abbe offset error description.

settings, significantly less than the 4.0-μm Abbe offset error budget.

Although more severe tests are likely to result in poorer fits to the data, the precision we have obtained thus far makes us confident that we can meet the allotted error budget.

Tests of Optical Test Bed (OTB). We used the OTB to verify alignment algorithms, demonstrate alignment performance under system design pressures, and help develop component control software.
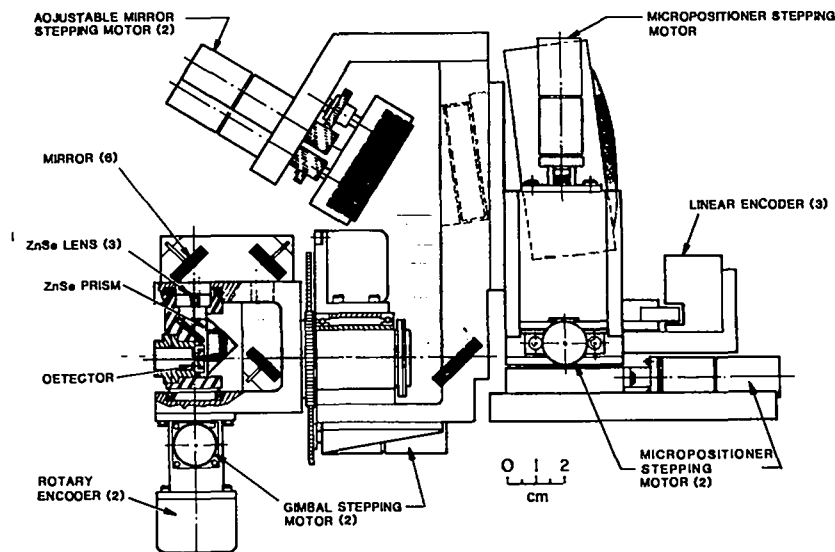
Fig. II-12. The AGP positions the DVS for each beam sector at the target position.

20
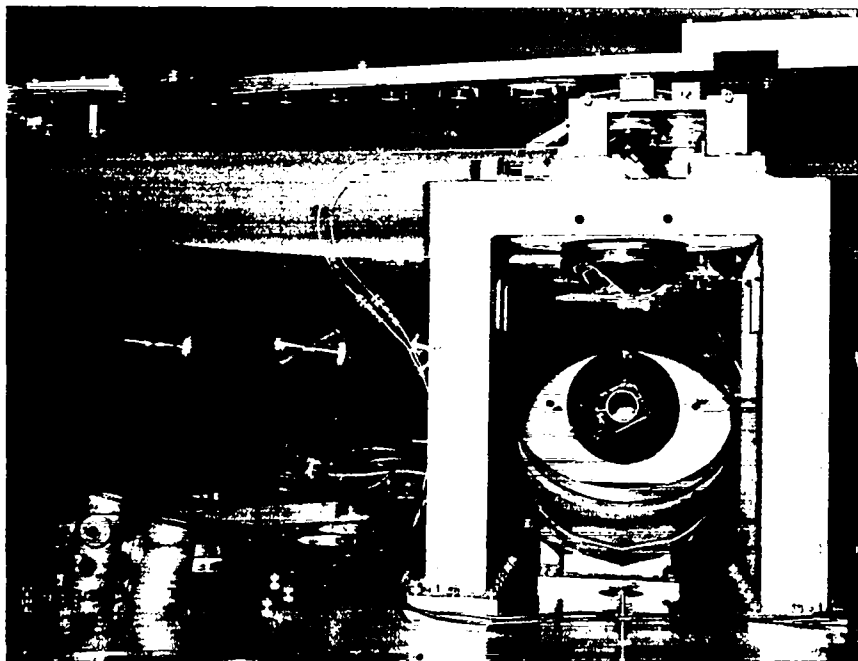
Fig. II-14. Rotating wedge assembly and polyhedron beam splitter mounted in power amplifier. The wedge rotates to each sector being aligned; it compensates for the wedged exit salt window and provides a light source for beam alignment to the periscope mirror. The image of the polyhedron beam splitter reflected from the micromachined copper mirror surface indicates the high optical quality.

TABLE II-I. Configuration Data For Prospective AGP Linear Bearings

Configuration Number	Roundness or Lubrication and Configuration Description	Parallelism of Rail or Roller (μm)	Surface Finish[a] (μm)
1	Dry, crossed roller bearings	1.25	<0.2
2	Fomblin-lubricated bearing ways and square cross-section rails	1.0	0.05
3	Nedox-coated bearing ways and circular cross-section rails	1.25	<0.2
5	Fomblin-lubricated bearing ways and circular cross-section rails	1.25	<0.2
6	Fomblin-lubricated rollers	1.25	<0.2

[a]RSS.

We checked out procedures for the installation of optics and automatic alignment equipment. Figure II-14 shows the installed rotating wedge (for visible alignment compensation), the polyhedron, and the first turning mirror viewed from the beam input port. The back-reflector light-source flip-in is in front of the absorber-gas salt window in the assembled Power Amplifier 5 (Fig. II-15). Figure II-16 shows the assembled alignment station for Beamline 5.

Verifying alignment algorithms on the OTB was an extension of work begun in the OEL, where central obscuration of the telescope prevented evaluation of coupled-mirror alignment. The telescope in the OTB was a refractor with no obscuration; it permitted alignment of the polyhedron and back reflector. Both procedures employ a coupled-mirror alignment algorithm. Test results show that all sources examined could easily be aligned within the designated error budget.

Because the calibration data required to align the system are extensive, we need a single set of data for alignment regardless of system pressure or vacuum. We conducted tests to determine whether the system under pressure could be aligned with calibration data generated at ambient pressure. By using atmospheric data, we could align the pressurized system without difficulty. All light sources remained within the video tracker gate when we brought the system up to pressure.

The alignment algorithms as well as the pressure testing were verified with an interim LSI-11 computer. This experience helped us develop a software specification for the Antares computer. Now component control and the associated man/machine interface (MI) are operational on the OTB.

DIAGNOSTICS (J. Sollid)

Calorimeters

The diagnostic system measures the laser parameters on the large-aperture portion of the Antares laser system from the power amplifier input to the target. The
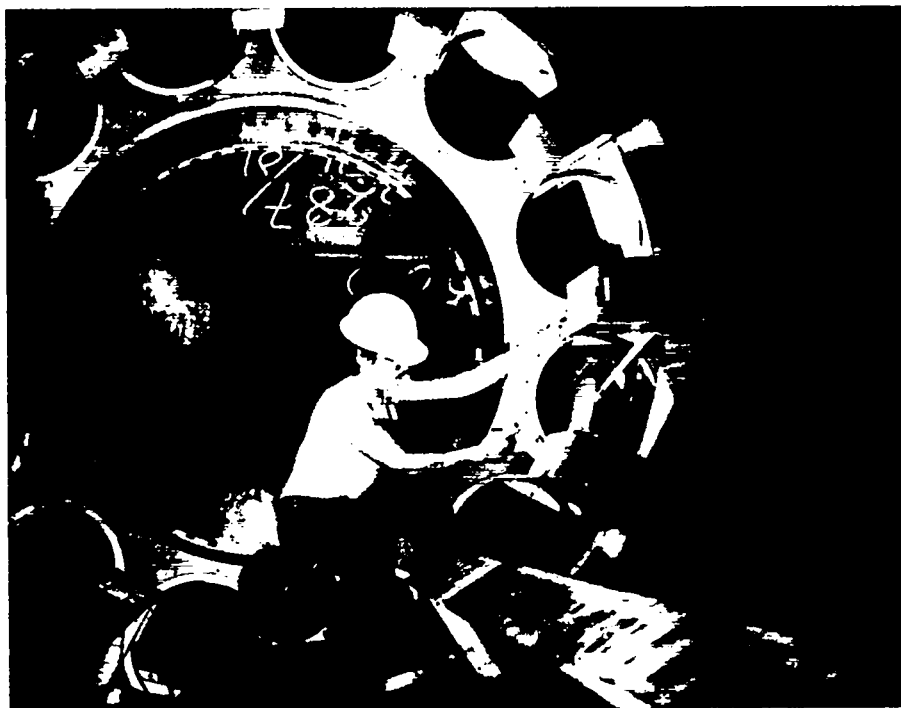
Fig. II-15. Flip-in light source mounted in place in power amplifier. An 18-in.-diam salt window is installed with a flip-in light source for beam alignment to the back reflector. We will mount 11 additional salt windows in the final configuration.
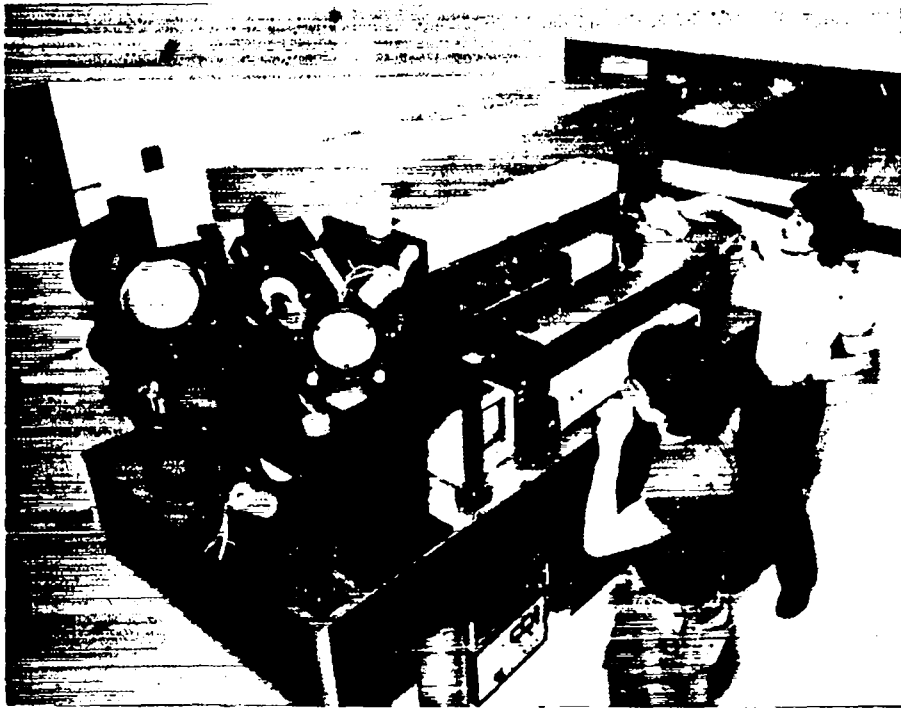
Fig. II-16. The alignment station in the front-end room contains a visible and CO_2 alignment laser and large-aperture variable focus telescope. It will be used to align the beamline from the power amplifier to the target position.

diagnostics for the front end and the driver amplifier are all available commercially, but nearly all other devices from the power amplifier to the target are custom made.

Energy and temporal pulse shape are the primary parameters to be measured. Energy is measured at five positions along the beamline: (1) at the input of the power amplifier by the input calorimeter; (2) at the input to each sector in the power amplifier by the input-sector calorimeters; (3) at the output of the power amplifier by the power amplifier full-power calorimeter; (4) at the turning chamber by the turning-chamber calorimeter; and (5) in the target chamber by the target-chamber full-power calorimeter. Neither full-power calorimeter is used during operation. Figures II-17 and II-18 point out the locations of the calorimeters in the system.

The calorimeter diameters range from 2.0 to 150.0 cm. We have developed both a Kapton/copper volume-absorbing isoperibol calorimeter and a beryllium oxide twinned calorimeter.

Beryllium Oxide. Using BeO as the radiation-absorbing element in isoperibol calorimeters has two advantages. First, we can use hybrid circuit-fabrication tech-

niques to apply solder pads for the desired number of thermocouples. This eliminates the need for thermally conducting epoxies that are expensive, require 4 to 8 h of curing time, and contribute nonlinear thermal properties. Second, using the same techniques, we can sinter calibration resistors directly onto the BeO substrate to allow electrical heating with known energy. Inked thermocouple materials can also be used; however, metallic thermocouples (chromel/constantan) were chosen for their high responsivity (60.2 μV/K).

These calorimeters may be used for any radiation that deposits energy in the BeO. They have been used for protons as well as for 10.6-μm radiation. At 10.6 μm their sensitivity is $\sim$1 mV/J. Their sensitivity to electrically deposited heat is about twice as high, showing that the effective absorptivity of the BeO for 10.6-μm radiation is $\sim$50%. The absorbing BeO wafer was 32 mm square and 0.25 mm thick. The cooling mechanism for these pulse-measuring calorimeters is primarily radiative. To within 2%, they behave as ideal isoperibol (constant environment) calorimeters. The maximum radiance before we detect surface flashing is $\sim$1 GW/cm^2.

Fig. II-17. Calorimeter locations in the power amplifier. The input calorimeter measures the energy into the amplifier; the input-sector calorimeter measures the energy into each of the 12 sectors.

Fig. II-18. Beam-diagnostic location in the target-system beamline. The turning-chamber instrumentation package contains both calorimeter and temporal measuring devices.

Kapton Copper. Because BeO is expensive, BeO calorimeters are limited to small sizes. For large-aperture use (150 mm and larger, for example), we have developed a Kapton/copper calorimeter.
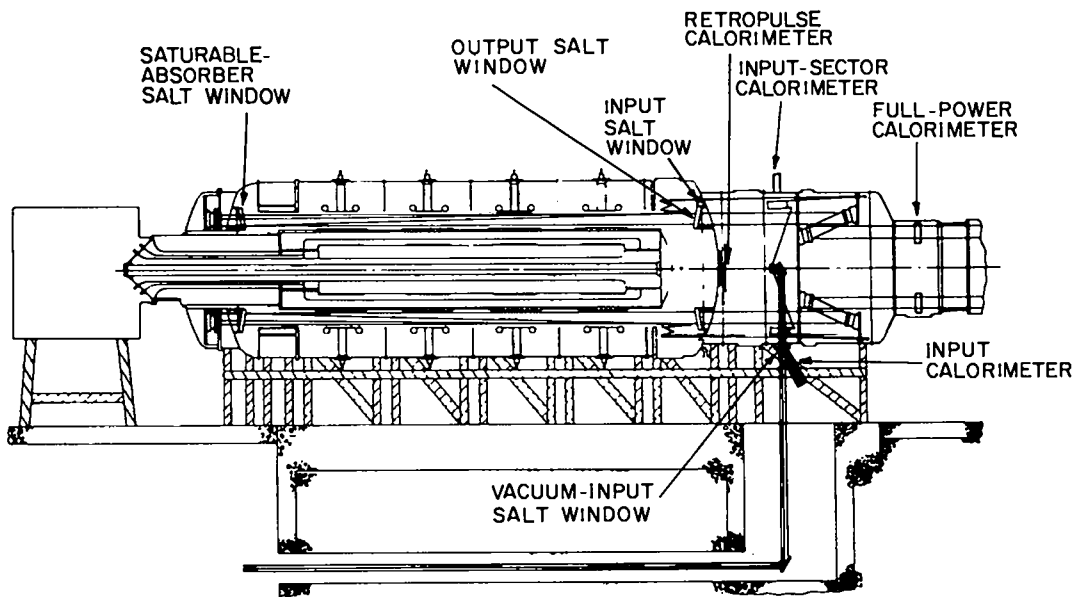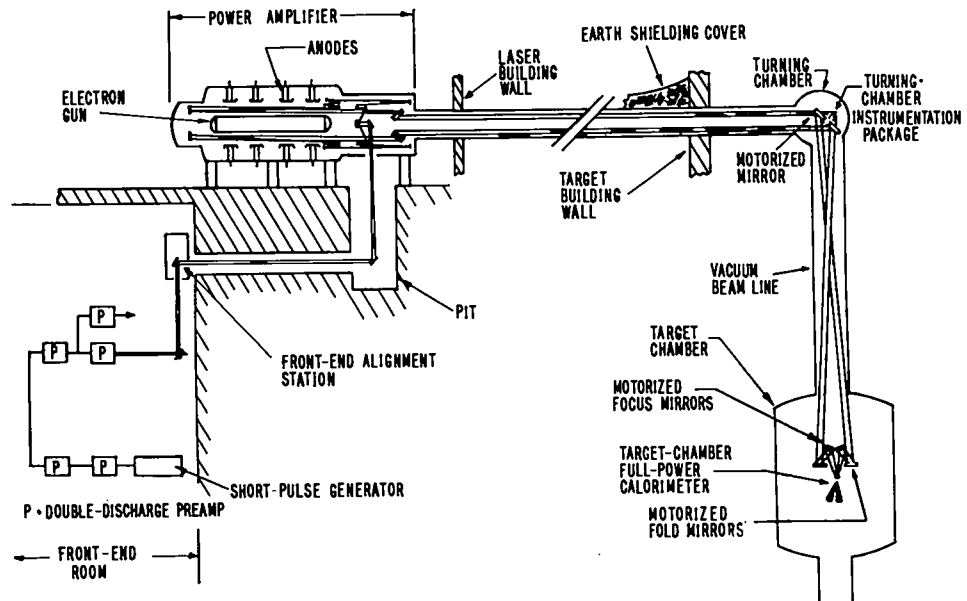
For pulsed-energy measurements in apertures up to 1.5 m, Kapton/copper laminate foils will be used as isoperibol calorimeters. These are volume-absorbing calorimeters in which the radiation is absorbed in a layer tens of wavelengths thick. The volume absorption reduces the surface temperature and increases the damage threshold as compared to surface-absorbing calorimeters. Kapton was chosen for its high absorption coefficient [330 cm^{-1} at the P(20) line of the 10-μm band of CO_2] and its useful short-pulse damage threshold (2.8 J/cm^2 or ~2.8 GW/cm^2). The copper backing integrates the absorbed heat pulse, and the resultant temperature pulse is sensed by Type-E thermocouples (chromel/constantan) soldered to the copper. We can then analyze time-vs-voltage traces of the thermocouples to obtain the energy absorbed. Using photolithographic techniques, calorimeters are fabricated to virtually any size or shape. We further expand the versatility of this technique by using single elements or several units in a thermocouple. Table II-II lists typical results for both the BeO and Kapton/copper calorimeters.

Fast Oscilloscopes

To faithfully record laser output pulses, a 3- to 5-GHz bandwidth is required. We use a 3.5- to 4.0-GHz instrument built by Los Alamos with a Tektronix, Inc. custom tube, the Model-1776 Microchannel Plate Oscilloscope. The trace is read by a silicon-intensified TV camera; it gives a 512-bit serial string composed of a 4-digit numerator and a 4-digit denominator that locate the centroid of the trace. The video digitizer is also designed and built by Los Alamos. The 10.6-μm power amplifier radiation detectors built at Los Alamos are two-segmented devices. Their signal is so strong that no amplifiers are required to drive the oscilloscope. A typical problem with ultra-high-speed recording devices is low sensitivity; however, by constructing the pyroelectric detectors with two segments, we achieved a high responsivity that obviates the use of amplifiers.

Testing. To test the temporal measurement method and hardware, we installed on Helios a prototype system or demonstration channel. A schematic of the system is shown in Fig. II-19. The system was constructed and its bandwidth was replaced. By removing the detector from the system and driving the system with a 20-ps step

TABLE II-II. Antares Large Beam-Diagnostic Calorimeters

Calorimeter Type	Input Characteristics		Signal Levels	
	Energy (E)	Flux (ϕ)	Output Voltage (V_0)	Output Resistance (Ω)
Input calorimeter Kapton/copper	0.4 J < E < 8 J	3.5 mJ/cm^2 < ϕ < 70 mJ/cm^2	2.0 mV < V_0 < 40 mV	432 Ω
Input sector Calorimeter BeO	0.050 J < E < 0.200 J	10 mJ/cm^2 < ϕ < 40 mJ/cm^2	80 μV < ϕ < 320 μV	288 Ω
Full-power calorimeter[a] Kapton/copper	32 J < E < 1600 J per sector	40 mJ/cm^2 < ϕ < 2000 mJ/cm^2	0.5 mV < V < 26 mV per element	120 Ω/ element
Turning-chamber calorimeter Kapton/copper	0.26 J < E < 31 J	0.39 mJ/cm^2 < ϕ < 47 mJ/cm^2	1.7 mV < V < 510 mV	1.8 kΩ

[a]There are 12 sectors, each of which is divided into a 5 × 5 array of elements (300 elements totally).
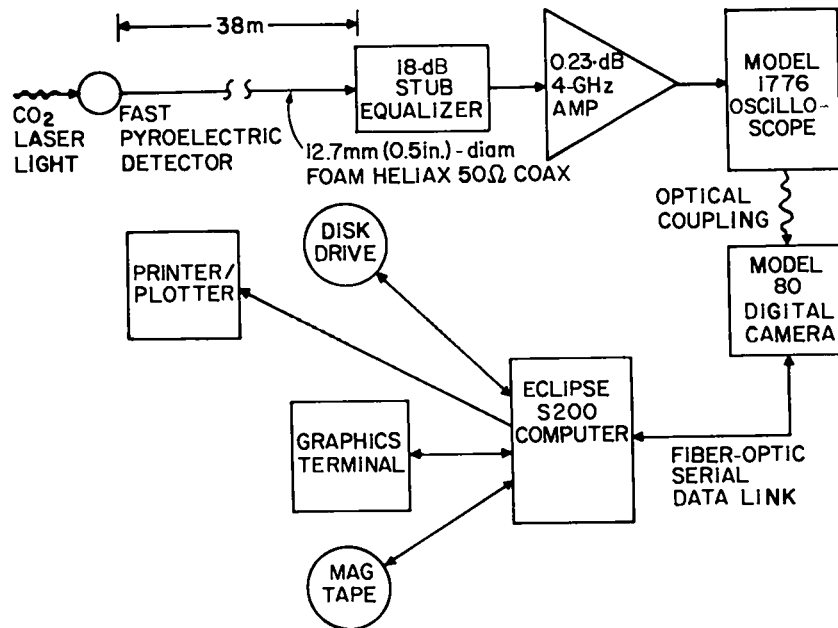
Fig. II-19. Schematic for testing fast oscilloscopes.

function, we attained an ~3-GHz bandwidth, as predicted. Figure II-20 shows the transformed time-domain data; the gain of the system was ~5dB.

We then applied the signal from the detector to a matched power divider. One output fed a close-in diagnostic recorder ~4.5 m from the detector, and the other fed the system being tested ~38 m away. The bandwidth of the close-in system was known to be ~1.5 GHz. Figure II-21 shows the results of a laser shot as
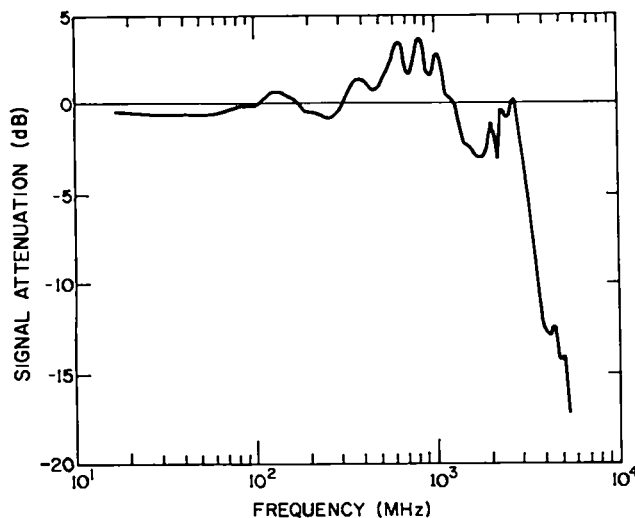
Fig. II-20. Model-1776 oscilloscope system response.
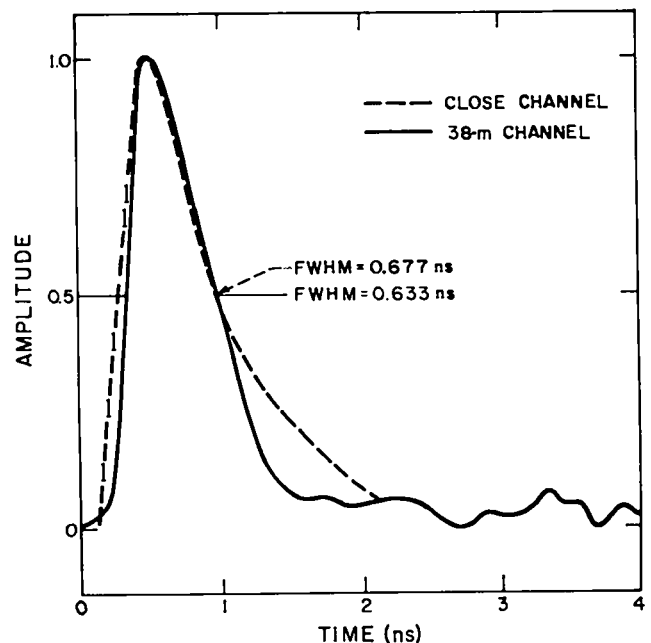
Fig. II-21. Laser pulse shapes, one produced by a close detector (dashed line), the other from a similar detector with a 38-m length of heliax (solid line).

seen on both channels viewing the same detector. Although the measured laser pulse was not severely band limited by either recording system, some differences can be seen in the overlay. The major feature is the long tail on the pulse shape of the close-in channel that is attributed to the reduced bandwidth of the close-in channel. This reduction was caused by the ~4.5 m of ~1-cm (3/8-in.) -diam foam dielectric coaxial cable used to connect the oscilloscope to the detector. We attributed additional minor differences in the two recorded pulse shapes to differences in the film-digitization methods employed. The close-in channel was digitized from Polaroid film on a digitizing pad to allow for a gross undersampling of the recorded trace. The remote channel was recorded on transparent film and then read on a 30X magnification film reader. Because of this difference, the close-in channel seemed to wash out some of the detail seen in the remote-channel trace. However, for the parameters of risetime, FWHM, and peak amplitude, the similarity is remarkable.

Results. Our work on Helios demonstrated a system capable of recording multigigahertz electrical signals from diagnostic detectors at a distance of ~38 m. This type of system provides a radiation- and noise-free environment to record fast, transient events produced by laser fusion. The system also encourages future expansion of diagnostic capabilities by not limiting diagnostic instrumentation to the immediate target-chamber area.

CONTROLS (M. Thuot)

Computer Control of Energy System and Power Amplifier on Beamline 2

The Antares control system computer network (ACN) provides three levels of laser control. The lowest, the MI, is composed of 38 LSI-11 microprocessors and a set of standardized interface hardware that serve as data multiplexers; these directly control valves, relays, and data-collection devices. Four subsystem-control computers (SCCs), PDP-1160s, control the major subsystems: optics and target, front end, Beamline 2, and Beamline 5. Most of the closed-loop control resides at this level. These computers also support a man/MI, so that each subsystem can be operated separately and concurrently. A PDP-11/70 computer will provide overall system control by coordinating the operation of the four SCCs and will provide the operator/MI for the entire system (Fig. II-22). The system design accommodates over 4000 control and data channels, as well as control of nearly 150 interacting processes. The control system has been designed and tested to operate without errors in the severe EMI environment generated by the laser.

The locally developed network communication software, TENnet, supports communication between computers in the network. This software also provides the required error-detection and recovery functions for link errors, loss of link, loss of a network processor, and loss of power.

Control Hardware. Hardware implementation of the Beamline 2 system control includes 10 computers operating in a hierarchical network. A PDP-11/60 minicomputer functions as the beamline controller, actively supervising nine MI computers that are distributed through functionally and physically independent parts of the beamline. Two MIs control the high-voltage power supplies. One MI computer-control and data-acquistion package is attached to each of the five pulsers. Each has a high-quality EMI-shielded enclosure that allows error-free operation in the high electromagnetic fields that surround the pulsers. Further, all data and control connections to these MIs are made with fiber-optic cables to eliminate conducted electrical noise. Another MI-controlled data-acquisition subsystem is located in the shielded room adjacent to the laser power amplifier (Fig. II-23). This subsystem has more than 100 fiber-optic data channels that record voltage and current waveforms as well as timing information from the power amplifier during operation. The ninth MI is the central timing controller that provides fiber optically transmitted triggers to the pulsers and data-acquisition systems.

This control system has been in operation for over 1200 shots since the electron gun was installed in the power amplifier. Relatively minor changes in the hardware, software, and timing system let us make extensive modifications to the electron gun, including the addition of a diverter gap and another trigger system. These late modifications did not change the basic system design, and the new software modules were integrated into system operation in a few weeks.

Control Software. The software system design now supporting Beamline 2 operation is the first version of the kernel software. The kernel software modules provide a
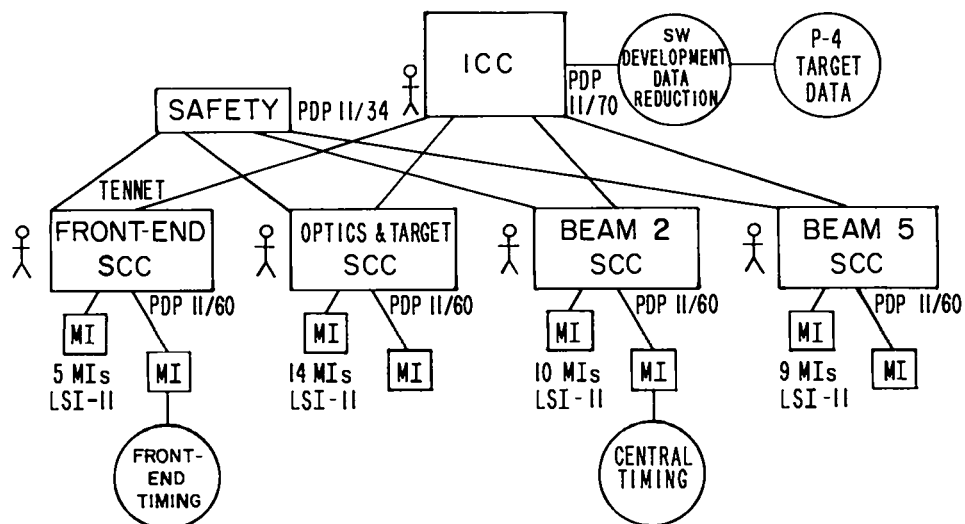
ICC — INTEGRATED CONTROL CENTER
SCC — SUBSYSTEM CONTROL CENTER
MI — MACHINE INTERFACE PROCESSOR
SW — SOFTWARE

Fig. II-22. Antares control system computer network (ACN).
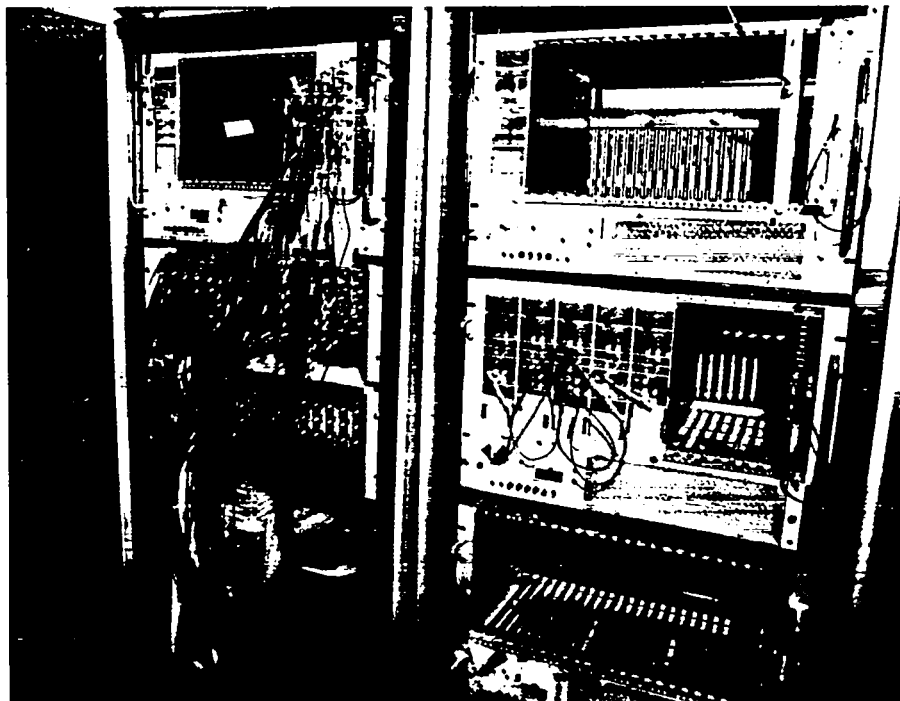
Fig. II-23. Power amplifier data system.

28

standard interface between the application control programs and the laser or operator. Two levels of applications programs have been written for Beamline 2 control. The first is called component control; it allows a low-level interface to each component (for example, relay, valve, or switch) in any controlled device. Using predefined kernel software modules now allows the computer to generate this application software almost entirely from the signal name list in the software specification. The low-level control access is used extensively to install, check out, and maintain the hardware.

Second-level control is provided by an application program called "charge and fire" that creates integrated operation of a beamline. The operator selects one of the five pulsers to operate, the level of charge voltage, the pressure settings, the fire timing, and other parameters. The operator also sets up data-acquisition channels in the power amplifier current-density measurement system. The computer then runs a test on the laser interfaces and control equipment and begins charging the pulsers. The charge process is represented graphically in real time on the operator's console. The operator is notified when the charge is complete and the energy system is fired. After the shot, the voltage and current waveforms, current-density waveforms, and timing data are displayed to the operator and transferred to a data base. The data base stores the raw data and makes the information readily available for analysis. A data analysis program that allows many mathematical functions to be applied to the data provides a processed graphical output.

Operation. The process of integrating the control and operation of Beamline 2 produced several changes in the implementation of the control system. These changes were in the area of operator interface, calibration, and data analysis. The major improvements in the operator interface will be addressed by the Version 2 man/MI described in the following section. Some changes were incorporated in the Version 1 programs used by the laser operators to increase their involvement in the control process. The system now provides more real-time data to the operators.

Calibration of the data system was revised in several areas. Hardware testing methods were devised to decrease data channel variability. Data-acquisition hardware was modified by the CAMAC vendor to improve interchangeability of modules. The calibration programs were revised to give the operator more data while calibration was in progress.

Data recall from the data base and analysis of the data produced several operational problems. The system had been designed for a batch-mode process, but the operators wanted to analyze data after each shot. The normal time for file transfer through the network delayed some operations. We will address this problem in the Version 2 beamline-control software to be available in spring 1982. We treated the immediate problem by training the operators to use the system more efficiently.

Automatic Alignment Controls

Introduction. A fully automatic computer-controlled system will align the laser beam. The alignment computers are an integral part of the ACN. There will be alignment control stations at the front end, the power amplifiers, the turning chambers, and the target chamber. Operators will be located in the central control room where color graphics terminals and television monitors are located.

Alignment is accomplished by establishing a known reference with respect to the front-end output beam at the alignment station in the front end. Everything in the rest of the beam path is aligned to that known reference by working mirror by mirror through the system. Light sources along the beam path are inserted in sequence. At each mirror a video processor at the front-end station looks through the downstream optics to the associated light source and determines the beam location. Error signals are sent to the control system, which then moves the mirrors so that the light source is positioned correctly. When this process is completed for all mirrors on a beam path, alignment is complete.

There are control functions to (1) turn on the light source, (2) search for the source when necessary, (3) read the tracker error signals, (4) calculate mirror movements, (5) execute mirror movements through stepping motors, and (6) verify that the process is complete. These steps are done sequentially along the beam path from front end to target.

Alignment Control Hardware. The ACN optics SCC is a PDP-11/60 minicomputer that controls the automatic alignment process. Seven LSI/11 microcomputers and their interface hardware, MIs, are located at the alignment stations and are connected to the SCC. The

MIs control and monitor stepping motors, light sources, TV trackers, and other miscellaneous components. A typical alignment MI includes an LSI/11 microcomputer, a stepping motor controller, binary control and monitor equipment, fiber-optic interfaces, power supplies, and EMI-shielding equipment. All components are from standard parts inventory for Antares.

The motor controller is a special system designed at Los Alamos and standardized for all Antares stepping motors. Each motor controller is linked to the MI. Motors are connected to a motor controller through a variable-sized matrix. The largest matrix possible in each motor controller is 8 × 32, for a maximum of 256 motors. We chose this design instead of commercially available motor controllers to reduce the number of motor controllers, reduce the amount of wiring to motors in power amplifiers, and reduce the number and cost of vacuum feedthrough connectors on the power amplifier and TVS. The design, installation, and testing are complete for one beamline's front-end and power amplifier alignment MIs. The computer can control and monitor 140 stepping motors, set and read tracker error data, and control 39 light sources required for front-end and power amplifier alignment.

Alignment Control Software. Alignment component control software was initially written with Version 1 kernel software to support hardware installation and testing. We use the Version 2 kernel software to implement the automatic alignment system.

The Version 2 kernel software expanded the capabilities of Version 1 in several key areas. It provides the necessary error-detection and alarm functions for closed-loop mirror-positioning control. It provides a true data base function to store and retrieve the nearly 15 000 constants, settings, and parameters in the alignment process. And it provides support for the high-performance Version 2 man/MI. This interface improves the interaction between the operators and the control system by providing immediate response and control verification to the operator, improving the control input function with a full-screen touch panel, and providing context changing, full-color display replacement, in less than 2 s.

The automatic alignment applications software now provides several Version 2 displays (Fig. II-24). We have implemented and tested the alignment calibration function of constants, parameter entry, and editing. We have also tested the basic control functions such as reading the tracker or moving a motor. In addition, we are testing the design and coding of the automatic alignment

software for the power amplifier. We expect full automatic alignment through the power amplifier by March 1982.

RETROPULSE ISOLATION (T. Sheheen)

In all high-energy laser fusion systems, we must protect front-end oscillators and optical components from damage by laser pulses that are reflected into the laser systems from fusion targets. Any apparatus used in isolating the retropulse should be efficient, should have a high forward transmission and low backward transmission, be of minimum complexity for reliable operation, and (for Antares) should function in vacuum.

We have demonstrated that a CO_2 (10.6-μm) laser-initiated plasma may be formed at the aperture of a LiF spatial filter in a 10^{-6}-torr vacuum of sufficient density and lifetime to block the retropulse from re-entering the laser system. Plasma initiation is controlled by the fluence incident on the aperture edge of the spatial filter.

Our experiments use a CO_2 laser with a 1.1-ns pulse width and pulse energies up to 3 J. A chopped cw CO_2 probe laser at 9.6 μm was used to determine the blocking time of the laser-initiated plasma. Figure II-25 shows the paths and experimental configuration schematically.

With a 1.1-ns pulsed 10.6-μm CO_2 laser incident on the LiF aperture, at a 63-J/cm^2 fluence level on the edge of the 0.7847-mm-diam aperture, we have found that within the 1.1-ns pulse a plasma is initiated that produces a small-signal transmission of 64%. Within 40 ns, the plasma reaches a critical density of 10^{19} cm^{-3}—sufficient to block the 9.6-μm probe laser. The plasma persists at or above the critical density for 680 ns, which exceeds the retropulse return time for the Antares laser fusion system.

These experimental results indicate that an effective, passive retropulse-isolation system can be simply implemented in the Antares system.

CONCLUSION (H. Jansen)

In 1981 we have seen a significant change in the Antares project—from procurement and installation to testing of the hardware in laboratories or on the real machine. The culmination of all these efforts was a recently performed test on Power Amplifier 2. The entire power amplifier system with the energy-storage devices for the electron gun and the 48 laser discharges worked
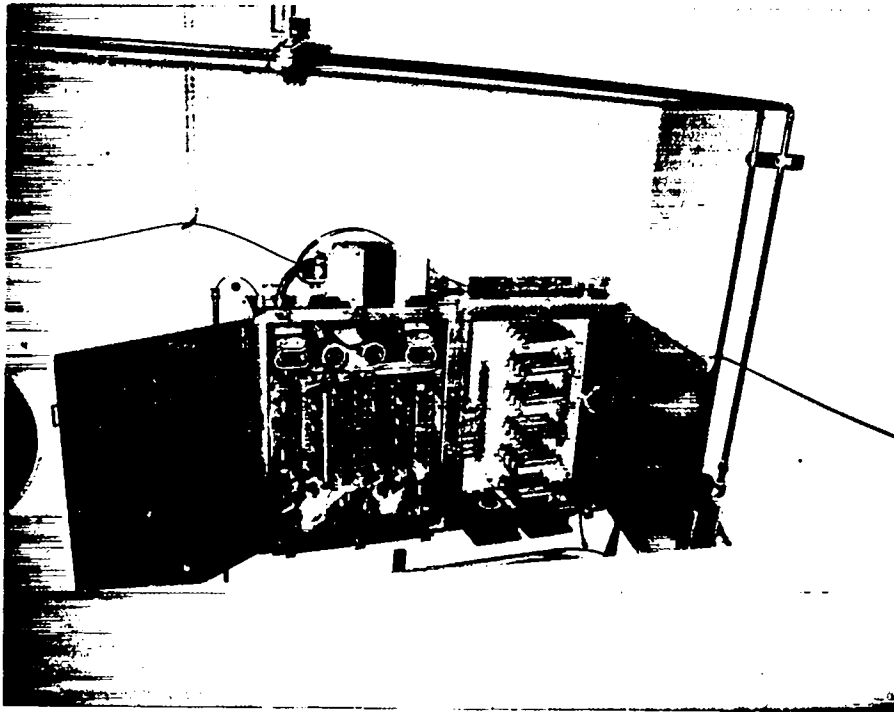
Fig. II-24. Front-end alignment motor driver.

in harmony under computer control from the control room. A small probe laser was sent through all four axial sections of the power amplifier and was amplified to design criteria. Next year, we will see energy extraction on three beams, and we plan to place one beam on target.

1 LASER PULSE FROM LUMONICS	8 LiF SPATIAL FILTER
2 GENTEC ENERGY DETECTORS	9 cw PROBE-LASER CHOPPER
3 CoF ATTENUATORS	10 CO_2, 9.6-μm PROBE LASER
4 WEDGE SPLITTER	11 VIDEO SYSTEM
5 INPUT NoCℓ WINDOW	12 (Hg, Cd)Te DETECTOR
6 NoCℓ BEAM-FOCUSING LENS f/20	13 NoCℓ COLLECTING LENS f/15
7 PUMPING CHAMBER	14 9.6-μm ±3% BAND-PASS FILTER

Fig. II-25. Experimental setup to investigate plasma formation.

III. TARGET EXPERIMENTS
(P. Goldstone)

Through a series of target experiments and comparison with theoretical calculations, we are gaining new understanding of the conversion of 10-μm light to hot electrons and the subsequent transport of energy within targets. This understanding is fundamental to our ability to determine whether, and at what energy, CO_2 lasers can be used to compress fusion targets to ignition conditions. High hot-electron temperatures and significant decoupling of energy into suprathermal ion expansion can pose problems for target design, but vacuum insulation shows promise for controlling target preheat.

INTRODUCTION

Our goal is to understand the interaction of 10-μm light with targets and the subsequent partition of energy within the targets. In addition, we want to determine the feasibility of CO_2 lasers as inertial fusion drivers. To this end, we are studying both the basic energy budget of irradiated targets (including absorption of laser light and energy losses such as the production of fast ions) and the production and transport of hot electrons.

Absorption, as inferred from the energy of fast (suprathermal) and slow (thermal) ions from target disassembly at up to 800 J incident, has been measured at the Gemini laser. These experiments have confirmed an absorption of ~25% of incident energy on microballoons, consistent with earlier low-energy measurements of optical absorption. They also have indicated that a significant fraction (~50%) of the absorbed energy is emitted as fast ions from these low-mass targets. Such a large energy loss may have serious consequences for target heating and ablation. Direct measurements of backscattered light have shown no significant evidence that stimulated Brillouin processes, which could reduce absorption, build up late in the laser pulse.

We have studied transport of hot electrons across vacuum gaps. Space-charge effects limit the speed of electrons crossing such gaps to the characteristic ion sound speed of the coronal plasma. The effect is generally known as vacuum insulation. In these recent experiments we characterized the speed of electron transport for both low- and high-Z target materials. Reduction of the electron-transport speed (and the distance necessary for vacuum insulation for a given laser pulse duration) observed with high-Z materials indicates that this technique may prevent target preheat that otherwise would hinder compression.

We briefly investigated the effect of hydrogen contamination and the geometry of the target on hydrodynamic expansion. Analysis of the data indicates that the presence of hydrogen significantly affects the velocity distribution of the bulk target ions (in this case carbon).

In a number of high-intensity experiments at Helios, we have studied the hot-electron spectrum and transport using the bremsstrahlung produced when these electrons collisionally deposit their energy in high-Z material. We have determined (1) that the hot electrons are produced throughout the laser pulse (the time-resolved bremsstrahlung follows the laser pulse) and (2) that both the bremsstrahlung spectrum and the effective range of hot electrons in spherical targets appear consistent with hot-electron temperatures of several hundred keV. This electron temperature is higher than we had believed on the basis of previous experiments and poses additional problems for target design.

MEASUREMENT OF FAST-ION ENERGY LOSS AND ABSORPTION (W. Ehler, J. Kephart)

Time-resolved charge collectors at Helios were used to monitor fast ions associated with the suprathermal plasma and slow ions from the overdense plasma produced by a CO_2 laser pulse incident on various targets. Two charge collector pairs were used: one pair at the pole and another pair on the equatorial plane of the target chamber. These measurements indicated that a large fraction of the absorbed laser energy appeared in fast ions and a much smaller fraction in slow ions.

The Helios results prompted a more detailed experiment using the Gemini laser system to verify the fast-ion energy fraction. We distributed around the target

chamber nine ion charge collectors; seven were filtered to permit detection of fast ions only. Understanding the mean ion charge detected as a function of time is crucial to the interpretation of charge collector data. Therefore, in addition to the charge collectors, we distributed seven ion calorimeters around the chamber at locations close to those of the ion collectors. The calorimeters were primarily intended to measure absorption by determining the total energy invested in plasma kinetic energy. However, one of the ion calorimeters was provided with an absorber consisting of 0.1 μm of copper on a 0.2-μm substrate of parylene. This absorber, which was supported on a screen, provided a measurement of the energy radiated as fast ions (>50 keV for protons), which are sufficiently energetic to pass through the foil. A Thomson ion spectrograph (to determine the ion charge states seen by the charge collectors) and two ion TOF detectors were also included in the diagnostics.

The fast-ion charge collector consisted of a grounded 0.5-μm nickel foil filter placed in front of a negatively biased brass collector. The nickel filter blocks soft radiation and plasma electrons but passes protons with energy >120 keV and carbon ions with energy >850 keV. Analysis of the data indicates that ions of lower energy, which are stopped by the foil, contribute only a small fraction to the total fast-ion energy. Slow-ion detectors are identical to the fast-ion detectors except that they are without the nickel filter. The negative bias on these detectors rejects secondary electrons produced by ion impact on the brass collector. The slow-ion signal can only be interpreted for ion energies less than 10 keV/amu because of the slow oscilloscope sweep rate and contamination of the signal in the unfiltered detectors caused by prompt x rays and scattered light from the target.

When a fast ion passes through a thin foil, it will emerge in an equilibrium charge state that is a function of its energy and atomic weight but not of its initial charge state. For these high-energy ions, the secondary electron emission at the collector also depends only on the energy and mass of the ion. We designed a computer program to take these factors into account in analyzing a digitized scope trace and providing a value for the total fast-ion energy. However, uncertainties still arise unless the atomic species incident on the detector are known.

Both laser beams of the Gemini laser system, with a total energy of about 800 J, were focused on various spherical targets [CH- or Au-coated glass microballoons (GMBs) and solid glass spheres]. The Thomson spectrum for each of these targets shows spectrum lines at A/Z = 1 (protons) and at A/Z = 2 (these ions could be silicon, oxygen, carbon, etc.). If we assume for a GMB target that all ions detected in the charge collector were silicon or oxygen, the fast-ion energy deduced from the charge-cup measurements would be nearly three times the incident laser energy. However, the Thomson data indicate that protons, presumably from hydrocarbon contamination of the target surface, are a large component of the fast-ion expansion. If we assume that the detected ions are protons up to a time T, which is the TOF of the fastest A/Z = 2 ion detected by the Thomson spectrograph, and that the ions detected thereafter are CH, analysis of the charge-cup data indicates that 17% of the incident laser energy appears as expanding fast ions. A 200-Å coating of hydrocarbon would be sufficient to provide the necessary protons and carbon ions. If we assume that the slow ions have the same atomic composition as the bulk of the target, only a few per cent of the incident laser energy appears as slow ions. Also, almost all the target atoms can be accounted for in the slow ions.

The ion calorimeter data indicate an absorption of about 28% of the 10.6-μm laser light by 300-μm-diam spherical targets at incident energies of 800-1000 J. The calorimeter with the filter indicates that about 43% of the absorbed energy (or 12% of the incident energy) appears in the fast ions (here >50 keV). The discrepancy between the amount of energy in the fast-ion component (17 vs 12% of incident) as measured by these two methods has not been resolved. We are now recalculating the fast-ion energy from the charge collectors with more realistic assumptions of the CH ratio as a function of time, using detailed analysis of the Thomson spectra. A measurement at the National Research Council (NRC), Canada, performed with 20 J of 10.6-μm radiation, showed ~75% of the absorbed energy reappearing as fast ions.[1]

In conclusion, experiments have shown that for these low-mass microballoons, production of fast ions is a very significant part of the energy budget. Our investigation will be continued and expanded on Helios.

BACKSCATTER FROM SPHERICAL TARGETS
(D. E. Casperson)

Two of the eight CO_2 laser beamlines at Helios have collecting optics for obtaining f/2.4 samples of directly backscattered light. One of these two retrochannels uses a fast pyroelectric detector and a Model-1776 fast oscilloscope to observe the temporal behavior of both the

fundamental 10.6-μm backscatter and the target-generated second harmonic of the laser light. Measurements of the total backscattered energy and incident pulse shape allow us to calculate the time-dependent plasma reflectivity from the targets.

We have obtained temporally and spectrally resolved backscatter measurements for a number of targets, consisting of (nominal) 300-μm-diam GMBs with 1-μm-thick walls and gold coatings ranging from 0.1 to 14.0 μm in thickness. We also studied GMBs coated with 7 μm of iron and nickel spheres coated with 11 μm of tungsten. The laser beams were defocused to provide intensities between 10^{14} and 10^{15} W/cm². The directly backscattered energy in one calibrated retrochannel remained fairly constant at ~3% of the incident energy in that beamline, independent of target coating material and thickness. To determine the absolute timing of the backscatter with respect to the incident laser pulse, we assumed that second-harmonic light, recorded on the same detector channel with known time separation from the fundamental (Fig. III-1), is produced most strongly at the peak of the incident pulse. Figure III-2 compares the digitized incident and fundamental (10-μm) backscatter pulse shapes. The 10.6-μm temporally resolved backscatter generally followed the incident laser pulse. It showed approximately constant reflectivity, with little sign of plasma instabilities (such as stimulated Brillouin scattering) building up late in the pulse when one would expect greater amounts of underdense plasma to surround the target. These findings are consistent with other measurements of backscatter under similar irradiation conditions.[2]

The second retrochannel was used to observe the time-integrated, spectrally resolved 10.6-μm backscatter from these targets. A 750-mm f/6 spectrometer with a 128-element high-resolution pyroelectric array detector placed at the film plane provided ~20 Å of resolution at 10.6 μm. The backscattered spectrum showed the multiline content of the Helios laser (typically, 3 to 4 rotational lines in the P-branch of the 10.6-μm band) with the lines separated by 200 Å (Fig. III-3). The entire spectrum was consistently blue-shifted by 100-150 A. If we assume that these spectra are dominated by the specular component of backscatter, that is, the component reflected from the target critical surface moving radially outward, then the inferred critical surface velocity from the Doppler shift is 1.4×10^7 to 2.0×10^7 cm/s. With the gold-coated GMBs, there was no strong correlation between coating thickness and Doppler shift. However, the tungsten and iron targets did generate quite

reproducible blue shifts of ~90 and 144 Å, respectively, suggesting a possible Z-dependence of the shifts.

VACUUM INSULATION IN CO_2 LASER-IRRADIATED TARGETS (T. H. Tan)

We have investigated the possibility of using vacuum insulation to stop hot electrons from preheating the interior of a fusion target during high-power CO_2 laser irradiation. A previous study had been performed at ~1 × 10¹⁴ W/cm² intensity with very thin plastic targets and limited diagnostics.[3] The present experiment used double-foil flat targets irradiated by one beam of Gemini to study hot-electron energy transported from the front illuminated surface to the back foil as a function of hot-electron temperature, foil separation, and such front-foil parameters as atomic number, thickness, area, and density.

Theoretically, the percentage of electron current density transported across the vacuum gap can be represented by the expression[4]

$$ j = \exp[-1 - D/c_i t] \ , \tag{III-1} $$

where D is the foil separation distance, c_i is the ion sound speed, and t is the duration of electron transmission. In this model, the electron current is controlled by the expansion of the isothermal plasma, which is characterized by the hot-electron temperature. The transported electron energy is experimentally determined by the time-integrated K_α line radiation intensity from the titanium rear foil and by the ion energy emitted into the front and back directions. (The K_α intensity is related to the energy deposited in the material by collisional stopping of hot electrons.) An extensive array of instruments, including a visible-light streak camera and an array of filtered x-ray pinhole cameras, monitored the temporal and spatial profiles of the transported plasma.

We performed experiments with front target foils of CH, 2 μm and 25 μm thick, and 1-μm-thick gold 0.5 to 5 mm in diameter. The second foil is titanium, nominally 25 μm thick and 5 mm in diameter; however, to improve measurement of ion emission from the rear foil, CH films were sometimes used in this position. We used a single Gemini laser beam that delivered between 280 and 700 J in a 1.2-ns pulse. The hot-electron temperature (inferred from ion measurements) ranged between 15 and 97 keV.
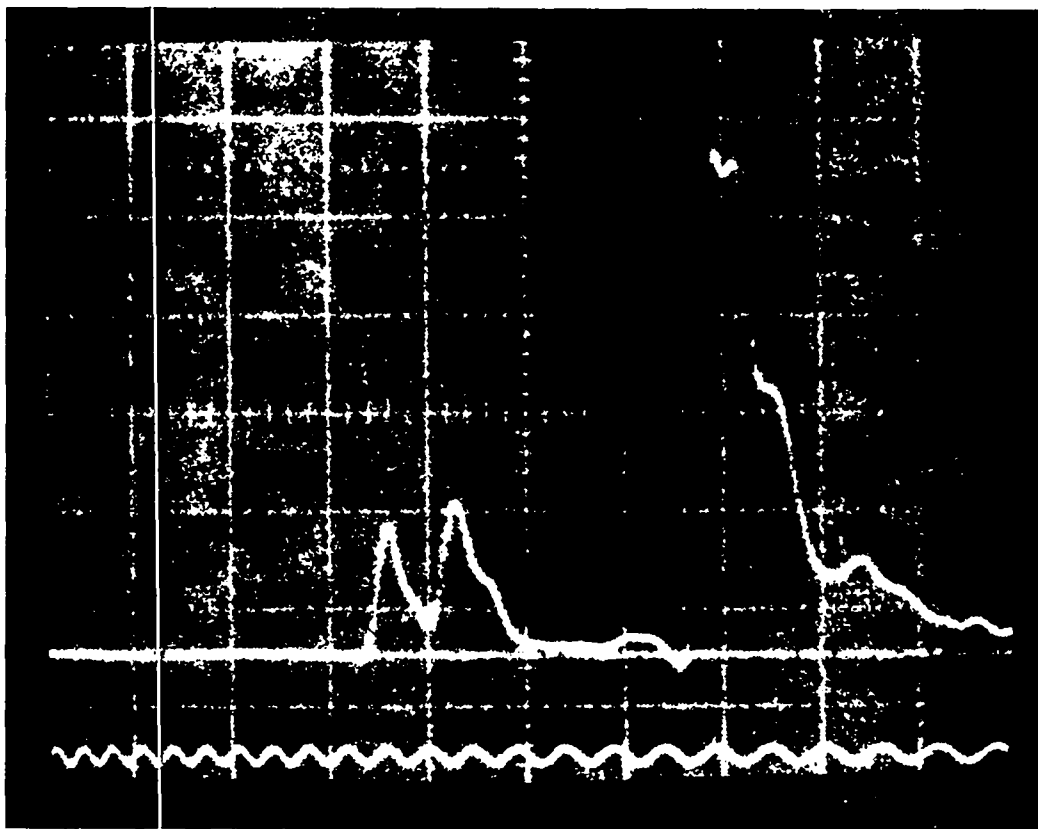
Fig. III-1. Temporally resolved backscatter from a 6.7-μm iron-coated spherical target. The two pulses at the left are identical samples of second-harmonic light Fresnel-reflected from the front and back surfaces of the salt window that provides the retropulse signal. The single sample of 10.6-μm backscatter is optically delayed by 2.87 ns. Only one sample of 10.6-μm backscatter is obtained because one of the window surfaces is antireflection-coated for 10.6-μm light. The lower calibration trace is a 2-GHz sine wave.

Figure III-4 shows experimental data in which the titanium K_α line intensity is plotted against the foil separation distance for different foils and irradiation parameters. The results can be summarized as follows.

- The K_α signal and ion energy emitted from the rear foil were significantly decreased for foil separation D of >2.5 mm for CH_2 and >0.6 mm for gold.
- From the separation at which the K_α signal decreases and from the laser pulse length τ, the average shorting velocity D/τ for CH_2 is estimated to be $\simeq 2.1 \times 10^8$ cm/s (which is comparable to an ion sound speed c_i of 2.2×10^8 cm/s for H^+ ions at $T_{hot} = 50$ keV).
- The average shorting velocity is much slower for gold ($\sim 5 \times 10^7$ cm/s) and, when set equal to the ion sound speed c_i at $T_{hot} = 50$ keV, implies an average charge state of ~ 10.
- A smaller front foil diameter does not alter the observation.

In conclusion, we have demonstrated that vacuum insulation works and that the experimental results are consistent with theory at high current levels. Results for gold foils seem more optimistic than theory has predicted. These slower plasma expansions suggest that preheat can be significantly reduced for high-Z targets. We have yet to investigate vacuum insulation at lower current levels, which might be a problem for pellet preheat.

EFFECT OF HYDROGEN IN CO_2 LASER-CREATED CARBON PLASMAS (F. Begay)

Previous experimental results[5] have suggested that target geometry and contamination of surfaces with hydrogen can affect the behavior of energy transport in laser-produced plasmas. We have, therefore, performed
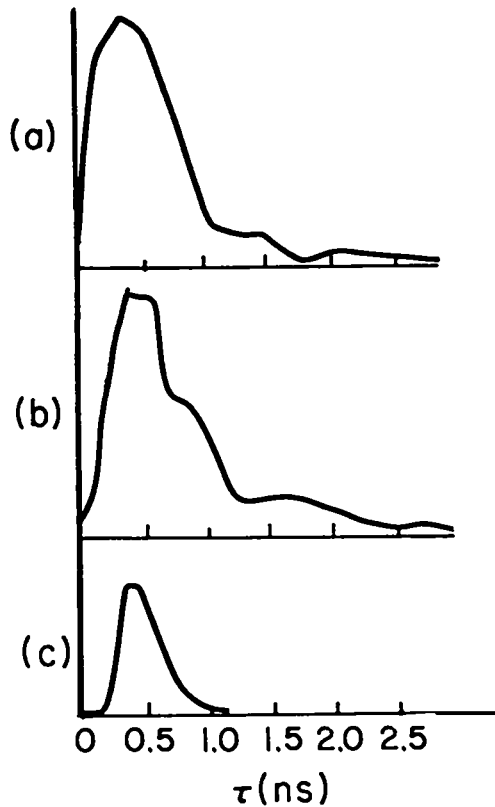
35

Fig. III-4. The titanium·K_α line intensity is plotted against the foil separation distance for front CH foils of 2-mm and 25-μm thickness and 1-μm-thick gold foils of 5-mm and 0.5-μm diam. Solid curves represent theoretical prediction for different values of T_{hot} with hydrogen plasma. The dashed lines illustrate abrupt behavior of the data at larger separations for CH and gold.

Fig. III-2. (a) Incident and (b) backscattered pulse shapes from a 6.7-μm iron-coated spherical target. (c) The second harmonic. Amplitudes are not to scale; horizontal (time) scales are equal.
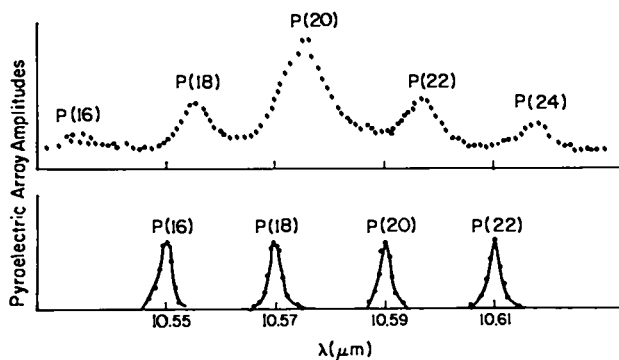

Fig. III-3. Backscattered 10.6-μm spectrum from a GMB with 14 μm of gold, upper trace. Individual lines, identified from the incident spectrum, are labelled according to the CO_2 transitions. Lower spectrum (unshifted) is the calibration obtained from a cw CO_2 laser.

experiments to study the plasma dynamics, as determined by the velocity distribution of fast ions, in targets from which surface hydrocarbon contaminants could be removed. The results suggest that ion velocity distributions and hot-electron temperatures inferred from the slope of the velocity distribution are dependent on both geometry and the presence of hydrogen.

We performed experiments at Gemini on targets consisting of carbon wire (250-μm diameter) or polyethylene (CH_2) foil. A single laser beam of 80-160 J, 1 ns FWHM, was focused on the target with a focal spot diameter of ~100 μm. The wire targets were heated by an electrical current to a temperature of approximately 1500°C to eliminate impurities in the wire. Experimental conditions are summarized in Table III-I. Typical results are given for plasmas formed from a pure carbon wire target, a carbon wire target with hydrogen impurities, and a CH_2 foil target.

A Thomson parabola mass analyzer[5] and the cellulose-nitrate-film particle detector measured the ion velocity distribution. The reproducibility of the Thomson data is quite sensitive to details of the laser-target interaction process. The structure of the supersonic

TABLE III-I. Summary of Experimental Conditions

Target	Laser Energy (J)	Laser Pulse Width at FWHM (ps)	Laser Irradiance (W/cm²)
Pure carbon wire	83.2	1100	9.6×10^{14}
CH foil	85.5	1100	9.9×10^{14}
CH wire	161.7	1100	1.87×10^{15}

expansion of the outer low-density region of a laser-irradiated target depends sensitively on the laser intensity[6] and on the electron distribution function.[7] In addition, various charge states in the expanding plasma can further complicate the expansion process. Experiments show that several different charge states are typically present and that the ions are accelerated at different rates,[8,9] possibly because acceleration of ions in the ambipolar field is proportional to the charge-to-mass ratio Z/A if ion-ion collisions are sufficiently weak. Once the different ion species begin to separate, they are susceptible to an ion-ion streaming instability[10,11] that may have a variety of nonlinear consequences. Separation will primarily occur in regions of high-density gradients, for example, at rarefaction shock fronts.[7] Because the strongest rarefaction shock can occur at the critical surface,[6] most ion species can separate near the critical-density region. If they fail to separate in this front, they will not separate farther out in the corona because of adiabatic cooling of the ions.

In addition to the above considerations, ion angular distributions[12] measured with sheets of CR-39 solid-state film at large solid angles show that the emission characteristics of the ion source exhibit a complicated nonuniform structure. The Thomson instrument, which has a small solid angle, would measure a limited portion of the ion source.

Figures III-5 and III-6 show the raw data from the Thomson parabola instrument for the pure carbon and for the CH₂ plasma, respectively. In Fig. III-6 there is a parabolic trace between the C^{+1} and C^{+2} parabolic traces, which is apparently caused by contaminants in the target. Also, the carbon parabolic traces in Fig. III-5 terminate at the high-energy end on a horizontal line, indicating that the maximum ion energy per ion charge state is a constant. On the other hand, the carbon traces

in Fig. III-6 terminate at the high-energy end on a tilted line, indicating that the maximum ion energy is a constant.

Figures III-7, III-8, and III-9 show ion velocity distributions for pure carbon and CH₂ plasmas. In Fig. III-8, the presence of hydrogen induces a cutoff[13] in the carbon velocity distribution at a velocity of approximately 5×10^8 cm/s. This density cutoff was also reported in Ref. 13. The general flattening of the dn/dv curves below 5×10^8 cm/s arises from particle-track saturation of the film. The cutoff at the low-velocity end is apparently caused by a cutoff in the film response. Consequently, with the cellulose-nitrate film, we can typically obtain good spectra with ion velocities $>4 \times 10^8$ cm/s to make hot-electron temperature determinations.

In Figs. III-7 through III-9 we show a least squares fit of the function $\exp(-v/v_0)$ to each ion species, where v is the ion velocity and v_0 is the scale velocity. The particle-track-saturated portion of the dn/dv curve was not included. Table III-II shows the scale velocities obtained by this method. If these scale velocities are interpreted as the speed of sound for the various species, we can infer an electron temperature for an isothermal expansion. The reproducibility of electron temperature measurements depends on how well one can reproduce the details of the laser/target interaction process. This table also gives the maximum ion energy for each species. For pure carbon plasma, the inferred electron temperature is ~31 keV, and the maximum kinetic energy-to-ion charge ratio is a constant. On the other hand, the CH plasma is accelerated with an apparent electron temperature of ~12 keV, and the maximum kinetic energy for the carbon ions is a constant. In this case, we are not able to fit a scale velocity for the carbon flow because most of the velocity distribution in the fast-ion region is missing.
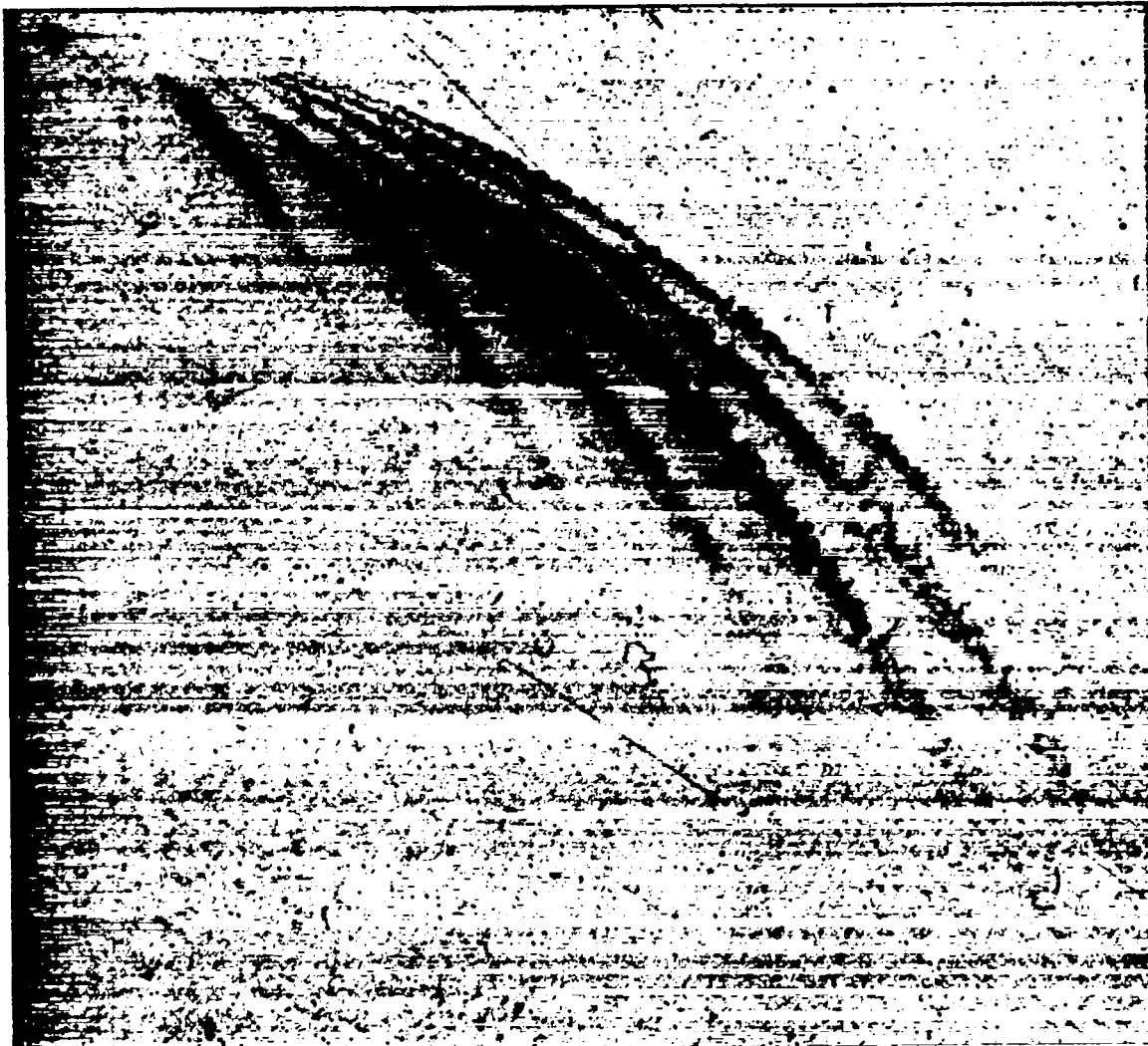
Fig. III-5. Raw data from Thomson instrument for pure carbon plasma.

Physical conditions near the critical surface can be estimated from experimental results for the coronal region and from theoretical results reported by Forslund et al.[14] The hot-electron energy[14] (in keV) is given approximately by

$$T_h \simeq 14.0 (I\lambda^2)^{1/3} T_c^{1/3} \quad , \tag{III-2}$$

where I is the laser intensity in units of 10^{16} W/cm^2, λ is the laser wavelength in micrometers, and T_c is the background electron temperature at the critical density. Forslund et al. also show that the ratio of the hot-electron density to the critical electron density can be expressed as

$$\frac{n_h}{n_{cr}} = \alpha \frac{v_0}{v_e} \quad , \tag{III-3}$$

38

where α is the fraction of the incident laser flux absorbed, $v_0 = e\,E_0/m_e\omega$ is the electron oscillating velocity, e is the electronic charge, E_0 is the laser free-space electric field, ω is the laser frequency, and $v_e = 4.19 \times 10^7 T_c^{1/2}$ cm/s is the electron thermal velocity. We assume a = 0.35.

From the experimental data, Eqs. (III-2) and (III-3), and the penetration density $n_u = (2 - \alpha)I/cT_c$, we obtain the plasma parameters near the critical surface (Table III-III). The high densities to which the CO_2 laser apparently penetrates are consistent with strong profile modification. The most remarkable finding is that the presence of hydrogen in the target greatly reduces the temperature near the critical surface. One explanation is that the absorbed laser energy does not remain in the laser spot when hydrogen is present. Either it goes into fast-ion blowoff or into heating more material outside the laser spot. The experimental data reported here show no evidence for more energy in fast-ion blowoff when hydrogen is present. However, data indicating strong lateral heat conduction were obtained recently in experiments at the NRC[15] and at Los Alamos.[16]

Table III-III also lists results from an experiment with a CH wire illuminated with 1.88×10^{15} W/cm^2. Although the carbon wire was heated electrically to 1500°C in the CH experiment, small amounts of hydrogen remained in the target and altered the behavior of the carbon plasma. The hot-electron temperatures for the carbon wire and CH wire experiments are approximately the same; this suggests that the hot-electron temperature depends on target geometry because a lower hot-electron temperature was determined for the CH foil. This may be caused by a larger lateral transport on the foil than on the wire. Furthermore, the characteristics of the carbon ion flow in the CH wire are similar to the characteristics of the carbon ion flow in the CH; that is, the presence of hydrogen in the CH wire does induce a cutoff in the carbon ion velocity distribution.

A theoretical model was developed to treat the problem of the collisionless expansion of an isothermal electrostatic multi-cold-ion quasi-neutral plasma. Details of the model and this experiment are discussed in Ref. 17.

In summary, the presence of hydrogen significantly affects the velocity distribution of carbon ions. The addition of hydrogen or a planar geometry appears to reduce the hot-electron temperature inferred from the ion distribution, possibly because of cooling of the critical region by lateral heat transport.

TABLE III-II. Plasma Parameters for CH and Pure Carbon Plasmas

Ion Type	Scale Velocities (10^7 cm/s)		Electron Temperature (keV)		E_{max} (MeV)	
	Carbon Plasma	CH Plasma	Carbon Plasma	CH Plasma	Carbon Plasma	CH Plasma
H$^+$	---	10.6 ± 0.044	---	11.7 ± 0.02	---	0.56 ± 0.001
C^{+1}	5.45 ± 0.22	---	37.2 ± 0.05	---	0.4 ± 0.002	1.47 ± 0.002
C^{+2}	6.84 ± 0.27	---	29.3 ± 0.05	---	2.2 ± 0.004	1.47 ± 0.002
C^{+3}	8.36 ± 0.33	---	29.2 ± 0.06	---	3.8 ± 0.006	1.63 ± 0.003
C^{+4}	9.98 ± 0.4	---	31.2 ± 0.05	---	5.8 ± 0.01	1.65 ± 0.003
C^{+5}	10.9 ± 0.44	---	29.8 ± 0.05	---	7.3 ± 0.01	1.61 ± 0.003
C^{+6}	12.2 ± 0.5	---	31.0 ± 0.05	---	8.9 ± 0.01	1.87 ± 0.003
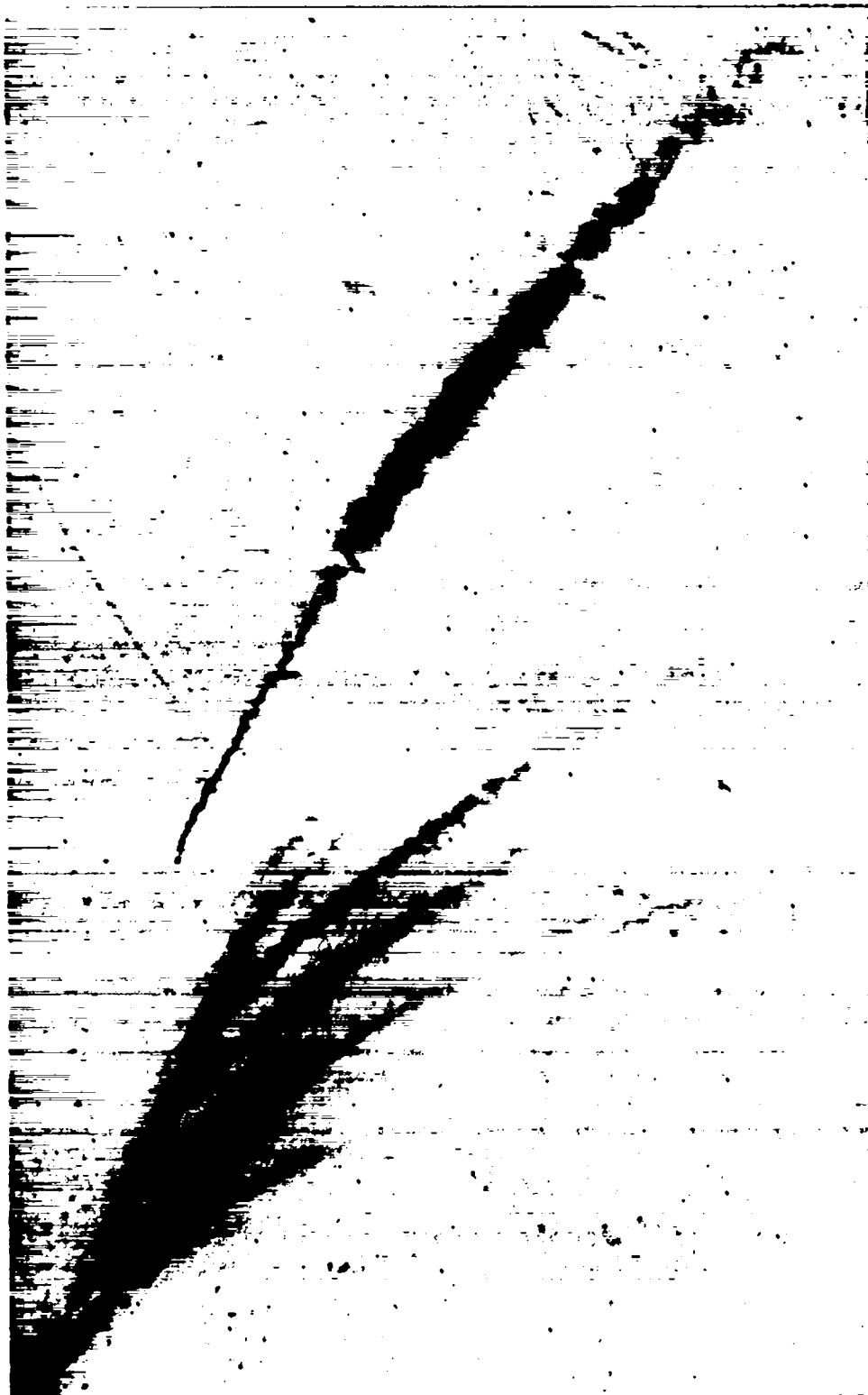
Fig. III-6. Raw data from Thomson instrument for CH plasma.
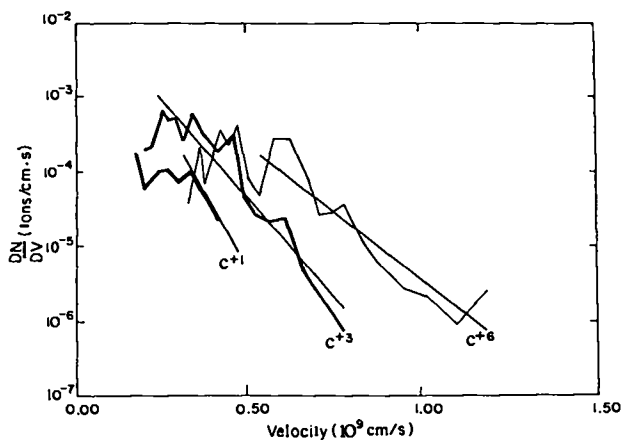
Fig. III-7. C^{+1}, C^{+3}, and C^{+6} in pure carbon plasma, electron temperature ~31 keV.
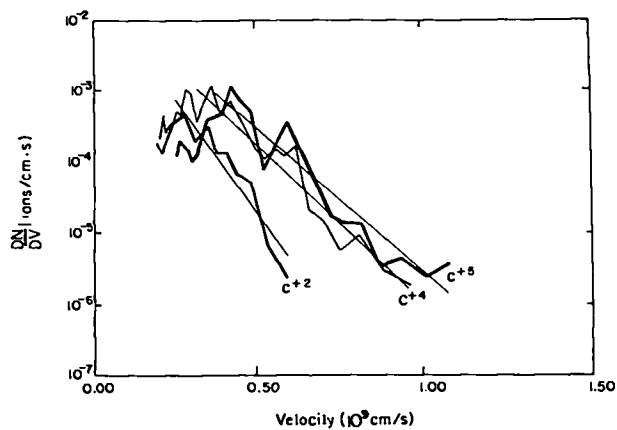
Fig. III-8. Experimental ion velocity distribution for C^{+2}, C^{+4}, and C^{+5} in pure carbon plasma. Electron temperature ~31 keV, errors for velocity less than 10%.
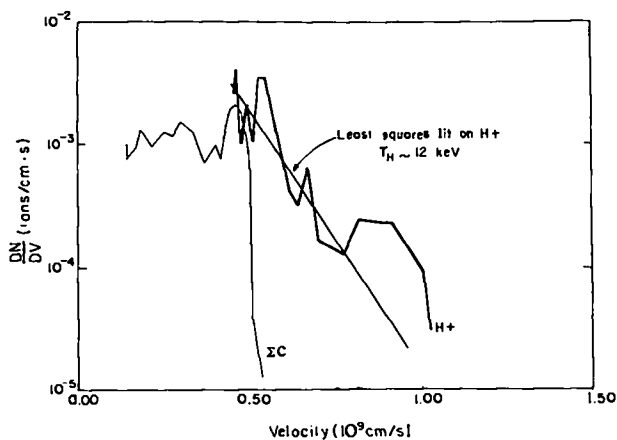
Fig. III-9. Experimental ion velocity distributions for CH plasma. Carbon plasma is represented as a single fluid, electron temperature ~12 keV. Errors for velocity less than 4%, errors for density less than 10%.

TABLE III-III. Plasma Parameters Near the Critical Region

	Carbon wire	CH film	CH Wire
Laser intensity I, W/cm²	9.6×10^{14}	9.9×10^{14}	1.88×10^{15}
Hot-electron temperature T_H, keV	31.0	12.0	23.0
Cold-electron temperature T_C, keV	1.0	0.060	0.205
Hot-electron density n_h, cm⁻³	2.23×10^{19}	9.2×10^{19}	7.3×10^{19}
Penetration density n_u, cm⁻³	3.3×10^{20}	5.6×10^{21}	3.15×10^{21}
T_H/T_C	31.0	211.0	74.0
v_0/v_e	6.37	26.3	14.4
n_h/n_u	0.11	0.027	0.049
n_u/n_{cr}	20.0	340.0	103.0

41

TIME-RESOLVED BREMSSTRAHLUNG
(W. Priedhorsky, R. H. Day)

The time history of the hard x-ray (>100-keV) emission from a laser fusion target can help us understand the mechanisms for generating high-energy electrons. We have measured the time history of hard x-ray emission from 10.6-μm laser-irradiated microballoons and found that the emission closely follows the laser pulse shape. We also found that the high-energy x-ray emission is generated simultaneously with the low-energy x-ray emission to ± 150 ps.

The measurements were made with a single-channel detector, CYCLOPS, which consists of an NE111 scintillator quenched with 3% benzophenone coupled to an ITT4014 photodiode. The scintillator impulse time response is 240 ps, and the cable system has a response time of 330 ps for a system time response of 400 ps. CYCLOPS can discriminate by TOF against background for ions or electrons of energy <500 keV.

Figure III-10 shows the spectral response curve of CYCLOPS, calculated from the filter transmission and the energy absorption cross section of the plastic. This sensitivity was normalized to the spectra measured from 80 to 240 keV with the APACHE detector system.

CYCLOPS measured the high-energy x-ray emission from a high-Z microballoon target. A comparison between the incident laser pulse shape and the x-ray emission for the same shot is shown in Fig. III-11. The x-ray pulse length, 820 ps FWHM, is close to the laser pulse length, 670 ps, convolved with the detector response time; the shape of the signals is similar. There is

Fig. III-11. Comparison of CYCLOPS hard x-ray signal and laser pulse shape.

no evidence for a late-time signal that might be caused by electron- or ion-induced background; however, the absolute timing between the two signals was not measured. We measured the absolute time difference between the onset of soft and hard x-ray emission and found that the two signals are simultaneous to within ± 150 ps for CO_2 illumination on microballoon targets.

HOT-ELECTRON ENERGY DEPOSITION IN SPHERES (W. Priedhorsky, R. H. Day)

Recent experiments show that high-intensity illumination of laser fusion targets with 10.6-μm laser radiation generates a very intense high-energy electron distribution, as discussed in the Appendix. The transport and energy deposition of these electrons in the target is of critical concern in target design. We have investigated this process by irradiating CH-coated gold shells with CO_2 radiation and measuring both the temperature and the yield of high-energy x-ray bremsstrahlung as a function of plastic thickness. Results indicate that (1) the hot-electron spectra for CH and gold absorbers are identical; (2) persistence of hard x-ray emission at large plastic thicknesses implies an electron temperature >100 keV; and (3) hard x-ray slope, absolute yield, and variation with CH thickness can be fit either with a one-dimensional Maxwellian electron distribution (temperature 390 keV and 25% absorption) or a three-dimensional Maxwellian electron distribution (temperature 340 keV and 19% absorption). Comparisons to LASNEX calculations corroborated the data.

Fig. III-10. Spectral response of CYCLOPS.

Figure III-12 shows a typical target, a 2-μm-thick nickel shell coated with 12 μm of gold. Layers of CH, varying in thickness from 0 to 200 μm, were applied to the surface of the target. All eight beams of Helios symmetrically illuminated the target at a peak laser intensity of 5×10^{15} W/cm^2. The laser energy ranged from 5.9 to 7.4 kJ in a 0.75-ns pulse. The hard x-ray emission was measured by the 10-channel APACHE filtered detector system described in Sec. V.

The 10 APACHE channels were then fit to the relationship

$$E_x = CE_L \, e^{-h\nu/kT} \quad , \qquad \text{(III-4)}$$

where E_L is the input laser energy and E_x is the high-energy x-ray output. The x-ray temperature kT and the conversion efficiency parameter C are fit by a minimum χ^2 criterion. Table III-IV lists the results of the experiment, showing the target parameters (ΔxAu, ΔxCH, and target diameter); the number of each type of target n; and the x-ray spectral characteristics, temperature T_H, and hard x-ray yield E_x/E_L.

We conclude (1) that the characteristic electron spectra are independent of the medium absorbing the energy and that the hard x-ray temperature remains the same, whether the laser irradiates a bare gold ball or strikes a plastic-coated shell; and (2) that the hot-electron spectrum is very penetrating because 200 μm of plastic is insufficient to shield the gold shell from the energetic electrons. The electron energy must be in excess of 100 keV to penetrate such a thick layer. These conclusions are corroborated by the detailed modeling with LASNEX that is reported in Sec. IV.
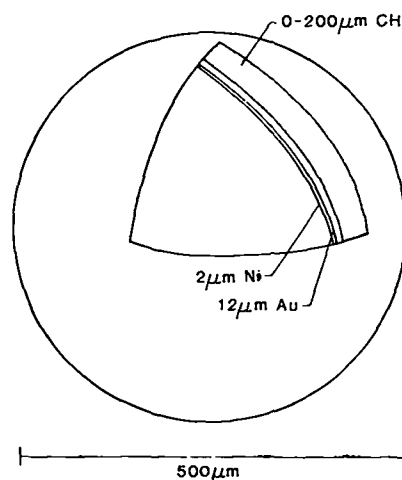
Fig. III-12. Target configuration for hot-electron deposition experiment.

TABLE III-IV. Hot-Electron Deposition Experiment

Target Type	No. of Targets	Diameter[a] (μm)	ΔxAu[a] (μm)	ΔxCH (μm)	T_H(x ray)[b] (keV)	E_x/E_L
Bare	5	501 ± 4	13.5 ± 1.5	0	202 ± 9	0.227 ± 0.008
Thin CH	6	513 ± 2	13.3 ± 1.8	2.9 ± 1.5	196 ± 7	0.172 ± 0.009
50-μm CH	5	493 ± 13	10.1 ± 0.8	45.8 ± 1.9	195 ± 6	0.107 ± 0.011
125-μm CH	4	500 ± 7	11.6 ± 1.8	126 ± 3	203 ± 8	0.041 ± 0.004
200-μm CH	2	507 ± 14	8.9 ± 1.9	205 ± 7	200[c]	0.013 ± 0.007

[a] 1-σ scatter.
[b] 1-σ error of mean = σ/n.
[c] Assumed to calculate E_x/E_L.

REFERENCES

1. D. M. Villeneuve, G. D. Enright, M. D. Burgess, R. Fedosejevs, and M. C. Richardson, Phys. Rev. Lett. 47, 515 (1981).

2. Francis F. Chen, "Stimulated Brillouin Scattering," Internat. Conf. on Plasma Physics, Nagoya, Japan, April 7-11, 1980, UCLA Reprint No. PPG-486.

3. "Laser-Fusion Program at LASL, January 1—June 30, 1976," Los Alamos Scientific Laboratory report LA-6510-PR (November 1976), p. 79; "Laser Fusion Program at LASL, January 1—June 30, 1977, Los Alamos Scientific Laboratory report LA-6982-PR (April 1978), p. 75.

4. K. Lee, D. Forslund, and J. Kindel, Nucl. Fusion 19, 11 (1979).

5. A. W. Ehler, F. Begay, T. H. Tan, J. Hayden, and J. McLeod, J. Phys. D: Appl. Phys. 16, L30 (1980).

6. K. Lee, D. W. Forslund, J. M. Kindel, and E. L. Lindman, Phys. Fluids 20, 51 (1977).

7. B. Bezzerides, D. Forslund, and E. Lindman, Phys. Fluids 21, 2179 (1978).

8. A. W. Ehler, J. Appl. Phys. 46, 2464 (1975).

9. R. DeCoste and B. H. Ripin, Appl. Phys. Lett. 31, 68 (1977).

10. D. W. Forslund and C. R. Shonk, Phys. Rev. Lett. 25, 281 (1970).

11. R. J. Faehl and W. L. Kruer, Phys. Fluids 20, 55 (1977).

12. J. Kephart, A. W. Ehler, S. Gitomer, R. Goldman, F. Begay, T. H. Tan, A. Williams, D. van Hulsteyn, S. Pederson, J. Hayden, and J. Sollid, Bull. Am. Phys. Soc. 26, 934 (1981).

13. C. Joshi, M. C. Richardson, G. D. Enright, Appl. Phys. Lett. 34, 625 (1979).

14. D. W. Forslund, J. M. Kindel, and K. Lee, Phys. Rev. Lett. 39, No. 5, 284 (1977).

15. R. Fedosejevs, I. V. Tomov, N. H. Burnett, G. D. Enright, and M. C. Richardson, Phys. Rev. Lett. 39, No. 15, 932 (1977).

16. A. W. Ehler, F. Begay, T. H. Tan, and P. H. Castine, J. Phys. D: Appl. Phys. 13, L65 (1980).

17. F. Begay and D. W. Forslund, "Acceleration of Multi-Species Ions in CO_2 Laser-Produced Plasmas: Experiments and Theory," Phys. Fluids (to be published), LA-UR-81-1137.

Hard-X-Ray Measurements of 10.6-μm Laser-Irradiated Targets

W. Priedhorsky, D. Lier, R. Day, and D. Gerke

University of California, Los Alamos National Laboratory, Los Alamos, New Mexico 87545

(Received 1 June 1981; revised manuscript received 16 November 1981)

The first measurements of high-energy x-ray emission ($h\nu \sim 30-300$ keV) by high-Z microballoon targets irradiated at $5\times10^{14} < \psi < 2\times10^{16}$ W/cm^2 by 10.6-μm laser light are reported. An exponential spectrum with a slope $kT_H \sim 250$ keV provides the best fit to spectrometer data at $\varphi_1 = 10^{16}$ W/cm^2. The hard-x-ray yield indicates that a substantial fraction, probably between 10% and 100%, of the absorbed laser energy is converted to hot electrons. The slope kT_H is proportional to the fastest ion energy.

Laser-fusion target performance can be significantly limited by fuel preheat. Energetic electrons created at the laser absorption surface deposit energy in the fuel, preventing efficient compression. The electron distribution may be diagnosed by measurement of high-energy x-ray bremsstrahlung created by electron interaction with the target material. We report the first such measurements of targets irradiated by the 10.6-μm Helios CO$_2$ laser facility.[1]

The slope of the target hard-x-ray continuum was determined by a least-squares fit to signals from a ten-channel array of broadband filter-scintillator channels spanning the region $h\nu \approx 30-300$ keV. Five of the channel response functions are shown in Fig. 1. Priedhorsky and Lier describe the instrument, and its calibration, analysis, and background tests in detail.[2]

A series of gold- or tungsten-coated solacels (hollow nickel microballoons) were irradiated at a range of focus conditions. The laser energy ranged from 2 to 8 kJ in a 0.75-ns (full width at half maximum) pulse. The targets were 300 and
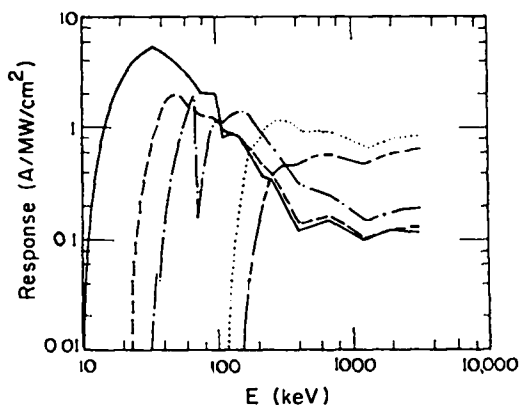

FIG. 1. Five typical spectral response functions from the ten-channel high-energy x-ray spectrometer.

1000 μm in diameter, with 1-2-μm nickel walls coated with 10-15 μm of high-Z material. There is no direct measurement of laser intensity; it is instead estimated from the peak laser power, measured with a pyroelectric detector and normalized by calorimeter data, and from the nominal laser spot size. The laser spot-size diameter containing 50% of the laser energy was determined from earlier encircled energy measurements; shots were taken with 85-, 120-, and 300-μm spot sizes, corresponding to a focus 150, 400, and 1000 μm beyond the irradiated surface. The peak laser intensity averaged over the half-power diameter is $\varphi_{1/2} = \frac{1}{2}P/A$, where P is the peak laser power, and A is the half-energy area.

The observed signals could be fitted well by an exponential spectrum,

$$F(h\nu) = A \exp(-h\nu/kT_H),\tag{1}$$

where A is in units of J/keV sr. The kT_H were determined by a least-squares fit. Combining errors in calibration and signal readout, we estimate 1σ errors ranging from 10% to 25% in the detector signals. The smallest errors correspond to the most recent measurements. The spectrometer data were fitted by exponentials with acceptable χ^2. Given an exponential fit, all kT_H which fit the data with $\chi^2 < \chi_{min}^2 + 1$ are acceptable at a 1σ level of confidence.[3] This confidence level includes random and systematic errors; the relative shot-to-shot error is smaller.

Computer simulations indicate that kT_H is an underestimate of the hot-electron temperature. The calculations assume a Maxwellian electron distribution,

$$dN/dE_e \propto E_e^{(n/2)-1} \exp(-E_e/kT_e).\tag{2}$$

The electron energy is E_e, kT_e is the hot-electron temperature, and n is the dimensionality of the Maxwellian distribution. Theoretical studies of hot-electron generation indicate a Maxwellian electron distribution, with dimensionality n from 1 to 3 depending on the mechanism generating the hot electrons.[4] Most hot electrons are bound by the target potential, so that they deposit their energy in the vicinity of the target.[5] In that case, they might produce a "thick-target" bremsstrahlung spectrum, similar to that from an x-ray tube, where the electrons are completely stopped by the target. The classical thick-target bremsstrahlung cross section would yield an approximately exponential x-ray spectrum, with slope kT_e, for an electron distribution as in Eq.

(2). However, preferential loss of energy to fast-ion expansion from the most energetic electrons softens the bremsstrahlung spectrum. Variation of bremsstrahlung cross section and time averaging over the laser pulse also contribute to the discrepancy between kT_H and the peak kT_e. For $kT_e = 100-500$ keV, the simulations yield approximately exponential x-ray spectra with $kT_H = (0.5-0.8)kT_e$.

The total radiated energy implied by Eq. (1) is $E_x = 4\pi A kT_H$, under the assumption of symmetrical radiation. Because of the flat response of the detectors, E_x can be measured more accurately than the slope kT_H. E_x is calculated from the best-fit spectrum, but for any acceptable kT_H, the implied E_x is within 10% of the best-fit value. E_x is normalized to a fractional x-ray yield $Y = E_x/E_L$, where E_L is the laser energy.

By comparing a Ross-filtered pair of spectrometer channels, we have determined that strong gold K-line emission is not interfering with our estimate of the continuum slope. To a 2σ level of confidence, tungsten $K\alpha$ emission is less than 6.4% of the total integrated hard-x-ray flux.

The best-fit x-ray temperature, kT_H, from the hard-x-ray spectrometer is plotted against $\varphi_{1/2}$ in Fig. 2. The data are best fitted by the power law

$$kT_H = 93 \left(\frac{\varphi_{1/2}}{10^{15} \text{ W/cm}^2} \right)^{0.42 \pm 0.12} \text{ keV},\tag{3}$$

for $5 \times 10^{14} < \varphi_{1/2} < 2 \times 10^{16}$ W/cm^2. The uncertainty of the exponent obtains mostly from uncertainty in the laser spot size, and thus $\varphi_{1/2}$. We assume that $\varphi_{1/2}(150\text{-}\mu\text{m defocus})/\varphi_{1/2}(1000\text{-}\mu\text{m defocus})$ is known to within a factor of 2. The scaling of kT_H with energy at constant focal condition is consistent with Eq. (3) (see Fig. 2).
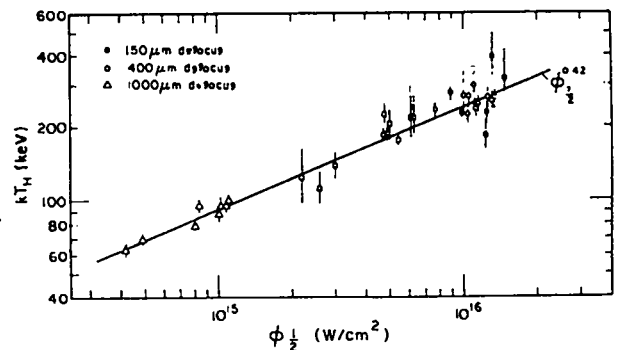
Previous experimental studies have shown

FIG. 2. X-ray continuum slope kT_H as a function of $\varphi_{1/2}$ for high-Z shell targets.

much lower x-ray temperatures at 10.6-μm laser intensities which nearly overlap ours.[6,7] For instance, Enright, Richardson, and Burnett find $kT_H = 10$ keV at $\varphi_{1/2} = 2\times10^{14}$ W/cm^2,[7] a value inconsistent with a modest extrapolation of Eq. (3). The earlier experiments involved single-beam illumination of low-Z slabs with a 50–100-μm focal spot, unlike the present high-Z, multiple-beam, large-focal-spot (at low intensity) experiment. Additionally, Enright, Richardson, and Burnett measured the x-ray spectrum from 4 to 25 keV, while the present measurement is weighted to much higher energy. Kephart, Godwin, and McCall showed that the x-ray spectrum at $\psi_{1/2} \approx 10^{14}$ W/cm^2 hardens with increasing photon energy[6]; measurement at higher energies thus yields higher temperatures. Our higher kT_H, compared to Refs. 6 and 8, is therefore not surprising. The intensity scaling of Eq. (3) is not inconsistent with previous experimental and theoretical studies, which suggest $kT_H \sim \varphi^{1/3}$.[7,9]

We observe that the hard-x-ray yield increases with x-ray temperature. Figure 3 shows Y as a function of kT_H. The yield data are bounded by the relationship

$$Y = (1.2^{+0.6}_{-0.4})\times10^{-5}kT_H \text{ (keV)}. \qquad (4)$$
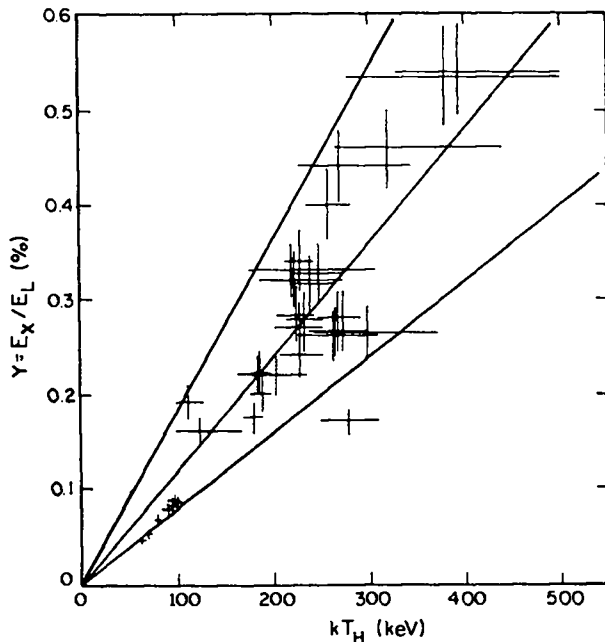
FIG. 3. High-energy x-ray yield Y as a function of kT_H. Y is the fraction of incident laser energy radiated in high-energy x rays. The solid lines show the best fit, and bounds, $Y = (1.2^{+0.6}_{-0.4})\times10^{-5}kT_H$ (keV).

The proportionality between Y and kT_H is reminiscent of the classical thick-target bremsstrahlung yield,[8]

$$f_x = 1.1\times10^{-6} ZE_e, \qquad (5)$$

where f_x is the bremsstrahlung efficiency for monoenergetic electrons of energy E_e (keV) incident on a target of atomic number Z. Keeping in mind that the fast-ion effects which reduce kT_H relative to kT_e also reduce the hard-x-ray yield from a given electron distribution, we would like to derive an estimate of the total energy in hot electrons required to produce the observed spectrum. One calculates, for the spectrum of Eq. (2) and dimensionality $n = 1$ to 3, a classical thick-target yield

$$Y_{tt} = (1.3-2.2)\times10^{-4}\alpha kT_e \text{ (keV)}, \qquad (6)$$

where α is the efficiency of conversion of incident laser energy to fast electrons. Equations (4) and (6) imply

$$\alpha = (0.04-0.14)(Y_{tt}/Y)(kT_H/kT_e). \qquad (7)$$

For Y_{rr}/Y and kT_H/kT_e of order unity, Eq. (7) suggests that the inferred electron spectrum is a substantial fraction of the absorbed laser energy (α could be no larger than the laser light fraction absorbed by the target, which is 0.25 for $\psi \approx 10^{13}-10^{15}$ W/cm^2).[10]

We observe the correlation between the velocity of the fastest ions emitted by the target and the kT_H from x-ray data, first reported by Tan, McCall, and Williams.[11] For planar targets irradiated with a single beam at $10^{12} < \varphi < 10^{14}$ W/cm^2,[11]

$$kT_H = 7.5\times10^{-18} v_i^2 \text{ keV}, \qquad (8)$$

where v_i is the fastest ion velocity in centimeters per second. Such a proportionality is to be expected for an isothermal expansion into vacuum.[12] At much greater intensity and in a spherical geometry, the same functional dependence holds. The present data can be fitted by

$$kT_H = 19\times10^{-18} v_i^2 \text{ keV}, \qquad (9)$$

over $5\times10^{14} < \psi_{1/2} < 2\times10^{16}$ W/cm^2.

Measurements of hard-x-ray radiation from 10.6-μm laser-illuminated gold microballoons indicate a very penetrating and intense spectrum, with a best-fit exponential slope ~250 keV for $\psi_1 \sim 10^{16}$ W/cm^2. The hard-x-ray yield implies that a significant fraction of the absorbed laser energy is converted to energetic electrons. The hot-electron population inferred from hard-x-

ray measurements presents a major problem for 10.6-μm laser-fusion target design at high intensities.

We would like to acknowledge helpful comments on the analysis and presentation of these results from D. Wilson, A. Petschek, S. Singer, D. Giovanielli, G. Stradling, and F. Cordova. This work was performed under the auspices of the U. S. Department of Energy.

[1]R. L. Carlson *et al.*, IEEE J. Quantum Electron. 17, 1662 (1981).

[2]W. Priedhorsky and D. Lier, to be published.

[3]M. Lampton, B. Margon, and S. Bowyer, Astrophys. J. 208, 177 (1976).

[4]K. Estabrook and W. L. Kruer, Phys. Rev. Lett. 40, 42 (1978).

[5]D. V. Giovanelli, J. F. Kephart, and A. H. Williams, J. Appl. Phys. 47, 2907 (1976).

[6]J. F. Kephart, R. P. Godwin, and G. H. McCall, App. Phys. Lett. 25, 108 (1974).

[7]G. D. Enright, M. C. Richardson, and N. H. Burnett, J. Appl. Phys. 50, 3909 (1979).

[8]A. H. Compton and S. K. Allison, *X-Rays in Theory and Experiment* (Van Nostrand, Princeton, 1957).

[9]D. W. Forslund, J. M. Kindel, and K. Lee, Phys. Rev. Lett. 39, 284 (1977).

[10]V. M. Cottles, Bull. Am. Phys. Soc. 22, 1090 (1977); D. Giovanielli, private communication; R. Kristal, Bull. Am. Phys. Soc. 25, 1014 (1980).

[11]T. H. Tan, G. H. McCall, and A. H. Williams, Los Alamos National Laboratory Report No. LA-UR-80-900, 1980 (unpublished).

[12]J. E. Crow, P. L. Auer, and J. E. Allen, J. Plasma Phys. 14, 65 (1975).

Our theoretical support activities are closely coupled to our experimental efforts to achieve a fundamental understanding of laser/target interactions, including relevant plasma physics and hydrodynamics. The close coupling of theory and experiment has made it possible to eliminate faulty theories and to design more reliable advanced targets for CO_2 laser drivers. In general, basic studies have shown that the design difficulties associated with long wavelengths are greater than those at much shorter wavelengths, but that breakeven target designs are attainable even in the presence of a hot-electron spectrum. These results have significantly increased our confidence that scientific breakeven can be demonstrated with CO_2 lasers in the megajoule range.

INTRODUCTION

Our theoretical support continues to address primarily the laser/target coupling problem with CO_2 light. Because there are no comparable lasers at shorter wavelengths, it is imperative that we accurately assess this problem and its effect on target designs. Our recent work has centered on the generation and transport of hot electrons. Although we are studying other mechanisms like Raman scattering in greater detail, we are still focusing on resonant absorption in strongly steepened density profiles as an important source of hot electrons. We are pursuing the possibility of flux-limiters in both hot- and cold-electron transport by refining our calculations for classical collisional transport further. A growing interest in the laser/target-interaction problems at short wavelength is evidenced by our work on inverse bremsstrahlung and its effect on transport.

HIGH HARMONIC LIGHT FROM STEEP DENSITY PROFILES
(B. Bezzerides, R. D. Jones, D. W. Forslund)

All work on harmonic generation in laser-irradiated plasmas, which has been discussed in general experimental[1,2] and theoretical papers,[3] has been confined primarily to second harmonic (SH) emission. Attempts made to explain SH by perturbation theory assume a weakly nonlinear response of the plasma in which the source current for the SH is due to beats between components of the first harmonic field. Higher harmonics up to the eleventh harmonic of CO_2 have been reported by a Canadian group.[4] The relative efficiency of the emitted lines in this work was a decreasing function of harmonic number, again the result of a weakly nonlinear plasma response. Recently, CO_2 harmonics as high as the 29th and even as high as the 46th have been reported.[5,6] The constant relative efficiency of the lines is a unique feature requiring a new explanation of the data that goes beyond any analysis based on mode-coupling and perturbation theory. Furthermore, these data are compelling evidence for an unexplored nonlinearity in the study of laser/plasma interactions.

To explain some of the properties of this nonlinearity, we start with the radiation field

$$\vec{B}(\vec{x},t) = \int \left(\frac{[\vec{J'}]}{cR} + \frac{[\vec{J'}]}{R^2} \right) \times \hat{R} \, dt \, , \qquad \text{(IV-1)}$$

where the brackets denote retarded time; the current $\vec{J} = -en\vec{v}$, with n and $\vec{v}$ being the electron fluid density and velocity, respectively; and $\hat{R} = \vec{x} - \vec{x}'$. Introducing the Lagrangian variables $\vec{x}' = \vec{x}_0' + \delta (\vec{x}_0', \tau')$, $\tau' = \tau'$, where $\delta = \int d\tau' \vec{v}(\vec{x}_0', \tau')$ and $n_e d^3 x' = n_0 d^3 x_0'$, we find for the far field

$$\vec{B}(\vec{x},t) = -\frac{e}{c^2} \left[\int d^3 x_0' n_0 \frac{\hat{R} \times (\partial/\partial \tau) \, \vec{v} \, (\vec{x}_0', \tau)}{R} \right] \, ,$$

$$\text{(IV-2)}$$

where n_0 is the fixed ion density. We have neglected relativistic corrections and used $\omega\delta/c \ll 1$, which requires $v_0/c \ll 1$, $v_0 = eE_0/m\omega_0$ with E_0 the incident field intensity, and $\hat{R} = \vec{x} - \vec{x}_0'$. This form for $\vec{B}$ is useful because it shows that only the fluid acceleration in Lagrangian coordinates is needed to calculate $\vec{B}$. Even though hot electrons are produced at high incident

intensity, Lagrange-transformed variables may be used for all time because fluid-element crossing does not occur if the full electron pressure is included in the electron Euler equation.[7] Except for the integral over the radiating material, Eq. (IV-2) is identical to the single-particle result and leads to the well-known Larmor formula for the total power radiated.

The acceleration is given by

$$\frac{\partial \vec{v}}{\partial t} + \frac{1}{2} \vec{\nabla} v^2 = -\frac{e}{m} \vec{E} - \frac{\vec{\nabla} \cdot \underline{P}_e}{mn_e} \, , \qquad (IV-3)$$

based on the relation $\vec{\nabla} \times \vec{v} = e\, \vec{B}/mc$, where $\underline{P}_e$ is the electron-pressure tensor. We now limit our attention to a layered medium with density gradient in the x-direction only. This limitation produces two important simplifications. First in Eq. (IV-3), $\partial/\partial x \, v_x^2 \gg \partial/\partial x \, v_y^2$ near the critical density because heating primarily occurs in the x-direction. Second, as a general result we observe that because of the symmetry of the layered problem, the functional dependence on y and t of all field quantities is in the combination $(y \sin \theta \omega/c - \omega t)$. Thus, as long as $v_y/c \sin \theta \ll 1$, we can write for the Lagrange-transformed acceleration from Eq. (IV-3) ($E = E_x$, $v = v_x$)

$$\frac{\partial \tilde{v}}{\partial \tau} = -\frac{e}{m} \tilde{E}(\vec{x}_0, \tau) - \frac{(\partial/\partial x) \tilde{P}_e}{m \tilde{n}_e} \, . \qquad (IV-4)$$

(The tilde denotes the corresponding Lagrange-transformed quantities.) From the x-component of Ampere's law and Poisson's equation, the field is given by

$$\frac{\partial E}{\partial \tau} + v \frac{\partial E}{\partial x} = c \frac{\partial B}{\partial y} - v \frac{\partial E_y}{\partial y} + 4\pi e n_0 v \, . \qquad (IV-5)$$

By using the arguments we relied on to derive Eq. (IV-4) from Eq. (IV-3) and by using the y-component of Ampere's law, we find from Eq. (IV-5)

$$\frac{\partial}{\partial \tau}(\tilde{E} + \sin \theta \tilde{B}) = 4\pi e n_0 \tilde{v} \, , \qquad (IV-6)$$

or

$$-\frac{e}{m} \tilde{E}(\vec{x}_0, \tau) = \frac{e}{m} \sin \theta B(\vec{x}_0 + \tilde{\delta}, \tau)$$

$$+ \int_{x_0}^{x_0 + \delta_x} dx_0' \omega_p^2 (x_0') \, . \qquad (IV-7)$$

The first term in Eq. (IV-7) is the effective driver caused by the obliquely incident field, whereas the second term is the plasma-restoring force. For gentle gradients, Eqs. (IV-4) and (IV-6) lead to the usual driven harmonic oscillator equation of resonant absorption.

For steep density profiles, numerical solutions of Eqs. (IV-4) and (IV-6) show that the more general form of the restoring force leads to a strongly anharmonic oscillator and almost impulse-like acceleration in the critical surface region. The other terms in Eq. (IV-4) can be ignored when the restoring force is strongly anharmonic. The pressure force is small for $\omega_{pu}^2/\omega^2 \gg 1$, with ω_{pu} the upper-shelf plasma frequency. Also the effect of hot-electron production on the harmonics can be ignored, because it occurs on a time scale of $2\pi/\omega$. Finally, the driving term acts only in the underdense region and thus can be ignored.

Next we show by way of a model how the restoring force produces emitted harmonic light. Consider a steeply rising density profile with plasma frequencies ω_{pu} and $\omega_{p\ell}$ ($\omega_{pu} \gg \omega > \omega_{p\ell}$) corresponding to the upper and lower density shelves, respectively. In the limit of a density jump for the profile at $x_0 = 0$, the restoring force is simply $-\omega_p^2 \delta$, with $\delta(x_0 = 0, \tau) = \delta$. Figure IV-1 shows the periodic solutions for δ and $\ddot{\delta}$. The solution in the overdense region is

$$\delta = (\delta)_u \cos\left(\frac{\omega_{pu}}{\omega} \theta\right) \, . \qquad (IV-8)$$
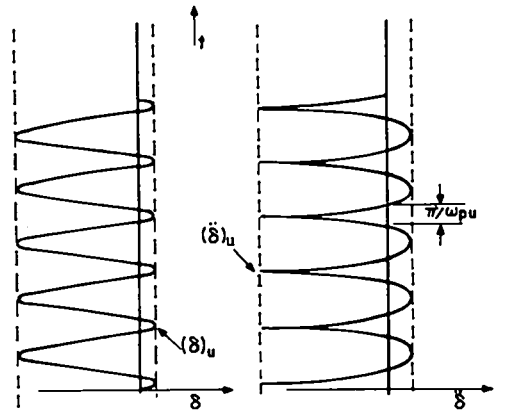
In contrast, in the underdense region

Fig. IV-1. Displacement δ and acceleration $\ddot{\delta}$ of a fluid element as it oscillates in and out of the density jump.

$$\delta = K \sin\left(\frac{\omega_{p\ell}}{\omega}\theta + \phi\right)\frac{v_0}{\omega}\cos(\theta + \psi) , \qquad \text{(IV-9)}$$

with $\theta = \omega\tau$, $v_0 = eE_0/m\omega$, where E_0 is the effective driven intensity. K, ϕ, and ψ are to be determined by the appropriate boundary conditions at the jump, namely,

$$\delta(\bar{\theta}) = 0 ,$$

$$\delta(2\pi - \bar{\theta}) = 0 , \qquad \text{(IV-10)}$$

and

$$\dot{\delta}(\bar{\theta}) = -\dot{\delta}(2\pi - \bar{\theta}) ,$$

where $\bar{\theta} = \omega\bar{\tau}$, with $\bar{\tau}$ the time at which δ crosses the step. Using $\omega_{pu}/\omega \gg 1$ and Eqs. (IV-8)-(IV-10), we find

$$K \sin\phi = -v_0/\omega ,$$

$$K \cos\phi = -(v_0/\omega)\tan\left(\pi\frac{\omega_{p\ell}}{\omega}\right) , \qquad \text{(IV-11)}$$

$$\sin\psi = 0 ,$$

and, therefore,

$$(\delta)_u = \left(\frac{n_c}{n_u}\right)^{1/2}\frac{v_0}{\omega}\left(\frac{n_\ell}{n_c}\right)^{1/2}\tan\left[\pi\left(\frac{n_\ell}{n_c}\right)^{1/2}\right] ,$$

$$\text{(IV-12a)}$$

and

$$(\ddot{\delta})_u = \left(\frac{n_u}{n_c}\right)^{1/2}\omega v_0\left(\frac{n_\ell}{n_c}\right)^{1/2}\tan\left[\pi\left(\frac{n_\ell}{n_c}\right)^{1/2}\right] . \quad \text{(IV-12b)}$$

The strong acceleration shown in Eq. (IV-12b), which occurs essentially over the time π/ω_{pu} as seen from Eq. (IV-8), will cause high harmonic emission from the step region.

To estimate the emission rate into the nth spectral line $\omega_n = n\omega$, we Fourier-analyze $\ddot{\delta}^2$ to obtain

$$(\ddot{\delta}^2)_{\omega_u} = \left(\frac{n_\ell}{n_c}\right)\tan^2\left[\pi\left(\frac{n_\ell}{n_c}\right)^{1/2}\right]\omega_{pu}\omega v_0^2\, A\left(\frac{n\omega}{\omega_{pu}}\right) ,$$

$$\text{(IV-13)}$$

where $A(x) \simeq 1$, $x \ll 1$ and $A(x) \to 0$, $x \gg 1$, which is consistent with the reciprocal relation between time and frequency for Fourier transforms. The detailed form of A is not crucial to our discussion. Recalling that Eq. (IV-2) leads to the well-known Larmor formula for total power emitted for a single particle, we can obtain a lower bound for the emission in the nth harmonic by assuming incoherent emission to find

$$I_n \simeq \frac{2}{3}\frac{e^2}{c^3}\left(\frac{n_\ell}{n_c}\right)\tan^2\left[\pi\left(\frac{n_\ell}{n_c}\right)^{1/2}\right]\omega_{pu}v_0^2$$

$$\int dx_0 n_0(x_0) \quad \text{for } \frac{n\omega}{\omega_{pu}} < 1$$

$$I_n \to 0 \text{ for } \frac{n\omega}{\omega_{pu}} \gg 1 , \qquad \text{(IV-14)}$$

where the integral in Eq. (IV-14) is over the depth of the radiating plasma. This result confirms the principal experimental observation that high harmonics have a flat spectrum with a well-defined cutoff and predicts a rolloff for the spectrum at

$$n_{max}^2 = \frac{n_u}{n_c} . \qquad \text{(IV-15)}$$

Thus, as suggested by a recent simulation study of high harmonic emission,[5] one can directly measure the upper density from Eq. (IV-15) given the cutoff harmonic number. In Ref. 5, Eq. (15) was empirically determined by performing a series of numerical simulations. In this analysis we see that the cutoff is a natural consequence of the anharmonic response of the plasma-restoring force. A lower bound on conversion efficiency is obtained by using Eq. (IV-14), assuming a radiating depth equal to the skin depth of the upper density c/ω_{pu}, and using $n_\ell/n_c \sim 0.1$, as indicated by high-power simulation studies. Then $\eta_n = I_n/I_{inc} \sim 1/4 \times 10^{-8}\, n_{max}^2/\lambda$, where λ is the vacuum wavelength in micrometers, a result that is about one-tenth that observed.[6] However, one must remember that the assumption of incoherent emission results in a lower bound estimate.

We have demonstrated that the principal source of high harmonic emission is the strong nonlinear restoring force, which exists when resonant absorption occurs in a highly steepened density profile. We have also shown that Eq. (IV-15) is a general and direct consequence of such a nonlinear form of resonance absorption that can be used with some confidence to determine the density of the upper shelf. In addition, we have demonstrated that the source of the harmonic emission originates in the critical surface. Therefore, if harmonic emission is temporally and spatially resolved, one can directly measure the position and velocity of the critical surface front, with wide-ranging implications for CO_2 laser/plasma diagnostics. These results are independent of the approximations used in the theoretical analysis. The finite gradient of the density profile will alter the time profile of the acceleration, but this change should merely affect the rolloff of the spectrum not the number of excited harmonics. An accurate determination of the excursion length δ into the low-density region of the profile would require accounting for the dissipation of the electrostatic wave in the step region of the profile, including hot-electron production, but this determination would only influence the calculation of the emission intensity.

THERMAL EFFECTS ON FIELD SATURATION
IN RESONANCE ABSORPTION
(S. J. Gitomer, B. Bezzerides)

We have used a Lagrangian warm-fluid model to study the saturation of the critical electric field in both wavebreaking and convectively stabilized regimes of resonance absorption. Comparison of our results with particle simulations shows that even in the convectively stabilized regime, hot-electron production is evident.

Since the classic work of Ginzberg,[8] the study of resonance absorption in a warm plasma has advanced by the use of particle simulation techniques.[9] Whereas the Ginzberg work achieves a saturated electric field level solely through the convective stabilization of the field produced by finite background temperature, particle simulations show the importance of hot-electron production for stabilization at sufficiently high values of the external field. Thus, for strong driving, the background temperature will probably be less important for establishing the final electric field level. Wavebreaking in cold-plasma models[10] has provided useful scaling laws when the background temperature can be completely ignored. Although the precise connection between wavebreaking

and hot-electron production is not understood, it is often argued[11] that the onset of wavebreaking in the fluid theory indicates the creation of hot electrons.

To assess the relative importance of background temperature on the level of the saturated electric field in resonance absorption, Kruer[11] combined results from the cold-fluid model[10] and a homogeneous undriven water-bag model.[12] This calculation predicts the effect of plasma temperature on wavebreaking amplitudes. The prediction is in reasonable agreement with the results of particle simulations for relatively low temperatures. In this section, we present a consistent fluid model of a driven, inhomogeneous, warm plasma. In such a model, the effect of hot-electron production is not included. Comparisons with particle simulations show that saturated field levels obtained from both the fluid model and an approximate analytic theory agree well with each other.

Consider an inhomogeneous plasma of mobile electrons and fixed ions. A fluid model consisting of the equations of continuity, momentum, and adiabatic pressure, coupled with Poisson's equation, forms our starting point:

$$\frac{\partial n}{\partial t} + \frac{\partial}{\partial x}(nv) = 0 \ , \tag{IV-16a}$$

$$\frac{\partial v}{\partial t} + v \frac{\partial v}{\partial x} = -\frac{e}{m_e}(E + E_0) - \frac{1}{m_e n}\frac{\partial P}{\partial x} \ , \tag{IV-16b}$$

$$\frac{P}{n^3} = \text{constant} \ , \tag{IV-16c}$$

and

$$\frac{\delta E}{\delta x} = 4 \pi e \left[n_0(x) - n(x, t) \right] \ . \tag{IV-16d}$$

In Eq. (IV-16), n and v are the fluid density and velocity, e and m_e are the electron charge and mass, E and E_0 are the self-consistent and driving electric fields, P is the pressure, and n_0 is the fixed ion density. In the Lagrangian warm-fluid model we use results from transforming the above Eulerian system of equations by using $x = x_0 + \delta(x,\tau)$ and $t = \tau$, where the Eulerian coordinates x,t are related to the initial fluid element coordinate x_0, the Lagrangian displacement δ, and the time τ. The fixed background ions have a linear ramp density profile with scale length L. By using the above transformation and

the functional relation $\tilde{f}(x_0,\tau) = f(x,t)$, we obtain the following equation of motion for δ:

$$\frac{\partial^2 \delta}{\partial \tau^2} + \nu \frac{\partial \delta}{\partial \tau} + \left[\omega_p^2(x_0) + \frac{\omega^2 \delta}{2L} \right] \delta$$

$$= -\frac{eE_D}{m_e} \sin \omega\tau \frac{1}{m_e n_0} \frac{\partial \tilde{P}}{\partial x_0} \ . \qquad \text{(IV-17)}$$

In this expression, ν represents both a spatially dependent ad hoc damping to avoid boundary anomalies and a linearized Landau damping contribution, ω_p is the local electron plasma frequency, and ω and E_D are the electric field driving frequency and amplitude, respectively. The pressure $\tilde{P}(x_0,\tau)$ is given by

$$\tilde{P}(x_0,\tau) = \frac{\tilde{n}^3(x_0,\tau)}{n_0^2(x_0)} kT_e \ , \qquad \text{(IV-18a)}$$

and the density $\tilde{n}(x_0,\tau)$ by

$$\tilde{n}(x_0,\tau) = \frac{n_0(x_0)}{1 + (\partial \delta / \partial x_0)} \ , \qquad \text{(IV-18b)}$$

where k is Boltzmann's constant and T_e the electron temperature.

The wavebreaking condition, which we use to evaluate our numerical solutions of Eq. (IV-17), is the peak velocity achieved in the fluid calculation before the mathematical condition $\partial \delta / \partial x_0 = -1$ is obtained. The contribution of linear Landau damping to the second term in Eq. (IV-17) is obtained from the inverse Fourier tranform

$$\nu(x,t) = \int \nu_L(K) \frac{\partial \delta}{\partial t}(K,t) \exp(iKx) \, dK \ . \qquad \text{(IV-19)}$$

Before considering the numerical solution of Eq. (IV-17), we present an approximate analytic solution. The equations we consider for δ and $\delta' = \partial \delta / \partial x_0$ (obtained by differentiation with respect to x_0 of the δ equation) are

$$\frac{\partial^2 \delta}{\partial \tau^2} + \omega_p^2 = x_D \omega^2 \sin \omega\tau - \frac{1}{mn_0} \frac{\partial P}{\partial x_0} \qquad \text{(IV-20)}$$

and

$$\frac{\partial^2 \delta'}{\partial \tau^2} + \omega_p^2 \delta' = -\frac{\delta \omega_p^2}{\partial x_0} \delta - \frac{\partial}{\partial x_0} \left(\frac{1}{mn_0} \frac{\partial P}{\partial x_0} \right) \ , \qquad \text{(IV-21)}$$

where $x_D = v_D/\omega$ and $v_D = eE_D/m_e\omega$. We assume Fourier-series solutions for δ and δ' of the form

$$\delta(\tau) = \delta_0(\tau) + \sum_{n=1}^{\infty} [C_n(\tau) \cos n\omega\tau + S_n(\tau) \sin n\omega\tau]$$

and

$$\delta'(\tau) = \delta_0'(\tau) + \sum_{n=1}^{\infty} [C_n'(\tau) \cos n\omega\tau + S_n'(\tau) \sin n\omega\tau] \ ,$$

where the Fourier coefficients are assumed to be slowly varying functions of τ. These solutions are substituted into Eqs. (IV-20) and (IV-21) and yield, after multiplication by $\sin \omega\tau$ or $\cos \omega\tau$ and integration over a period, equations for the $n = 1$ coefficients, which are evaluated at $\omega = \omega_p$. Where δ, δ', etc., appear explicitly, the cold-plasma results are to be used; that is, $\delta_0(\tau) = -\omega\tau/2 \ x_D \cos \omega\tau$, $\delta_0' = -1/2 \ (\omega\tau/2)^2 x_D L \sin \omega\tau$, $\delta_0''(\tau) = -1/3 \ (\omega\tau/2)^3 \ x_D/L \ 1/L \cos \omega\tau$, and $\delta_0'''(\tau) = 1/4 \ (\omega\tau/2)^4 \ x_D L (1/L)^2 \sin \omega\tau$.

The equations for $C_1(\tau)$ and $S_1(\tau)$ derived from Eq. (IV-20) are

$$\frac{\partial C_1}{\partial \tau} = \frac{v_e^2}{2\omega L} I_1 \qquad \text{(IV-22a)}$$

and

$$\frac{\partial S_1}{\partial \tau} = -\frac{v_e^2}{\partial \omega L} I_1 \frac{\omega\tau}{3} \ , \qquad \text{(IV-22b)}$$

where $v_e^2 = kT_e/m_e$. The integral I_1 is given by

$$I_1 = \frac{1}{\pi} \int_{-\pi}^{\pi} \frac{\sin\theta}{(1 - a\sin\theta)^3} d\theta = \frac{3a}{(1 - a^2)^{2.5}}$$

and $a = 1/2 \ (\omega\tau/2)^2 \ x_D/L$. The solution for S_1 (needed below) is then given by

$$S_1(\tau) = -\frac{4L}{3} \frac{v_e^2}{v_c^2} \left[\frac{1}{(1 - a^2)^{1.5}} - 1 \right] \ , \qquad \text{(IV-23)}$$

where v_c is the cold-plasma wavebreaking velocity[10] given by $v_c = (2\omega L v_D)^{1/2}$.

The equations for $C'_1(\tau)$ and $S'_1(\tau)$ are derived from Eq. (IV-21), with the additional feature that the temperature corrections to δ be included; that is,

$$\frac{dC'_1}{d\tau} = \frac{\omega}{2L} S_1(\tau) + \frac{v_e^2}{2\omega L^2} \left\{ \left[1 + \frac{7}{18}\left(\frac{\omega\tau}{2}\right)^2 \right] I_1 \right.$$
$$\left. + \frac{1}{12}\frac{x_D}{L}\left(\frac{\omega\tau}{2}\right)^4 I_2 \right\} \qquad \text{(IV-24a)}$$

and

$$\frac{dS'_1}{d\tau} = \frac{\omega}{2L} C_1(\tau) + \frac{v_e^2}{3\omega L^2} \frac{\omega\tau}{2} I_1 \ . \qquad \text{(IV-24b)}$$

In Eq. (IV-24a), the integral I_2 is given by

$$I_2 = \frac{1}{\pi} \int_{-\pi}^{\pi} \frac{d\theta}{(1 - a\sin\theta)^4} = \frac{2 + 3a^2}{(1 - a^2)^{3.5}} \ .$$

By hypothesizing that temperature corrections to δ'_0 will be important at a time $\omega\tau^*$ when the time derivatives of δ'_0 and C'_1 are equal, we arrive at an equation for this time given by
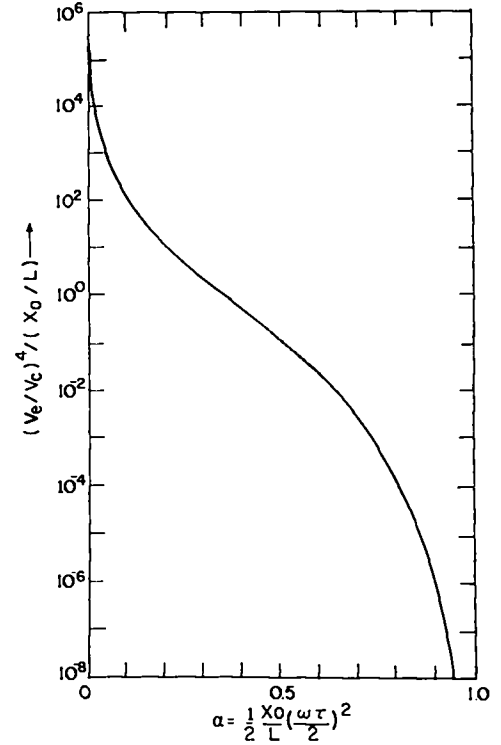
Fig. IV-2. Solution of Eq. (IV-25) of the text, $(v_e/v_c)^4/(x_D/L)$ vs α, provides approximate wave-breaking or convective saturation time given driver amplitude, background plasma temperature, and density scale length.

$$\frac{(v_e/v_c)^4}{x_D/L} = \frac{(1 - a^2)^7/18a^3}{\left\{ 1 - (4/9)\,a^2 + (x_D/L)\,[(1 - a^2)/a)] - (2/9)\,[(1 - a^2)^2/a^2]\,[1 - (1 - a^2)^{1.5}]\right\}^2} \ . \qquad \text{(IV-25)}$$

In Fig. IV-2 we display a plot of the right-hand side of Eq. (IV-25) vs α. The term $(x_D/L)(1 - a^2)/a$ has been ignored in obtaining the plot shown. Thus, for a given value of $(v_e/v_c)^4/(x_D/L)$, the corresponding α and $\omega\tau^*$ may be obtained. We will show how one can use this result to predict peak fluid velocities at breaking or saturation.

Consider the results of solving the fluid equations embodied in Eq. (IV-17) for two parameter choices: x_D/L = 1/250 (as was done in Ref. 11) and x_D/L = 1/6250. The solution of the fluid equations is followed in time either up to breaking ($x_D L$ = 1/250) or to convective saturation (x_D/L = 1/6250) for a number of background plasma temperatures. The results of these numerical

computations are shown in Figs. IV-3(a) and IV-3(b), where the peak fluid velocity v_p is plotted vs the thermal velocity v_e. Particle simulation results are included for comparison. The bands of particle simulation values in Fig. IV-3(b) result from the range of field maxima obtained over several tens of driver periods after saturation has occurred.

In addition, the results of the approximate analytic theory are used. That is, the time $\omega\tau^*$ predicted from Fig. IV-2 is inserted into the cold-plasma peak velocity formula, $v_p \approx \omega x_D \, \omega\tau^*/2$. (Note that $v_p/v_c = a^{1/2}$.) The fluid simulations, which exhibit breaking or saturation, show that the field growth faithfully follows the cold-plasma prediction. In both cases, finite plasma

54
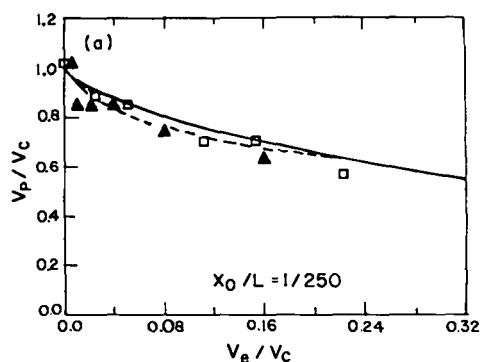
(a)
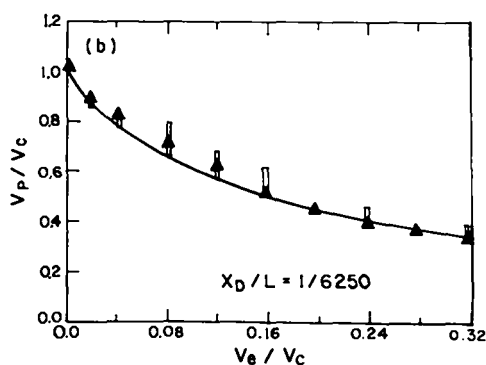
(b)

Fig. IV·3. Peak fluid velocity v_p vs thermal velocity v_e, both scaled to cold-plasma wavebreaking velocity v_c for (a) $x_D/L = 1/250$ and (b) $x_D/L = 1/6250$. Results from fluid simulations (triangles), particle simulations (squares[11] and bars), approximate analytic theory (solid curve), and theory from Ref. 11 (dashed curve).

(a)

(b)

Fig. IV-4. Fluid simulation results: magnitude of $\delta' = \partial\delta/\partial x_0$ vs time for (a) $x_D/L = 1/250$ and $v_e/v_c = 0.08$ and (b) $x_D/L = 1/6250$ and $v_e/v_c = 0.158$. Dashed lines represent the cold-plasma prediction that grows with time according to $(\omega\tau)^2$.

temperature causes the fluid to deviate from the cold-plasma result just at a time $\omega\tau^*$ given by the solution of Eq. (IV-25). Figs. IV-4(a) and IV-4(b) show this effect where δ' at the critical-density point is plotted vs time $\omega\tau$. The term $|\delta'|$ in Fig. IV-4(a) does not reach 1 because breaking occurs at a spatial point away from critical. The results of the fluid simulations, particle simulations, and approximate analytic theory shown in Fig. IV-3 are all in excellent agreement. Thus, as predicted in Ref. 11, the field saturation level decreases with increasing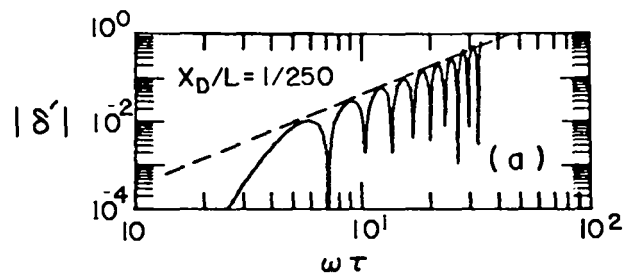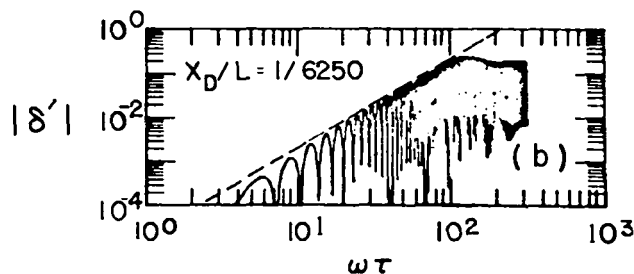 temperature. The effect appears to be more pronounced with weaker driving conditions or longer gradient lengths, that is, when x_D/L is smaller. This result was not

anticipated by Kruer[11] because scale-length-dependent theory did not enter into his final result.

The results displayed in Fig. IV-3 indicate a dependence on the particular value of x_DL. An alternative scaling may remove this dependence and yield a truly universal curve. We define a scaling parameter $\alpha = v_c/v_g$, where v_g is taken from the work of Ginzberg[8] in which the resonantly enhanced electric field saturates purely by convection in the warm plasma. The velocity v_g is given by $v_g = 1.2\, v_D\, (\omega L/v_e)^{2/3}$. The physical regimes encountered for various α values are (1) $\alpha \gg 1$—saturation by convection, no hot electrons; (2) $\alpha \approx 1$—saturation by convection, hot-electron production; and (3) $\alpha \ll 1$—wavebreaking, hot-electron production. In Fig. IV-5, the results of Fig. IV-3 are replotted, along with some additional data, as plots of v_p/v_g vs $\alpha = v_c/v_g$. As α increases from 0, the results approach the Ginzberg prediction.

If Figs. IV-5(a) and IV-5(b) are laid over each other, the results of the Lagrangian fluid simulations, particle simulations, and approximate analytic theory all follow

55
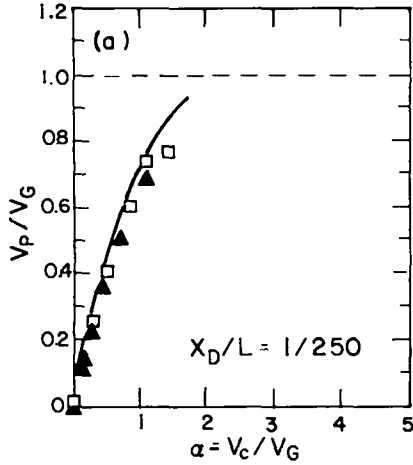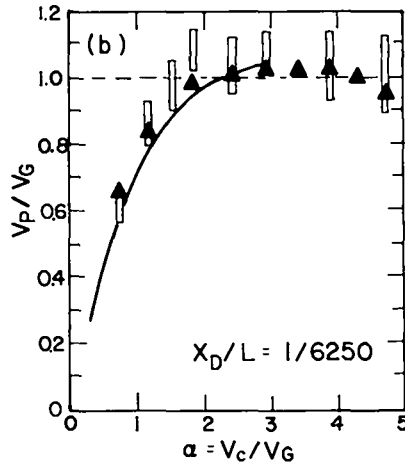
Fig. IV-5. Peak fluid velocity scaled to v_G vs the dimensionless parameter $\alpha = v_c/v_G$ for (a) $x_D/L = 1/250$ and (b) $x_D/L = 1/6250$. Results are from fluid simulations (triangles), particle simulations (squares[11] and bars), and the approximate analytic theory (solid curve). Dashed lines show the Ginzberg[a] prediction.

what appears to be a universal curve independent of x_D/L. Note that although all the particle simulations showed evidence of hot-electron production, only the fluid simulations with $x_D/L = 1/250$ exhibited wavebreaking. Thus, although we have not explained the connection between wavebreaking and hot-electron generation, we have shown that there is a regime, namely $\alpha \gtrsim 1$ in which hot electrons are observed without fluid wavebreaking.

We have derived the governing equation for a Lagrangian fluid model, which includes (in a consistent fashion) wavebreaking, warm-plasma effects, and convection. The model successfully predicts peak resonantly enhanced field values when compared with results from particle simulations. The dimensionless parameter α, which we introduced, provides a useful means to distinguish various regimes by isolating the physical effects responsible for field saturation.

ELECTRON TRANSPORT (R. J. Mason)

The identification of the physical mechanisms that require severe thermal-flux limiting on electron transport in laser-matter modeling has been a long-standing challenge to theorists.[13] Recently, our new, fully self-consistent Monte Carlo transport scheme[14] has been used to show[15] that the need for severe limiters derives from deficiencies in the classical diffusion modeling. These deficiencies cause excessive heating of the over-dense surface matter of a pellet, ignore coronal decoupling of the thermal electrons, and neglect the effects of electric fields on a return current through density gradients.

For the present calculations, we have retained many of the features of our earlier hybrid scheme,[16] except that now the ions and all the electrons are weighted particles. The weights are adjusted to match any initial density profile. The electrons are heated by giving them velocity increments from a Gaussian distribution at the heater temperature $k\Delta T = 2/3\ W$, where W is the absorbed particle energy per cycle cell. Heating is terminated when some prescribed temperature is achieved, or W is established in consistency with inverse-bremsstrahlung absorption up to the critical density. The electrons are scattered with the mean square deflection angle $<\theta^2> = 8\pi\ e^4 m^{-2} c^{-3}\ \Delta t Z n_i (Z + 1)\ \log \lambda \equiv 2\nu(c)\ \Delta t$. Here $c^2 = u^2 + v^2$, and v is the transverse velocity. However, now each electron loses energy and has its speed reduced by Coulomb drag against the other electrons, in accordance with $\Delta c = -4\pi e^4 (mkT_e)^{-1}\ \Delta t\ n_e\ G(\xi)\ \log \lambda$, $\xi = (mc^2/2kT_e)^{1/2}$, where $G(\xi) = 0.376\xi\ (1 + 0.542\xi - 0.504\xi^2 + 0.752\xi^3)^{-1}$ is a polynomial fit[14] to Spitzer's error function combination.

The lost energy is redeposited isotropically in the drift frame of the electrons by the usual heating procedure.

The electric field E is now calculated by the implicit-moment method,[14] which gives greater accuracy than plasma period dilation.[16] In this method, following the heating, scatter, and drag of particles, we accumulate the fluid density, flux, and total pressure moments $n_\alpha^{(m)}$, $j_\alpha^{(m)}$, and $_\alpha^{(m)}$ (α = h, c, and i for hot and cold electrons and ions, respectively). Then, we use the momentum, continuity, and Poisson equations to predict values ($\tilde{y}$) for the moments and fields at the end of the next cycle. Thus, storing all the information at level (m), we obtain

$$\tilde{j}_\alpha^{(m+1/2)} = j_\alpha^{(m)} - \frac{1}{m_\alpha} \left[\frac{\partial p_\alpha^{(m)}}{\partial x} - q_\alpha n_\alpha^{(m)} E^{(*)} \right] \frac{\Delta t}{2} ,$$

(IV-26a)

$$\tilde{n}_\alpha^{(m+1)} = n_\alpha^{(m)} - \frac{\partial}{\partial x} \left[\tilde{j}^{(m+1/2)} \right] \Delta t ,$$ (IV-26b)

and

$$\tilde{E}^{(m+1)} = 4\pi \int_0^x \sum_\alpha q_\alpha \tilde{n}_\alpha^{(m+1)} \, dx + \tilde{E}^{(m+1)}(0) ,$$ (IV-26c)

which, with the centering $E^{(*)} = [\tilde{E}^{(m+1)} + \tilde{E}^{(m)}]/2$, and the assumption $E(0) = j(0) = 0$ for a quiescent left boundary, rearrange to

$$\tilde{E}^{(m+1)} = 4\pi \left[\int_0^x \sum q_\alpha n_\alpha^{(m)} dx - \sum q_\alpha j_\alpha^{(m)} \Delta t \right.$$

$$\left. + \sum \frac{q_\alpha}{m_\alpha} \frac{\partial p_\alpha^{(m)}}{\partial x} \frac{(\Delta t)^2}{2} - \frac{\omega_p'^2 (\Delta t)^2}{4} \tilde{E}^{(m)} \right]$$

$$\left[1 + \frac{1}{4} \omega_p'^2 (\Delta t)^2 \right]^{-1} ,$$ (IV-27)

in which $\omega_p'^2 = (4\pi e^2/m)[n_e^{(m)} + (m/M)Z^2 n_i^{(m)}]$. For reduced noise with this centering, the n_α and j_α terms have been "softened" with the factors $\beta = \gamma = 0.25$, as described in Ref. 14. The particles are then advanced with $du/dt = q_\alpha E^{(*)}/m_\alpha$ and $dx/dt = u$.

With limited transport, one traditionally distributes the electron thermal energy in accordance with the following relations:

$$\frac{\partial T}{\partial t} = - \frac{\partial q_d}{\partial x} ,$$ (IV-28a)

$$q_d = \frac{q_u}{1 + |q_u| (f n_e m a^3)^{-1}} ,$$ (VI-28b)

$$a = \left(\frac{kT}{m} \right)^{1/2} ,$$ (IV-28c)

and

$$q_u = \frac{-K}{\gamma} (Z) \frac{\partial T}{\partial x} ,$$ (IV-28d)

where K is Braginskii's[17] conductivity given by

$$K = 5 \, n_e T \left(\frac{\tau_e}{2m} \right) ,$$ (IV-28e)

and τ_e is the scattering time for electrons off ions. For GMBs taking Z = 10, γ = 0.266. With classical limitation, f = 0.6; however, to model numerous experiments f ≤ 0.03 is required.

Figure IV-6(a)-(d) shows the results of applying the Monte Carlo scheme to transport in an end-heated uniform system. The electrons are heated from a background temperature of $T_c \equiv$ 0.43 KeV to a hot temperature of $T_h \equiv$ 1.72 keV over a test region 24 μm long. The plasma is at 10^{21} cm^{-3}, the critical density for 1.06-μm light. Cold electrons n_c are heated to become hot electrons n_h when they enter the heating region to the right. Frame IV-6(b) shows that $j_c^{\cdot}$ -j_h. Frame IV-6(c) compares the results for a standard diffusion calculation with f = 0.3, giving the T_d temperature profile and the Monte Carlo calculated temperature T_{MC}. It also shows the locally normalized heat flux is $f_{MC,d} \equiv |q_{MC,d}|$ $(mn_e a^3)^{-1}$. Although the fluxes agree at the heater
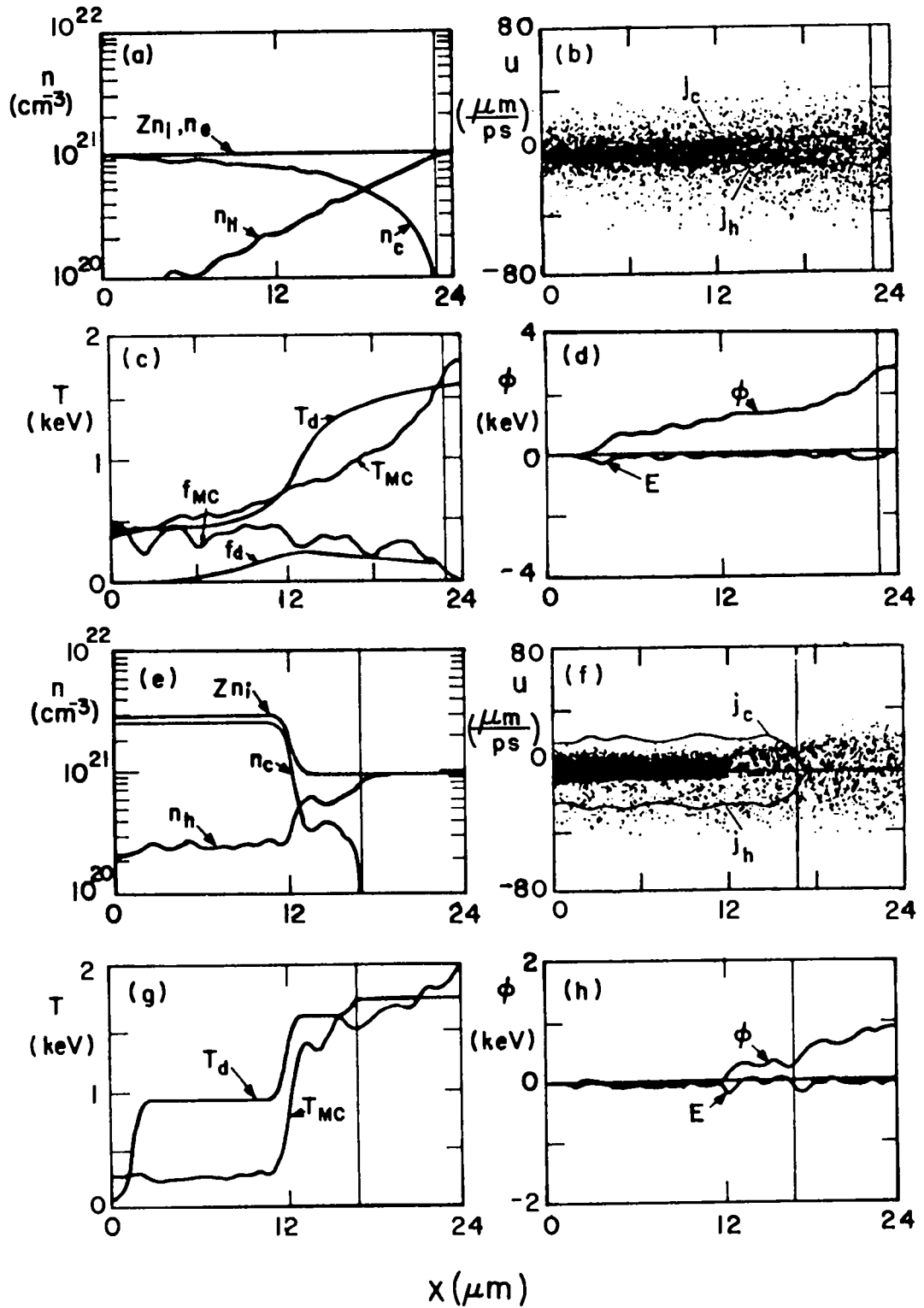
Fig. IV-6. An end-heated uniform plasma. (a)-(d). Transport through a density gradient. (e)-(h). $j_{h,c} \simeq 5 \times 10^{-21}$ $n_{h,c} u_{h,c}$ (u - cm^{-3}/ps), E in arbitrary units.

boundary, showing that f = 0.3 is the proper limit for this homogeneous problem, it is significant that $T_d \gg T_{MC}$ in the *body* of the plasma near the heater. This result is caused by the fact that the nonlinear limited diffusion front is convex, whereas the Monte Carlo front is concave, much like a free-streaming expansion. Thus, the diffusion wave heats matter adjacent to the heater to relatively higher temperatures, which should lead to relatively higher radiative emission and increased ablation. The Monte Carlo profile heats more matter in depth to lower temperatures. To bring the two body temperatures into greater accord, one could increase f at the expense of a thermal mismatch in the heater region.

The deficiencies in the diffusion modeling are more evident in the simulation of transport through an inhomogeneous plasma [Fig. IV-6(e)-(h)]. In this case, the density has been raised to 3×10^{21} cm^{-3} for x < 12 μm. The preponderance of hot electrons at low density, that is, *coronal thermal decoupling*, and the electric fields

needed to draw a return current down through the density jump result in both apparent and real thermal inhibition. In frame IV-6(g), the T_d front (for f = 0.6) is well ahead of T_{MC}, which is relatively stagnant at the density interface. However, with progressively larger f values, the penetration speed of the T_d front beyond the plateau is reduced, holding T_d closer to T_{MC}.

Finally, we study the combined consequences of these effects in Fig. IV-7. The energy is absorbed by inverse bremsstrahlung from a 1.06-μm laser at 10^{15} W/cm^2. Initially, the plasma runs from 5×10^{21} cm^{-3} down to a plateau at 10^{20} cm^{-3}, $T_e = 0.1$ keV, and Z = 10. In the limited single-group electron diffusion calculations used for comparison, the ions are accelerated by $E = -(en_e)^{-1} \partial(n_e T)/\partial x$. The results shown are for 9.6 ps.

Using the nucleon/electron mass ratio of 100, this snapshot corresponds to 41 ps of physical time. Frame IV-7(b) shows that the best match between the Monte Carlo and the diffusion *coronal density* profiles is
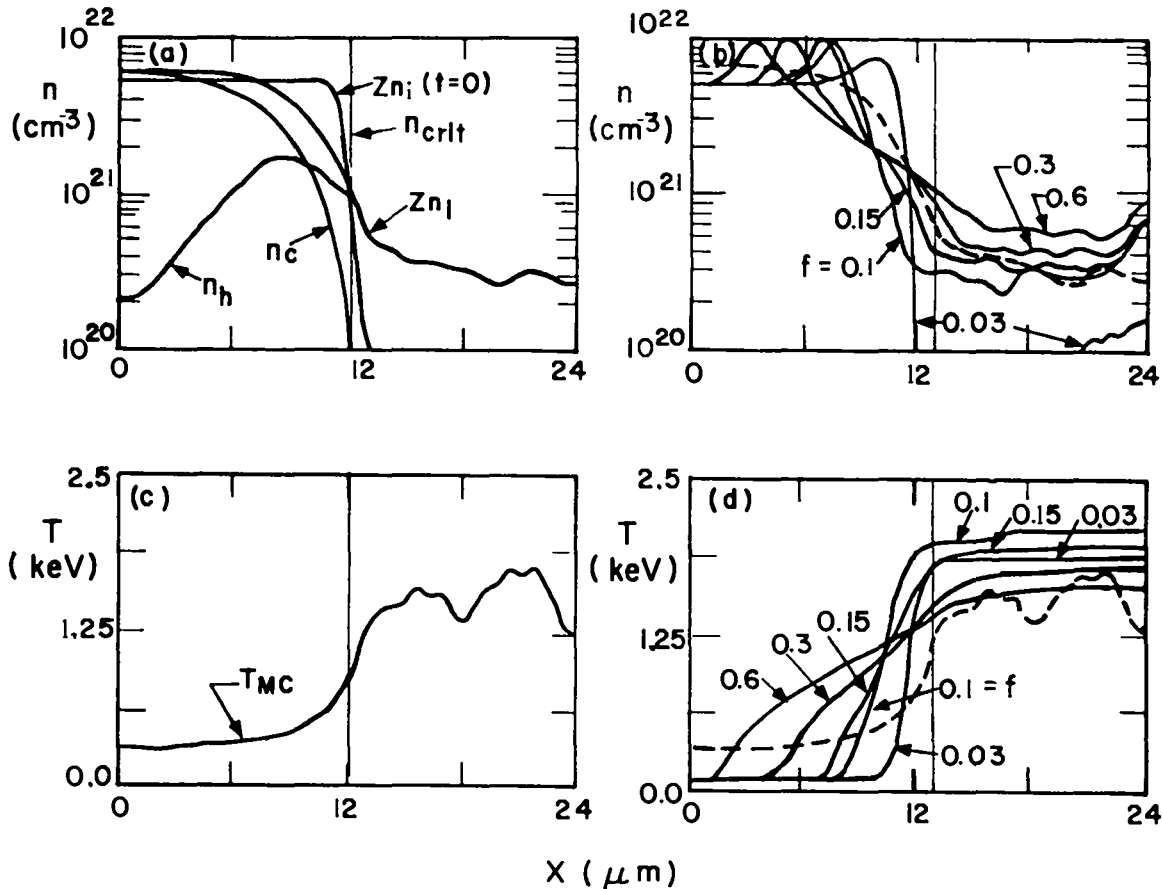

Fig. IV-7. Ablation calculated [(a),(c)] with Monte Carlo, and [(b),(d)] through flux-limited single-group diffusion, $-T_{mc}$, $-T_d$. Diffusion critical fiducial is for f = 0.6.

obtained with f = 0.15 or 0.1. Frame IV-7(d) shows a low-temperature Monte Carlo precursor ahead of all the diffusion fronts. However, in the *overdense plasma near critical*, $T_d \rightarrow T_{MC}$ as $f \rightarrow 0.6$. These two results are consistent with the apparent need for separate internal and coronal flux-limiters in the recent transport and absorption experiments at École Polytechnique.[18] Thus, the need for a severe transport flux-limiter has been traced to deficiencies in the diffusion modeling. Experimental temperature profile determinations near the critical surface should help to verify this conclusion.

HOT-ELECTRON PHYSICS (E. K. Stover)

The experiments on hot-electron transport and deposition described in Sec. III were modeled using the LASNEX hydrodynamics code. All simulations conducted were time-dependent, one-dimensional (radial) calculations in spherical geometry. We assumed that all absorbed incident laser light was absorbed at the critical surface and converted locally into suprathermal source electrons. We also assumed that these source electrons were uniformly distributed along the critical surface. We considered suprathermal source electrons defined by both 1D and 3D nonrelativistic Maxwellian spectra. The source electron temperature T_H was time dependent and constrained to track the laser pulse from the resonance absorption scaling expression

$$T_H(t) = \alpha \left[I(t)\lambda^2 \right]^{1/3} , \qquad (IV-29)$$

where $I(t)$, λ, and α are the laser intensity, the laser wavelength, and a constant, respectively. The background electron temperature dependence has been neglected. We modeled the laser pulse to have a 0.3-ns risetime and a 0.7-ns FWHM.

In LASNEX, suprathermal electron transport is modeled by a multigroup (energy) diffusion model. Suprathermal electron energy losses modeled include collisional losses to background ions and electrons, radiation loss, and collisionless losses arising from Joule dissipation and fast-ion losses. Collisionless energy losses occur primarily in the low-density corona; they serve as an energy sink for the suprathermal electrons that produce bremsstrahlung emission and collisionally loose energy in the bulk material. Gold is a diffusive material to energetic electrons because the electron range is an

order of magnitude greater than the scattering length. Therefore, suprathermal electrons will be locally isotropic as they slow down in gold. It may not be valid to consider CH a diffusive medium for suprathermal electrons. The ratio of electron-scattering length to range in CH is approximately one; therefore, the electron flux in CH probably will not be isotropic.

Bremsstrahlung radiation produced by interaction of suprathermal electrons with background material is transported by a LASNEX multigroup photon diffusion package. We used Elwert-corrected Bethe-Heitler bremsstrahlung cross sections to generate all LASNEX x-ray spectra discussed here.

Figure IV-8 compares suprathermal x-ray yields calculated by LASNEX with x-ray yields inferred from APACHE. The figure shows x-ray yields calculated by LASNEX for peak suprathermal source-electron temperatures ranging from 100 to 400 keV. We assumed 30% absorption of incident laser light. The plastic coating behaves like a relatively weak x-ray emitter and serves primarily as an energy absorber in these targets. This effect is evident in Fig. IV-8, in which both LASNEX and APACHE yields decay approximately one order of magnitude as plastic thickness increases
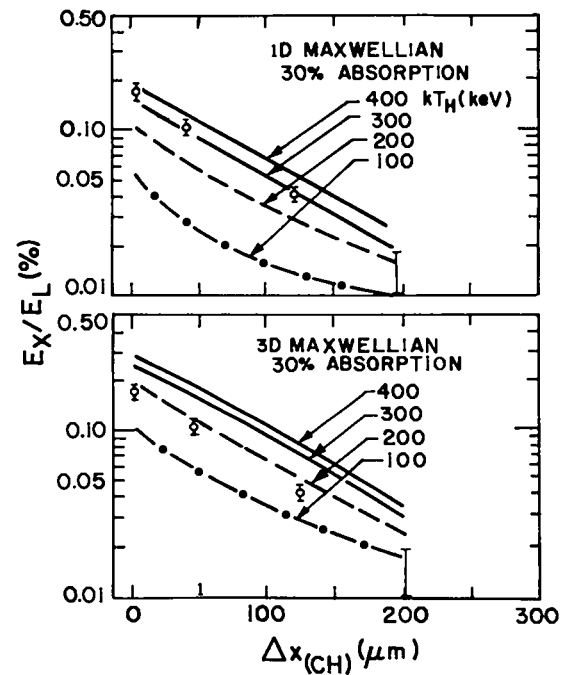

Fig. IV-8. Comparison of LASNEX and APACHE suprathermal x-ray yields.

from 5 to 200 μm. The 3D source-electron energy-distribution x-ray yields are higher than the corresponding 1D yields because the 3D source, average electron energy is higher than the 1D energy. Consequently, the 3D source electron has a greater probability for penetrating the plastic coating. The shape of the 100-keV source-distribution yield curve does not fit the experimental results; therefore, we have dismissed a sole, 100-keV source temperature from consideration. However, source temperatures of 200 keV or higher do reproduce the variation of x-ray yield with plastic layer thickness we have inferred experimentally. Unfortunately, the weak influence of the predicted x-ray yield curve requires that the source temperature be identified by matching other results. We compared the simulated with the APACHE x-ray temperature. This procedure is outlined in Fig. IV-9 in which the simulated x-ray temperature T_x is presented as a function of the peak suprathermal source-electron temperature T_H for targets coated with 50-μm-thick plastic. The LASNEX x-ray temperature was estimated from the slope of the simulated emission-vs-photon energy spectrum that was evaluated at the photon energy corresponding to the suprathermal electron temperature. This photon energy always lies within the sensitivity limits of the APACHE channels. We are examining the accuracy associated with comparing LASNEX x-ray temperatures calculated in this manner with APACHE x-ray temperatures. Fig. IV-9 shows that the 200-keV APACHE temperature can be matched

with either a 340-keV (3D) nonrelativistic Maxwellian source-electron distribution or a 390-keV (1D) nonrelativistic Maxwellian source-electron distribution. Using these source temperatures, the laser energy fraction converted into suprathermal electrons was estimated by interpolating the x-ray yield results in Fig. IV-8. Estimated laser energy absorption fractions of 25% for the kT_H = 390 keV (1D) source condition and 19% for the kT_H = 340 keV (3D) source condition are reasonable. We assumed that all absorbed laser energy resides solely in those components. Figure IV-10 presents interpolated LASNEX hard x-ray yields as a function of plastic thickness. Agreement between LASNEX and APACHE results is particularly good for plastic coatings ranging between 5 and 125 μm. At thicker plastic coatings ($t_{CH} \sim 200$ μm), the LASNEX yield is too high and barely touches the upper limit of the APACHE error bar. This result indicates that a smaller fraction of the source electrons is reaching the bulk material than was predicted by LASNEX. This discrepancy between LASNEX and APACHE could be attributed to the way in which LASNEX calculates fast-ion losses in the corona. This point will be discussed later in this section.

The canonical resonance absorption formula, Eq. (IV-29), with α = 30, predicts that resonance absorption should produce only 50-keV source electrons. Source electrons at 50 keV or at a lower temperature may have been produced in this plastic-coated target, but their
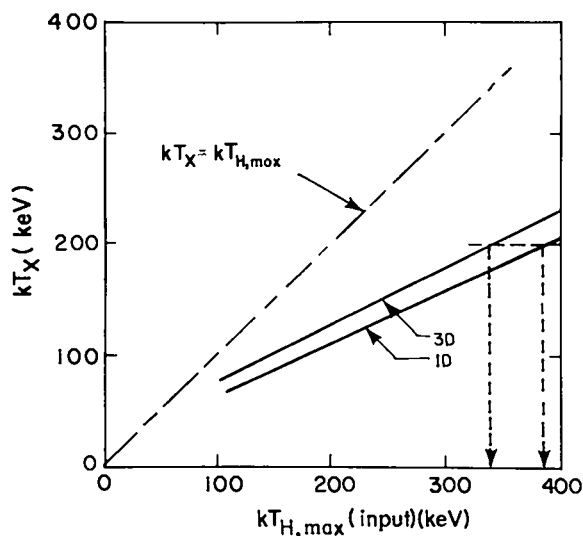

Fig. IV-9. Suprathermal x-ray temperature vs peak suprathermal electron temperature (LASNEX).
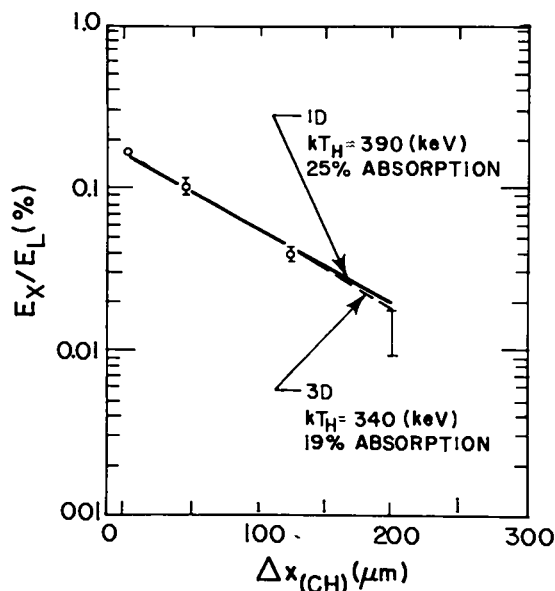

Fig. IV-10. Interpolated LASNEX suprathermal x-ray yield.

existence could not be verified by current experimental data.

The LASNEX simulation x-ray temperatures presented in Fig. IV-9 are significantly lower than the peak input source-electron temperature. This difference can be attributed to several factors. Hydrodynamic and joule heating losses in the corona soften the suprathermal electron spectrum, which is reflected in a reduction of almost 10% in kT_x. Furthermore, the laser pulse is time-dependent; therefore, the time-averaged source-electron temperature is lower than the peak value quoted at peak intensity. Constant-temperature simulations yield kT_x ~10% higher than the value observed for time-dependent source temperatures. Bremsstrahlung cross sections are dependent on both electron energy and emission photon frequency; consequently, one would not necessarily anticipate that source electron and x-ray temperatures be equal. This cross-section effect was observed by McCall[19] when local Maxwellian electron distributions were folded through thick-target x-ray spectra obtained from x-ray tube experimental results. The closest agreement between kT_x and the source-electron temperature was achieved when kT_x was evaluated at photon energies several times the electron temperature. This cross-section effect was observed in LASNEX simulations in which kT_x, evaluated at photon energies

several times the electron temperature, was nearly equal to the local electron temperature. In this experiment, x-ray spectra measurements were made at $h\nu \sim kT_H$; therefore, $kT_x \neq kT_H$.

Earlier, both fast-ion losses and joule losses were referred to as energy loss mechanisms in the collisionless corona. Suprathermal electron energy loss in the corona is not available for bremsstrahlung production in the overdense material where nearly all hard x-ray radiation is produced. Table IV-I shows the magnitude of predicted suprathermal electron collisionless energy losses in typical targets. The fractional energy loss (relative to total energy absorbed) increases with increasing T_H and accounts for ~60% of the total energy absorbed at suspected source-electron temperatures. Figure IV-11 compares LASNEX bremsstrahlung yields produced in targets both with and without suprathermal energy loss. All yields have been normalized to the 100-keV results. We simulated negligible suprathermal electron collisionless loss by irradiating the target with negligible laser energy to minimize target heating and by constraining the target to prevent hydrodynamic motion. When suprathermal electron collisionless losses are neglected, the calculated x-ray yield, normalized to the laser energy, increases linearly with increasing source-electron temperature. When these loss mechanisms are included,

TABLE IV-I. Suprathermal Electron Collisionless Losses

One-Dimensional Electron Energy Distribution

T_H (keV)	100	200	300	400
Fast-ion loss/Laser absorption	0.19	0.25	0.30	0.35
Joule dissipation/Laser absorption	0.24	0.28	0.30	0.27
Total fractional loss to collisionless processes	0.43	0.53	0.60	0.62

Three-Dimensional Electron Energy Distribution

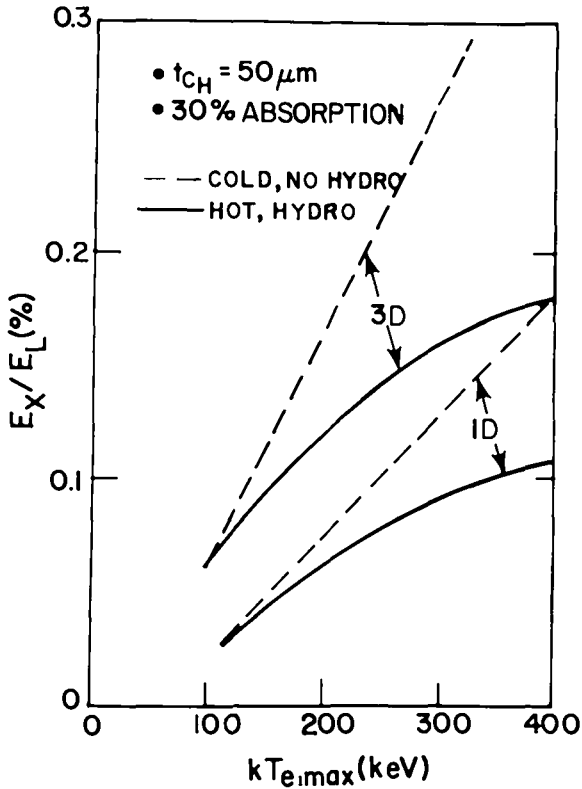|				
T_H (keV)	100	200	300	400
Fast-ion loss/Laser absorption	0.22	0.32	0.40	0.46
Joule dissipation/Laser absorption	0.13	0.18	0.21	0.18
Total fractional loss to collisionless processes	0.35	0.50	0.61	0.64

Fig. IV-11. Comparison of LASNEX suprathermal x-ray yields for simulations with and without collisionless losses.

sr. As a result, a large fraction of the source electrons may be free streaming around the target and losing their energy to the expanding plasma sheath rather than collisionally depositing their energy in the bulk material. The diffusion approximation does not adequately model the transport of these electrons. This transport effect may explain why the LASNEX x-ray yields are slightly higher than yields inferred from experiments at large plastic thicknesses (~200 μm). If we assume that suprathermal electron deposition in the gold shell scales as the solid angle of the gold shell (as observed at the critical surface) and the remainder is lost to fast ions, then the x-ray yield will decay with increasing plastic thickness as indicated in Fig. IV-12. The predicted x-ray yield for 200-μm plastic now lies below the experimental error bar. These results suggest that a Monte Carlo transport treatment of suprathermal electrons in a moving hydrodynamic fluid may describe more realistically than LASNEX the partitioning of suprathermal electron energy in typical targets. Recent magnetohydrodynamic (MHD) computer-modeling results[20] suggest that intense magnetic fields may be generated in the corona, which may also enhance decoupling of source electrons from the target.

The APACHE hard x-ray detector was used to diagnose the bremsstrahlung x-ray spectra produced in

the rate of increase in x-ray yield decreases as the suprathermal electron temperature is increased. The difference between these curves provides a qualitative feel for the influence of collisionless suprathermal electron losses on hard x-ray yield. These results are consistent with the trend suggested by the energy-partitioning results presented in Table IV-I. Collisionless suprathermal electron energy losses in the corona can, therefore, have a significant effect on collisional energy absorption in the target but have a relatively minor effect on the suprathermal electron temperature.

The validity of treating plastic as a diffuse medium to describe suprathermal electron transport is not clear. One can suggest that, in reality, fast-ion losses in the corona may be more severe than indicated by LASNEX. The LASNEX simulation for the 200-μm plastic target with a $T_H = 300$ keV (3D) driving condition indicates that the critical surface has expanded from a 250-μm radius to a 320-μm radius at peak laser intensity. The solid angle of the gold shell at that time is only 7.7×10^{-2}
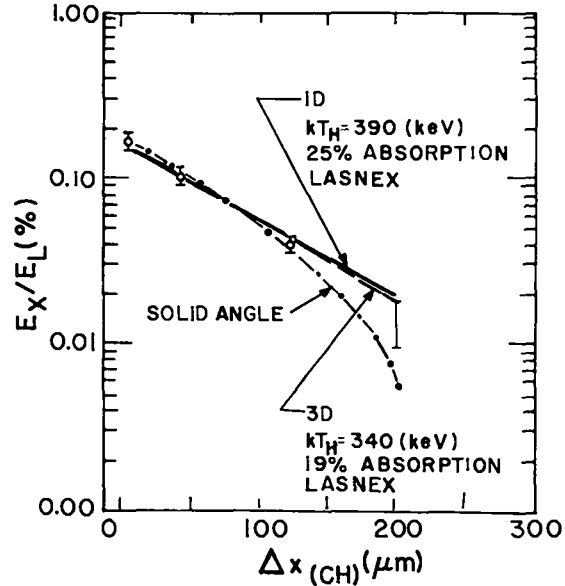

Fig. IV-12. Comparison of solid angle x-ray yield scaling with APACHE and LASNEX results.

plastic-coated gold-layered targets. From APACHE results, we inferred that the suprathermal source-electron temperature is independent of the material. Comparison of both hard x-ray spectra and yield with LASNEX results suggests that the source-electron temperature is significantly higher than the temperature estimated from the canonical resonance absorption formula. We estimated that the source temperature was 340 keV for the 3D electron energy distribution and 390 keV for the 1D electron energy distribution. The mechanism responsible for producing such hard source-electron spectra is not yet understood; we are considering Raman scattering of laser light in subcritical plasma and self-focusing of laser light, which may produce local hot spots. The fractional absorption of incident laser light was estimated to be 25 and 19% for the 1D and 3D distributions, respectively. Some question exists whether or not the diffusion approximation may be used to define suprathermal electron transport in the corona. This issue could be resolved by conducting hydrodynamic simulations in which suprathermal electrons are transported using Monte Carlo techniques. Finally, we must have increased diagnostic capability in future experiments before target performance can be more clearly identified. Specifically, soft x-ray measurements, K_α radiation measurements, and calorimetric measurements should be made in conjunction with APACHE measurements.

CLASSICAL ELECTRON TRANSPORT IN THE PRESENCE OF A LASER FIELD
(R. D. Jones, K. Lee)

Understanding the transport of electrons is critical for the success of laser fusion programs. Preheat, collisional heating, production of diagnostic x rays, and flux inhibition all depend on details of the electron-transport mechanism. Transport is well understood in the absence of a laser field, both with and without a static magnetic field, but the subject has been sorely neglected when a high-intensity laser field is present. Because the novel effects were expected to be dominant for high Z, we have restricted our attention to this type of plasma. Results of a systematic study[21] of the subject are presented in this section.

The time-averaged electron kinetic equation in a model laser field was obtained in three ways: in a simple heuristic calculation using the screened electron-ion interaction, in a Fokker-Planck type calculation, and in a BBGKY calculation. This kinetic equation is

$$\frac{\partial F'(\vec{p}')}{\partial t} = \int d\vec{p}_1 \frac{d\vec{k}}{(2\pi)^3} \sum_{n=-\infty}^{\infty} \left| \frac{4\pi Z e^2}{k^2} \right|^2$$

$$\frac{J_n^2(\vec{k} \cdot \vec{r}_0)}{|D(\vec{k}, \epsilon_{\vec{p}_1 \cdot \vec{k}} - \epsilon_{\vec{p}_1})|^2}$$

$$2\pi \, \delta\left(\epsilon_{\vec{p}} + \epsilon_{\vec{p}_1 \cdot \vec{k}} - \epsilon_{\vec{p}'} - \epsilon_{\vec{p}_1} \right)$$

$$\left[F'(\vec{p}' + \vec{k}) \, F_1(\vec{p}_1 - \vec{k}) - F'(\vec{p}') \, F_1(\vec{p}_1) \right] \; .$$

In this equation F' is the electron distribution function; ϵ_p is the particle energy, $\epsilon_p = P^2/2m$; J_n is a Bessel function of the first kind; r_0 is the quiver distance; and D is the quantum mechanical dielectric response

$$D(\vec{k}, \omega) \equiv 1 + \sum_\sigma \frac{\omega^2}{k^2} \int \frac{d\vec{k}'}{(2\pi)^3} \frac{F_\sigma(\vec{k} + \vec{k}') - F(\vec{k}')}{\omega - (\epsilon_{\vec{p}_1 \cdot \vec{k}} - \epsilon_{\vec{p}_1}) + i0^+}$$

$$\omega_\sigma^2 \equiv \frac{4\pi n_\sigma Z_\sigma^2 e^2}{m_\sigma} \; .$$

In the limit of glancing collisions and cold, infinitely massive ions, this kinetic equation reduces to

$$\frac{\partial f_e}{\partial t} = A \frac{\partial}{\partial \vec{v}} \cdot \frac{1}{v} \int \frac{dk}{k} \, S \, (\vec{k}, r_0, v_0) \cdot \frac{\partial f}{\partial \vec{v}} \; .$$

In this expression,

$$A = \frac{2\pi n_I Z^2 e^4}{m^2}$$

and S is given by

$$S_{vv} = \sum_{|n/q| \le 1} \frac{n^2}{q^2} \int \frac{d\phi}{\pi}$$

$$J_n^2 \left[\frac{v_0}{v} n \cos \alpha + \frac{v_0}{v} q \left(1 - \frac{n^2}{q^2} \right)^{1/2} \sin \alpha \cos \alpha \right],$$

$$S_{\alpha v} = S_{v\alpha} = \sum_{|n/q| \le 1} \frac{-n}{q} \left(1 - \frac{n^2}{q^2} \right)^{1/2} \int \frac{d\phi}{\pi} \cos \phi$$

64

$$J_n^2 \left[\frac{v_0}{v} n \cos\alpha + \frac{v_0}{v} q \left(1 - \frac{n^2}{q^2} \right)^{1/2} \sin\alpha \cos\alpha \right] ,$$

$$S_{\alpha\alpha} = \sum_{|n/q|\leq 1} \left(1 - \frac{n^2}{q^2} \right) \int \frac{d\phi}{\pi} \cos^2\phi$$

$$J_n^2 \left[\frac{v_0}{v} n \cos\alpha + \frac{v_0}{v} q \left(1 - \frac{n^2}{q^2} \right)^{1/2} \sin\alpha \cos\phi \right] ,$$

$$S_{\beta\beta} = \sum_{|n/q|\leq 1} \left(1 - \frac{n^2}{q^2} \right) \int \frac{d\phi}{\pi} \sin^2\phi$$

$$J_n^2 \left[\frac{v_0}{v} n \cos\alpha + \frac{v_0}{v} q \left(1 - \frac{n^2}{q^2} \right)^{1/2} \sin\alpha \cos\phi \right] ,$$

and

$$S_{\beta v} = S_{v\beta} = S_{\alpha\beta} = S_{\beta\alpha} = 0 \quad .$$

Here q is given by

$$q = \frac{kv}{\omega_0} \quad .$$

The coordinate system is shown in Fig. IV-13. In the limit of a small laser field, this equation becomes

$$\frac{\partial f_e}{\partial t} = A \frac{\partial}{\partial \vec{v}} \cdot \frac{1}{v} S \cdot \frac{\partial f_e}{\vec{v}}$$

Here, the Fs are given in Table IV-II and Fig. IV-14, ω_0 is the laser frequency, v_e is the thermal velocity, v_0 is the quiver velocity, and Λ is the plasma parameter. In the high-field limit, S becomes

$$S_{vv} \simeq \frac{2v}{\pi v_0} \ln\left(\frac{k_{max} v_e}{\omega_0} \right) \ln\left(\frac{v_0}{v_e} \right) \sin^2\alpha$$

and

$$S_{\alpha v} = \frac{2v}{\pi v_0} \ln\left(\frac{k_{max} v_e}{\omega_0} \right) \ln\left(\frac{v_0}{v_e} \right) P(a) \quad .$$

In this expression,

$$P(a) = \pm \frac{4}{\pi} \sin\alpha \int_0^{\pi/2} d\theta \sin\theta \left(1 - \sin^2\alpha \sin^2\theta \right)^{1/2}$$

$$= \pm \frac{2}{\pi} \sin\alpha \, B(1,1/2) F(1,-1/2;3/2; \sin^2\alpha) \quad .$$

Here B(x,y) is a beta function, F is a Gaussian hypergeometric function, and the ± sign is positive if α is between 0 and $\pi/2$ and negative if α is between $\pi/2$ and π.

$$S_{\alpha\alpha} \simeq \frac{-2v}{\pi v_0} \ln\Lambda \, \ln\left(\frac{v_0}{v} \right) \cos^2\alpha$$

and

$$S_{\beta\beta} \simeq \frac{-2v}{\pi v_0} \ln\Lambda \, \ln\left(\frac{v_0}{v} \right) (1 + 2\cos^2\alpha) \quad .$$

$$S = \begin{bmatrix} F_{\alpha\alpha}\ln\Lambda & 0 & -F_{\alpha v}\frac{v_0^2}{v^2}\ln\left(\frac{k_{max}\omega_0}{v_e} \right) \cos\alpha \sin\alpha \\ \\ 0 & F_{\beta\beta}\ln\Lambda & 0 \\ \\ -F_{\alpha v}\frac{v_0^2}{v^2}\ln\left(\frac{k_{max}\omega_0}{v_e} \right)\cos\alpha \sin\alpha & 0 & F_{vv}\frac{1}{2}\frac{v_0^2}{v^2}\ln\left(\frac{k_{max}\alpha_0}{v_e} \right) \sin^2\alpha \end{bmatrix} \quad .$$
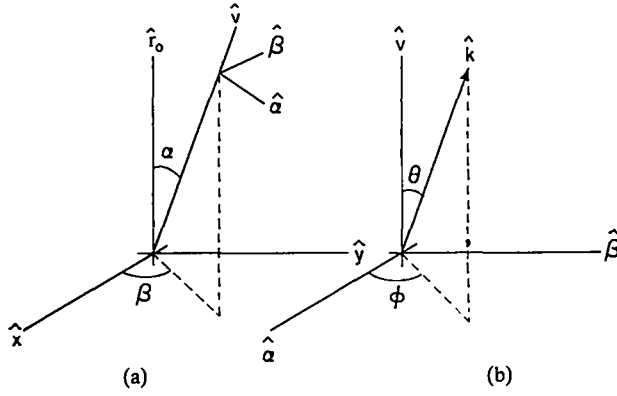
Fig. IV-13. Coordinate system defining (a) the direction of the particle velocity relative to the displacement v_0 and (b) the direction of the momentum transfer vector relative to the direction of the particle velocity.

Collisions produce harmonics in the electron distribution function. These harmonics generate currents that can produce harmonics of the laser light. The harmonics in the distribution are given in terms of the time-averaged distribution. The ℓth harmonic, $F(\ell\omega_0 0)$, of the electron distribution is given by

$$-i\ell\omega_0 \, F(\ell\omega_0) = \frac{-n_1}{m} \int d\vec{v}_1 \, \frac{d\vec{k}}{(2\pi)^3} \left(\frac{4\pi Ze^2}{k^2} \right)^2 \frac{\partial}{\partial \vec{v}_e'} \cdot \vec{k}\vec{k} \sum_{n=-\infty}^{\infty}$$

$$i^\ell \frac{1}{\vec{k} \cdot (\vec{v}_e' - \vec{v}_i) - (n+\ell)\omega_0} J_n(\vec{k} \cdot \vec{r}_0) J_{n+\ell}(\vec{k} \cdot \vec{r}_0)$$

$$\left(\frac{1}{m} \frac{\partial}{\partial \vec{v}_e'} - \frac{1}{M} \frac{\partial}{\partial \vec{v}_1} \right) f_e(\vec{v}_e')f_i(\vec{v}_1) .$$

For high and low v_0/v_e, the kinetic equation possesses self-similar solutions. In the low v_0/v_e case, the similarity solution found by Langdon[22] is recovered. For high v_0/v_e, when anisotropic terms are neglected, the similarity solution is a Maxwellian. Figures IV-15 and IV-16 show the low-field solution. The solid line is Langdon's similarity solution; the dotted line is a Monte Carlo simulation result; and the dashed line is a Maxwellian.

TABLE IV-II. Form Factors F as a Function of v_0^2/v^2 and α

F_{vv}						$F_{\alpha v}$				
v_0^2/v^2	$\alpha = 0$	$\pi/8$	$\pi/4$	$3\pi/8$	$\pi/2$	v_0^2/v^2	$\alpha = 0$	$\pi/8$	$\pi/4$	$3\pi/8$	$\pi/2$
0.1	1.48	1.42	1.16	0.962	0.897	0.1	1.17	1.10	0.951	0.843	0.805
0.2	2.29	1.96	1.29	0.919	0.813	0.2	1.39	1.19	0.888	0.713	0.660
0.3	3.75	2.65	1.39	0.872	0.742	0.3	1.70	1.28	0.814	0.605	0.549
0.4	6.57	3.48	1.45	0.826	0.683	0.4	2.14	1.35	0.733	0.515	0.459
0.5	12.7	4.41	1.48	0.780	0.631	0.5	2.81	1.38	0.653	0.441	0.391
0.6	28.4	5.38	1.49	0.736	0.586	0.6	3.90	1.36	0.574	0.379	0.332
0.7	79.2	6.28	1.47	0.695	0.547	0.7	5.87	1.28	0.501	0.328	0.290

$F_{\alpha\alpha}$						$F_{\beta\beta}$				
v_0^2/v^2	$\alpha = 0$	$\pi/8$	$\pi/4$	$3\pi/8$	$\pi/2$	v_0^2/v^2	$\alpha = 0$	$\pi/8$	$\pi/4$	$3\pi/8$	$\pi/2$
0.1	1.05	1.03	0.980	0.943	0.928	0.1	1.06	1.04	1.01	0.988	0.978
0.2	1.12	1.05	0.952	0.891	0.873	0.2	1.12	1.09	1.02	0.973	0.957
0.3	1.19	1.07	0.917	0.845	0.822	0.3	1.20	1.13	1.03	0.960	0.936
0.4	1.29	1.07	0.878	0.801	0.780	0.4	1.29	1.17	1.03	0.945	0.919
0.5	1.41	1.05	0.837	0.762	0.743	0.5	1.42	1.22	1.03	0.931	0.903
0.6	1.58	1.02	0.796	0.727	0.710	0.6	1.58	1.26	1.02	0.917	0.887
0.7	1.82	0.969	0.757	0.695	0.680	0.7	1.82	1.29	1.02	0.904	0.873
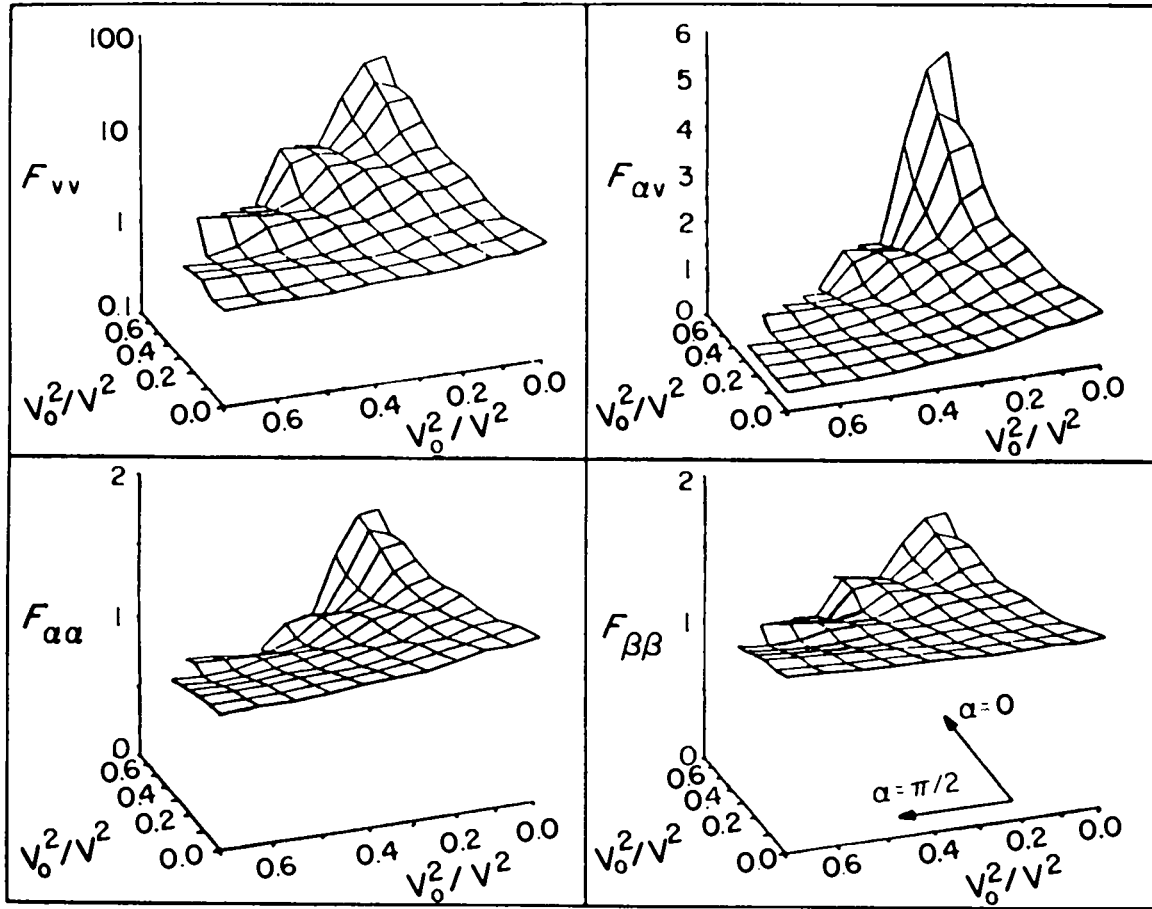
Fig. IV-14. Form factors as a function of v_0^2/v^2 and α. The vertical scales are different in each plot.

We obtained an expression for the anisotropy in the distribution and showed, for low v_0/v_e, that after a few collision times, the anisotropic portion of the distribution follows the isotropic portion adiabatically:

$$f_2(v,t) = \frac{-1}{3} \frac{v_0^2}{v} \frac{\partial f_0}{\partial v} - \frac{1}{18} v_0^2 v \frac{\partial}{\partial v} \frac{1}{v} \frac{\partial f_0}{\partial v} .$$

Here f_0 and f_2 are coefficients of P_0 (cos α) and P_2 (cos α), respectively, in an expansion of the distribution in Legendre polynomials. If Langdon's distribution is used for f_0, this equation becomes

$$f_2(v,t) = \frac{0.118}{2} \frac{v_0^2}{v_e^2} \left(\frac{v^3}{v_e^3} - \frac{0.118}{9} \frac{v^8}{v_e^{10}} \right) f_0 .$$

The inverse-bremsstrahlung heating rate was obtained. In the low-field limit, it is

$$\dot\epsilon = 0.446 \; \dot\epsilon_m ,$$

where

$$\dot\epsilon_m = \frac{4\pi}{3} \frac{1}{\sqrt{2\pi}} \frac{Z^2 n_1 n_e e^4}{m^2} \frac{m^{5/2}}{T^{3/2}} v_0^2 \ln \left(\frac{k_{max} v_e}{\omega_0} \right)$$

is the usual inverse-bremsstrahlung absorption rate for a Maxwellian distribution. The factor 0.446 is the Langdon factor. If anisotropy in the distribution is neglected, $\dot\epsilon$ is given in the high-field limit by

$$\dot\epsilon = \frac{4nmA}{\pi v_0} \ln \left(\frac{k_{max} v_e}{\omega_0} \right) \ln \left(\frac{v_0}{v_e} \right) .$$
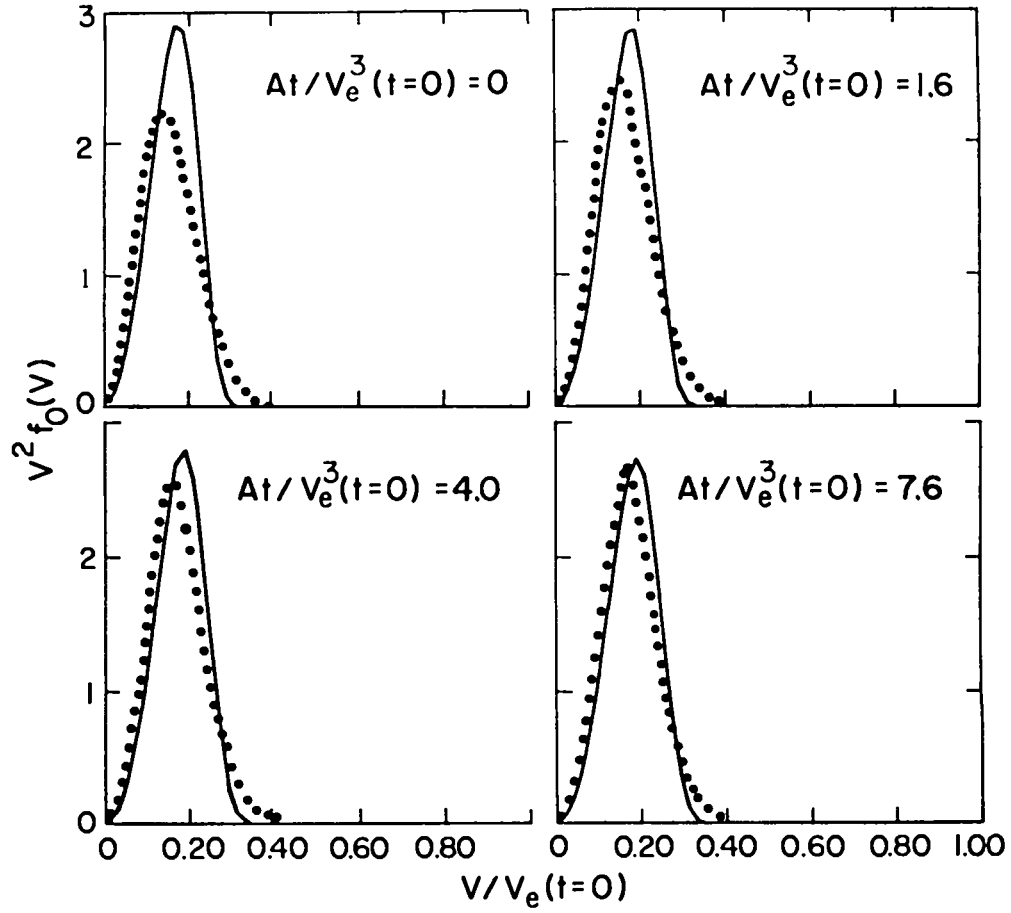
Fig. IV-15. Electron distribution as a function of time. In this simulation, the electron distribution (dotted curve) was started as a Maxwellian with $v_e = 2.0 \, v_0$. After a few collision times, the distribution is very close to a Langdon distribution (solid curve) with the same temperature. The normalization is arbitrary.
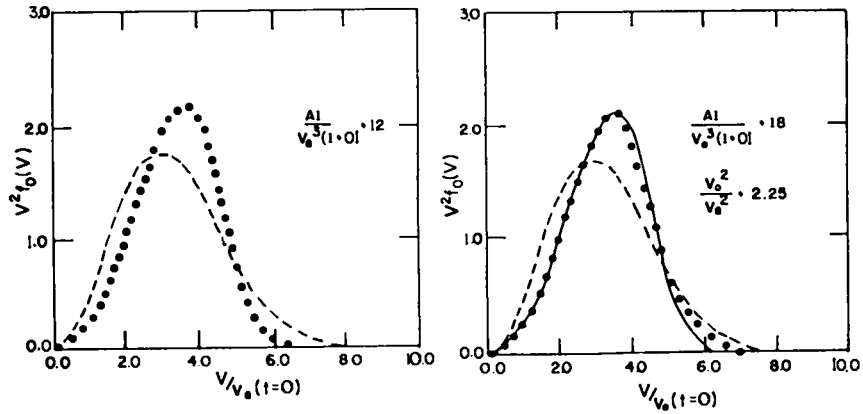
Fig. IV-16. Electron distribution as a function of time. Initial thermal velocity was $v_e = v_0/3.0$. The dashed curve is a Maxwellian with the same temperature as the simulation distribution (dotted curve). Even when $v_0^2/v_e^2 \simeq 1.0$, the distribution evolves to a Langdon distribution (solid curve) after a few collision times.

68

The above equation agrees with that obtained by Silin[23] and James.[24] Its comparison with the Monte Carlo code is shown in Figs. IV-17 and IV-18.

The bremsstrahlung emission rate was obtained. The spectral power emission per unit volume for the entire plasma is

$$P_\omega = \frac{4}{3\pi} \frac{Z_e^6 n_i n_e}{m^2 c^3} (\omega^2 - \omega_p^2)^{1/2} \int \frac{d\vec{k}}{k^2} d\vec{v} \frac{f_e(\vec{v})}{|D_\parallel(\vec{k},\omega)|^2}$$

$$\sum_n \delta(\omega - \vec{k}\cdot\vec{v} - n\omega_0) J_n^2(\vec{k}\cdot\vec{r}_0) \ .$$

The electron-pressure tensor was obtained:

$$P = nT \begin{bmatrix} 1 - \frac{1}{90}\frac{v_0^2}{v_e^2} & 0 & 0 \\ \\ 0 & 1 - \frac{1}{90}\frac{v_0^2}{v_e^2} & 0 \\ \\ 0 & 0 & 1 + \frac{1}{45}\frac{v_0^2}{v_e^2} \end{bmatrix} ,$$
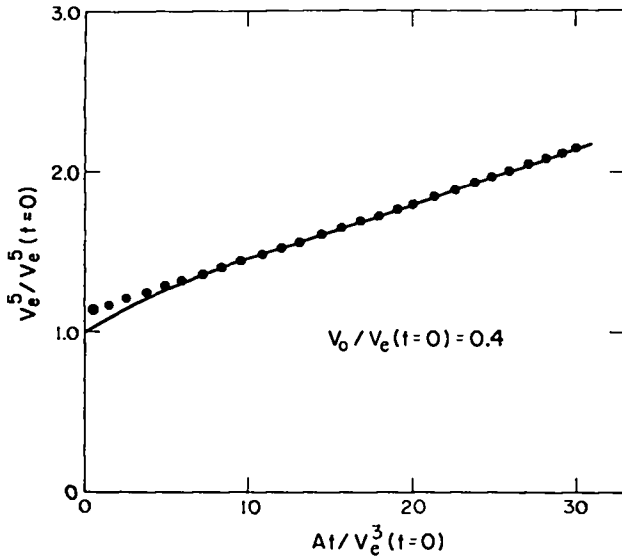
Fig. IV-17. Plot of v_e^5 as a function of time. The dotted line has a slope that corresponds to the Langdon heating rate. The solid curve is a simulation result. The simulation was started with $v_0/v_e = 0.4$. After a few collision times, the heating rate agrees very well with the Langdon heating rate.
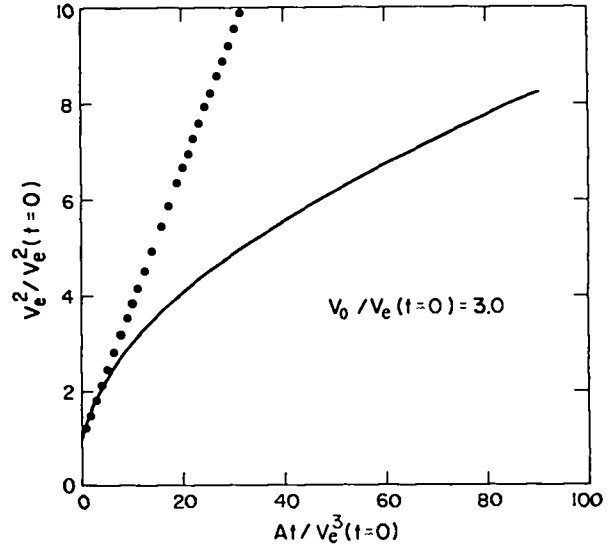
Fig. IV-18. Plot of v_e^2 as a function of time for the moderate field. The dotted curve is the heating formula given by Silin.[23] The simulation was started with $v_0/v_e = 3.0$. Initially the heating follows the Silin formula, but by the time the temperature is high enough so that $v_0^2/v_e^2 = 4.0$, heating is substantially slower.

where the z-axis is taken along the laser field.

We calculated the thermoelectric transport coefficients:

$$\vec{J} = 0.913 \ \sigma_{LG}\vec{E} + 0.663 \ \alpha_{LG} \nabla T \ ,$$

$$\vec{q} = -0.661 \ \beta_{LG}\vec{E} - 0.413 \ K_{LG} \nabla T \ ,$$

$$\sigma_{LG} = \frac{8}{(2\pi)^{3/2}} \frac{2m}{Ze^2 \ln \Lambda} \left(\frac{T}{m}\right)^{3/2} \ ,$$

$$\alpha_{LG} = \frac{24}{(2\pi)^{3/2}} \frac{2m}{Ze^3 \ln \Lambda} \left(\frac{T}{m}\right)^{3/2} \ ,$$

$$\beta_{LG} = \frac{64}{(2\pi)^{3/2}} \frac{m^2}{n_e Ze^3 \ln \Lambda} \left(\frac{T}{m}\right)^{5/2} \ ,$$

and

$$K_{LG} = \frac{160}{(2\pi)^{3/2}} \frac{m^2}{n_e Ze^4 \ln \Lambda} \left(\frac{T}{m}\right)^{5/2} \ .$$

And finally, we obtained the electron fluid equations:

$$\frac{\partial n_e}{\partial t} + \frac{\partial}{\partial \vec{r}'} \cdot n_e \vec{u} = 0 \ ,$$

$$\vec{u} = \frac{1}{n_e} \int d\vec{v}' \vec{v}' f_e(\vec{v}') \ ,$$

and

$$\frac{\partial}{\partial t}(mn_e \vec{u}) + \frac{\partial}{\partial \vec{r}'} \cdot (mn_e \vec{u}\vec{u}) =$$

$$- \frac{\partial}{\partial \vec{r}'} \cdot P + \rho_L \vec{E}_L + \frac{1}{c} \vec{J}_L \times \vec{B}_L - n_e \frac{\partial \phi_p}{\partial \vec{r}}$$

$$+ m \int d\vec{v}\vec{v} \ c(f_e, f_I) \ ,$$

where P is the electron-pressure tensor, and ρ_L and $\vec{J}_L$ are the low-frequency charge and current density, respectively. The second moment gives

$$\frac{\partial}{\partial t} \left\{ \left[\frac{1}{2} mn_e u^2 + \frac{3}{2} \frac{T_r P}{3} + ne\phi_p(\vec{r}') \right] \right\}$$

$$+ \frac{\partial}{\partial \vec{r}'} \cdot \left(\frac{1}{2} mnu^2 \vec{u} + \frac{3}{2} \frac{TrP}{3} \vec{u} + P \cdot \vec{u} + n_e \phi_p \vec{u} + \vec{q} \right)$$

$$= \vec{J} \cdot \vec{E} + \dot{\epsilon} \ ,$$

where $\dot{\epsilon}$ is inverse-bremsstrahlung absorption. We have neglected bremsstrahlung losses.

CODE DEVELOPMENT—THE VENUS CODE
(J. U. Brackbill)

New implicit methods for plasma simulation have been developed that significantly extend the range of this important tool. The new methods make it possible for today's computers to determine realistic parameters and advance the ability to study nonlinear plasma stability and transport.

Historically, plasma simulation has provided insight into nonequilibrium plasma processes and has enhanced our understanding of energy transport and stability. However, because of computer limitations and the inherent properties of standard explicit simulation methods, reduced dimensional and nonphysical parameters have been used to compress time and space scales. Thus, scaling the simulation results to realistic parameters has often been difficult. Sometimes, especially when nonlinear effects are important, the simulation results cannot be scaled. In such cases, simulations with realistic parameters are needed.

Increased computer capacity may eventually allow such simulations using standard methods. Since 1970, when two-dimensional electromagnetic codes were developed, the capacity of computer memories has been doubled and speed has increased fivefold. However, because of the difficulty of multidimensional problem scaling, these improvements represent only a 40% increase in problem size and a 100% extension in problem time, insufficient for the orders of magnitude that separate current simulation parameters from realistic ones.

Understanding how to apply implicit methods to particle simulations has caused a real breakthrough. Using implicit methods, we can obtain stable and accurate solutions for very large time steps; these solutions increase our ability to represent time and space scales tremendously.

To understand the impact of implicit methods, consider a typical simulation algorithm in which algebraic equations are incremented in time. The plasma is represented realistically by particles with charge, mass, position, and velocity except that there are fewer particles. From the particles, charge density and current are calculated on a computation mesh; from these, self-consistent electric and magnetic fields are calculated from Maxwell's equations; and finally, the particle equations of motion in the fields are solved to advance their positions. The process is repeated during each time step to generate the evolution of the plasma. Because the algorithm is explicit, the time interval over which the solution can be integrated must resolve all physical time scales. Otherwise, it would be unstable.

What makes implicit methods practical is that although the number of particles is too large to allow implicit formulation, the number of equations that must be solved to provide stable estimates of the fields is very much smaller. In the implicit-moment method as outlined by Mason,[14] the evolution of the charge and current density is approximated by fluid-like moment equations. The description is approximate because it does not include the higher order effects like heat conduction and viscosity that the particles do give. Nevertheless, over a

70

time step that is small compared with the time scale of interest, self-consistent solutions of the moment and fluid equations offer very good estimates of the fields. In the implicit-moment method, the moment equations are used as a computational device to permit large time steps, and they are simple enough to be differenced implicitly. Once estimates of the fields are obtained, the evolution of the plasmas is calculated by solving the particle equations of motion in the fields. During each time step, the moments are recalculated from the particles, and new estimates of the fields are generated.

A detailed analysis of the implicit-moment method[25] addresses (among other issues) the requirements for consistency between the particles and moment descriptions, and the linear and nonlinear stability of the algorithm. The need for accuracy and the need for suppressing an aliasing error common to all particle simulations impose constraints on time and space steps; the constraints are summed up in the criterion that when the time step is large compared with the plasma frequency, the plasma must be quasi-neutral on all resolved space scales. This requirement is not at all restrictive in practice and allows a tenfold increase in representable time and space scales. For two-dimensional, time-dependent problems, the implicit method is easily 1000 times faster than comparable explicit methods.

By implementing the implicit-moment method for two-dimensional, electromagnetic plasma simulation, we have developed a new code, VENUS. We significantly shortened the development time for VENUS by using as much as possible of an existing code, WAVE. Some aspects of the solution algorithm for the implicit equations are nonstandard but straightforward and, so far, reliable. In its present, but probably not optimum, form, VENUS is a valuable production tool.

Because the code can be used to study problems that, up to now, were beyond reach, there is a multitude of applications in magnetically confined plasmas, space plasmas, and laser-irradiated plasmas. Some recent papers are listed in Refs. 20 and 26 to indicate the scope of the problems that have been tackled.

In a recent simulation,[27] we examined the lateral transport in a laser-irradiated plasma. Specifically, we simulated the energy transport induced by a finite laser spot on a foil. As is well known, magnetic fields are generated thermoelectrically because of nonparallel density and temperature gradients. However, the simulations showed for the first time that although the magnetic fields inhibit lateral transport in the dense plasma, they enhance transport in the corona. In fact, electrons appear to be trapped in large magnetic fields in the corona, decoupled from the dense plasma. In time, the electron pressure accelerates ions from the surface and the energy is lost.

REFERENCES

1. K. Eidman and R. Sigel, Phys. Rev. Lett. 34, 799 (1975).

2. E. A. McLean, J. A. Stamper, B. H. Ripin, H. R. Griem, J. McMahon, and S. E. Bodner, Appl. Phys. Lett. 31, 825 (1977). The references in this article are also useful.

3. G. Auer, K. Sauer, and K. Baumgärtel, Phys. Rev. Lett. 42, 1744 (1979). The references in this article are also useful.

4. N. H. Burnett, H. A. Baldes, M. C. Richardson, and G. D. Enright, Appl. Phys. Lett. 31, 172 (1977). The references in this article are also useful.

5. R. L. Carman, D. W. Forslund, and J. M. Kindel, Phys. Rev. Lett. 46, 29 (1981).

6. R. L. Carman, C. K. Rhodes, and R. F. Benjamin, Phys. Rev. A 24, 2649 (1981).

7. B. Bezzerides and S. J. Gitomer, Phys. Rev. Lett. 46, 593 (1981).

8. V. L. Ginzberg, *Propagation of Electromagnetic Waves in Plasma* (Gordon and Breach, New York, 1961), Chap. IV, pp. 377-403.

9. See, for example, J. P. Friedberg, R. W. Mitchell, R. L. Morse, and L. E. Rudsinski, Phys. Rev. Lett. 28, 795 (1972); J. S. DeGroot and J. E. Tull, Phys. Fluids 18, 672 (1975); K. G. Estabrook, E. J. Valeo, and W. L. Kruer, Phys. Fluids 18, 1151 (1975); D. W. Forslund, J. M. Kindel, and K. Lee, Phys. Rev. Lett. 39, 284 (1977); and B. Bezzerides, S. J. Gitomer, and D. W. Forslund, Phys. Rev. Lett. 44, 651 (1980).

10. P. Koch and J. Albritton, Phys. Rev. Lett. 32, 1420 (1974); and J. Albritton and P. Koch, Phys. Fluids 18, 1136 (1975).

11. W. L. Kruer, Phys. Fluids 22, 1111 (1979).

12. T. P. Coffey, Phys. Fluids 14, 1402 (1972).

13. W. L. Kruer, Comments Plasma Phys. Controlled Fusion 5, 69 (1979).

14. R. J. Mason, J. Comp. Phys. 41, 233-244 (1981); and R. J. Mason, "Suprathermal Electron Transport in Laser Produced Plasmas," Proc. Am. Nucl. Soc./Eur. Nucl. Soc. Top. Meet.: Adv. Math. Methods Nucl. Eng. Probl., Munich, West Germany, April 27-29, 1981, Vol. II, pp. 408-423.

15. R. J. Mason, Phys. Rev. Lett. 47, 652 (1981).

16. R. J. Mason, Phys. Fluids 23, 2204-2215 (1980); and R. J. Mason, Phys. Rev. Lett. 43, 1795 (1979).

17. S. I. Braginskii, Rev. Plasma Phys. 1, 205 (1965).

18. C. Garban-Labaune, E. Fabre, and C. Max, Bull. Am. Phys. Soc. 25, 894 (1980); and R. Fabbro, F. Amiranoff, E. Fabre, C. Garban-Labaune, J. Virmont, and M. Weinfield, Bull. Am. Phys. Soc. 25, 894 (1980).

19. G. H. McCall, J. Phys. D: Appl. Phys. 15, 823-831 (1982).

20. D. W. Forslund and J. U. Brackbill, Bull. Am. Phys. Soc. 26, 873 (1981).

21. R. D. Jones and K. Lee, "Kinetic Theory, Transport, and Hydrodynamics of a High Z Plasma in the Presence of an Intense Laser Field," Phys. Fluids (submitted), LA-UR-80-2857.

22. A. B. Langdon, Phys. Rev. Lett. 44, 575 (1980).

23. U. P. Silin, JETP (USSR) 47, 2254 (1964); JETP (Engl. Transl.) 20, 1510 (1965).

24. R. P. James, K. Lee, Y. C. Lee, and T. K. Samel, Bull. Am. Phys. Soc. 25, 1985 (1980).

25. J. U. Brackbill and D. W. Forslund, "An Implicit Plasma Simulation for Electromagnetic Plasmas in Two Dimensions," J. Comp. Phys. (to be published), LA-UR-81-3197.

26. J. U. Brackbill, Bull. Am. Phys. Soc. 26, 1046 (1981); K. Lee, J. U. Brackbill, D. W. Forslund, and K. Quest, Bull. Am. Phys. Soc. 26, 920 (1981); K. Quest, J. U. Brackbill, D. W. Forslund, and K. Lee, Bull. Am. Phys. Soc. 26, 1001 (1981), and J. U. Brackbill and D. W. Forslund, Bull. Am. Phys. Soc. 26, 1010 (1981).

27. D. W. Forslund and J. U. Brackbill, "Magnetic Field Induced Surface Transport on Laser Irradiated Foils," Phys. Rev. Lett. (submitted), LA-UR-82-170.

V. DIAGNOSTICS DEVELOPMENT
(J. Carpenter)

The experimental investigation of laser/target interactions requires diagnostic techniques with spatial and temporal resolutions in the submicrometer and 1- to 100-ps regime, respectively. This need is being met with a vigorous diagnostics program in x-ray spectrometry, subnanosecond streak-camera development, charged-particle and neutron detection, and laser calorimetry.

INTRODUCTION

Continued development of visible, x-ray, and charged-particle diagnostic instruments has extended our understanding of laser/target interactions. We have obtained a high degree of temporal resolution in x-ray data through the use of streak cameras at both our Gemini and Helios facilities. Two new diagnostics have been developed at Helios: one for monitoring laser/target interaction by diagnosing the backscattered light, the other for measuring the pulse shape of the Helios output beams by using high-speed oscilloscopes and digitizing cameras. We have also added spatial resolution capability to our MULTIFLEX x-ray system using collimators.

X-RAY DIAGNOSTICS

X-Ray Streak Camera (A. Hauer)

Measuring the time history of x-ray emission from laser-driven targets is important to the understanding of target dynamics. The x-ray streak camera, which has recently been installed on the Helios target chamber, offers the experimenter both spatial and temporal x-ray information about laser/target interactions.

Figure V-1 shows the basic configuration of the x-ray streak camera as installed at Helios. The LOS from the target to the center of the photocathode forms an angle of ~6° with the axis of the streak tube to prevent hard x rays from directly exciting the streak-tube output phosphor. The camera incorporates a Hadland-Photonics Ltd. streak tube with a photocathode that can be easily changed to match particular experimental needs. To shield the camera against the very high EMI and x-ray background in Helios, all control cabling is fiber optically coupled. Ten different sweep-speed settings are available ranging from 0.04 to 0.9 ns/mm. The ultimate time resolution of the camera is ~20 ps.

Figure V-2 shows typical streaks obtained during Helios experiments. The three separate portions of the streaks result from filtering with 1 mil of aluminum, no filtering, and filtering with 0.5 mil of titanium. In addition, a 1/3-mil beryllium window covered the input to the
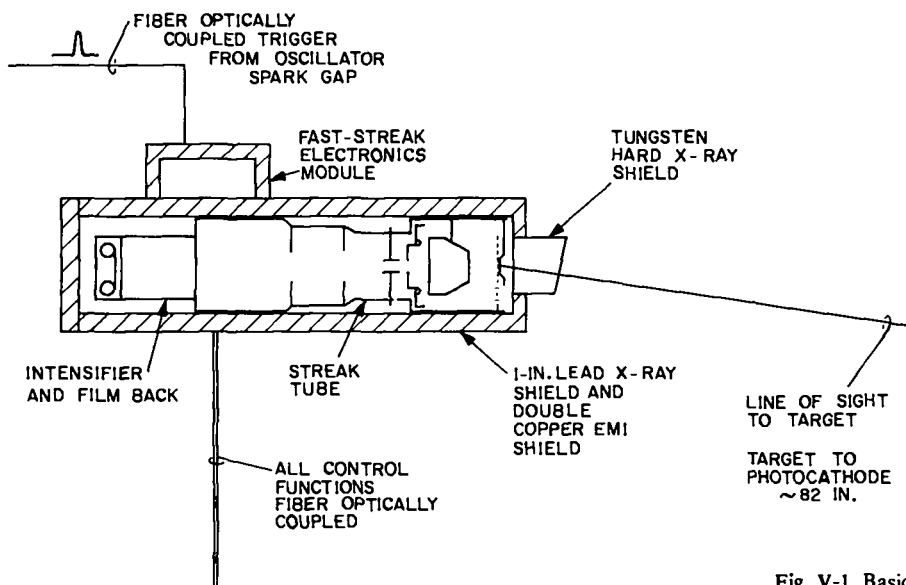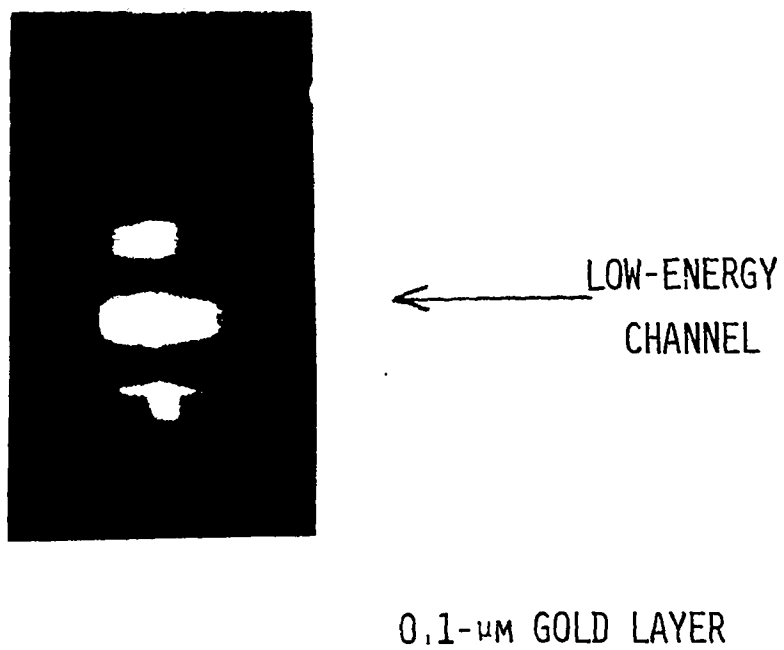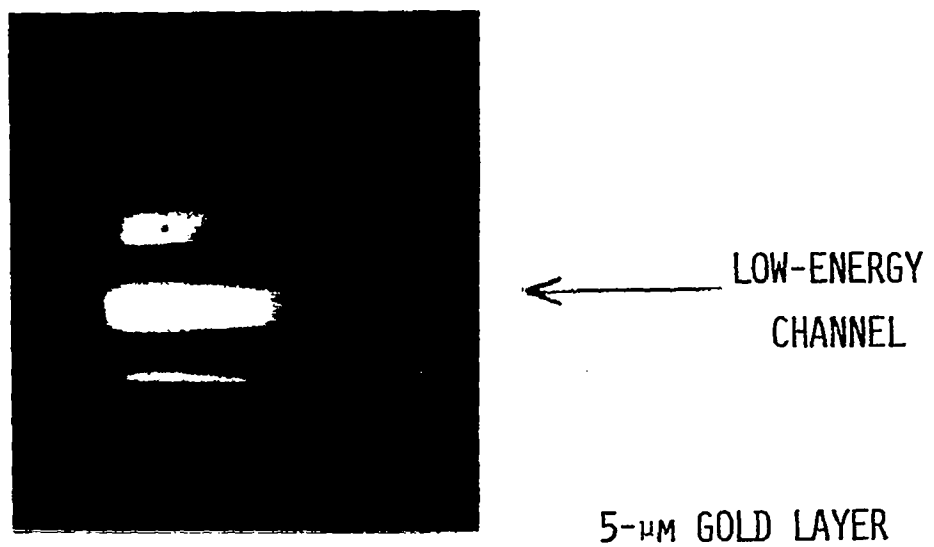

Fig. V-1. Basic configuration of Helios x-ray streak system.

LOW-ENERGY
CHANNEL

5-μM GOLD LAYER

LOW-ENERGY
CHANNEL

0.1-μM GOLD LAYER

1 ns

Fig. V-2. Typical x-ray streaks from Helios target experiments.

74

camera. The softest x-ray channel (1/3-mil beryllium) should be dominated by radiation between 1.0 and 1.5 keV (taking into account the photocathode response). The targets were GMBs coated with different thicknesses of gold.

An x-ray mirror collection system for use with the streak camera has also been developed (Fig. V-3). The collection system increases the sensitivity of the x-ray streak system, and its mirror eliminates high-energy x-ray background signals. In some applications, such as time-resolved spectroscopy, increased sensitivity is important because the camera is far away from the target. Figure V-4 shows the band pass of the mirror, in conjunction with various filters. A rather sharp band pass can be achieved.
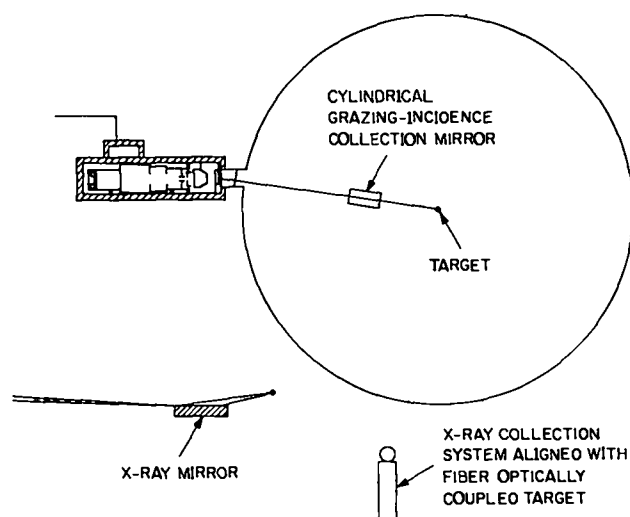

Fig. V-3. X-ray-streak mirror collection system used on Gemini laser.
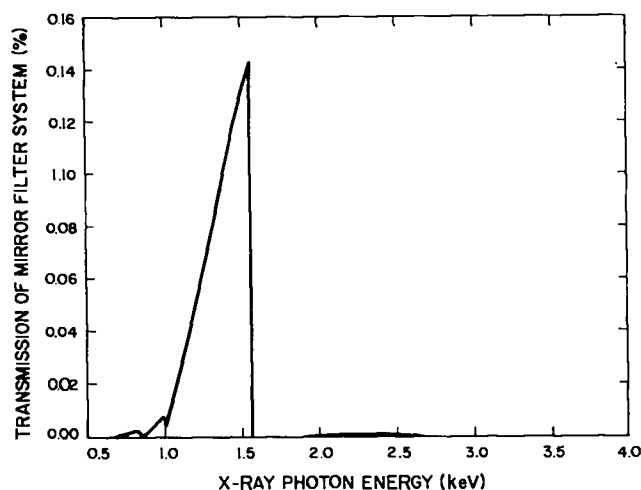

Fig. V-4. Spectral band pass of mirror collection system (with 10-μm aluminum foil filtration). Nickel mirror has 1.5° grazing angle.

MULTIFLEX (R. H. Day)

MULTIFLEX is a seven-channel x-ray detector designed to measure the time-dependent low-energy x-ray spectra from target shots at Helios. It incorporates discrete XRDs that view the x-ray sources through different filters to provide energy discrimination. The system usually covers the energy region from 20 eV to 2 keV with a resolving power, $E/\Delta E$, of 2 to 9 and a time resolution of $\sim$300 ps. The system has been highly automated, carefully characterized, and is used on most target shots to provide bench mark data.

In 1981, we developed an interface between the MULTIFLEX data-acquisition system, system status, and data base and the data-acquisition computer. A series of programs has been written to store all the system parameters on a shot-by-shot basis, generate system response functions, and compute x-ray spectral output in real time. In addition this year, we developed a collimator system that restricts the detector's field of view to a 400-μm-diam footprint on the target. This system required the installation of a precision, remotely operable positioning assembly to adjust the collimator's location near the target and unique optical alignment system to ensure proper collimator placement.

Development of a Collimated Soft X-Ray LOS for MULTIFLEX (P. D. Goldstone)

When measuring the x-ray emission from laser-driven targets with nonimaging detector systems, such as filtered XRDs, we must accurately define the area and position of the emitting source to determine the emitted flux for comparison with model calculations. For example, it is important to separate the emission from the high-density material from that of the corona. On microballoons or flat targets, a crude differentiation can be made by examining time-integrated photographs of the x-ray emission.

However, to define the source area for x-ray measurements accurately, we have developed a LOS collimator for the MULTIFLEX soft x-ray spectrometer system. The collimated MULTIFLEX system provides us now with simultaneous temporal resolution and spatial discrimination in x-ray flux measurements. The collimator (Fig. V-5) consists of a pair of 0.01-mm-thick tantalum plates, each with seven pinholes. For mechanical support, these plates are sandwiched between 1-mm-thick beryllium/copper and tantalum disks, with large clearance holes at the pinhole locations. The first set of

Fig. V-5. MULTIFLEX x-ray collimator.
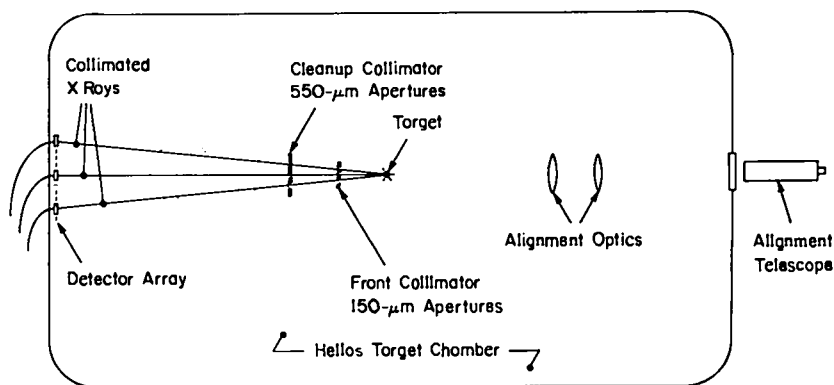
apertures limits the field of view of each of the seven MULTIFLEX diodes to a 400-μm-diam spot at the target. The pinholes are positioned so that the seven 400-μm-diam footprints viewed by the detectors overlap (to an accuracy of ±25 μm) at the target surface, ensuring that the different detectors sample the emission from a common 400-μm-diam source area. The second set of apertures ensures that no detector can see the target through any of the other primary pinholes.

Table V-I lists the aperture sizes and distances from the target. Diameters of the base circles on which six of the seven detectors and pinholes lie are also given. The seventh detector (and pinhole) is at the center of the hexagonal pattern of the outer LOSs. Figure V-6 shows some of the ray paths for one of the LOSs. To ensure that the footprints viewed by the detectors are positioned within ±25 μm, we use an optical alignment scheme in which the pinholes are placed along a line, defined by a precision alignment telescope, between the center of the target and the center of the detector. The optical system has a resolution of ~5 μm. To align the collimator, we retract the primary and cleanup aperture plates from the field of view of the telescope and the central LOS is established. The collimator plates are then reinserted into quasi-kinematic mounts (repositioning accuracy, <25 μm) and independently positioned to the LOS.

When the distance of each aperture plate from the target is adjusted, each LOS is checked optically.

We have used the collimated MULTIFLEX system in several recent experiments. No significant alignment errors have been detected, and on shots in which the primary apertures were misaligned by ~500 μm, no detectable background signal was observed.

APACHE (R. H. Day)

Measurement of the hard x-ray spectrum produced by laser-irradiated targets is critical in the evaluation of laser fusion target scaling. Fuel preheating from energetic electrons created in the laser absorption region can severely limit pellet compression and yield. The magnitude of preheating depends on the number of hot

TABLE V-I. Collimator Aperture Design for 400-μm Footprint

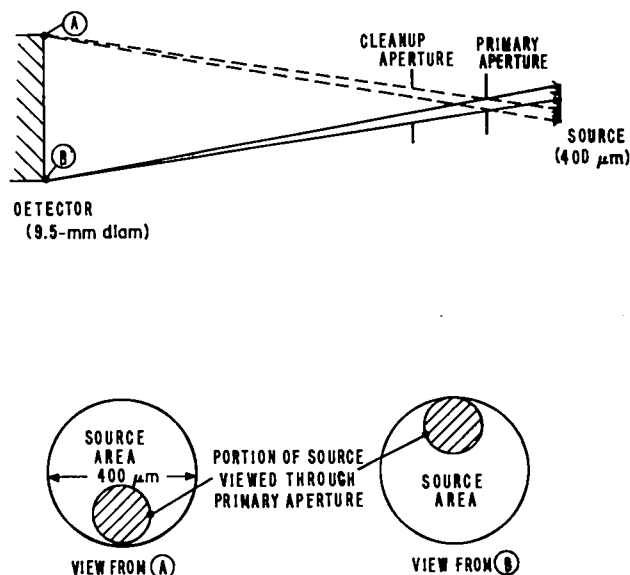|	Distance from Source (cm)	Aperture Diam (μm)	Base Circle Diam (mm)
Primary Apertures	5	156	3.562
Cleanup Apertures	10	552	7.126

Fig. V-6. Ray paths for one x-ray LOS in multiplex.

electrons, on energy distribution, and on energy transport. An important diagnostic of hot-electron distribution is the bremsstrahlung spectrum generated in the target. This spectrum can be quite hard, with temperatures defined by the slope of the spectrum ranging up to several hundred keV.

APACHE is a 10-channel x-ray detector designed to measure time-integrated high-energy x-ray emission from target shots at Helios. The detector incorporates photodiode-fluor combinations, which view the x-ray source through different filters to provide coarse energy discrimination. The detectors are highly collimated and shielded so that only high-energy x-ray emission from the target is measured. The system covers the energy range from 50 keV to 2 MeV with resolving power of a few keV and time resolution of ~3 ns. The data are fit to a single temperature exponential to provide bench mark data on nearly all target shots. Data acquisition and reduction can be performed routinely, and system reliability has been verified.

CHEROKEE (R. H. Day)

High-energy x-ray measurements at Helios have been performed with the APACHE filtered detector system. Because of the very low resolving power of this instrument, we have not measured the detailed x-ray spectrum but have only compared the outputs of the detectors with those expected from an exponential spectrum and found they are consistent.

CHEROKEE is an attempt to measure the time-integrated high-energy x-ray spectrum directly. A spectrometer that uses LiF crystals in the Laue mode detects the x rays; then the spectrum is recorded on film. The crystals cover the energy range from 50 to 400 keV; prefilters calibrate the energy of the system and suppress low-energy x-ray background. Thus shielding is provided to suppress the direct beam, and the slits at the spatial focus suppress scattered radiation, yielding a very low background environment for the recording film. The system has a resolving power, $E/\Delta E$, of ~10 and is time integrated.

The system has been interfaced with the Helios target chamber, and crystal, as well as recording film, has been characterized. CHEROKEE has been used on a few target shots and corroborates the APACHE results.

CYCLOPS (R. H. Day)

The CYCLOPS fast hard x-ray channel has been installed in Helios for preliminary measurements of the target suprathermal x-ray signal. CYCLOPS responds to x rays of $h\nu > 150$ keV with a time response of ~400 ps FWHM.

The timing of the target x-ray signal relative to the laser pulse indicates the onset of plasma instabilities that may trigger hot-electron production. The interaction of hot electrons with high-Z material is significantly delayed, possibly by vacuum insulation, and might also delay the hard x-ray signal. CYCLOPS is a first attempt at observing such effects; it incorporates a scintillator viewed by a fast optical detector that is coupled to a fast oscilloscope. The NE111 scintillator, quenched with 3-benzophenone, has an impulse response of 240 ps FWHM. The scintillator is optically coupled to an ITT S-20 4014 photodiode in a matched housing. This detector has a measured time response of 120 ps FWHM. The detector has a separate high-voltage lead, so that the photocathode can be connected directly to the oscilloscope by cable.

Grazing-Incidence Spectrograph (P. Lee)

A preliminary study of the soft x-ray emission spectra from CO_2 laser-produced plasma has been carried out on Helios with a spatially resolved, time-integrated, 1-m grazing-incidence grating spectrograph (Fig. V-7). A Bausch & Lomb, Inc. 576-lines/mm 1-m grating was used for the experiment. The instrument had a nominal resolving power, $\lambda/\Delta\lambda$, of 500. A 100-μm-wide horizontal imaging slit provided spatial resolution. The magnification of the instrument varied from 2 at 300 eV to ~3 at 15 eV.

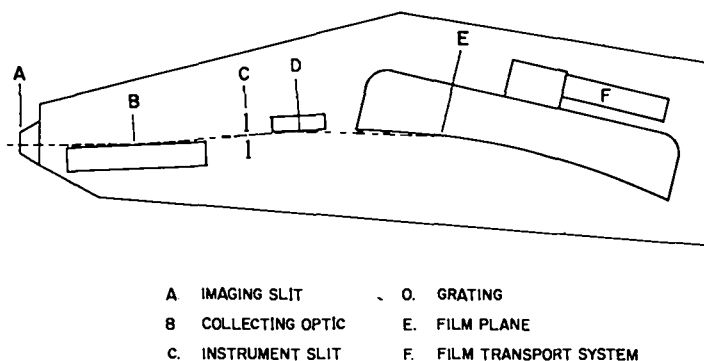| A. | IMAGING SLIT | D. | GRATING |
| B. | COLLECTING OPTIC | E. | FILM PLANE |
| C. | INSTRUMENT SLIT | F. | FILM TRANSPORT SYSTEM |

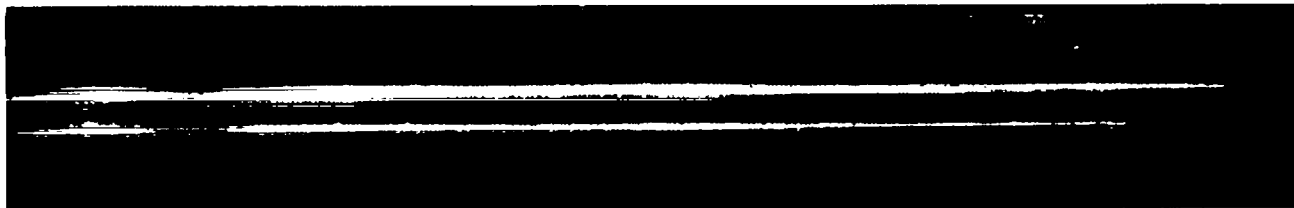Fig. V-7. Grazing-incidence grating spectrograph.

Fig. V-8. X-ray spectrographs for various targets. For both traces, the laser beams were focused on the upper and lower surfaces of the targets.

Typical spectrographs are shown in Fig. V-8. An x-ray emission spectrum from a 300-μm-diam GMB is shown in the top trace. The emission region is relatively uniform spatially, with the line spectra clearly visible far from the GMB surface. The total laser energy on target was 4.2 kJ. The lower trace is the emission spectrum of a 500-μm-diam copper/beryllium sphere with four beams each focused on the upper and lower surfaces of the target. Total laser energy on target was 4.5 kJ. Clearly discernible are the hot spots corresponding to the laser-irradiated regions and a cool region along the equatorial plane of the target. Note the distinct lack of line emission, characteristic of high-Z targets at high irradiances.

Figure V-9, Line A shows a microdensitometer scan through the center of the GMB spectrograph discussed above. Figure V-9, Line B shows a similar scan, displaced 300 μm from the target center. For comparison, in Fig. V-9, Line C, we show a microdensitometer scan

of a GMB obtained from five shots of a Nd:glass laser with a total accumulative energy of ~25 J. Some prominent lines have been identified.

For higher Z targets like nickel, the emission spectra are relatively free of lines (Fig. V-10). Line A of Fig. V-10 is the microdensitometer trace through the center of a nickel Solacel with a nominal diameter of 300 μm. Figure V-10, Line B shows a similar scan, displaced 300 μm from the target center. As in Fig. V-9, Line C, a five-shot nickel Solacel spectrum from a Nd:glass laser with a total accumulative energy of ~20 J is shown in Fig. V-10, Line C. Lack of information on nickel emission spectra[1] made line identification extremely difficult. Detailed model calculations similar to those of Duston and Davis[2] for aluminum must be made to understand the nickel data.

As an example of high-Z spectra, Fig. V-11, Lines A and B show the x-ray spectra from gold-coated GMBs. Figure V-11, Line A reflects a 3-μm gold coating,
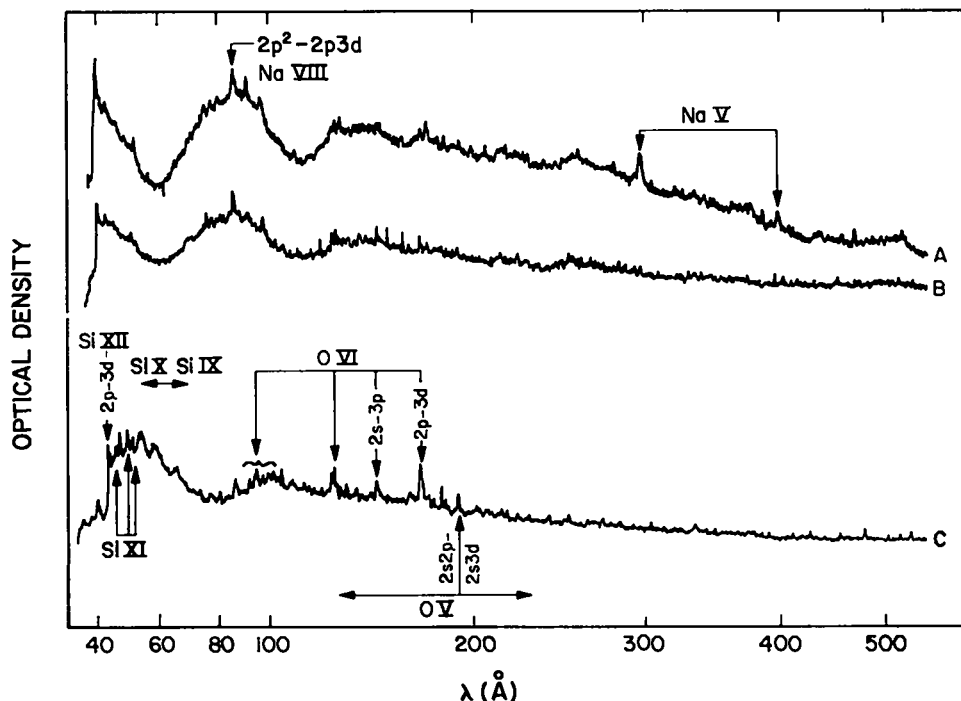
Fig. V-9. Microdensitometer scans of GMB targets: (a) through the center, and (b) 300 μm from the center of a 4.2-kJ laser shot; (c) low-energy result at ~25 J.
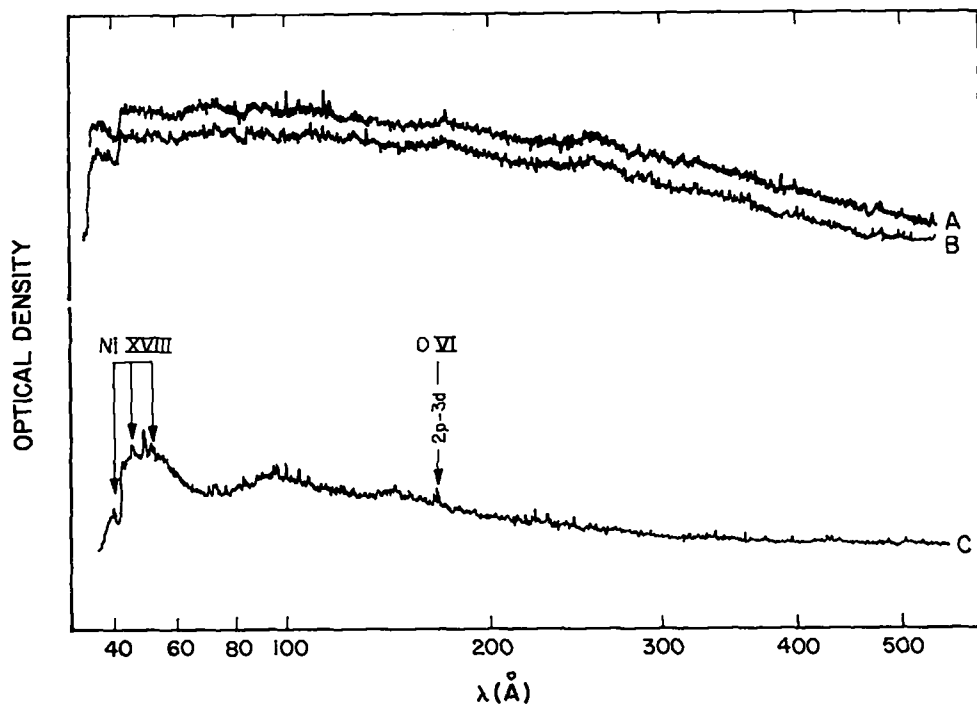
Fig. V-10. Microdensitometer scans of nickel Solacel targets: (a) through the center and (b) 300 μm from the center of a 5.2-kJ laser shot; (c) low-energy result at ~20 J.
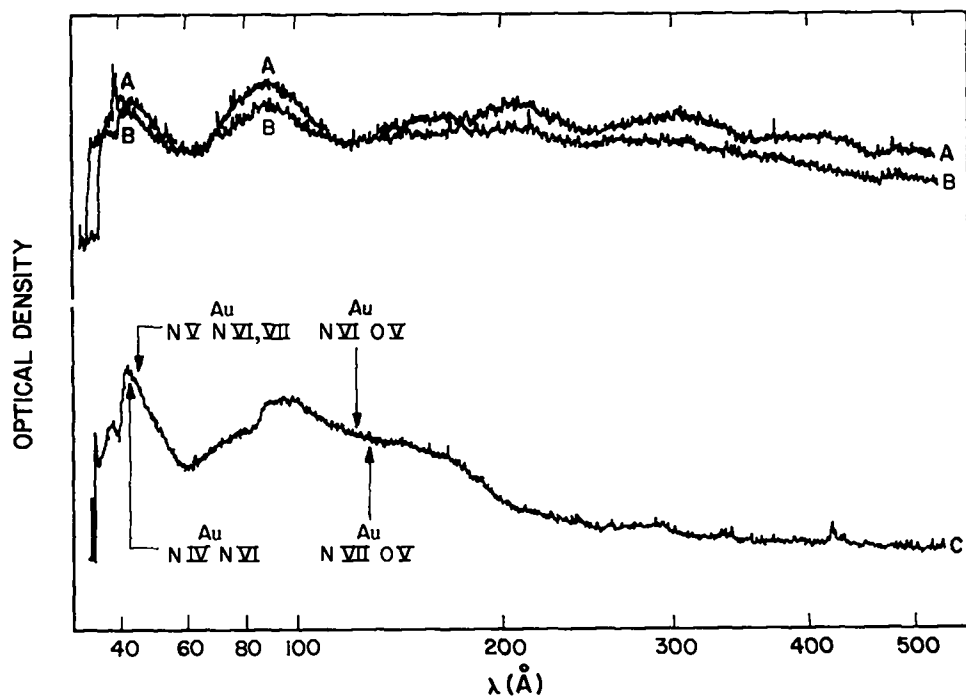
Fig. V-11. Microdensitometer scans of gold-coated GMBs: (a) 3-μm-thick gold coating, (b) 0.1-μm-thick gold coating of a 300-μm GMB plus 5-μ-m-thick CH, and (c) low-energy gold foil result at ~20 J. Laser energy in (a) and (b) was ~5 kJ.

whereas Fig. V-11, Line B reflects a 0.1-μm-thick gold coating of a 300-μm-diam GMB target coated with 5 μm CH. For comparison, Fig. V-11, Line C shows the x-ray spectra of 500- by 500-μm gold foils obtained from five shots of a Nd:glass laser with a total energy of ~20 J. Large emission spectra have been observed near the gold $N_{IV}N_{VI}$ edge.[3]

K_α Crystal Spectrograph (K. Mitchell)

We have developed concave-crystal focusing spectrographs to improve the detectability of K_α x-ray line radiation. The integrated reflectivity from a flat crystal is limited by the rocking curve or useful solid angle accepted by the crystal for monochromatic radiation.

79

This solid angle can be greatly increased by making the Bragg angle the same for all points across the crystal. This condition implies a concave focusing crystal. For best efficiency and resolution, the crystal is bent to a radius twice that of a Rowland circle radius, and the surface is ground to a radius that conforms to the Rowland circle radius. The spectrograph employing a bent LiF crystal shown in Fig. V-12 is designed specifically to measure the nickel K_α radiation at 7.48 keV. In addition, we have designed and fabricated instruments to measure the K_α radiation of copper and titanium. For limited spectral coverage, these instruments provide two-dimensional spatial resolution of the source.

The integrated reflectivity of the copper and nickel instruments was measured by using a Henke x-ray source with a copper and a nickel anode, respectively. Measurements for the copper instrument were 4.4×10^{-2} and for the nickel instrument, 4.0×10^{-2}. Their values correspond to a gain of ~200 in reflectivity over a flat LiF crystal ($R \simeq 2 \times 10^{-4}$). A spectral resolution $\lambda/\Delta\lambda$ of ~500 was measured from the separation of the $K_{\alpha 1}$ and $K_{\alpha 2}$ lines of nickel for an equivalent source size of less than 0.4 mrad.

Copper and nickel K_α line measurements were made during two Helios experiments with these instruments as main diagnostics. These instruments performed well,

with less background fog exposure than previously recorded on spectrographs. The major limitation in radiometric x-ray calibration is the use of photographic film as a recording medium. We hope to improve the data-reduction and analysis procedures and eventually to replace the film with an active readout system.

X-Ray Pinhole Cameras (D. Van Hulsteyn)

For the past several years, x-ray pinhole cameras have been used at Gemini and Helios to permit the experimenter to view the laser/target interaction in x-ray light. When different filters are placed in front of these cameras, we obtain time-integrated spectral and spatial information.

A second retractable x-ray pinhole camera was installed in the Helios target chamber this year. These cameras provide views of the laser/target interaction from points almost directly above and below the target.

Both cameras have their own vacuum airlock mechanisms, which operate independently of the target-chamber vacuum-pumping system; therefore, they can be removed and installed on a shot-by-shot basis. Data are thus available within minutes after the laser has been fired; no longer is it necessary to break the vacuum. When film cassettes were employed, the x-ray background often darkened or damaged the film, making analysis of an entire day's data difficult or impossible.

Both cameras are equipped with pinhole snouts that contain lead collimating plugs. These plugs have been invaluable in protecting the pinholes and affording a place for protective shielding. As a result, destruction of apertures has been minimal. More importantly, the pinholes are examined while the film is being processed. Damaged apertures are replaced, and the pinhole size is thus known precisely for each shot. This knowledge is crucial for data reduction of the images.

Another advantage of the cameras is the possibility of selecting the aperture size most compatible with the target. The choice depends on a tradeoff between intensity and resolution. For example, a 300-μm-diam target, requiring 30-μm accuracy, may be irradiated in one shot, followed by a 2000-μm target, requiring only 100-μm resolution. Pinholes may be preselected for both to optimize the data. Furthermore, multiple-aperture arrays may be used; each aperture is filtered to pass certain x-ray energy bands.

In the retractable cameras, disks of film are used, allowing the installation either of very stiff film, such as
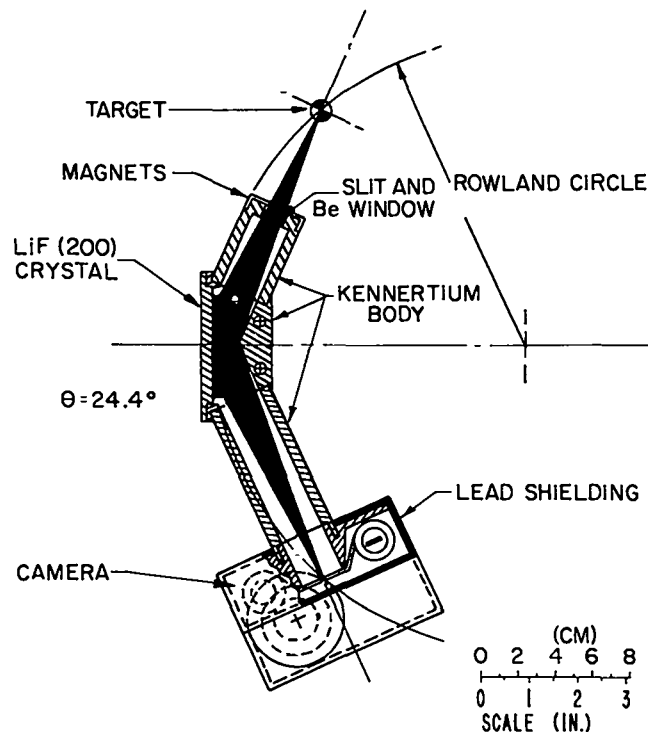

Fig. V-12. Curved-crystal spectrograph.

medical no-screen, or of sensitive film, such as 101-01. Because neither of these films could be used in the transporting cassettes, the data available were limited. The standard film pack now used in a Helios target shot is a piece of Kodak 2497 backed by a disk of no-screen. The energy responses of these two films to x rays are in the 1- to 10-keV and 1- to 100-keV ranges, respectively. Thus, the films provide different pieces of information from the target, a feature very useful in data evaluation.

One possible drawback of the cameras is the fact that they are installed semipermanently. The guide tubes can sit only in prescribed positions and can be relocated only with a full day's effort. However, once they are aligned, the guide tubes do not have to be realigned. Images are, therefore, always centered and always properly oriented for correct reading. Furthermore, the magnification is four and is invariant.

PARTICLE DIAGNOSTICS

Thomson Mass Spectrometer (F. Begay)

The Thomson parabola[4] method of mass spectroscopy is used to investigate ion production in laser-produced plasmas. Figure V-13 shows the general features of the Thomson instrument. The analyzer consists of an aperture and soft iron electrodes that serve as electrostatic deflectors and as pole pieces to produce a magnetic field. Homogeneous parallel electrostatic and magnetic fields are applied orthogonally to a stream of charged particles delimited by the aperture. Particles are deflected in the direction of the electric field in proportion to their charge-to-energy ratio Z/E and at right angles to the magnetic field in proportion to their momentum-to-charge ratio P/Z.

If we assume that the electrostatic field E and the magnetic field B are along the z-axis, then the deflection of the ions in the (y,z) plane can be expressed as

$$y^2 = \frac{ZeB^2}{EAm_p(c^2)} \ell \left(\frac{\ell}{2} + L \right) z .$$ (V-1)

In this expression, Z is the ion charge number, A is the ion mass number, m_p is the proton mass, e is the electronic charge, and c is the velocity of light in vacuo. Ion motion is along the x-axis. Thus for a constant value of Ze/Am_p, ions of all velocities lie on this parabola.

The ion velocity distribution, dN/du, can be expressed as

$$\frac{dN}{du} = \frac{dN}{dA} w \frac{ZeB\ell(\ell/2 + L)}{Am_p c(u^2)} \sqrt{1 + 4 (cE/B)^2 \, 1/u^2} \quad ,$$ (V-2)

where dN/dA are the tracks per unit area, w is the width of the parabolic trace, and u is the ion velocity. Thus, dN/du is expressed in terms of experimentally determined quantities.

Furthermore, for isothermal plasma expansions, we find that

$$\frac{dN}{du} = k_0 e^{-u/c_s} \quad ,$$ (V-3)

where c_s is the ion sound speed.

Using CR-39 film[5] as a detector, we have recorded protons with kinetic energies between 100 keV and 8 MeV at Helios. This film provides excellent contrast between acceptable tracks and noise tracks.

The detector film is chemically etched in a NaOH solution (6.25 N) at 333 K (60°C). The recorded ions then appear as small tracks on the surface of the film (track diameter, ~5-10 μm).

From Eq. (V-2) we see that we need to measure dN/dA, w, and u from the etched CR-39 plates to compute the ion velocity distribution. To automate the measurement of these parameters, we have designed an electro-optical system that allows us to measure these parameters at the rate of one ion coordinate per 30 to 40 s.

We have developed a modified Bausch & Lomb, Inc. Omnicon Alpha Image Analysis System for data reduction; in this system a word processor transfers digitized
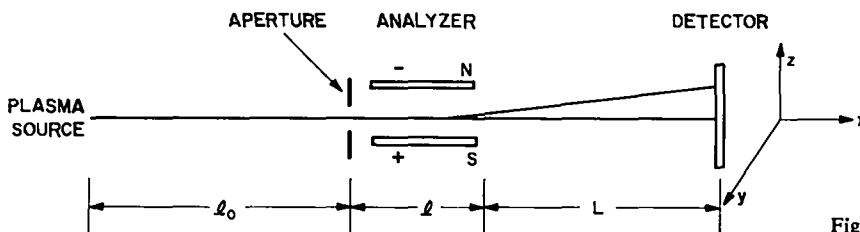

Fig. V-13. Diagram of Thomson mass spectrometer.

data on track size, track number, and track location to a floppy disk. Software in the PDP-11/70 computer processes the data on the floppy disk and generates the following information:

- ion velocity, energy, and density distribution;
- total ion energy content in each energy distribution;
- electron temperature; and
- initial ion density computed at a time approaching the laser pulse width at FWHM.

We have used the Thomson spectrometer to study isothermal plasmas as a function of target geometry and hydrogen content. Data have also been correlated with time-resolved Faraday cup ion-current measurements in an attempt to determine the energy in the fast-ion distribution. We have also developed a model that describes the dynamics of multi-ion species in an isothermal, collisionless expanding plasma.[6]

Ion Calorimetry (J. Kephart, W. Ehler)

Energy balance measurements are of great importance to the study of laser/target interactions. Previously we have used Ulbricht (integrating) sphere techniques to measure the 10.6-μm light scattered from irradiated targets; the difference between the incident light and the scattered light, of course, represents the energy absorbed by the target. This method has produced good results at low energies. We have also used Faraday cups to measure the total energy carried off in fast ions and in expanding plasma. This method has required a knowledge of the ion species involved and of the production of secondary electrons at the detector. The results obtained with Faraday cups have been difficult to interpret.

Therefore, to make more accurate measurements of the absorption and energy balance, we have developed ion-sensitive calorimeters for absolute measurement of the total energy carried off in the plasma expansion. Gold-coated sintered BeO offers several advantages as the absorbing element for ion calorimetry in the presence of intense CO_2 radiation. The gold surface of the absorbing element has a reflectivity of ~98% for 10.6-μm light. Because typical values for the absorption of laser light at the target are higher than 20% (with the energy absorbed in the target consisting principally of expanding plasma, energetic ions, and x rays), laser light will account for less than 10% of the energy deposited in the calorimeter. Thin nickel (or other) foils interposed between the target and the calorimeter absorb the soft x rays, the expanding plasma, and the 10.6-μm light while passing the energetic ions.

Using sintered BeO as a substrate for the thin gold layer offers several advantages. It is an excellent thermal conductor and electrical insulator, and allows the application of solder pads for the 32 chromel-constantan thermocouples. Thus calibration resistors can be sintered directly onto the BeO substrate to allow electrical heating with known energy. The 0.25-mm-thick BeO substrate provides total absorption for protons with energies up to 5 MeV and for carbon ions with energies up to more than 100 MeV.

The calorimeters, with an area of 10 cm², have a sensitivity of ~2 mV/J absorbed, enough to provide output signals ranging from a few microvolts to several hundred microvolts. An array of 7 calorimeters has been used in the Gemini target chamber with good results; a system of 20 calorimeters is being installed in Helios. The outputs from these calorimeters will be amplified and digitized for transmission to the data system.

Electron-Imaging Magnetic Lens Monochromator (J. S. Ladish)

Although it is generally accepted that the hot electrons generated in the laser/plasma interaction play the dominant role in the initial stages of energy transport within the target, the details of this transport and the initial energy and spatial distribution of these electrons are not well known. An instrument that could directly measure these electron parameters would yield information critical to the design of targets proposed for inertial fusion by laser drivers.

To develop such an instrument, we have constructed a thin-lens magnetic electron spectrometer capable of imaging an electron spatial source distribution of selectable energy onto a predetermined image plane. This instrument has been thoroughly evaluated and calibrated in the laboratory, and its performance has been carefully checked against the results predicted by a 2D trajectory ray-trace code, which uses a field mesh generated from an actual 2D magnetic field map of the lens. Within experimental errors associated with the laboratory measurements, the experimental results are in good agreement with the ray-trace predictions.

The instrument has been used for the first time on Gemini in a one-beam experiment. Figure V-14 shows the instrument, with the annular region of acceptance clearly visible. Figure V-15 shows a series of images obtained with the instrument in its first use. The results must be regarded as preliminary, with interpretation
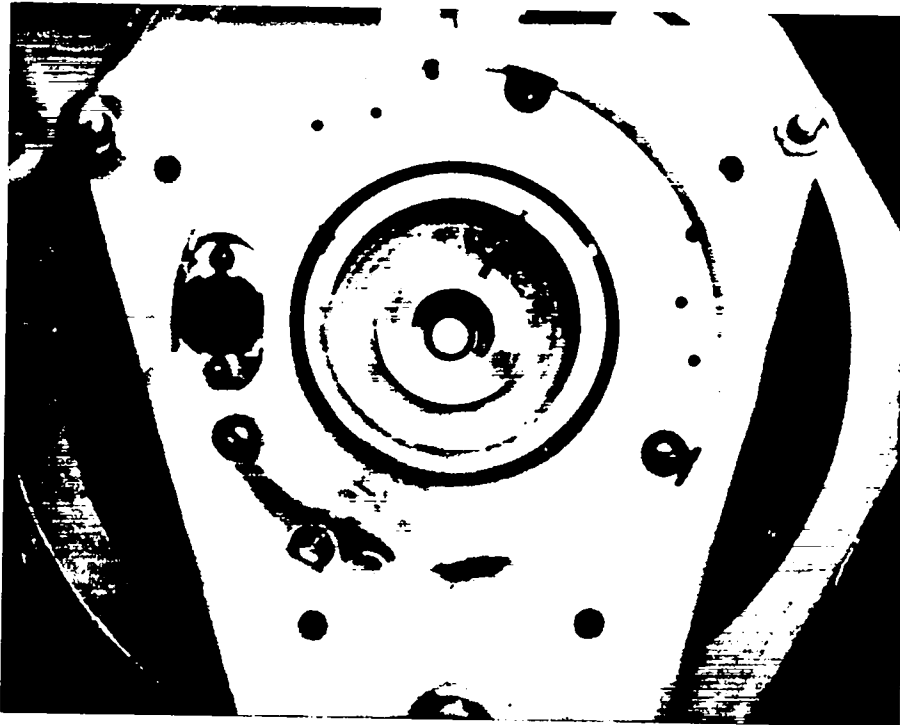
(a)

(b)

Fig. V-14. Composite photograph of electron-imaging monochromator: (a) front view of mono-chromator showing annular beam aperture, (b) side view.
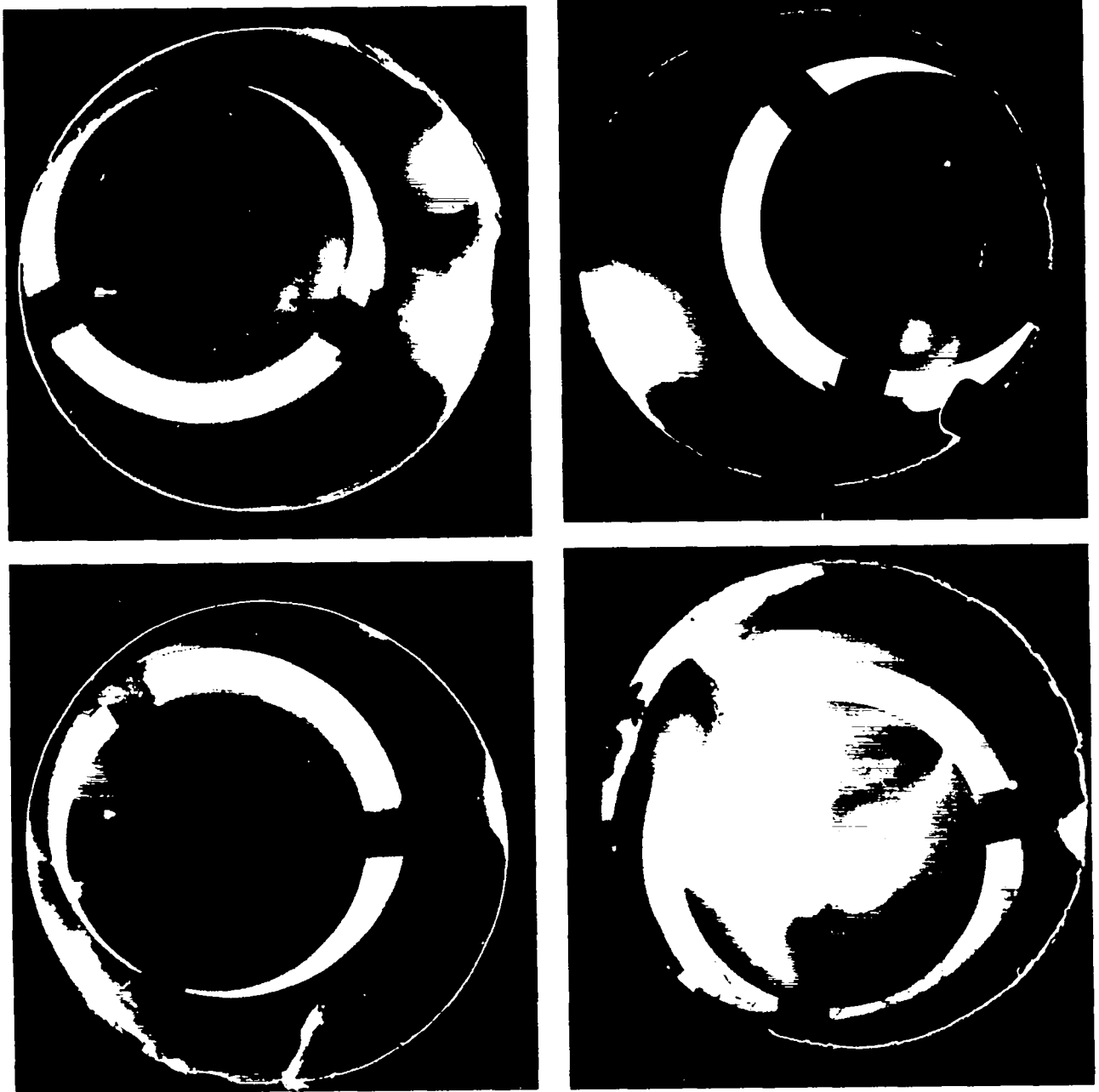
Fig. V-15. Electron image data recorded on photographic film. The annular image is due to x rays. Bright spots around the film edge are probably caused by light leaks in the film holder assembly.

awaiting more careful cross-correlation with other spatially resolving diagnostics.

INFRARED DIAGNOSTICS

Backscatter Infrared Measurements (D. Casperson)

We installed a new screen room diagnostic facility in the main laser hall of Helios. This x-ray- and EMI-shielded room with its associated beam trains was constructed to collect and analyze direct backscattered light from two of the eight Helios beamlines. The infrared diagnostics include energy content of the backscatter (fundamental and low harmonics), temporally resolved backscatter using fast pyroelectric detectors and fast oscilloscopes, and spectrally resolved time-integrated measurements. These optical diagnostics are useful in identifying the laser/plasma interactions that take place

at the target and therefore in providing a measure of how laser light couples to the target.

The two-segment, strontium/barium/niobate, fast pyroelectric detectors used with the Model-1776 fast oscilloscopes measure time-dependent backscatter with an overall resolution of ~170 ps. A sensitivity of ~3 V/MW in these detectors enables us to observe both the 10.6-μm fundamental backscatter and the target-generated second harmonic at 5.3 μm. Harmonic measurements are obtained with infrared band-pass filters that usually have bandwidths of 5% of the central wavelength. The filters we use in the backscatter diagnostic facility include those for the 2nd, 3rd, 4th, 5th, and 3/2 harmonic of 10.6-μm light. We also use an assortment of long-wave-pass filters to observe light at wavelengths exceeding 10.6 μm, generated, for example, by stimulated Raman scattering in underdense plasmas.

The recent development of uncooled high-resolution pyroelectric array detectors has made it possible to obtain infrared spectra relatively easily. A 128-element detector with 100-μm spacing between elements,* placed at the film plane of a 0.75-m Czerny-Turner spectrometer, is in use on one of the two Helios backscatter channels. The overall resolution is ~20 Å at 10 μm, which allows easy observation of the multiline content of the Helios laser system. (Successive rotational lines in the P-branch of the 10.6-μm band are separated by ~200 Å.) This resolution also allows observation of the time-integrated spectral shifts arising from motion of the target critical surface. The backscattered 10.6-μm spectra have provided the only measure of critical surface velocity on Helios targets.

Laser Beam Diagnostics (R. L. Carlson)

The laser beam diagnostics of Helios have been extensively modified and expanded. We have improved the forward beam-diagnostics area mechanically and optically. We have a new screen room adjacent to the control room for consolidating laser beam, multiplex, and other multigigahertz target diagnostics.

A review of the mechanical and optical integrity of the forward beam-diagnostics area led to several improvements.

- Three mirrors were eliminated in each diagnostic beam path.

---

*Manufactured by Spiricon, Inc., 2600 North Main, Logan, UT 84321.

- A system was provided for the simultaneous alignment of the diagnostic and amplifier beam paths.
- The mechanical stability of the optical system was improved by eliminating off-axis and cantilevered optical supports.
- Four modular prealigned and calibrated diagnostic modules were installed. Each diagnostic module consists of two pyroelectric detectors, two photon-drag detectors, and various optical elements.

A prepulse energy from each of the eight beams arranged in pairs from each diagnostics module is optically summed onto a helium-cooled Ge:Hg detector; this detector senses any energy arriving on target and detects a minimum of 10 W. Its dynamic range is limited only by the bulk damage threshold of the germanium element itself. The detector also times the fast oscilloscopes and other instrumentation by using low-energy pulses from the front-end system.

Two of the eight beams are sampled with pyroelectric detectors (1 by 1 mm; risetime, ≤30 ps) that drive 5-GHz oscilloscopes built by Los Alamos. Eight photon-drag detectors (4 by 4 mm; risetime, ≤250 ps), each monitoring one beam, are sampled by high-speed digitizers to provide a check on any postpulse energy.

A two-segment pyroelectric detector (3 by 3 mm) has been built at Los Alamos and provides a linear pulse output of 6 V into 50 Ω. It has a sensitivity of 4 V/MW and a time-domain reflectometer falltime of less than 80 ps. After suitable testing, this detector will be installed in the beam-diagnostic modules to provide pulse-shape data and will eliminate alignment problems associated with the present 1- by 1-mm detector. Its higher output will also improve the signal-to-noise ratio of the recording system.

To monitor the energy of each of the eight beams, we have built and installed modified pyroelectric joulemeters (Gen-Tec, Inc. ED-500) containing amplifier/line-driver circuits. Although each joulemeter is calibrated to 15 V/J ±5% against a tertiary standard traceable to the National Bureau of Standards (NBS) and is directly interchangeable, the scale factors between the energy delivered to the target and that sampled by these detectors will be determined by calibration against full-power calorimeters.

A new full-power (40.6-cm-diam) calorimeter has been fabricated and awaits further testing. Calorimeter calibration will be traceable to the NBS. Specifications should allow absolute calibrations of beam-energy diagnostics to within ±10%. The calorimeter uses several mils of Kapton (a plastic volume-energy absorber)

laminated to a copper sheet connected to an array of thermocouples. The calorimeter is divided into a 3 by 3 matrix, which not only provides a measure of total energy but also a measure of its uniformity. This calorimeter mounts directly onto the parabola in the Helios target chamber. A second type of total-energy-absorbing box calorimeter is being designed and fabricated to measure the full beam energy at the focus of any beam of the Helios system. This calorimeter will enable us to calibrate the energy monitors of the beam-diagnostics area to much better than $\pm 10\%$, referenced to NBS calibration, and will allow operational verification for similar units being designed for Antares.

Diagnostic Acquisition Systems
(R. C. Smith, P. B. Lyons, R. L. Carlson)

Two 4-GHz data-recording channels were installed as demonstration projects. This system allows high-resolution temporal-history diagnostics in a remote location that offers high radiation immunity. Located adjacent to the Helios control room, this system will gather effectively all relevant forward-beam-diagnostic, retropulse-diagnostic, and target data. The system has demonstrated that a 3-GHz bandwidth can be maintained over 38 m of equalized foamflex cable with an amplifier and can be displayed on a Model-1776 oscilloscope. Frequency and pulse characteristics are shown in Figs. V-16 and V-17. One demonstration channel was fed by a fast pyroelectric detector for beam pulse-shape data; the other is yet to be tested with an XRD detector. Two 1776 oscilloscopes were modified, equalizers were designed, and a 20-db gain, 5-GHz amplifier was tested. Although system response to a 3-GHz bandwidth has been demonstrated, we intend to digitize the trace data on line and to unfold the data to a 4-GHz bandwidth by a dedicated Nova computer system. A laboratory prototype of the digitizing camera and software has been tested successfully.

Because the initial multigigahertz demonstration system was successful, we installed a gigahertz screen room and associated racks in Helios late in 1981. This new diagnostics area will eventually accommodate 14 channels of multigigahertz data: 4 laser pulse-shape channels, 7 XRD channels associated with MULTIFLEX, and 3 channels not yet specified. The area will also contain dry-run, timing, and control systems, and other equipment associated with laser beam diagnostics. These diagnostics will provide common timing information for the driving laser pulses and the target-induced data on a
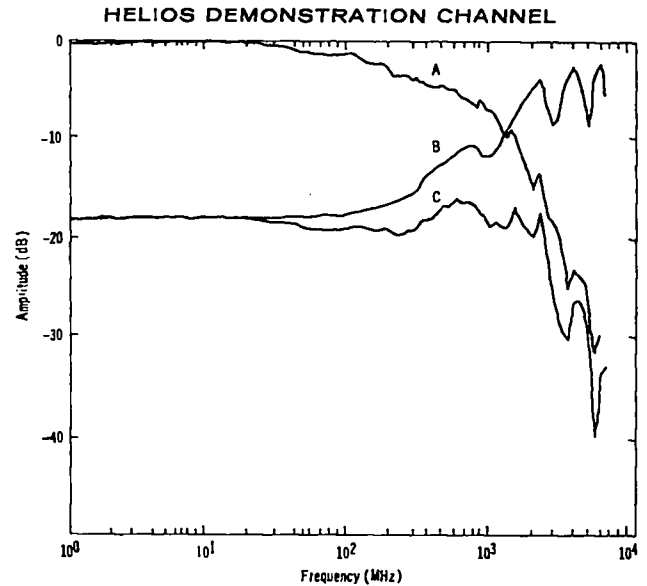
Fig. V-16. Measured system frequency response (curve A) for the Helios beam-diagnostic channel, which consists of 38 m of 1.27 cm coaxial cable, an amplifier, a 1776 oscilloscope, and a scope trace digitizer. Calculated equalizer response (B) and anticipated system response (C) are also shown.
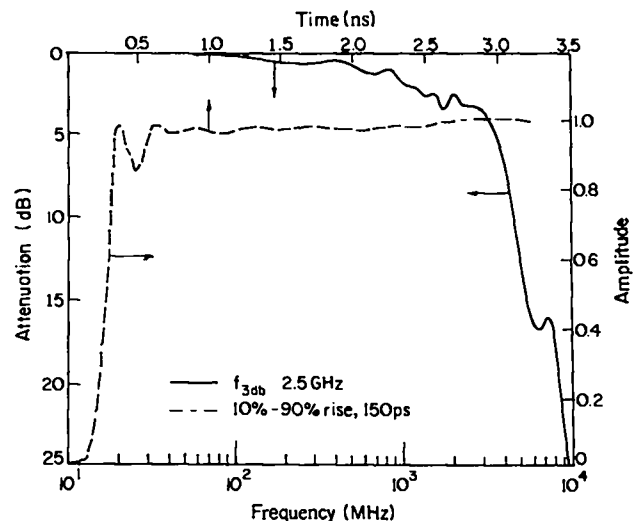
Fig. V-17. System response of the Helios beam-diagnostic channel. Dashed line shows the measured step response for the final system. The solid line shows the frequency response derived from the step response.

time scale of less than 50 ps, satisfy the needs of experimenters, centralize operations, and consolidate maintenance. Finally, the multigigahertz demonstration system will serve as the test-bed for diagnostics to be installed in Antares.

REFERENCES

1. R. L. Kelly and L. J. Palumbo, *Atomic and Ionic Emission Lines Below 2000 Angstroms* (US Government Printing Office, Washington, D.C., 1973).

2. D. Duston and J. Davis, Phys. Rev. A 23, 2602 (1981).

3. J. Mizni, N. Yamaguchi, and S. Takagi, IPPJ-498, Nagoya University (1980).

4. J. J. Thomson, Philos. Mag. 13, 561 (1907); 20, 752 (1910); 21, 225 (1911); 24, 209 (1912).

5. B. G. Cartwright, E. K. Shirk, and P. B. Price, Nucl. Instrum. Methods 153, 457 (1978).

6. F. Begay and D. W. Forslund, "Acceleration of Multi-Species Ions in CO_2 Laser-Produced Plasmas: Experiments and Theory," Phys. Fluids (to be published), LA-UR-81-1137.

VI. LASER FUSION TARGET FABRICATION
(R. J. Fries)

The target fabrication effort supplies targets for ICF compression, heating, and basic physics experiments and develops advanced materials and fabrication techniques for future targets. Because the ongoing experiments are so diverse, these targets range in complexity from simple metal or plastic-coated GMBs or plastic films to very complex multilayered component structures. The fabrication of new targets requires extensive theoretical investigation to develop the necessary materials and the methods to characterize and measure each target. After these investigations have been completed, the target is fabricated and precisely aligned in a target-insertion mechanism for correct laser focus spot in the laser target chamber.

INTRODUCTION

In 1981, our target fabrication and assembly section delivered 1935 targets; most were irradiated in our Gemini and Helios CO_2 laser systems. Because of the large number of target requests, two-thirds of our personnel are assigned to target production.

During 1981 we discontinued our cryogenic target development effort. Calculations had shown that the yield of targets containing thermonuclear fuel could be increased substantially at high laser energies if the fuel was frozen as a solid layer of DT ice onto the inside surface of the innermost pusher shell. However, we stopped our efforts in this area when we determined that cryogenic targets designed for our laser systems up to and including the 40-kJ energy level of Antares would provide only small gains for cryogenic (vs high-pressure gaseous) fuel.

We are continuing developmental work in metal and plastic coating techniques, target characterization, and target assembly techniques, because specifications for current and advanced target designs approach or exceed state-of-the-art techniques. We require target microballoons and coatings (metal and/or plastic) of uniform thickness ($\leq$1% variation), surface smoothness ($\leq$0.1% deviation), and almost perfect sphericity ($\leq$1% variation).

We are trying to deposit a wide variety of metals onto many types of substrates, including GMBs, Solacels, and other metal or plastic microspheres, as well as all types of planar substrates. Techniques now in use include electro-electroless plating, chemical vapor deposition (CVD), physical vapor deposition (PVD), and sputter deposition. These deposition techniques allow us to deposit a wide range of thin metal coatings (<1 μm) with surface smoothnesses very near the requirement and with adequate thickness uniformity. However, although we have deposited various metals in thicknesses exceeding 1 μm, surface smoothness of these coatings has been completely inadequate. Therefore, improvement of surface finishes on thick coatings is one of our prime objectives.

Because of recent requests for low-density metal layers, we have developed and can deposit "gold black" at a density no greater than 1% that of bulk gold in thicknesses up to 300 μm on planar and spherical substrates.

Using plastic coatings as absorber/ablators in advanced targets required new deposition techniques to meet coating specifications. These include low-pressure-plasma polymerization (LPP), vapor-phase pyrolysis (VPP), and sorption/diffusion (S/D). Using these techniques we have been able to produce hydrocarbon coatings on a wide variety of substrates, ammonia-borane coatings, perfluorocarbon coatings, very thick plastic coatings (600 μm), smooth transparent coatings, organometallic coatings, and graded density coatings. We can also produce high-quality, low-density, plastic foams of small cell size for use as cushions between shells in advanced targets. One type, a machinable foam, has a density of 0.05 g/cm^3 and a 20-μm cell size. We have also produced moldable foams with a density of 0.05 g/cm^3 and 2-μm cell size.

Because of rigid specifications, we must completely characterize each target to understand its performance. We are measuring and documenting all targets we deliver and are developing new, automated, high-resolution methods of characterizing target parts. We can now adequately characterize sphericity and wall-thickness uniformity, but we are still developing our techniques to characterize surface roughness. We are extending present capabilities in several measurement areas such as

electron microscopy, x-ray microradiography, and optical-transmission and optical-reflection interferometry.

Because of our flexible assembly techniques and large inventory of materials, we have been able to respond rapidly to changes in target designs and specifications. In micromanipulation and precision micromachining, our techniques advanced the state of the art. We can fabricate metal and plastic hemispheres with a surface roughness of <0.025 μm and maintain sphericity to 1 μm. Newly developed techniques have also enabled us to fabricate free-standing gold and tungsten shells with wall thicknesses of ~1 μm.

TARGET FABRICATION AND ASSEMBLY
(S. Winn)

Introduction

Our primary assignment in target fabrication is the assembly, delivery, and postshot analysis of targets for Gemini and Helios. In addition, we must be capable of responding to changes in target design and specifications. This assignment also includes the mounting of targets onto a wide variety of mounting fixtures and the precision alignment of the targets on target-insertion

mechanisms. The latest developments in micromachining and preparation of thin-walled metal shells are discussed below.

Precision Micromachining of Laser Fusion Parts
(J. Feuerherd, R. LaGasse)

High-performance ICF targets fabricated from metal and plastic hemispheres require surface finishes of 0.025 μm and sphericity to within 1 μm. Because commercially available lathes either were too expensive or could not meet the sphericity tolerances and surface-finish requirements, we have designed and built from commercially available components an air/vacuum-bearing lathe (Fig. VI-1) that meets these requirements.

This new design incorporates many state-of-the-art precision micromachining features into one unit. The rotary air-bearing spindle with its vacuum chuck is driven by an electric motor through a magnetic coupling we also developed (Fig. VI-2). This coupling prevents the transmission of vibrations to the spindle and vacuum chuck. Another rotary air bearing with attached tool holder is mounted on top of the air/vacuum-bearing x-y stages. These stages enable us to do both spherical and conventional machining without special attachments for
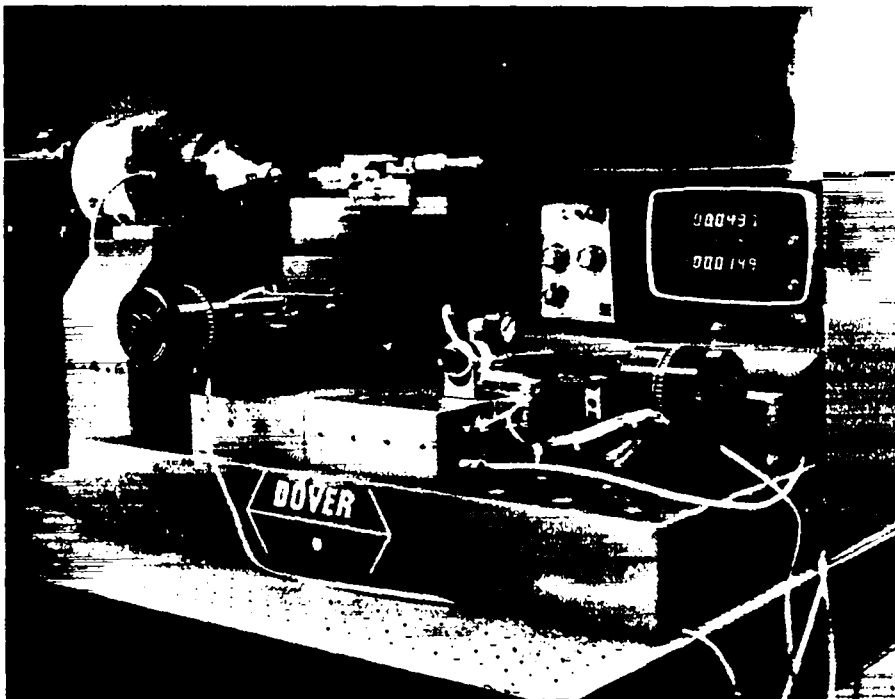

Fig. VI-1. Precision air/vacuum-bearing micromaching lathe.

Fig. VI-2. Magnetic coupling.

radius turning. Two digital micrometers, each with 50 mm of travel and a resolution of 0.1 μm, control and indicate tool location. Total travel in the y-direction is 50 mm. Travel in the x-direction was extended from 50 to 150 mm by mounting the x-axis micrometer on a piggyback air-vacuum slide that can be locked into position by vacuum. To isolate the lathe from all external sources of vibration, its table has been provided with a Newport Corp. pneumatic vibration-isolation system.

ORGANIC COATINGS
(R. Liepins)

Introduction

The use of various organic materials in fusion experiments, especially those containing only CH, is increasing. Typically, plastic coatings have been used as absorber/ablator layers, but recent target designs show an expanded use of organic materials including low-density plastic foams and organometallics. These organometallics typically contain from 1 to 4 at.% high-Z elements atomically dispersed in the plastic.

We are also fabricating low-density small-cell plastic foams for use as target cushion layers and very thin, uniform plastic films with high concentrations of specific atoms for use as x-ray fluorescent materials and filters.

Thin-Film Development
(B. Jorgensen)

Thin films containing a large fraction of oxygen are required for use as x-ray fluorescent materials or filters. Consequently, we have developed a technique to fabricate uniformly thick (±10% variation) films of polyformaldehyde (54 wt% oxygen) in thicknesses of 0.32, 0.63 (Fig. VI-3), and 1.26 μm. This is the first time that such submicrometer films have been made. We also provided films with high carbon content from polyethylene in thicknesses of 0.76, 1.34, and 2.69 μm.

We use a solution-casting process in which a solution of the desired polymer is deposited (cast) onto a suitable substrate and the solvent allowed to evaporate. The resulting polymer is then floated off the substrate in water. In this process, film thickness and uniformity are dependent upon the type of solvent and polymer used,
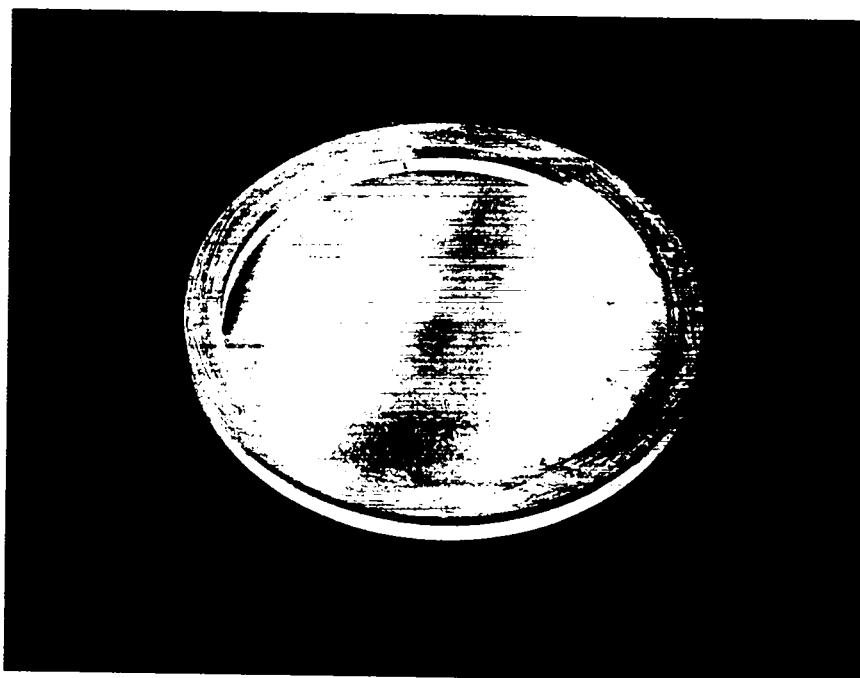
Fig. VI-3. Polyformaldehyde film (0.63 μm thick). The coloration is caused by interferometric effect.

temperature and concentration of the solution, temperature of the substrate, and rate of solution drainage. To provide the widest possible temperature range for the solution, and thus for film thickness, we are using solvents with boiling points well above the dissolving temperature of the polymers. For polyformaldehyde, the solvent benzyl alcohol was chosen and for polyethylene film, xylene was used.

To provide a method of controlling the rate of solution drainage, we built a large film-casting apparatus (Fig. VI-4). Not only does this device allow for the very fine control of drainage rate, it also allows control and adjustment of solution temperature with a heating mantle and tape (Fig. VI-5). Such temperature control is necessary because both polyformaldehyde and polyethylene are insoluble at room temperature. In this apparatus, the solution is forced up into the heated funnel by air pressure. A heated glass substrate is then placed in the solution-filled funnel. Heating of the substrate to a temperature slightly higher than the solution prevents cooling the solution at the substrate to below its gel point and aids in the evaporation of the solvent after deposition. The solution is obtained from the funnel by releasing the air pressure in the lower flask.
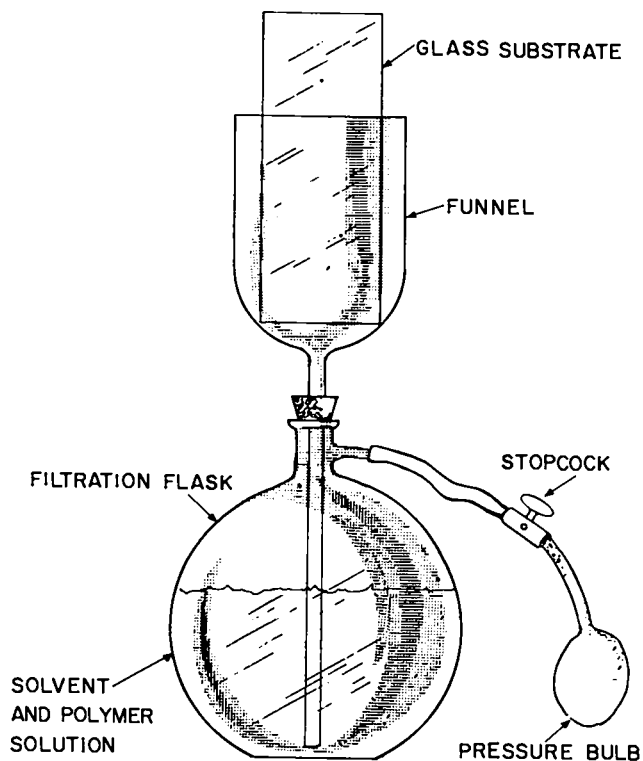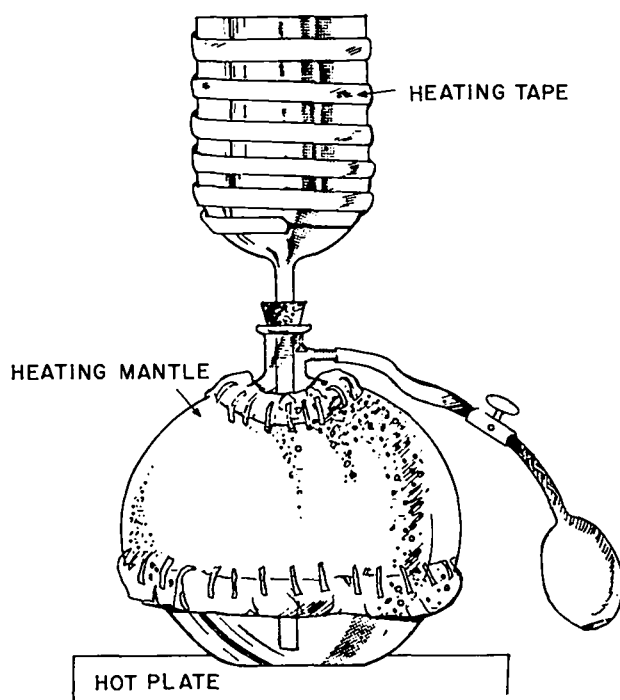

Fig. VI-4. Film-casting apparatus.

Fig. VI-5. Film-casting apparatus with heating tape and mantle.

Floating the thicker films off their substrates was sometimes difficult until we held the substrates over hot steam or soaked them in hot water for several minutes. Films are removed from the water by gently lifting them onto 7.62-cm-diam aluminum rings.

After fabrication, we characterize each film: thickness uniformity is measured with a Jamin-Lebedef interference microscope and thickness is determined by alpha attenuation.

TARGET CHARACTERIZATION
(L. Foreman)

Introduction

Because experimental results depend strongly on target diameter, wall thickness, thickness uniformity, surface finish, and fuel content, each target must be well characterized. To ensure that target components and finished targets meet or exceed specifications, we are continuing our developmental effort in target characterization. Our current target characterization technology provides numerous techniques and

procedures to ensure compliance with specifications. Current techniques include electron microscopy, contact radiography/image analysis, x-ray peak ratioing, and optical-reflection interferometry. We are also making significant progress in the development of new high-resolution characterization techniques such as light scattering, acoustic microscopy, and automated surface mapping. During 1981, we developed a technique to measure thin films and made improvements to our contact x-ray microradiographic system.

Thin-Film Thickness Measurement Using X-Ray Peak Ratioing (N. Elliott)

Measuring thin films has been a problem because the films are often opaque and the spherical surfaces of the targets are small. The ratioing of x-ray peak signals generated in a SEM provides an excellent method of measuring these thin films.

The targets we have examined are GMBs coated with thin gold films. The principle of our technqiue is shown in Fig. VI-6. A beam of energetic electrons from the SEM impinges on the surface of the target with sufficient energy to penetrate the gold film and to enter the glass substrate where it is eventually stopped. Emitted gold and silicon x rays are then detected, and the ratio of the integrated counts in the gold and silicon peaks is calculated and converted to a thickness using the calibration curve in Fig. VI-7. Calibration is accomplished by measuring films deposited on flat substrates for which accurate thickness measurements can be made using interferometry or stylus instruments.

To achieve good results with this technique, certain conditions must be controlled. Most important is that the x-ray takeoff angle used during determination of the calibration curve be repeated during target measurements. The takeoff angle is defined as the angle between the central ray of the cone of x rays intercepted by the detector and the plane of the target surface. The high mass-absorption coefficient of gold for silicon x rays will give erroneous results if the absorption path length changes from calibration standard to target. We must also duplicate composition and density between standards and the target to be measured.

Applying our technique to targets produced with varying deposition geometries, we have estimated that the measurement technique has an accuracy of ~5%. The useful range for our application of gold on a glass substrate is 100 to 2000 Å. The upper limit is determined
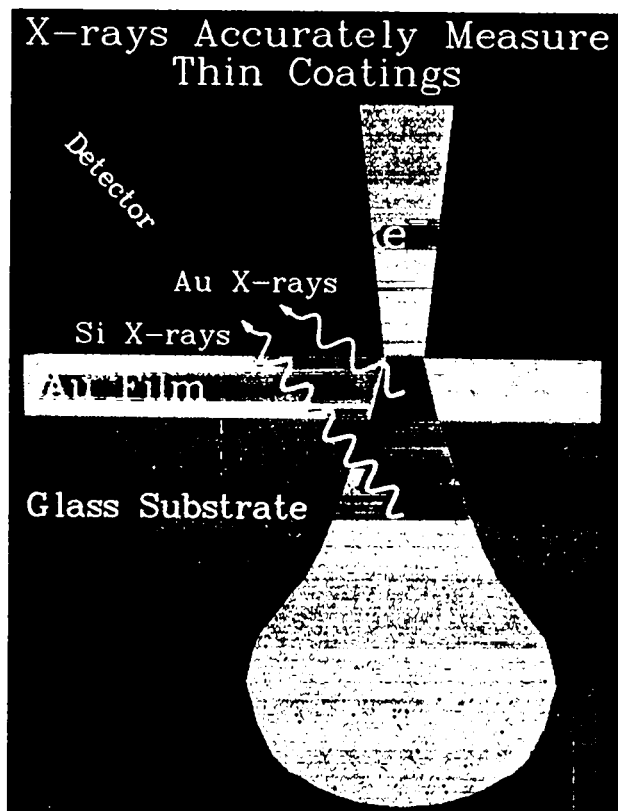
Fig. VI-6. X-ray peak ratioing schematic. The use of the ratios of the gold x rays to the silicon x rays allows an accurate measurement of the gold film on the blue glass substrate.
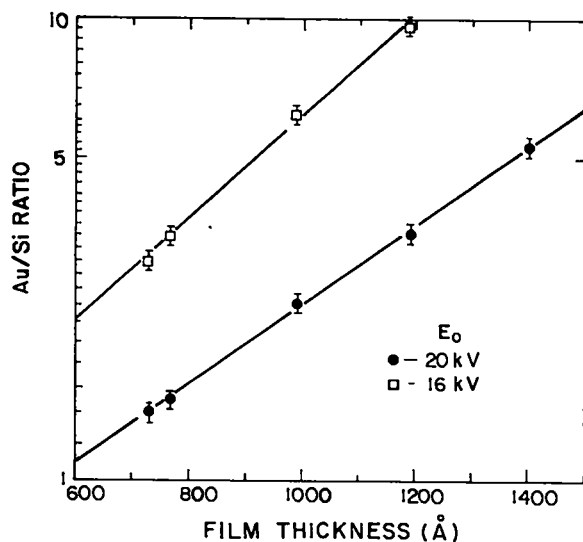

Fig. VI-7. X-ray peak ratioing calibration curve.

by the 20-kV accelerating potential of our SEM. An accelerating potential of 30 kV would extend the range to ~5000 Å.

The technique can be applied to curved surfaces and extremely small areas, is nondestructive, and can provide measurements over 4π sr for laser fusion targets. The method is applicable to any coating on any substrate as long as the electron energy is sufficient to penetrate the coating and substrate and to produce x-ray signals that can return through the coating and be detected.

Contact X-Ray Microradiography
(D. Stupin)

We are improving the characterization of targets and target components by contact x-ray microradiography. During 1981, we completed a Microradiographic Analysis System (MIRAS) (Fig. VI-8), which automatically
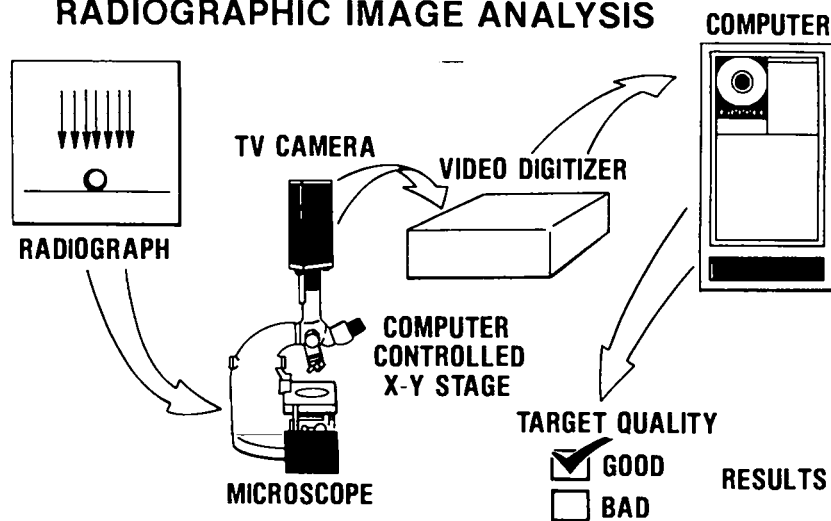
RADIOGRAPHIC IMAGE ANALYSIS

Fig. VI-8. MIRAS.

reads contact microradiographs and measures concentricity, sphericity, and small-scale defects in coatings and shells. We use a television camera to digitize the radiographic information rather than the flatbed densitometer previously used. MIRAS is as sensitive to defects in concentricity ($\pm 0.5\%$) and sphericity ($\pm 2.0\%$) as the flatbed densitometer. Images of 10 microballoons were digitized by both systems and the data were processed with the MIRAS defect detection code. The results differed by only 1%.

Contact microradiographs of targets are made on photographic emulsions with an x-ray source. The images are then placed on a microscope stage where their enlarged images are recorded by the MIRAS television camera. The video signal from the camera is converted to digital information and stored in a Data General Corp. Eclipse computer. This information is then used to calculate defects, if any, in concentricity and sphericity. Because the x-y stage of the microscope is computer controlled, up to 200 images may be processed by MIRAS after initial setup by the operator. This addition to our system will significantly increase the rate at which targets can be characterized.

VII. ADVANCED LASER TECHNOLOGY

(J. F. Figueira)

We have applied the expertise gained in developing CO_2 laser technology to related issues for other lasers. Optical-damage testing and saturable-absorber development, which were so successful in the CO_2 program, have been extended to ultraviolet systems, specifically to the KrF laser (wavelength 248 nm). The demonstration of highly reflecting dielectric coatings with damage thresholds of 4 J/cm² at a pulse length of 20 ns, the characterization of saturable-absorber processes, and the identification of anthracene as a promising material for this application are noteworthy results. Optical phase conjugation, which we first demonstrated at 10.6 µm, was obtained at the KrF wavelength.

I. INTRODUCTION

The optical-damage threshold of materials used for the optics, specifically the amplifier output windows and the beam focusing optics, limits the design of large-aperture high-energy lasers. The fundamental limits imposed by the materials themselves can be reduced by surface finishing and coating techniques. Our goal is to identify and measure the damage thresholds of prospective materials and processes so that we can characterize the damage. Then we can determine the parameters affecting the threshold and make improvements. Damage thresholds as high as 5 to 10 J/cm² for short pulses are needed for feasible designs. Such values have been achieved for 10.6-µm laser optics and we are making significant progress with ultraviolet laser optics.

A second limit on laser amplifier designs is imposed by optical parasitic oscillations that may occur at the high-gain levels of such systems. A highly successful development program for Helios, based upon saturable gaseous absorbers to suppress low-level optical sources of parasitics, allows us to operate this laser system at design levels. Although specific designs do not yet exist for high-power gas lasers in the ultraviolet, we have begun to characterize the processes and materials that could be valuable for such designs.

We are exploring nonlinear optical phase conjugation to remove aberrations from large optical systems, because this technique offers great promise for improved performance and reduced costs. After demonstrating and characterizing this process for CO_2 lasers, we have extended this work to ultraviolet wavelengths.

DAMAGE THRESHOLD STUDIES

(B. Newnam, S. Foltyn)

Introduction

Los Alamos and Lawrence Livermore National Laboratory (LLNL) laser personnel have recently compared results of separate laser damage tests at 248 nm for 12 multilayer-coated optical parts. The samples consisted of 10 highly reflecting and 2 antireflection coatings deposited on 5-cm (2-in.) -diam BK-7 glass and fused silica substrates. The coating manufacturers were Optical Coating Laboratory, Inc. (OCLI), Battelle Northwest, Design Optics, CVI Laser Corp., and Acton Research. In the following paragraphs, we discuss the magnitude and possible origin of the differences in threshold values measured by the two laboratories. Six examples from the two sets of data may be used to identify coating deposition parameters and designs that are used to attain increased damage thresholds.

Threshold Definitions and Results

Test parameters used in damage tests at Los Alamos and LLNL were substantially different; the greatest difference lies in the number of shots per test site: 1000 (Los Alamos) vs 1 (LLNL). Table VII-I lists the other test parameters for direct comparison, and Table VII-II presents the respective thresholds. For proper interpretation, it is necessary to review the definitions of threshold and upper limit. The Los Alamos values were derived

TABLE VII-I. Comparison of Los Alamos and LLNL Damage Test Parameters

	Los Alamos	LLNL
Laser	KrF, 248 nm	KrF, 248 nm
Pulse width	10 ns	20-ns equivalent in 3-pulse segments
Spot-size diameter	0.6-mm (I/e^2) smooth profile	0.1-mm² hot spot within uniform multispike profile of 2-mm diam
No. shots/site	1000	1
No. sites irradiated	40 to 80	6 to 8
Repetition rate, Hz	35	0.2
Damage detection technique	Visual observation by 25 to 100X magnification with bright white-light illumination before and during laser irradiation	Dark-field Nomarski photographs at 100X before and after laser irradiation

TABLE VII-II. Comparison of Los Alamos and LLNL Measurements of 248-nm Laser Damage Thresholds of Multilayer Dielectrics

Sample Type and Materials	ID No.	Coatings Manufacturer	Los Alamos Multiple-Shot[a] Threshold (J/cm²)		LLNL Single-Shot[b] Thresholds (J/cm²)
			Threshold (0 of 10)	Upper Limit (10 of 10)	
AR, Al_2O_3/MgF_2	A-1298	Design Optics	4.4	4.7	4.3 ± 0.5 both surfaces
AR ---	B-1293	CVI	2.8	3.5	2.1 ± 0.5 one surface
HR ---	C-1296	Design Optics	---	<0.2	0.3 ± 0.2
HR ---	D-1295	Acton Research	---	<0.6	1.0 ± 0.1
HR, Sc_2O_3/MgF_2	16	OCLI	3.9	4.7	6.0 ± 1.0
HR, Sc_2O_3/MgF_2	21	OCLI	2.5	4.3	5.9 ± 0.6
HR, Sc_2O_3/MgF_2	27	OCLI	1.4	2.6	2.6 ± 0.3
HR, Sc_2O_3/MgF_2	45	OCLI	3.1	3.7	8.5 ± 0.9
HR, Sc_2O_3/MgF_2	71	OCLI	3.9	4.8	6.3 ± 1.0
HR, Sc_2O_3/MgF_2	818[b]	OCLI	2.7	3.4	4.0 ± 0.4
HR, $Al_2O_3SiO_2$	2504	Battelle NW	--	≤2.0	2.3 ± 0.2
HR, Y_2O_3/SiO_2	2520	Battelle NW	~0.7	<1.3	0.7 ± 0.1

[a]See Table VII-I for Los Alamos and LLNL test parameters.
[b]All reflectors are on BK-7 glass substrates except one, which is on fused silica.

from graphs such as that shown in Fig. VII-1, which displays the fraction of sites that are damaged at a given laser fluence. Ten sites were tested at each fluence; by extrapolating the line drawn through the points, we obtain both the damage threshold (0 of 10 sites damage intercept) and the upper limit (10 of 10 sites damage intercept). Using such graphs, we have found consistently (for ~100 samples) a significant spread in the damage resistance of various test sites on a sample.

The LLNL definition of damage threshold is the fluence level midway between the highest fluence at which no damage was observed and the lowest fluence at
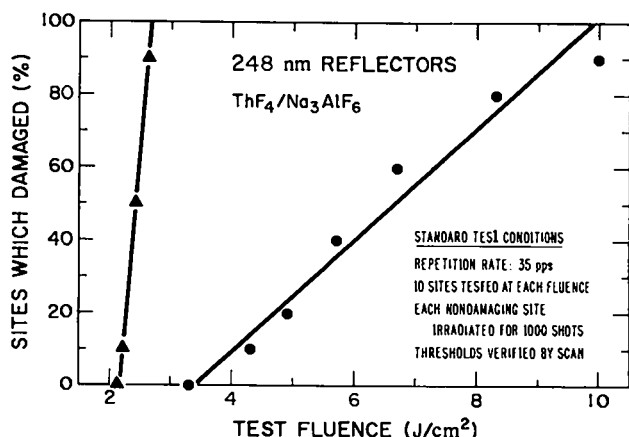
Fig. VII-1. Probability of damage vs peak test fluence for two 99% reflectors at λ = 248 nm. Damage threshold is the 0% intercept.

which damage occurred. It is significant that no crossovers in the incidence of damage were observed. That is, in the six to eight shots used to establish a threshold for each sample, the lowest damaging fluence was not exceeded by a nondamaging fluence. Further, the ± values appended to their thresholds represent the gap between nondamaging and damaging shots. The LLNL results imply a very sharp threshold boundary, in contrast to the Los Alamos observations of variable damage resistance across the area of a sample.

It is appropriate to compare directly the lower Los Alamos threshold (0 to 10 sites damage intercept) with the LLNL threshold range and to compute a ratio. For example, for Sample A-1298, the ratio of 0.86 to 1.09 is obtained by dividing 3.8 to 4.8 by 4.4. We find that the common ratio for samples A, B, C, D, 2504, and 2520 is approximately unity. Evidently, the test parameter variations between the two laboratories had no effect on these results. However, the common ratio for the OCLI Sc_2O_3/MgF_2 reflectors is 2.0 ± 0.3, which elicits our interest and further discussion.

Influence of Test Parameters

When we examine the respective test parameters, it is not surprising that the LLNL values for the OCLI reflectors exceed those of Los Alamos (by an average of 100%). Higher damage thresholds, in terms of J/cm², are expected for LLNL's longer pulse width ($\tau \sim 20$ ns). Pulse width scaling of the threshold has been observed empirically to be less than or equal to $\tau^{1/2}$. At most, then,

pulse width scaling could account for 40% of the difference $[(\sim 20/10)^{1/2} = 1.4]$.

The remaining 60% difference should be accountable by other paramters. (1) The sample area irradiated by the Los Alamos beam (0.6-mm diam at $1/e^2$ peak fluence) was larger than the 0.1-mm² hot spot of LLNL's beam. However, the area of the Los Alamos beam within 5% of its peak fluence is comparable to the LLNL beam, so that substantial difference is not expected from this parameter. (2) The difference in number of shots per site (1000 vs 1) probably did not alter the thresholds. For the coating materials of these reflectors (Sc_2O_3/MgF_2), damage at Los Alamos was either detected within the first 5 shots or the site survived the entire 1000 shots. (3) We do not believe that the low 35-Hz repetition rate at Los Alamos should give results that differ from those of intermittent pulsing. However, tests at several repetition rates should verify this assumption. (4) The different damage detection techniques used at the two laboratories are not suspected of causing much threshold discrepancy. On a single-shot basis, LLNL's dark-field Nomarski photographs probably make threshold damage (micrometer-sized pits) easier, but multiple-shot irradiation of a damage site, as at Los Alamos, generally increases the extent of the damage to readily visible dimensions. (Perhaps 5 to 10 shots occur after damage is detectable before the Los Alamos operator can block the laser beam.)

The remaining parameter, number of sites irradiated (40 to 80 vs 6 to 8), may be the source of most of the threshold difference. As shown in Fig. VII-1, a fraction of the sites irradiated above the threshold (0 of 10 sites damage) resisted damage. Therefore, we conclude that the coatings have nonuniform damage resistance across their surface or that damage may be a probability. Los Alamos attains adequate sampling of the surface by irradiating 10 sites at each fluence (4 to 8 levels) in addition to a 25-mm scan just below the threshold fluence.

We have only been able to speculate on the reasons for these differences in thresholds reported by Los Alamos and LLNL. Most of the remaining uncertainty could be greatly reduced or eliminated if the two laboratories used nearly identical test parameters. We propose another comparative test program on a new set of samples. The common test parameters would be (1) 10-ns pulse width, (2) 40 sites per sample, (3) 10 shots per site, and (4) a repetition rate of 5 Hz or less. The remaining parameters would be those currently used (Table VII-I).

Influence of Coating Design and Deposition Parameters

Table VII-III compares the influence of several coating design and deposition parameters for the OCLI Sc_2O_3/MgF_2 reflectors. A half-wave (HW) overcoat of SiO_2 almost doubled the damage thresholds over that of a standard uncoated reflector. (The overcoat insulates the outer Sc_2O_3 layer from atmospheric contamination.) Further, Los Alamos results indicate even higher thresholds when MgF_2 is used. When deposited optimally, MgF_2 has greater damage resistance than SiO_2; as a HW overcoat, it must withstand a very high standing-wave electric field.

OCLI frequently observed that reflectors on fused silica substrates developed stress-relief lines after removal from the deposition chamber, which were caused by differential thermal expansion coefficients of film and substrate. The thermal expansion of BK-7 glass more closely matches that of the coatings, and therefore OCLI tried BK-7 glass as a substrate for the reflectors. Los Alamos' damage results showed no effect on the threshold by the choice of substrate. However, our upper limit value and LLNL's threshold value were lower for the reflector on fused silica. Evidently, it is important to use appropriate deposition parameters to minimize the net tensile stress in the coatings.

Neither laboratory discerned any influence by substrate temperature between 423 and 523 K (150 and 250°C). However, the data of the two laboratories led to opposite conclusions on the effect of 31- vs 19-layer reflectors. This discrepancy has not been resolved.

In summary, a HW overcoat on these reflectors successfully increases damage resistance. The effect (if it exists at all) of the other parameters (substrate, substrate temperature, and number of layers) is not significant. However, a lower substrate temperature of 423 K (150°C) will decrease film stress problems.

TABLE VII-III. The 248-nm Laser Damage Thresholds for Sc_2O_3/MgF_2 Total Reflectors

Sample No.[a]	Coating Parameter	Los Alamos[b] Multiple-Shot Thresholds (J/cm^2)		LLNL Single-Shot[b] Thresholds (J/cm^2)
		Threshold (0 of 10)	Upper Limit (10 of 10)	
Overcoat				
27	None	1.4	2.6	2.6 ± 0.3
21	HW of SiO_2	2.5	4.3	5.9 ± 0.6
16	HW of MgF_2	3.9	4.7	6.0 ± 1.0
Substrate				
21	BK-7	2.5	4.3	5.9 ± 0.6
818	SiO_2	2.7	3.4	4.0 ± 0.4
Substrate deposition temperature				
16	423 K (150°C)	3.9	4.7	6.0 ± 1.0
71	523 K (250°C)	3.9	4.8	6.3 ± 1.0
No. of layers				
16	19 + HW of MgF_2	3.9	4.7	6.0 ± 1.0
45	31 + HW of MgF_2	3.1	3.7	8.5 ± 0.9

Standard design: $S(HL)^9HL^2$ deposited at 423 K (150°C)
where S = BK-7 substrate
H = Sc_2O_3, n = 2.05
L = MgF_2, n = 1.40
L^2 = MgF_2 overcoat, HW thick (except SiO_2 on two samples)

[a]These six reflectors were produced by Optical Coating Laboratory, Inc., Santa Rosa, California.
[b]See Table VII-I for test conditions.

SATURABLE ABSORBERS AT 248 nm (W. B. Lewis)

Introduction

In the development of KrF fusion laser systems, saturable absorbers at 248 nm will play an important role as optical components. The purpose of this study has been to (1) identify potential absorbers, (2) evaluate saturation and photochemical performance of promising compounds, and (3) develop a model for understanding the photophysics of such absorbers in terms of cross sections, lifetimes, and relaxation or quenching rates.

Saturable absorbers can be classified into two types: (1) those that undergo photodissociation upon absorption of a photon, followed by rapid recombination of the products between laser pulses and (2) those that undergo excitation to some very short-lived singlet excited state, which in turn relaxes to a lower excited state with a lifetime approximately that of the KrF pulse length ($\sim$10 ns) or longer.

We have usually described the time-dependent performance of saturable absorbers in terms of analytical expressions for 2-, 3-, and 4-level absorbers. However, none of the absorbers we shall consider here saturates in a way that can be treated with the aid of such expressions. The latter are derived on the assumption that a steady state is achieved in a time shorter than the laser pulse length; actually, in a photodissociative absorber, a steady state is never achieved, and in the 10-ns length of a KrF pulse, the various state populations of the absorber are still far from steady state [even in Type (2) absorbers]. Furthermore, even four levels are inadequate to describe the performance of the absorbers.

Reversible Photodecomposable Absorbers

We assume that photodissociative absorber molecules dissociate within one vibrational period upon the absorption of a photon at 248 nm. (This is essentially instantaneous on the 10-ns time scale that is appropriate for a KrF laser pulse.) If the absorber with density n_0 and thickness x_0 is exposed to a rectangular pulse in a collimated beam at time $t = 0$, the rate equation for the disappearance of the absorber can be simplified by assuming that the effective thickness of the absorber x changes with time rather than with the molecular density. The rate equation can then be integrated to obtain

$$\frac{(e^{\sigma n_0 x} - 1)}{(e^{\sigma n_0 x_0} - 1)} = e^{-I_0 \sigma t} , \qquad (VII-1)$$

where σ is the absorber cross section in cm^2 molecule^{-1}. If the absorber transmission at $t = 0$, $e^{-\sigma n_0 x_0}$, is taken as 1%, the irradiance of the transmitted beam I(t) is given by

$$\frac{I(T)}{I_0} = \frac{1}{(1 + 0.99\, e^{-I_0 \sigma t})} . \qquad (VII-2)$$

For other initial transmission, the factor 0.99 can be replaced by $(e^{-\sigma n_0 x_0})$. Figure VII-2 gives plots of Eq. (VII-2) for several values of the product $I_0\sigma$. A figure of merit for saturable absorbers of this type is the product of the time required for the laser beam to consume half of the absorber molecules t and the beam irradiance I_0:

$$\frac{I_0 t = 2.398}{\sigma} . \qquad (VII-3)$$

If the pulse fluence in W/cm^2 is used for I_0, to obtain t, the right side of Eq. (VII-3) must be multiplied by the factor 7.993×10^{-19} J/photon. The half-time $t_{1/2}$ corresponds to an increase in I(t)/I_0 from 0.01 at $t = 0$ to 0.10.
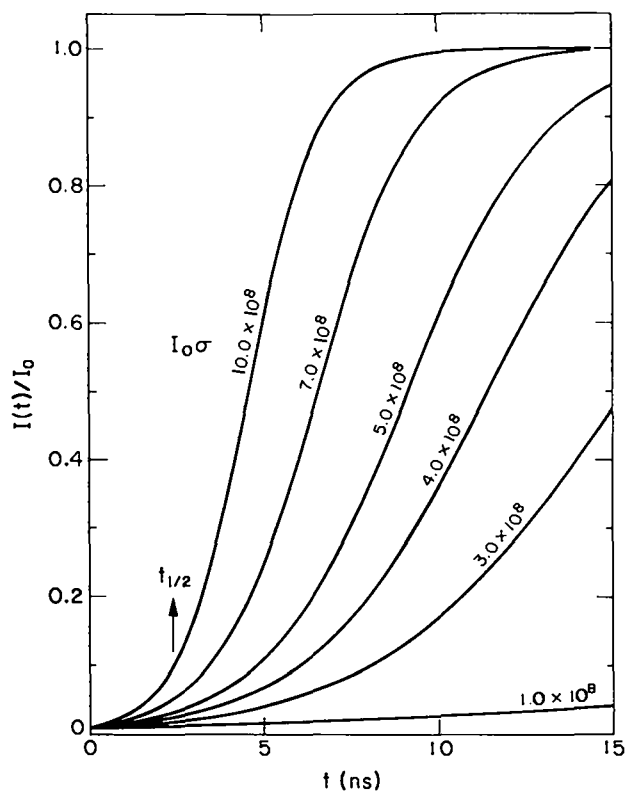

Fig. VII-2. Time-dependent transmission by reversible photodissociative absorbers.

Because we can detect changes in $I(t)/I_0$ smaller than twice the initial value of 0.01, the product $I_0\sigma$ can be as small as 1×10^8. The damage threshold of 2 J/cm^2 limits us to measurements with $I_0 < 2.5 \times 10^{26}$ photons/cm^2· s or to the detection of saturation with $\sigma > 4 \times 10^{-19}$ cm^2. Therefore, we cannot study absorbers with $\sigma < 4 \times 10^{-19}$ cm^2 in cells with windows like those we have employed in our study. However, such absorbers require power levels in excess of 500 MW/cm^2, which corresponds to the total peak power for an entire KrF fusion laser system and would not be of interest here. The desired absorbers must have a value of $\sigma > 4 \times 10^{-19}$ cm^2 to saturate at lower powers, but this is a very restrictive requirement if the absorber must be reversibly photodecomposable as well.

Table VII-IV lists some potential photodissociative absorbers that have been selected from the literature. Only three have values of $\sigma > 4 \times 10^{-19}$ cm^2—O_3, CH_3I, and CrO_2Cl_2. The products of CH_3I dissociation are principally CH_3 and I, and CH_3 radicals recombine with each other at near-gas kinetic rates so that there is almost no hope of obtaining full recovery of the CH_3I after the initial laser pulse. The products of CrO_2Cl_2 dissociation are CrO_2 and Cl. It is well known that the CrO_2 radical deposits on windows, so there is little hope of recovery of CrO_2Cl_2 in that case either. Of the compounds in Table VII-IV, only O_3 shows promise, and even it saturates at a fairly high level of 0.36 J/cm^2 or 36 MW.

Because the only KrF laser available with fair power density was a Lumonics 860 with an output of 0.070 J/cm^2, we postponed any saturation measurements on ozone. A larger cable-driven KrF laser injection-locked to a Math Science NW Excilite laser will eventually produce 0.75 J/cm^2, but extreme delays in obtaining the necessary custom-coated mirrors have made it temporarily unstable at 248 nm.

Absorbers with Electronic Relaxation

Substances that relax back to the ground state in approximate times of the KrF laser pulse length of ions are typically aromatic or large unsaturated heterocyclic molecules. An extensive literature already exists on the photophysical properties of such molecules, expecially aromatic hydrocarbons. After a literature survey of the uv spectra of such molecules, we selected anthracene as the most promising. In addition to having a very large cross section at 248 nm and a reasonable fluorescence lifetime of 5 ns, anthracene is one of the most thoroughly studied aromatic molecules. Phenanthrene was later added to the study because of its much longer fluorescence lifetime and similar excited-state absorption.

Experimental Procedure

The method of measuring saturation was simple, consisting of (1) a Scientech Inc. Model 362 Power Meter; (2) a 1-cm-path-length Suprasil-II quartz cell connected to a 500-cm^3 reservoir through a recirculation loop that included a variable-speed magnetically coupled micropump; and (3) another quartz cell for adding

TABLE VII-IV. Performance Parameters for Potential Photodissociative Absorbers

| Absorber | Absorption Coefficients | | Saturation Level | |
	σ (cm^2/molecule)	α (cm^{-1}/torr^{-1})	2.4 hν/σ (J/cm^2)	(MW/cm^2)
O_3	5.25×10^{-18}	0.17	0.36	36
F_2	1.53×10^{-20}	0.00050	125	12 500
ClF_3	1.53×10^{-19}	0.0050	12.5	1 250
Cl_2	3.7×10^{-21}	0.00012	520	52 000
NO_2,O_2	3.1×10^{-20}	0.0010	62	6 200
N_2O_4,O_2	3.7×10^{-19}	0.012	5.2	520
NOCl	2.7×10^{-19}	0.0088	7.1	710
CH_3Br	1.4×10^{-20}	0.00046	137	13 700
CH_3I	7.6×10^{-19}	0.025	2.5	250
CrO_2Cl_2	1.33×10^{-18}	0.043	1.4	140

attenuator solutions to vary the laser beam power over an optical density of three units. The laser source was a Lumonics Model 860 KrF laser.

To avoid any exposure of the power meter to thermal radiation produced by the laser beam along its path, after passage through the attenuator solution the beam was turned 90° by a dielectric-coated mirror. The beam then passed through a 1- by 1-cm copper iris backed by 1 cm of ceramic foam insulation. Before entering the power meter, it passed through a Suprasil-II quartz window to absorb thermal radiation of <5 μm.

The power meter has advantages over other detectors; it handles high power levels and has a dynamic range of 10^5 when thermal radiation is rejected. We calibrated the instrument just before initial measurements. In this experiment the only practical way to vary the beam power over a wide range was to use attenuators or beam splitters. However, commercial devices capable of handling high power were only available on custom order, entailing long delays; therefore, we developed a solution or volume absorber with sufficient stability for up to 30 s, which was needed for a single measurement of $I(t)/I_0$. The absorber consisted of mixtures of CCl_4 in n-hexane. We estimated approximate attenuation values for various mixtures and measured I_0, the power incident on the absorber, with the absorber removed from the beam. The transmission coefficient T is then the ratio of the power transmitted with absorber in place to the incident power I_0, provided a correction is applied for the absorption and reflection by the cell filled with neat hexane. Fresh attenuator solution was mixed for each measurement, and the cell windows were carefully cleaned to remove carbon deposits.

Saturation in Anthracene

Anthracene has one of the largest cross sections of all molecules, and the oscillator strength for the $^1A_{1g}^- \rightarrow$ $^1B_{3u}^-$ band centered at 251 nm is 0.57, or near the theoretical limit of 1.00. Figure VII-3 shows the structure of the electronic energy level for anthracene. Although many levels appear below 50 000 cm^{-1}, only two medium or strong bands are observed. For the purpose of saturable-absorber performance, we can regard anthracene as a six-level system: $^1A_{1g}^-$ ground state S_0; $^1B_{2u}^+$ first excited singlet state S_1, the emitting level with lifetime of about 5 ns in liquid hexane; B_{3u}^+ second excited singlet state S_3 reached by absorption of a single 248.4-nm photon; unidentified higher singlet state S_n
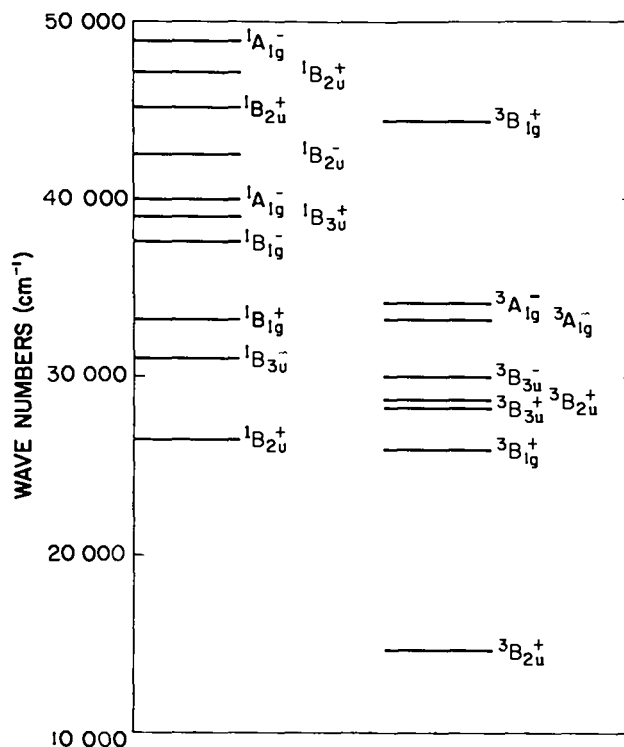
Fig. VII-3. Electronic energy level structure for anthracene.

reached from S_1 by absorption of a photon; $^3B_{2u}^+$ lowest triplet state T_1 populated by intersystem crossing from S_1; and unidentified triplet state T_n reached by absorption of a single 248.4-nm photon from the T_1 state. Figure VII-4 shows these six electronic levels with their associated vibronic sublevels and the more important
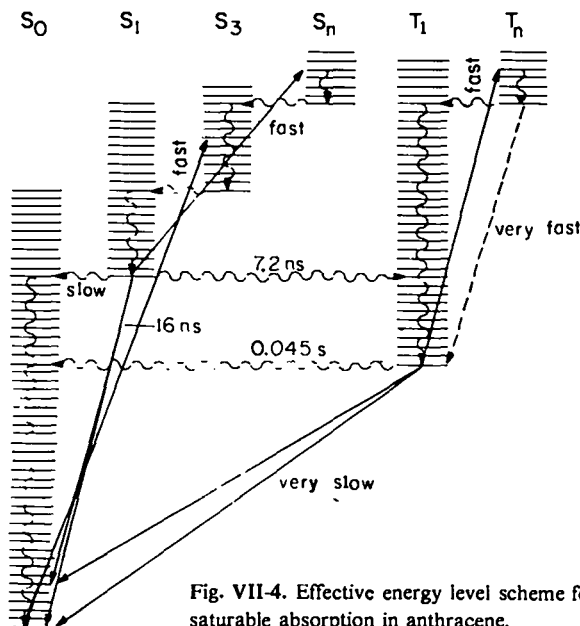
Fig. VII-4. Effective energy level scheme for saturable absorption in anthracene.
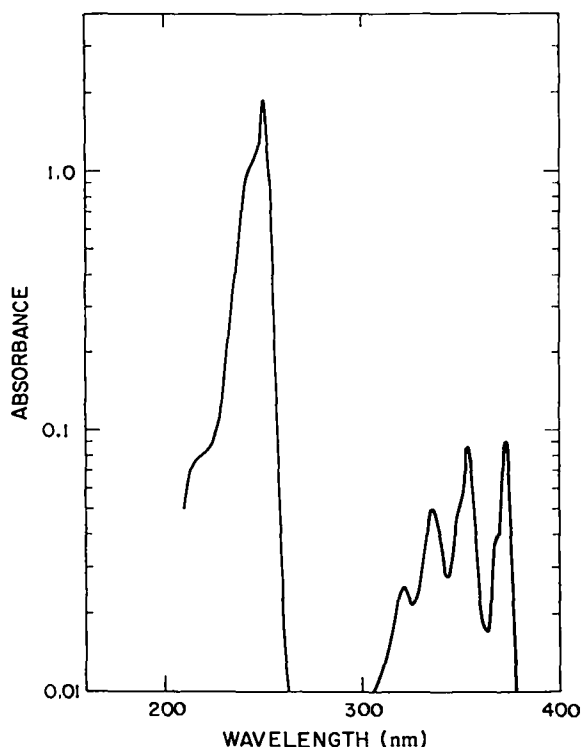
Fig. VII-5. Near-uv absorption spectrum of anthracene (1.0 ×
10^{-5} molecules in hexane).

relaxation, excitation, and radiative pathways intercon-
necting the various states. Figure VII-5 shows the
absorption spectrum of anthracene above 200 nm.

For the above reasons, the saturation performance in
anthracene is too complex to be described with an
analytical expression, and we must doubly integrate the
rate equations [Eq. (VII-4) below], once with respect to
time and once with respect to distance in the absorber.
The rate equations are as follows, the numbering of
states corresponding to the order in which they are listed
above.

$$\dot{n}_1 = I_0\sigma_{13}(n_1 - n_3) + A_{21}n_2 + A_{51}n_5$$

$$\dot{n}_2 = I_0\sigma_{24}(n - n_4) - A_{21}n_2 + A_{32}n_3 + A_{42}n_4 - A_{25}n_2$$

$$\dot{n}_3 = I_0\sigma_{13}(n_1 - n_3) - A_{32}n_3$$

$$\dot{n}_4 = I_0\sigma_{24}(n_2 - n_4) - A_{42}n_4$$

$$\dot{n}_5 = I_0\sigma_{56}(n_5 - n_6) - A_{51}n_5 + A_{25}n_2 + A_{65}n_6$$

$$\dot{n}_6 = I_0\sigma_{56}(n_5 - n_6) - A_{65}n_6 \ . \qquad\qquad \text{(VII-4)}$$

All missing relaxation terms ($A_{ij}n_j$) are considered negli-
gibly small. After integration of Eq. (VII-4) with respect
to time for an initial increment Δx, the following
expression is then integrated with respect to x to obtain I
(x,t),

$$\frac{dI}{dx} = -I[\sigma_{13}(n_1 - n_3) + \sigma_{24}(n_2 - n_4) + \sigma_{56}(n_5 - n_6)] \ . \quad \text{(VII-5)}$$

Reference 1 tabulates the known parameters A_{ij} for
anthracene, and we take the average values: $A_{21} = 6.2 \times
10^7$, $A_{25} = 1.38 \times 10^8$, and $A_{51} = 2.2 \times 10^6$ (O_2-free) or 8
$\times 10^6$ (air-saturated). The very fast rates A_{32}, A_{42}, and
A_{65} are unknown; we assume they are approximately 1.0
$\times 10^{11}$. We set all other A_{ij} to zero. The cross sections σ_{13}
and σ_{56} are reported in the literature, but σ_{13} is easily
determined to be 4.6×10^{-16} cm^2/molecule at 248.4 nm
with a Cary-17D spectrophotometer. The triplet T_1 cross
section is reported to be 8.7×10^{-17} cm^2/molecule at
77 K,[2] but our data are fit better by 9.3×10^{-17}, which is
in good agreement considering the large difference in
temperatures.

The solid curve in Fig. VII-6 shows the fit of this
model to the data when O_2 is absent and in Fig. VII-7
when air is present. Evidently neither the model calcula-
tions (solid line) nor the data are greatly affected by the
presence of O_2 when the solution is recirculated at a
sufficient rate. However, without recirculation the triplet
molecules in the irradiated zone persist from pulse to
pulse so that saturation is achieved at much lower power
levels when O_2 is absent and the pulse repetition rate is
10 Hz. At very low repetition rates of <1 Hz, relaxation
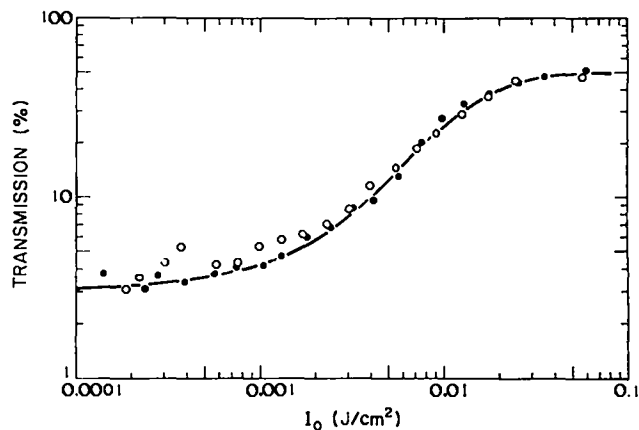of the T_1 state would be complete in any case.

Fig. VII-6. Saturable absorption in 1.25×10^{-5} molecules/cm^3
anthracene in n-hexane in the absence of O_2. Theory (solid
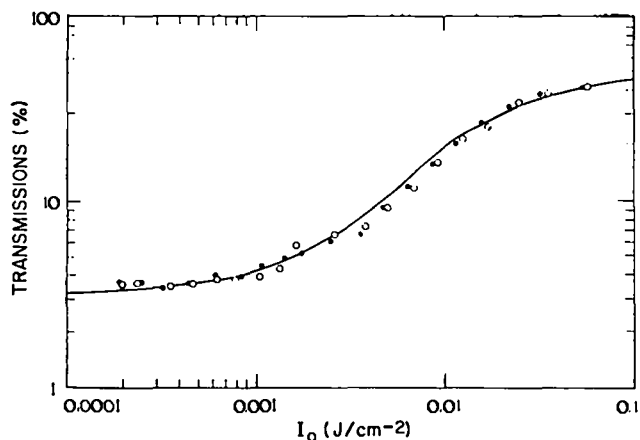line), data set 1 (closed circles), and data set 2 (open circles.)

Fig. VII-7. Saturable absorption in 1.25×10^{-5} molecules/cm³ anthracene in n-hexane saturated with air. Theory (solid line), data set 1 (closed circles), and data set 2 (open circles).

Saturation in Phenanthrene

The mechanism of the saturation process in phenanthrene is somewhat different from that in anthracene. In anthracene the S_1 lifetime is 5 ns, significantly shorter than the pulse, which results in nearly all molecules being left in the triplet state T_1 by the time the laser pulse is turned off. However, with phenanthrene the S_1 lifetime is 60 ns (Ref. 4) or much longer than the pulse. As a result, most molecules remain in the S_1 state after the laser pulse, and very few reach the T_1 state through decay from S_1.

The effect of oxygen on saturation in phenanthrene is likewise small (Figs. VII-8 and VII-9). With adequate recirculation, oxygen quenching of either the S_1 and T_1 states must take place within the laser pulse duration to

The fluence in the laser beam varies greatly over the 1-by 1-cm cross section used in the above measurements, and it might seriously affect the saturation data. By traversing the beam with a 1-mm iris, we determined that the half-power width in the vertical direction is 4.9 mm and that the power profile is roughly Gaussian. With an analytical expression for the transmission T through a four-level saturable absorber derived by Hercher,[3] the maximum error in our experiments (assuming uniform intensity distribution over a 1- by 1-cm beam area) was only 10%. We have therefore not attempted to correct for it.

We tried to measure saturation in anthracene vapor because the temperature needed to achieve a density of 7.53×10^{15} molecules/cm³ is only about 373 K (100°C). Without any inert gas present, the experiment failed as a result of very rapid carbon deposition on the cell windows. Because of the difficulty in maintaining a known uniform density of anthracene in an inert gas at 373 K, we did not attempt to determine the effect of adding such a gas to the vapor. The molecule retains too much vibrational energy after absorption of a single 248-nm photon, and a second photon absorbed during the same laser pulse can then easily dissociate the molecule. In a liquid, vibrational energy is very rapidly dissipated on a 10-ns time scale, but whether it would be sufficiently rapid in the gas phase at 1 atm is uncertain. However, the excited molecule would probably still have too much vibrational energy after 10 ns to survive the absorption of a second photon, because within this time only a small number of collisions occur.
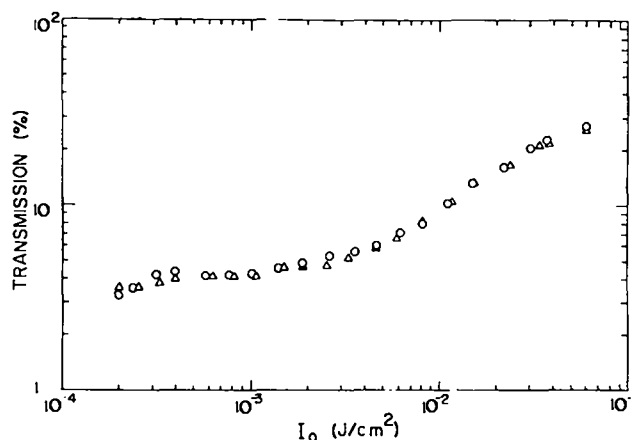

Fig. VII-8. Saturable absorption in 2.64×10^{-5} molecules/cm³ phenanthrene n-hexane in the absence of O_2. Data set 1 (circles) and data set 2 (triangles).
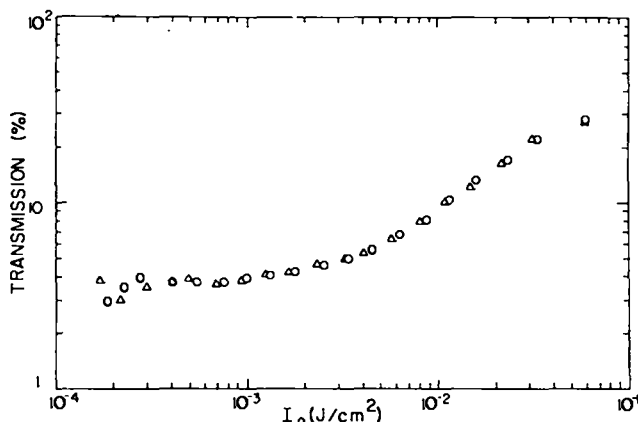

Fig. VII-9. Saturable absorption in 2.64×10^{-5} molecules/cm³ in n-hexane saturated with air. Data set 1 (circles) and data set 2 (triangles).

have a detectable effect on net beam transmittance. Because oxygen quenching of fluorescence in aromatic hydrocarbons is essentially a diffusion-limited process, the rates do not vary greatly from one compound to another, and we may use the same quenching-rate constant for phenanthrene as measured for anthracene, that is, 7×10^7/s for S_1 quenching.[5] (See also Ref. 1, p. 500.) The quenching-rate constant for the triplet state T_1 is lower by 1/9 or 8×10^6/s (Ref. 5). Calculations with the model have not been completed for phenanthrene, but we anticipate no difficulty in accounting for saturation.

Photodecomposition Rates in Anthracene and Phenanthrene

An important consideration when selecting a saturable absorber to use with KrF lasers is their photochemical promise. We determined the half-time for photochemical decomposition of both anthracene and phenanthrene in a 16-cm^3 cell in which the irradiated volume was $1\ \text{cm}^3$. The only stirring occurred before absorbance measurements. We measured solutions both with and without air present. Table VII-V presents results in which T represents the halftime for the survival of a molecule in the irradiated volume in terms of pulses with an energy of 50 to 70 mJ/cm². Oxygen greatly increases the stability of both molecules; we attribute this increase to the effect of O_2 on the relaxation of both the S_1 and T_1 states back to the ground state. The ground state is evidently relatively stable with respect to absorption of a single photon, whereas the S_1 and T_1 states are much less stable. The variation of T with pulse energy in anthracene solutions saturated with air has been investigated at energy levels in the region of saturation (>15 mJ/cm²). We found that T varies inversely with pulse energy to the first power. This suggests that the mechanism of photodecomposition involves absorbing a photon by either the S_1 or T_1 state molecules and internally converting the resulting

TABLE VII-V. Photodecomposition Rates for Anthracene and Phenanthrene

Solution	T (Pulses)
Anthracene (O_2-free)	34
Anthracene (air-saturated)	135
Phenanthrene (O_2-free)	24
Phenanthrene (air-saturated)	47

excess vibronic energy into predominantly vibrational form. There is then a finite probability that the molecule will dissociate before collisions in the liquid phase can dissipate this vibration energy. There is still the possibility that two-photon photodecomposition will be observed at higher pulse energies, but in the energy range of our present experiments, there is no evidence that it occurs at 248 nm.

Nonlinear Absorption in Hexane Solvent

We made an attempt to observe nonlinear effects in the hexane solvent because such effects might present serious problems at higher fluences. However, the effort was unsuccessful even with beam focusing; neither self-focusing nor stimulated Raman emission was detected, although the beam fluence at times exceeded the damage threshold of quartz windows. At 1.06 μm the nonlinear refractive index n_2 of n-hexane can be estimated roughly from the data of Cherlow et al.[6] on the coefficients of self-induced polarization change and their estimate of c_{1221} for CS_2 to be $\sim 2 \times 10^{-13}$ or only 1/50 that for CS_2. Consequently, we expect the threshold for nonlinear effects to be fairly high in hexane. On the other hand, these effects can be demonstrated in hexane with a third-harmonic YAG laser at 355 nm. We are, therefore, inclined to attribute the failure in this case to the poor beam quality of the Lumonics 860 laser.

Summary

Anthracene in hexane solvent is a promising saturable absorber at 248 nm with a saturation level of 0.0035 J/cm² (0.35 MW/cm²) and a half-life at 0.070 J/cm² of 135 pulses. The half-life decreases linearly with the reciprocal of the pulse energy at this energy level. Phenanthrene is both less stable photochemically and more strongly absorbing in the excited state S_1 than anthracene. However, a more extensive search should reveal compounds with properties even more favorable than anthracene.

OBSERVATION OF PHASE-CONJUGATE REFLECTION USING A KrF LASER

(I. J. Bigio, B. J. Feldman, R. A. Fisher, M. Slatkine)

Introduction

Optical phase conjugation[7] uses nonlinear optical techniques to precisely reverse the direction of propagation of each plane wave in an incoming beam. This

causes the beam to retrace its own path, even in the presence of aberrating and polarization-distorting (birefringent) materials. Phase conjugation provides an adaptive optics technique that performs optical processing in real time. We use such a system to point and correct for distortion in laser fusion.[8]

Earlier demonstrations of phase conjugation operated on either visible or infrared light. The only demonstration in the ultraviolet thus far used the fourth harmonic of a Nd:YAG laser.[9] It is important to evaluate the prospects of phase-conjugation systems that are applicable to excimer lasers because of their anticipated use in laser fusion systems. We are now able to markedly improve the beam quality and to reduce the spectral linewidth of our excimer lasers.

Our laser was an injection-locked, unstable KrF double-discharge resonator with 200-mJ, 20-ns output in a <0.1-Å-bandwidth (coherence length ~ 1 cm) nearly diffraction-limited beam.[10] With this laser we investigated phase conjugation and image retention properties of three different nonlinear processes: degenerate four-wave mixing, stimulated Brillouin scattering, and stimulated Raman scattering.

Degenerate Four-Wave Mixing

We observed confirmed phase-conjugate reflection using a number of liquid solutions, for example, DMSO diluted in ethanol, CS_2 in hexane, β-carotene in hexane, anthracene in hexane, and various dilute optical dyes. We obtained maximum reflectivity R of $\sim 10^{-4}$ (in an anthracene-hexane mix) at a pump intensity of ~ 1 MW/cm^2 in a 1-mm-thick sample. When the laser bandwidth was increased to 5 Å, no phase-conjugate reflection could be observed down to the limit of our detection apparatus (R = 10^{-7}), indicating the importance of KrF laser coherence in the interaction region.

The reflectivity of 10^{-4} was not optimized; optical damage on the turning mirrors had forced us to reduce the pump-wave intensities. If other optics had been available, we probably would have attained phase-conjugate reflectivities of several percent.

Stimulated Brillouin Scattering

In efforts to obtain higher phase-conjugate reflectivity, we investigated the process of backward-stimulated Brillouin scattering.[11] In these experiments the output of the injection-locked laser (beam diameter ~ 2 cm) was focused with a 15-cm lens to just below the surface of various liquids contained in an open beaker. Backward stimulated Brillouin scattering was observed from ethyl alcohol, isopropyl alcohol, and hexane at threshold intensities of $\sim 10^9$ W/cm^2. Reflectivities approaching 100% were observed with some image retention properties and significant temporal pulse compression. However, the reflected beam did not possess the diffraction-limited character of the laser pulse, and only 10-20% of the stimulated Brillouin light could be made to pass through the 50-μm aperture in an f/25 optical focus that passes 85% of the laser light. Image retention properties were clearly discernible, although somewhat blurred. These observations and others raise some doubt about the phase-conjugate quality of the reflected beam, suggesting that the beam is retroreflected somewhat incoherently across its transverse dimensions. Backward-stimulated Brillouin scattering was also observed in a light-pipe geometry, but with no observable image retention properties. In all cases, no backward stimulated Brillouin scatter was observed with broad-bandwidth laser light even at intensities as high as 10^{11} W/cm^2 in the focal volume.

Our subsequent work with an XeF excimer laser (3511 Å) has shown that the introduction of a slight linear absorption (to mimic the KrF case) can cause a "perfect" Brillouin phase conjugator to reproduce the KrF results we are reporting. The detrimental role of absorption is being investigated.

Stimulated Raman Scattering

When liquid N_2 was substituted for the Brillouin liquids, high-efficiency backward-stimulated Raman scattering was observed at the first Stokes wavelength of 2630 Å. Threshold for the Raman process was $\sim 10^{10}$ W/cm^2. No backward-stimulated Brillouin light was observed in this material. Image retention properties of the Raman light, while still discernible, were substantially degraded in comparison to the Brillouin scatter. Again, the backward stimulated Raman signal disappeared when the laser output was broadband.

Conclusion

Efforts are under way to gain a better understanding of the phenomena observed, in particular the role of laser

coherence length, in an effort to improve the reflectivity of the phase-conjugate process. Our improved understanding should also affect the study of phase-conjugation processes for other uv excimer laser systems.

REFERENCES

1. J. B. Birks, *Photophysics of Aromatic Molecules* (John Wiley & Sons, Inc., New York, 1970).

2. Y. H. Meyer, R. Astler, and J. M. LeClercq, J. Chem. Phys. 56, 801 (1972).

3. M. Hercher, Appl. Opt. 6, 947 (1967).

4. J. B. Birks and S. Georghiou, J. Phys. B. 1, 958 (1968).

5. W. R. Ware, J. Phys. Chem. 66, 455 (1962).

6. J. M. Cherlow, T. T. Yang, and R. W. Hellwarth, IEEE J. Quantum Electron. 12, 644 (1976).

7. See, for example, A. Yariv, IEEE J. Quantum Electron. QE-14, 650 (1978).

8. See, for example, N. G. Basov and I. Subarev, Appl. Phys. 20, 261 (1979).

9. B. J. Feldman, R. A. Fisher, and S. L. Shapiro, Opt. Lett. 6, 84 (1981).

10. I. J. Bigio and M. Slatkine, Opt. Lett. 6, 336 (1981).

11. B. Ya. Zel'dovich, V. I. Popovichev, V. V. Ragul'skii, and F. S. Faizullov, Zh. Eksp. Teor Fiz. Pisma Red. 15, 160 (1972). For English translation see JETP Lett. 15, 109 (1972).

VIII. HEAVY-ION FUSION DRIVER DEVELOPMENT
(G. A. Sawyer, R. Bangerter)

The Los Alamos National Laboratory has been assigned a leading role in developing heavy-ion accelerators as ICF drivers. Our efforts in accelerator development, magnetic focusing systems, and target design are described in this section.

INTRODUCTION

An inertial fusion driver for commercial power production must have a lifetime of $\geq 10^9$ pulses and a high average power capability. It must also be reliable and efficient. High-energy ion accelerator technology can meet these requirements, particularly that of efficiency. The efficiency of accelerators for turning electric power into ion kinetic energy can be as high as 20-40%, compared with a typical laser efficiency of $\leq 10\%$. For ICF, the fusion energy gain is defined by $Q = \eta G$, where η is the efficiency of the driver and G is the target energy gain. Most analyses show that Q must exceed 10 for economical commercial power production. According to present calculations, some suggested driver/target systems are unable to meet this criterion. In any case, high Q is advantageous. As a general rule, G increases with increasing driver output energy E and increasing target complexity. The yield of a target is given by EG; therefore, at a given Q, high η allows operation at low yields and/or with relatively simple targets. This in turn can ameliorate combustion chamber and target fabrication problems.

We are addressing the following significant questions.
- Inertial fusion requires beams that can be focused to high power density (10^{15} W/cm^2). What is the best accelerator technology for producing these high-quality beams?
- The magnetic lens system that focuses the ion beams onto the target must be compatible with combustion chamber requirements. How does one design this system?
- What are the best target concepts for ion-beam drivers?

The first part of this section describes our research on accelerators for inertial fusion. We have emphasized RFQ and radio-frequency octupole systems because they appear capable of producing the high-quality beams required for fusion. Later in the section we present some preliminary calculations on magnetic focusing systems.

Finally we discuss fusion target design, in particular, target performance as a function of target and beam parameters such as power, energy, ion range, and uniformity of illumination.

ACCELERATOR INERTIAL FUSION
(H. R. Crandall, R. H. Stokes, T. P. Wangler)

Introduction

We have continued to investigate several areas that are essential to the use of rf linear accelerators for HIF. The RFQ has been developed further, and two new representative designs have increased the xenon currents available from a single RFQ channel. At 12.5 MHz, a frequency used at Argonne National Laboratory (ANL), we were first able to obtain 50 mA, but then, at the optimum frequency of 2.7 MHz, we obtained a design current of 275 mA. This optimum frequency corresponds to the shortest possible RFQ.

In addition, we are investigating low-frequency structures for RFQ use, the funneling of ion beams, the use of higher multipoles for radial focusing, and the newly developed program, CHARGE 3D, that solves Laplaces's equation in three dimensions to assist in RFQ pole-tip design.

12.5-MHz Xenon RFQ Design

Improvements in our algorithms led to a new RFQ design called HIF5. Table VIII-I presents parameters and performance characteristics. The peak surface field assumed was 20 MV/m. This example shows that at 12.5 MHz, a beam current of 50 mA can be bunched and accelerated in a single channel, provided the peak surface field of 20 MV/m can be attained and the injection energy is at least 300 keV. Details of this design were reported at the 1981 Particle Accelerator Conference.[1]

At the request of ANL, we prepared a second xenon RFQ design, called ANL6, as a possible low-velocity accelerator for their HIF accelerator program. Table VIII-I shows parameters and performance characteristics. This design assumed a more conservative peak surface field of 17.5 MV/m.

2.7-MHz Xenon RFQ Design

The computer program CURMAX, which chooses the design frequency to maximize the beam current in an RFQ, was used to generate a Xe^{+1} RFQ with maximized beam current. Table VIII-I lists the parameters and performance characteristics for this HIF6 design. We assumed a peak surface field of 20 MV/m. The increased beam current and the reduced length, as compared with the HIF5 design, result from lowering the frequency from 12.5 MHz to an optimized value of 2.7 MHz. This result shows that significant improvements should be possible in the low-velocity linac if the frequency can be lowered from previously considered values.

Low-Frequency Structures

For frequencies below 20 MHz, the four-vane RFQ cavity radial dimensions become so large that fabrication problems arise. An initial study of RFQ resonant cavity structures has identified the ones that are more attractive for low-frequency applications. Both the spiral resonator structure and the modified split-coaxial structure appear to warrant further quantitative study to evaluate their size, mechanical properties, and power efficiency. We used a lumped circuit model to compare the properties of a variety of TE-mode resonators. The application of this model to TE-mode RFQ cavities of a fixed frequency suggests an approximate inverse relation between power and radial dimensions.

Funneling of Ion Beams

An essential component in the rf linear accelerator approach to HIF is a device to combine charged particle beams. To produce a final beam of high energy and high current, the linear accelerator system must start with multiple low-frequency linacs, each having a low-current beam. Pairs of these beams are then combined into single beams suitable for further acceleration in linacs operating at twice the frequency. This process, called funneling, combines two bunched beams by deflecting interlaced microstructure pulses until they are collinear. Funneling requires time-varying deflection systems. In principle, it can be performed with no emittance increase, so that the radial brightness of the final beam is doubled after each funneling operation. By repeating this process, we can produce a single final beam of the required intensity and energy.

While the two beams to be combined are suitably deflected until they are collinear, funneling requires that radial focusing be maintained and that the beams not be allowed to debunch. To meet this requirement, a new approach has been suggested* that uses the RFQ as a deflector. The tip of the RFQ pole is modified to generate an electric dipole field that produces a first-order transverse force on the beam pulses. While the beam is being deflected, the bunching and focusing functions of the RFQ are maintained. After the two beams are deflected toward each other, another deflection is required to produce a final collinear beam. To bring about this final coalescence, we are developing other special forms of the RFQ structure.

Octupole Focusing in Transport and Acceleration Systems

The RFQ linac is capable of accelerating high-current, low-velocity ion beams. In accelerator systems consisting

TABLE VIII-I. RFQ Design Parameters

	RFQ Designs		
	HIF5	ANL6	HIF6
Ion	Xe^{+1}	Xe^{+1}	Xe^{+1}
Frequency, MHz	12.5	12.5	2.7
Input energy, MeV	0.30	0.25	0.30
Output energy, MeV	10.0	3.0	10.0
Nominal current, mA	50	30	275
Transmission efficiency, %	93	97	98
Output emittance*	0.011	0.009	0.09
Length, m	27.7	15.5	14.2

*RMS-normalized area/π in cm-mrad units.

*G. N. Minerobo, Los Alamos National Laboratory, provided this information in "Notes on Funneling Systems," private communications dated January 16, February 12, and February 17, 1981.

of an RFQ and higher velocity accelerating structures, the current is high in most cases, but linacs with even higher currents may be required. We have begun to study[2] higher multipole systems to determine their capability for focusing and accelerating very high currents. First, we examined a rf octupole transport system and developed a smooth-approximation analytical description that includes the conditions for input radial matching of a zero space-charge beam. Then, we constructed a multiparticle beam dynamics-simulation program that accepts the low-current matched beam and gradually increases its current as the beam is transported. This produces a matched high-current beam; the procedure can be used to determine the saturation current limit of a periodic octupole system. As we expected, at high currents the beam develops a hollow radial distribution that reduces the space-charge defocusing. Initial results show that high currents can be transported. For acceleration, we have formulated the design parameters for a section of a rf octupole linac, including the potential function, acceleration, and focusing efficiencies, and the geometry of the radially modulated pole tips.

The CHARGE-3D Program

An important parameter in RFQ design is the peak surface electric field on the RFQ vanes. In many cases, particularly for high beam currents, the focusing electric fields should be as high as possible without exceeding the sparking limit. Until recently, we have used a two-dimensional model to calculate the peak surface fields, ignoring the effects of the longitudinal modulation of the vanes. Our newly developed program, CHARGE-3D, solves Laplace's equation in three dimensions and allows the surface fields to be determined on modulated vanes. Using this program we have learned that the modulation often significantly raises the electric fields, a fact we must take into account fully in our design procedures. CHARGE-3D also allows us to determine the strength of the higher focusing harmonics produced by new RFQ vane shapes, which are attractive because they are simple to machine. These focusing harmonics can be used in simulation programs to determine their effects on beam dynamics.

MODELING OF A MAGNETIC FOCUSING SYSTEM (W. A. Reupke)

Introduction

In this analysis, we assume that focusing an ion beam onto a target is governed by three conditions: space-charge forces that limit ballistic focusing, matching the emittance of the beams to the lens system,[3] and the strong focusing (Maschke) current limit. The relevant condition, the one specifying the design of the final focusing magnet, is determined by the specific characeristics of the ion beam, the fusion target, and the ICF reactor vessel.

The first of these conditions can be relaxed by neutralization. The second must be met. The last was originally derived for very long transport systems and is probably a conservative limit for the short systems considered here. However, because the effects of geometric and chromatic aberrations have not yet been considered, our findings must be considered preliminary. We have studied the dependence of the size and weight of the final focusing magnet on the magnet standoff distance L and on the bulk supercurrent density in the magnet when the ballistic focusing condition prevailed. This condition usually dominates in cases of commercial ICF applications. We selected the standoff distance and the bulk supercurrent density because they have a significant effect on the costs of the focusing magnets and the ICF reactor cavities.

Analysis and Results

In our analysis, we assume that two 8-beam clusters of singly charged uranium ions are used to deliver 3 MJ of energy to the target. Table VIII-II lists the operating parameters.

We know that a quadrupole magnet focusing in the horizontal plane is defocusing in the vertical plane and that the magnetic lens (composed of two identical quadrupole magnets, one of which is rotated 90° relative to the other) focuses in both planes but not at the same position. However, a pair of nonsymmetric quadrupole magnets having different focusing characteristics can be designed in such a way that the beam will focus to the

TABLE VIII-II. Operating Parameters

Driver energy, MJ	3
Ion species, charge state	U^{+1}
Ion kinetic energy, GeV	10
Spot size, mm	2.5
Pulse width at target, ns	16
Driver emittance $\epsilon\eta/\pi$ for each of four beams, mrad	8.3×10^{-6}
Emittance dilution per four-way split	1.1
Number of final beams	16
Quadrupole gradient, T/m	10
Superconductor bulk current density, MA/m^2	60
Magnetic iron saturation strength, T	2.0
Dewar insulation thickness, m	0.1

same spot in both planes. We found that a properly designed nonsymmetric pair of quadrupole magnets requires less material and occupies a smaller volume than a symmetric triplet with the same focusing characteristics. Therefore, we consider only the nonsymmetric doublets.

Using Garren's analysis and procedure,[4] we can easily determine the dependence of the overall characteristics of the magnetic focusing lens on the standoff distance; the results are presented in Table VIII-III. In this table $L_1 + L_2$ is the combined length of the quadrupole pair, R_L is the beam radius at the exit from the magnet, R_B is the radius of the magnet bore, and B is the pole-tip field. Figure VIII-1 illustrates the configuration and notation; Fig. VIII-2 graphs the results. It shows that as the standoff distance increases from 6 to 12 m, the combined magnet length decreases from 10 to 8 m, but the magnet bore radius increases from 0.15 to 0.20 m. The pole tips at the field strengths remain well below practically achievable values.

TABLE VIII-III. Dependence of Magnet Bore Size on Focal Length L

L (m)	$L_1 + L_2$ (m)	R_L (m)	R_B (m)	B (T)
6	9.55	0.056	0.153	1.5
8	8.78	0.076	0.168	1.7
10	8.22	0.096	0.184	1.8
12	7.77	0.118	0.206	2.1

We estimated the magnet dimensions and weights corresponding to the parameter values presented in Table VIII-III for an assumed coil bulk current density of 60 MA/m^2, using the procedure developed by Westinghouse Electric Corp. under contract to DOE/OIF.[5] The results are presented in Table VIII-IV, where ΔR_c is the superconductor thickness, ΔR_s is the iron magnetic shield thickness, and R_M is the overall radius of the magnet including the two 0.1-m-thick dewars. The calculated results indicate that the superconducting coil occupies only a small fraction of the space and that the weight is dominated by the magnetic shield. The individual magnet weight ranges from 41 to 63 × 10^3 kg and the standoff distance increases from 6 to 12 m. Therefore, the total weight of the 16 focusing magnets ranges from 640 to 960 × 10^3 kg. This result shows that the increase in the overall magnet radius outweighs the decrease in the magnet length because the weight depends on the square of the radius but only on the first power of the length. The variation of the weight is graphed in Fig. VIII-2.

To investigate the dependence of magnet dimensions and weights on the superconductor bulk current density, we repeated the calculations for the 6-m standoff distance for current densities of 30, 40, and 50 in addition to the nominal value of 60 MA/m^2. Table VIII-V presents the results. The weight increases sharply as the current density decreases.

The specifications of the entire eight-magnet cluster were determined for the current density of 60 MA/m^2 and for distances varying from 6 to 12 m; the dimensions of complete conical bundles are shown in Table VIII-VI. Here R_{Bu} is the approximate radius of the outside of the bundle where the magnets touch, α is the half-angle containing the bundle, $\alpha^2/90^2$ is the fraction of the solid angle occupied by the complete double cone, and A_p is the area of the port circumscribed within the magnets that is available for reactor cavity evacuation. The values of R_{Bu} are compatible with the small first-wall radii that may be feasible with the wetted-wall reactor cavity protection scheme when neutron damage lifetime determines the wall radius. Half-angles are sufficiently small to allow flexibility in neutronics design.

Summary

Our study shows that a final focusing-magnet system for a 16-beam reactor matched to a 3-mJ 4-beam heavy-ion driver requires magnet lengths of 8 to 10 m,
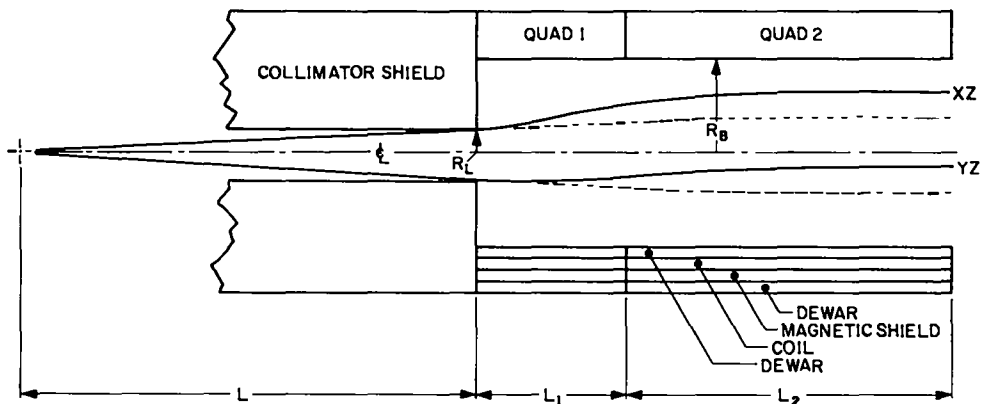
Fig. VIII-1. Relationship of pellet, collimator shield, and quadrupole magnet pair. Before entering the magnet, 14-MeV neutrons are attenuated in bulk shield. Excursion of beam envelope (solid lines) in horizontal and vertical planes requires that magnet bore be recessed from nominal focus path (dotted lines). The bore lies partially in shadow created by ion-beam hole and neutron collimator hole in shield. Magnetic shield surrounding superconductor coil isolates magnetic field from effect of adjacent magnets.
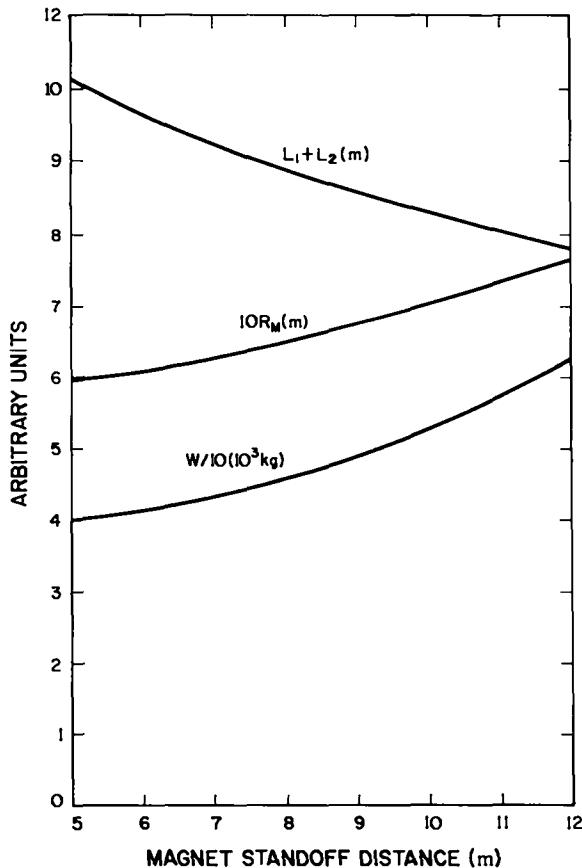

Fig. VIII-2. Dependence of magnet design parameters on standoff distance from fusion pellet. $L_1 + L_2$ are combined length of asymmetric quadrupole magnet pair, R_M is the radius of the magnet clearance bore, and W is the weight of one quadrupole magnet pair. Increase of magnet transverse dimensions with increasing standoff distance outweighs decrease of magnet length.

apertures of 0.3 to 0.4 m in diameter, overall magnet diameters of 1.2 to 1.5 m, and single-magnet weights of 40 to 63 $\times$ 10^3 kg for magnet standoff distances varying from 6 to 12 m. For bulk superconductor current densities much less than the 60 MA/m^2 value, assumed weight penalties may be significant. Characteristics of the complete magnet bundle system show good dimensional compatibility with a variety of first-wall protection schemes, negligible incursions on blanket tritium-breeding performance, and adequate room if an additional vacuum pumping port is required.

The principal uncertainty in the study is the impact of neutron collimator and shield performance on the permissible magnet clearance bore. More detailed studies of neutron collimator and shield concepts are needed to reduce this uncertainty.

SCALING LAWS FOR SIMPLE HEAVY-ION TARGETS (W. P. Gula; G. R. Magelssen, Argonne National Laboratory)

Introduction

Serious attention has been given in recent years to the possibility of producing beams of high-energy heavy ions that may be capable of inducing thermonuclear fusion by imploding small targets. Single-shell DT-gas-filled spherical targets, irradiated by a heavy-ion beam pulse of constant power, do not produce high gain. However, they can be analyzed to derive scaling laws and, therefore, could be used as an experimental tool.

TABLE VII-IV. Dependence of Magnet Dimensions and Weights on Focal Length at 60 MA/m^2

L (m)	R_B (m)	ΔR_c (m)	ΔR_s (m)	R_M (m)	W (10^3 kg)
6	0.153	0.0427	0.213	0.608	41.1
8	0.168	0.0458	0.239	0.653	45.8
10	0.184	0.0491	0.268	0.701	52.0
12	0.206	0.0535	0.311	0.770	63.1

TABLE VIII-V. Dependence of Magnet Dimensions and Weights on Superconductor Bulk Current Density[a]

J (MA/m^2)	R_B (m)	ΔR_c (m)	ΔR_s (m)	R_M (m)	W (10^3 kg)
30	0.153	0.1039	0.296	0.753	71.9
40	0.153	0.0705	0.250	0.673	53.7
50	0.153	0.0532	0.226	0.633	45.6
60	0.153	0.0427	0.213	0.608	41.1

[a]L_M = 6 m.

This section describes our numerical model including the ion deposition physics, discusses the behavior of one simple target as calculated by a hydrodynamic code, and presents our analytical model. We compare analytical and numerical calculations and discuss results that might affect future experiments.

Numerical Model

In our numerical calculations, we employed a Lagrangian hydrodynamic code[6] that included a three-temperature, one-fluid model. For example, the ions and electrons moved at the same speed, but the ions, electrons, and radiation field had separate temperatures. Only one-dimensional spherically symmetric calculations were performed. The model included the SESAME equation of state,[7] flux-limited thermal conduction,[8] and alpha-particle transport. A diffusion model was used in the alpha-particle transport technique. The heavy-ion deposition model developed by T. A. Mehlhorn[9] considers four contributions to the absorbed power:

TABLE VIII-VI. Selected Characteristics of Eight-Magnet Cluster

L_M (m)	R_{Bu} (m)	α (deg)	$\alpha^2/90^2$	A_p (m^2)
6	2.19	20.9	0.054	12.1
8	2.35	16.8	0.035	13.8
10	2.53	14.5	0.026	16.0
12	2.78	13.3	0.022	19.3

(1) stopping by bound electrons calculated from the Bethe equation with shell corrections in the high-energy range. (In the low-energy range, the model of Linhard et al.[10] is used.)

(2) stopping by Coulomb forces of the nucleus.

(3) stopping by free electrons.

(4) stopping by plasma ions.

Hydrodynamic Calculation

To exemplify the targets for which we have developed scaling laws, we will describe the calculation of one such target. The target (Fig. VIII-3) was a gold shell with an initial outer radius of 3 mm, 0.2 mm thickness, 19.32 g/cm^3 density, and 2.5 × 10^{-5} keV temperature. It was filled with a 50:50 mixture of deuterium and tritium, initially at 2.5 × 10^{-5} keV temperature and 2 mg/cm^3 (10 atm) density. The ion beam impinging on this target was a 6.4-GeV xenon beam with a length of 10 ns and a constant power of 300 TW for a total energy of 3 MJ. We assumed all the energy was absorbed according to the ion range calculations described earlier. The yield ratio (thermonuclear energy produced divided by energy absorbed) of this target was calculated to be 14.

A snapshot of the pellet at 10 ns (Fig. VIII-4), just after the ion beam has turned off, shows the density and the ion, electron, and radiation temperatures as a function of radius. At this time the pusher has moved a third of its initial radius inward. The inner region of the gold is still cold, and a portion of it has been compressed to about three times solid density. The fuel density, and ion and electron temperatures are barely above their initial values. The outer region of the gold shell that has absorbed the ion beam has been heated to a maximum temperature of ~250 eV and has started to blow off.

Compare this condition (Fig. VIII-4) to a snapshot of the pellet at peak burn (~35 ns) (Fig. VIII-5). The fuel density is now ~80 g/cm^3 and its ion temperature is about 30 keV. The gold is much colder and now has three regions. The first is a long blowoff region; the second is a highly compressed pusher region (~4000 g/cm^3); and the third is a region expanding into the fuel that has a density of ~300 g/cm^3. Ion temperatures of elements with different masses are shown in Fig. VIII-6

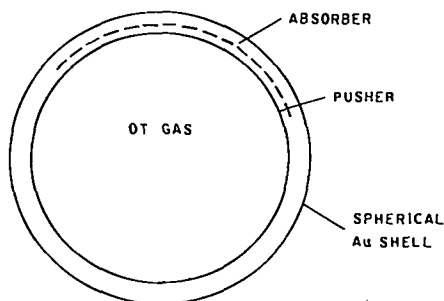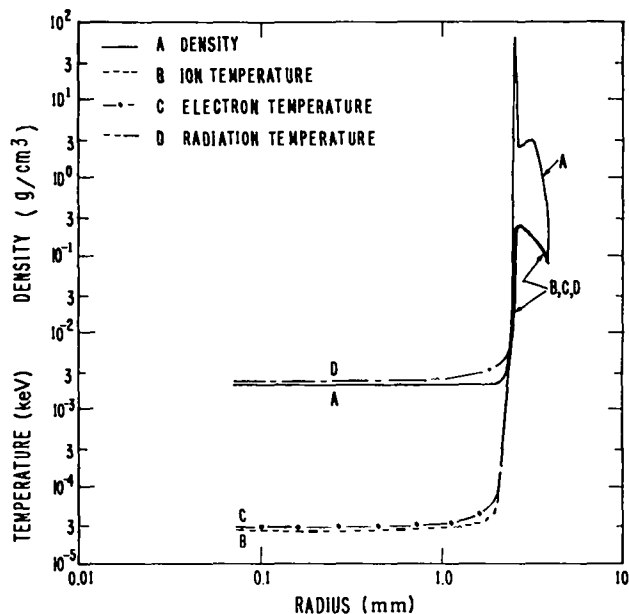Fig. VIII-4. Temperature and density profiles of pellet at ion-beam turnoff show regional behavior of target.

Fig. VIII-3. Single-shell gold target.
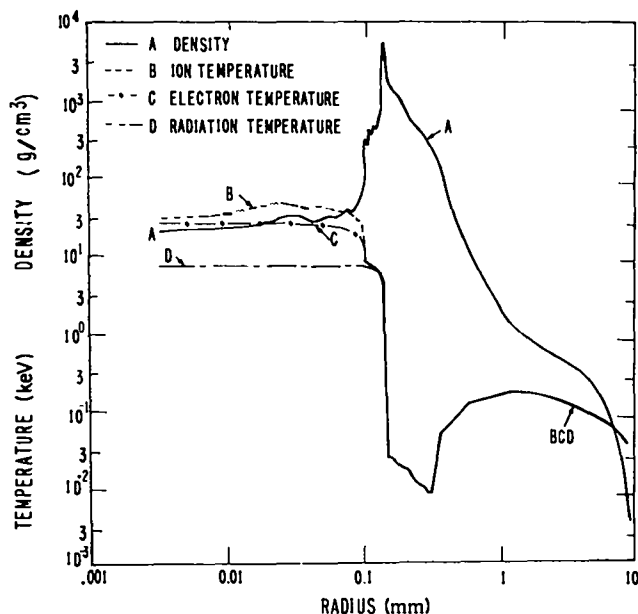
Fig. VIII-5. Temperature and density profiles of pellet near peak burn.
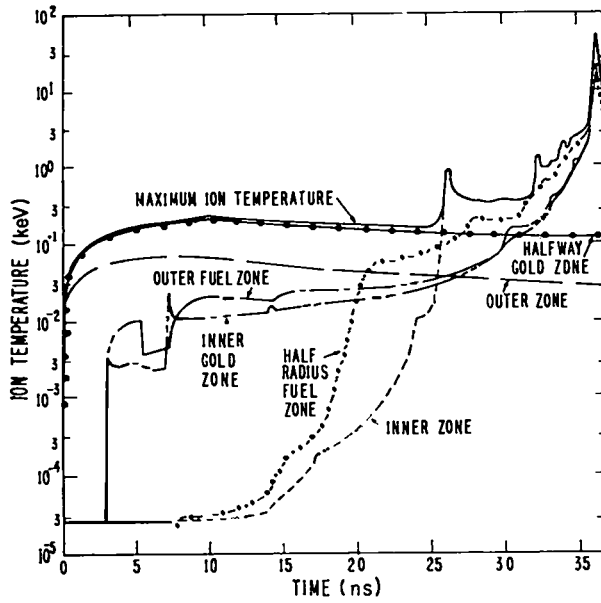
Fig. VIII-6. Plots of ion temperature vs time.

$$\frac{M}{2}\frac{d}{dt}v^2 = P \ , \qquad\qquad \text{(VIII-1)}$$

where M is the pusher mass, v is the average pusher velocity, and P is the power achieved in the target. Thus,

$$V = \left(\frac{2P}{M}\right)^{1/2} t^{1/2} \ . \qquad\qquad \text{(VIII-2)}$$

Equation (VIII-2) can be written approximately as

$$\frac{dr}{dt} = \left(\frac{2P}{M}\right)^{1/2} t^{1/2} \ . \qquad\qquad \text{(VIII-3)}$$

The pusher collapse time is, therefore, given by

$$t_c = \left(\frac{3}{2}\right)^{2/3} \left(\frac{M}{2P}\right)^{1/3} r_0^{2/3} \ , \qquad\qquad \text{(VIII-4)}$$

as a function of time. The temperature curve of the inner zone shows preheating caused by thermal conduction and shocks. The strongest shock reaches the center at 25 ns, about 10 ns before peak burn.

Analytical Model

Computational results similar to those presented above suggest that heavy-ion targets consisting of a spherical shell can be modeled in a simple way. The target can be divided into three regions: (1) the hot absorber (100-400 eV), (2) the cold pusher (a few eV), and (3) the DT gas (Fig. VIII-4). The dividing line between the absorber and the pusher remains constant in the sense that the mass of each region is constant. Radiation and thermal conduction play a secondary role.

To develop a target model, we determine how pusher collapse time, velocity, and maximum kinetic energy depend upon the target parameters. The pusher kinetic energy and velocity behavior are particularly useful in designing a target because computational results suggest they are the primary variables in determining whether the target will ignite and burn. The model presented below assumes that constant driver power gives rise to a constant power within the target. The driver power is on throughout shell collapse. The momentum equation for the pusher can be written as

where r_0 is the initial radius from the sphere center to the inner edge of the pusher. Substituting into Eq. (VIII-2) gives for the final pusher velocity

$$v_f = \left(\frac{3}{2}\right)^{1/3} \left(\frac{2P}{M}\right)^{1/3} r_0^{1/3} \ . \qquad\qquad \text{(VIII-5)}$$

The maximum pusher kinetic energy K, v_f, and t_c, therefore, scale in the following way:

$$K \propto (\Delta r \rho_0)^{1/3} P^{2/3} (r_1 - \Delta r)^{4/3} \ , \qquad\qquad \text{(VIII-6)}$$

$$v_f \propto \left(\frac{P}{\Delta r \rho_0}\right)^{1/3} (r_1 - \Delta r)^{-1/3} \ , \qquad\qquad \text{(VIII-7)}$$

and

$$t_c \propto \left(\frac{\Delta r \rho_0}{P}\right)^{1/3} (r_1 - \Delta r)^{4/3} \ . \qquad\qquad \text{(VIII-8)}$$

In these expressions, we have substituted $4\pi \Delta r \rho_0 r_0^2$ for M; Δr is the initial pusher thickness, ρ_0 is the initial pusher density, and r_1 is the initial radius from the sphere center to the outer edge of the pusher.

114

Comparison with Numerical Results

For comparison with our analytic model, we have numerically studied the pusher collapse time and kinetic energy as a function of beam power, pusher thickness, and target radius. Figure VIII-3 shows the target design used in our calculations. In the graphs that follow, points represent our numerical results and solid curves represent our analytic results. The heavy-ion particle energy for Figs. VIII-7 through VIII-12 was 6.4 GeV.

Figure VIII-7 plots collapse time as a function of power for targets with a 200-μm-thick shell. Collapse time is defined as the time from initial beam absorption to the time of maximum pusher kinetic energy. Analytical dependence of $P^{-1/3}$ and numerical results are in good agreement. Figure VIII-8 plots maximum pusher kinetic energy as a function of driver power; again there is good agreement with theory.

The collapse time as a function of inner radius (the shell thickness was 200 μm with a 50-μm pusher) is shown in Fig. VIII-9, and the kinetic energy as a function of inner radius is depicted in Fig. VIII-10. Both results compare well with the predicted $r^{4/3}$ dependence.

The plots in Figs. VIII-11 and VIII-12 display the collapse time as a function of pusher shell thickness. Initial target radii in Figs. VIII-11 and VIII-12 were 1.0 and 1.5 mm, respectively. Our results compare reasonably well with the predicted $(r_1 - \Delta r)^{4/3}$ radial dependence. The deviation at a pusher thickness of 25 μm is due to ion range shortening during the pulse. In every
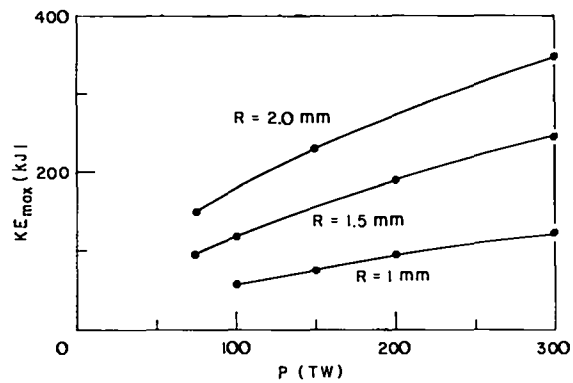
Fig. VIII-8. Maximum kinetic energy vs power for 200-μm-thick gold shells.

Fig. VIII-7. Collapse time vs power for 200-μm-thick gold shells.
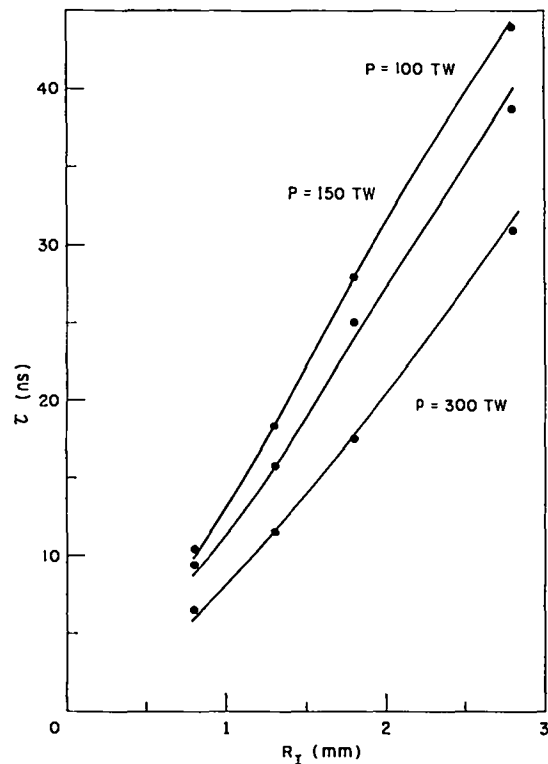
Fig. VIII-9. Collapse time vs initial inner radius for 200-μm-thick gold shells.
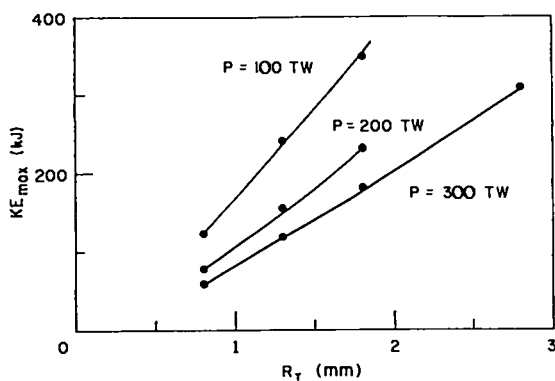
Fig. VIII-10. Maximum kinetic energy vs initial inner radius for 200-μm-thick gold shells.
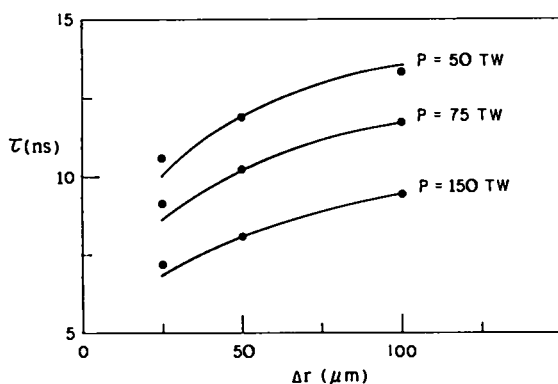
Fig. VIII-11. Collapse time vs shell thickness for 1-mm-radius targets.
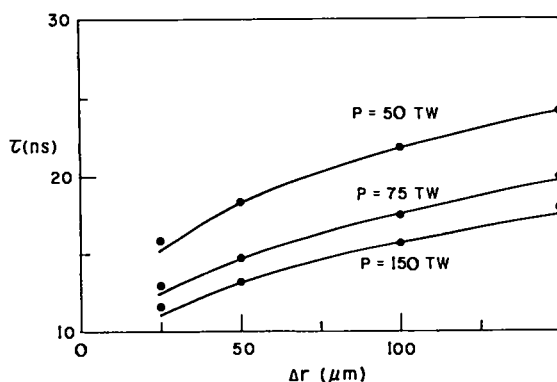
Fig. VIII-12. Collapse time vs shell thickness for 1.5-mm-radius targets.

case, the collapse time is longer than the predicted result. (The 50-μm pusher shell calculations were used to determine the curves.) Range shortening, in effect, increases the pusher mass (Δr) and, therefore, the collapse time. For the results shown, we assumed Δr was the initial pusher thickness. If the time-averaged value of Δr is used, agreement is better.

Figures VIII-13 and VIII-14 show how the incoming ion particle energy affects the shell collapse time and the maximum kinetic energy. For each calculation we chose the total shell thickness that would give a pusher shell thickness of 50 μm. The targets with inner radii of 0.8 and 1.3 mm were irradiated by 100 and 150 TW, respectively. From Fig. VIII-14 it is apparent that the maximum pusher kinetic energy is achieved with an incoming ion energy of 5-10 GeV for the 0.8- and 1.3-mm targets. The maximum pusher kinetic energy decreases with increasing ion particle energy (above 10 GeV) because of the increase in the ion range. Because the same energy is absorbed in a greater mass because of the longer range, the maximum plasma temperature is reduced. This temperature drop results in smaller pressure gradients and, therefore, a smaller force on the pusher.

For a given power, the plasma temperature increases as the absorbing mass decreases (ion particle energy decreases). This temperature increase and mass decrease
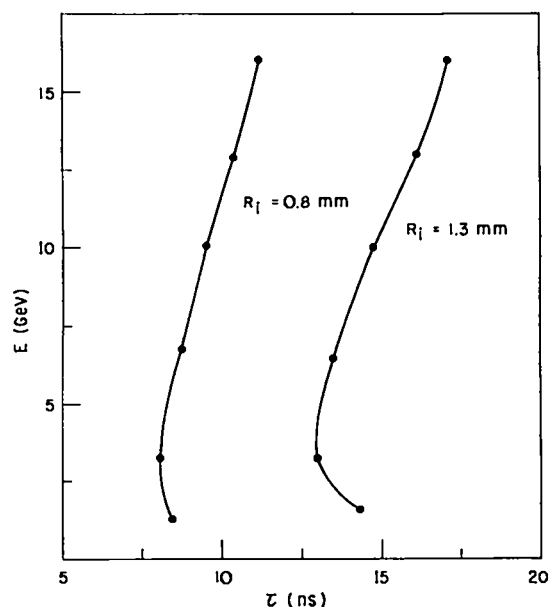
Fig. VIII-13. Ion particle energy vs collapse time.

116

can also eventually produce negative effects (Fig. VIII-14). The pusher kinetic energy begins to drop when the plasma temperature becomes so high that the blowoff expansion carries away too much energy.

Conclusions

We have derived analytical scaling laws for single-shell DT-gas-filled targets and have shown that the laws are in good agreement with numerical calculations. If the ion deposition model represents the physical processes well, the laws could be used as a straightforward way of comparing the theory of hydrodynamic implosions with experiments. An example would be the experimental study of shell collapse time as a function of pusher mass. Our results suggest that breakeven is possible at 75 TW for 6.4-GeV xenon ions impinging on a target with an inner radius of 0.8 mm. Targets with a total radius less than 1 mm were not considered because focusing 6.4-GeV xenon at 75 TW to spot sizes less than 1.0 mm is difficult. For a given pusher, DT mass, and inner radius, there is an optimal ion particle energy for maximizing the pusher kinetic energy. As the incoming ion energy is increased to higher values, higher power is needed to create fuel conditions similar to those of the lower particle energy case.

EFFECTS OF NONSPHERICALLY SYMMETRIC ION-BEAM DEPOSITION ON SPHERICALLY SYMMETRIC TARGETS (W. P. Gula)

A directly driven heavy-ion-beam inertial fusion target is very desirable because it converts energy efficiently. However, such a target requires a high degree of symmetry in beam illumination, at least according to conventional theory. Most of the target calculations have been one-dimensional. As a result, we could not show various effects, for example, asymmetric target illumination. To rectify the situation, we used a two-dimensional cylindrical Lagrangian hydrodynamic computer code in which ion-beam deposition is as described by Mehlhorn,[9] and the ion beam is followed in the manner described by Rinker and Bohannon.[11] We used a double-shell cryogenic target. The original one-dimensional target design had been prepared at LLNL.[12] The ion beam in these calculations was a 5-GeV uranium beam with a peak power of 90 TW and a total energy of 1.7 MJ. The energy gain of the target was 260. The objective of this study was to observe the behavior of the target under nonsymmetric ion-beam illumination.

To test the symmetry of the computer code, we set up a two-dimensional symmetrically illuminated run. Figures VIII-15 and VIII-16 show the Lagrangian mesh of the inner fuel region at 42.5 and 45 ns, respectively. In

Fig. VIII-14. Ion particle energy vs maximum kinetic energy.
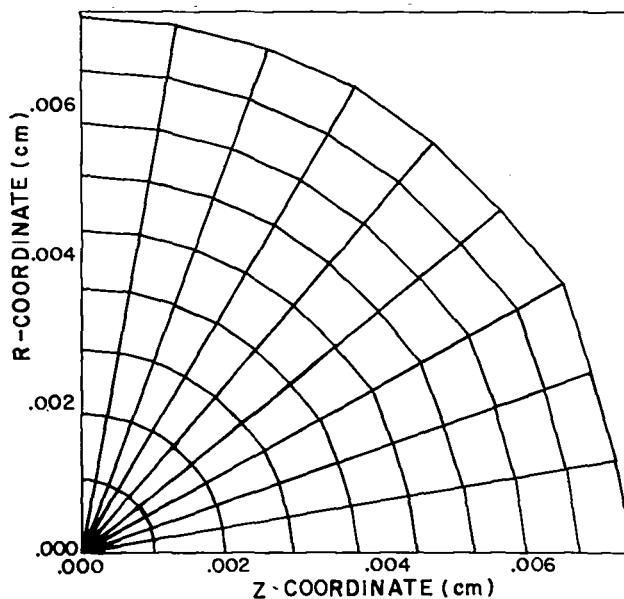
Fig. VIII-15. Lagrangian mesh of inner fuel region at 42.5 ns for the symmetric two-dimensional case.

117
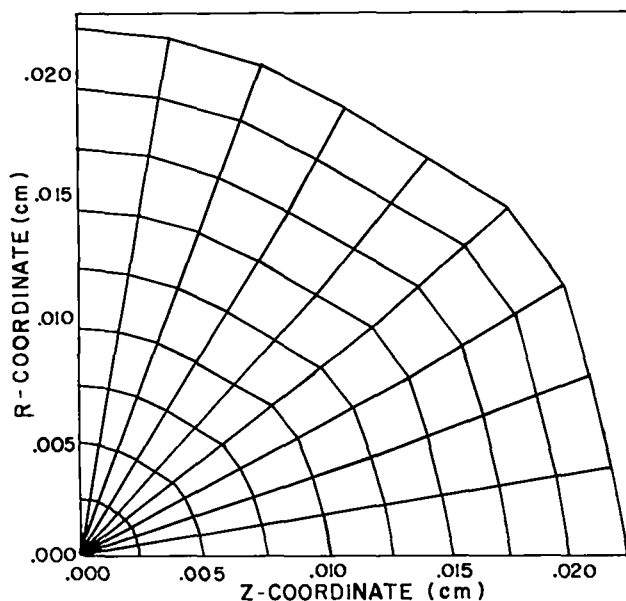
Fig. VIII-16. Lagrangian mesh of inner fuel region at 45 ns for the symmetric two-dimensional case.

these figures, the x-axis is an axis of rotational symmetry and the y-axis is a plane of symmetry. Figure VIII-15 shows conditions near peak compression; a slight asymmetrical flattening at the equator (at the top of the figure) can be seen. The inner fuel region has expanded and the asymmetries, though small, are more obvious (Fig. VIII-16). They may be produced by Rayleigh-Taylor instabilities introduced because a sphere cannot be represented by a Lagrangian mesh exactly with this code.

Let us describe two asymmetric cases. First, consider two cylindrical beams, one on each side of the target, with a flat radial power profile. Figures VIII-17 through VIII-19 show the mesh and the rays representing the ion beam at 0, 20, and 35 ns, respectively. Beam penetration into the absorbing layer of the outer shell shows that at the equator the beam penetrates much less deeply in the radial direction than at the pole (Fig. VIII-17). At 20 ns minor asymmetries develop (Fig. VIII-18), and at 35 ns the outer shell is very asymmetric (Fig. VIII-19). The pole has moved inward to a radius of 0.12 cm, while the
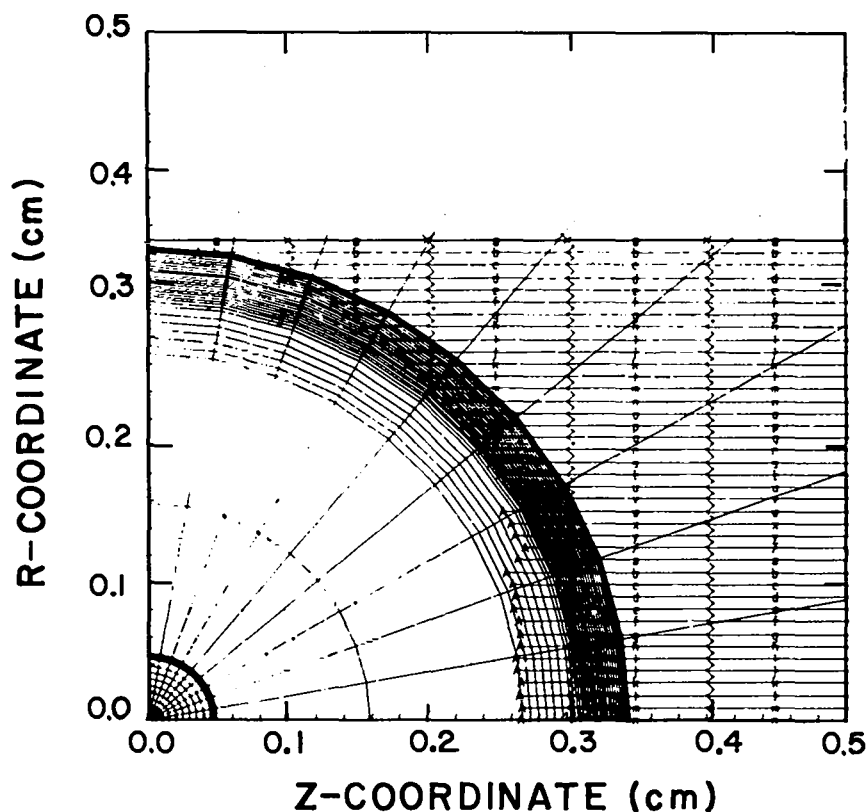
Fig. VIII-17. Lagrangian mesh with ion rays at 0 ns for the cylindrical beam case.

equator is at a radius of 0.30 cm. Ion-beam deposition as a function of the cosine of the polar angle at the initial time is shown in Fig. VIII-20 for different radii. The figure indicates that beam deposition is indeed asymmetric.

In the second case we attempted to study the effects of a finite spot size for the ion-beam focal spot. However, Fig. VIII-21, showing the initial ion-beam deposition as a function of the cosine of the polar angle, indicates that the initialization procedure was in error and that the deposition varied from equator to pole by ~50%. The results of this variation on the outer shell are shown in Figs. VIII-22 through VIII-24. At 0 ns the mesh is undisturbed (Fig. VIII-22); slight asymmetry is shown at 20 ns (Fig. VIII-23); and at 35 ns the asymmetry is obvious (Fig. VIII-24).

We will continue to investigate the effects of different kinds of beam asymmetries and will investigate the possibility of designing asymmetric targets.
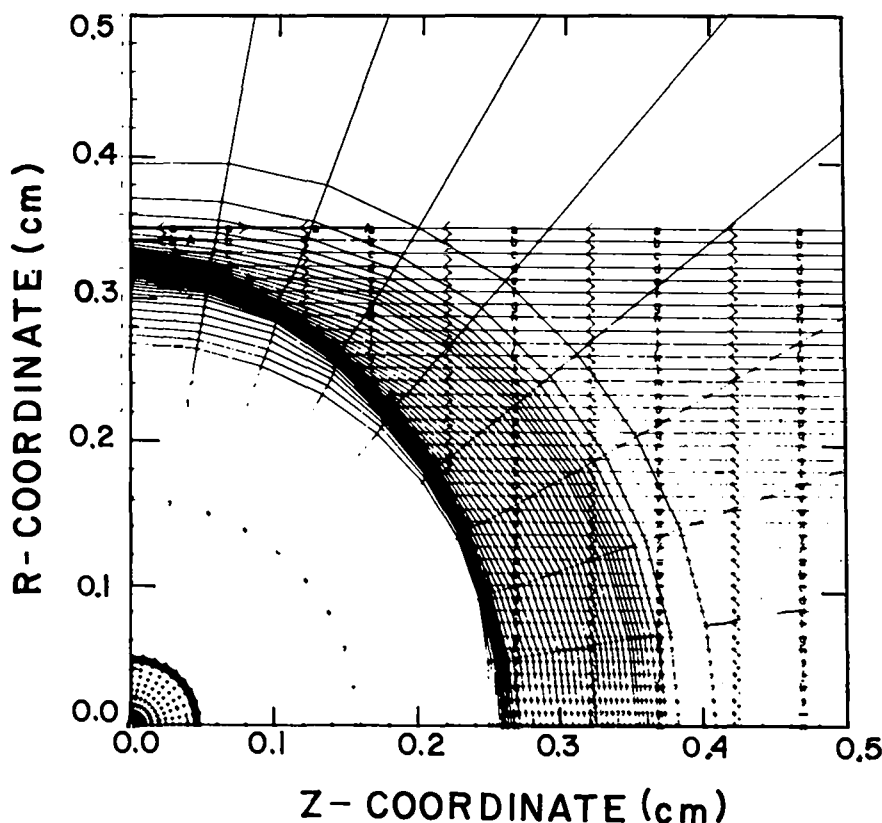
Fig. VIII-18. Lagrangian mesh with ion rays at 20 ns for the cylindrical beam case.
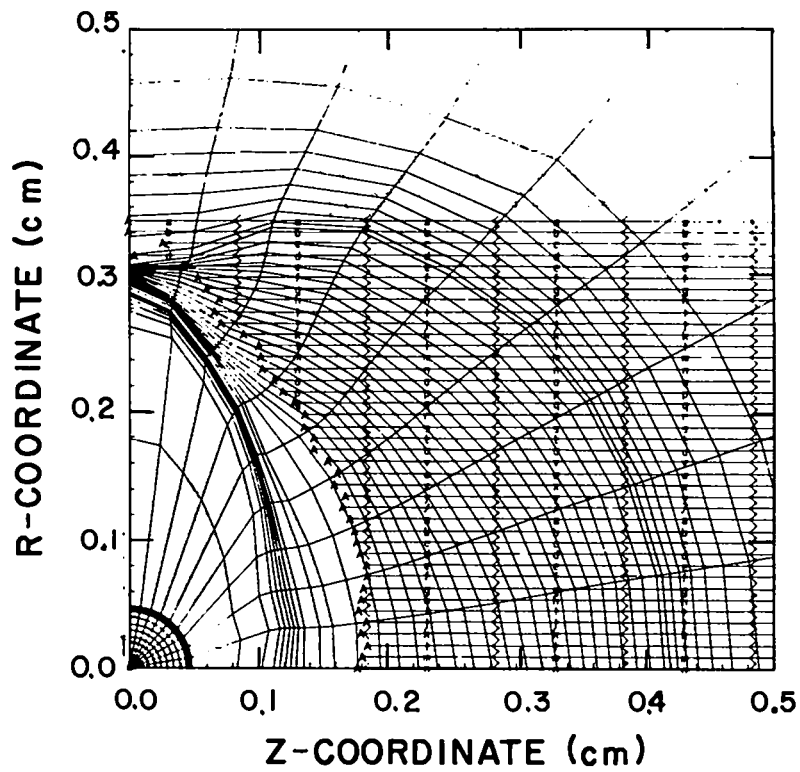
Fig. VIII-19. Lagrangian mesh with ion rays at 35 ns for the cylindrical beam case.

Fig. VIII-20. Plot of initial specific energy deposition as a function of the cosine of the polar angle for different radii for the cylindrical beam case.
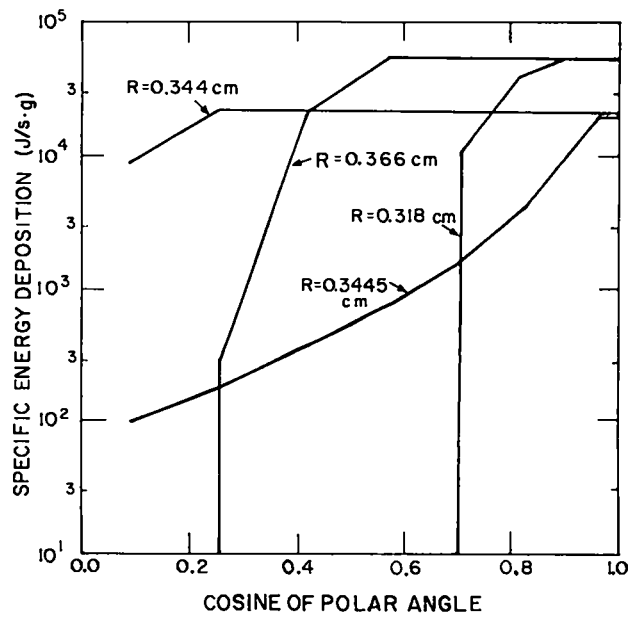
Fig. VIII-21. Plot of initial specific energy deposition as a function of the cosine of the polar angle for different radii for the finite focal-spot case.
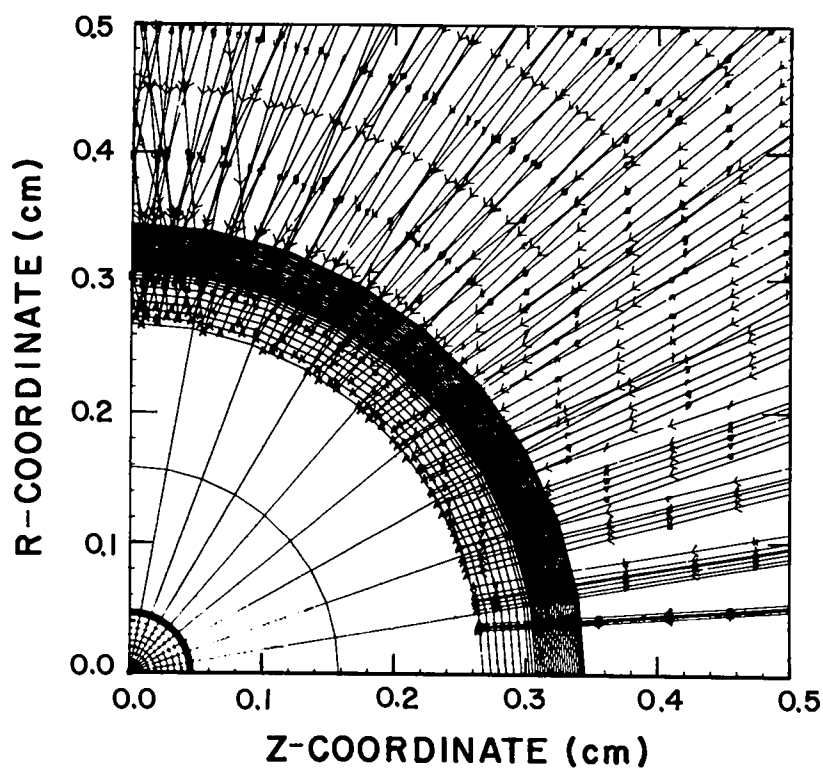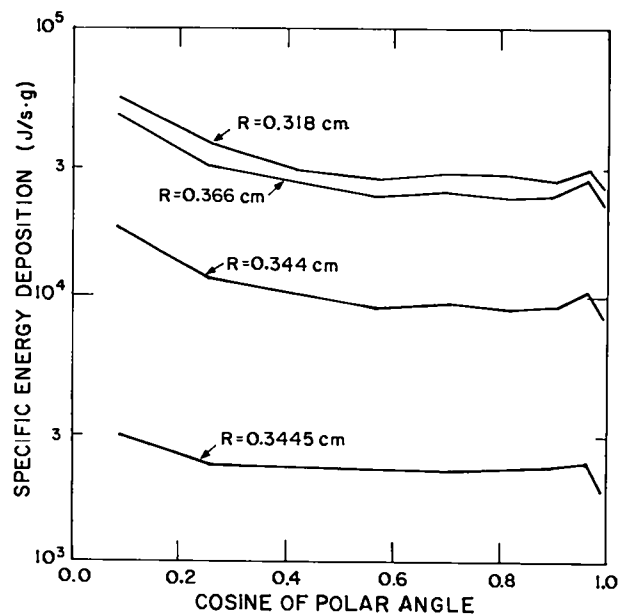
Fig. VIII-22. Lagrangian mesh with ion rays at 0 ns for the finite focal-spot case.
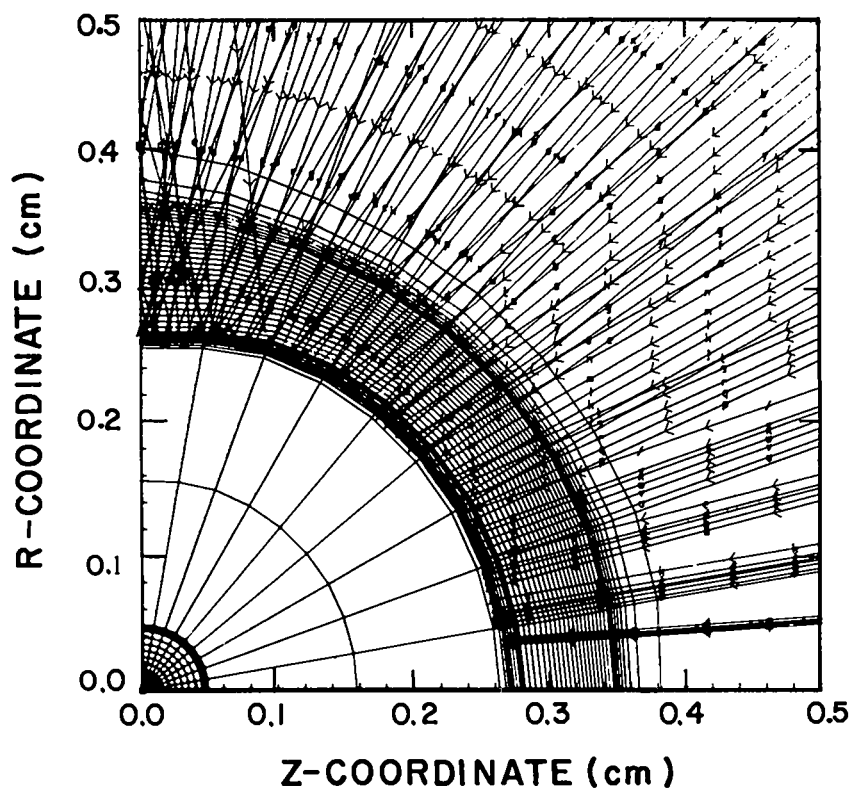
Fig. VIII-23. Lagrangian mesh with ion rays at 20 ns for the finite focal-spot case.
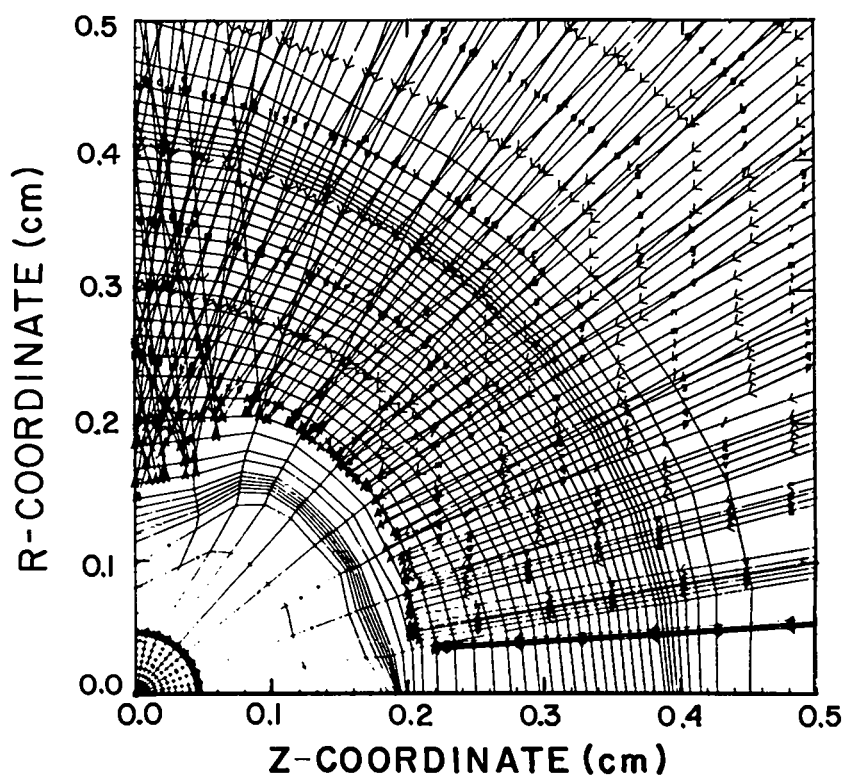
Fig. VIII-24. Lagrangian mesh with ion rays at 35 ns for the finite focal-spot case.

122

REFERENCES

1. R. H. Stokes, T. P. Wangler, and K. R. Crandall, "The Radio-Frequency Quadrupole—A New Linear Accelerator," Proc. 1981 Part. Accel. Conf., Washington, D.C., March 11-13, 1981, IEEE Trans. Nucl. Sci. NS-28, 1999 (1981).

2. K. R. Crandall, M. Pabst, R. H. Stokes, and T. P. Wangler, "Octupole Focusing in Transport and Accelerating Systems," Proc. 1981 Linear Accel. Conf., Santa Fe, New Mexico, October 19-23, 1981.

3. L. C. Teng, "Accelerator Parameters," in ERDA Summer Study of Heavy Ions for Inertial Fusion, Oakland/Berkeley, California, July 19-30, 1976, Lawrence Berkeley Laboratory report LBL-5543 (December 1976), p.13.

4. A. A. Garren, "Final Focusing of the Ion Beams of a Pellet Fusion Reactor by Quadrupole Doublets," in ERDA Summer Study of Heavy Ions for Inertial Fusion, Oakland/Berkeley, California, July 19-30, 1976, Lawrence Berkeley Laboratory report LBL-5543 (December 1976), p. 102 and Appendixes 7 and 8.

5. E. W. Sucov, "Inertial Confinement Fusion Central Station Electric Power Generating Plant, Final Report for the Period March 1, 1979—September 30, 1980, WFPS-TME-81-001 (February 27, 1981), Vols. I and II.

6. R. J. Mason, Nucl. Fusion 15, 1031 (1975).

7. B. I. Bennett, J. D. Johnson, G. I. Kerley, and G. T. Rood, "Recent Developments in the Sesame Equation-of-State Library," Los Alamos Scientific Laboratory report LA-7130 (February 1978).

8. L. Spitzer, Jr., *Physics of Fully Ionized Gases* (John Wiley & Sons, Inc., New York, 1962).

9. T. A. Mehlhorn, J. Appl. Phys. 52, 6522-6532 (1981).

10. J. Linhard, M. Scharff, and H. E. Schiott, Kgl. Dan. Videnskab. Selskab. Mat. Fys. Medd. 33, No. 14 (1963).

11. G. Rinker and G. Bohannon, IEEE Trans. Plasma Sci. PS-8, 55 (1980).

12. D. J. Meeker and R. O. Bangerter, "A Tamped, Split Fuel Layer Ion-Beam Target," Proc. 4th Int. Top. Conf. High-Power Electron Ion-Beam Res. Technol., Palaiseau, France, June 29-July 3, 1981 (Laboratoire de Physique des Milieux Ionises École Polytechnique, Palaiseau, France, 1981), p. 315.

IX. SYSTEMS AND APPLICATIONS STUDIES OF INERTIAL FUSION
(T. G. Frank, I. O. Bohachevsky)

The objectives of systems and applications studies are to (1) identify potential applications of ICF, (2) devise conceptual devices and systems that will ensure economic viability of these applications, (3) define the technology required for the realization of ICF systems, and (4) link research and technology developments to ensure compatibility and complementarity of these activities. We are investigating both laser and heavy-ion-beam drivers. The applications studied include electric power generation, fissile-fuel production, process heat generation, synthetic fuel production, and weapons-related research. The studies consist of conceptual designs of devices, construction of mathematical models to analyze their technical feasibility and performance characteristics, and development of costing algorithms and computer programs to investigate whether various ICF applications are economically competitive.

INTRODUCTION

To be effective, systems and applications studies should consist of two complementary activities. The objective of the first activity is to devise the integrated systems—ICF reactors—necessary to realize and exploit potential applications of the ICF process. The objective of the second activity is to devise analyses for the mathematical modeling of technical and economic characteristics and performances of generic classes of ICF reactor systems and subsystems. These analyses provide a quantitative basis for tradeoff studies and comparative assessments of different ICF reactor concepts, suggest promising novel concepts or configurations, and point out the most profitable research directions.

The performance analysis of the reactor design based on the wetted-wall reactor cavity showed that the fuel pellet firing frequency was limited by the time required to remove the lithium vapor and pellet debris through an exhaust nozzle. Recent modeling and approximate analysis of the restoration of the interpulse cavity conditions showed that removal process duration is proportional to the ratio of cavity volume to nozzle-throat area when the cavity is evacuated through an exhaust nozzle. However, that duration is proportional to the ratio of volume to cavity surface area when evacuation occurs by condensation on the cavity wall.[1] In practical ICF reactor concepts, the ratio of the nozzle-throat area to the cavity surface area will be very small by design; therefore, this simple estimate suggests modifying the original wetted-wall reactor cavity so that the liquid lithium flow allows cavity evacuation by condensation on the relatively cold

liquid layer.[2,3] Based on this concept, the operating frequency of the reactor cavity could be increased 50- to 100-fold.

In 1981 we investigated three topics and obtained results that increased our understanding and modeling capability. These topics are (1) response of liquid lithium layers to neutron and x-ray pulses,[4] (2) plasma behavior in magnetically protected ICF reactor cavities,[5-7] and (3) cyclic temperature excursions and thermal-stress fluctuations in fusion reactors.[8,9]

RESPONSE OF LIQUID LITHIUM LAYERS TO NEUTRON AND X-RAY PULSES
(I. O. Bohachevsky)

Introduction

Many currently proposed ICF reactor-vessel concepts employ liquid lithium in blankets and/or in relatively thin layers that protect the inner wall of the vessel from products of fuel pellet microexplosions. Thermal loads on the liquid lithium are imposed by intense pulses of nonuniform spatial intensity that are much shorter than hydrodynamic and thermal relaxation times; therefore, they generate pressure pulses and/or pressure waves.[1] We have investigated responses of lithium blankets and layers analytically and numerically; results show that these responses will not pose severe design problems.

We distinguish two cases: when the lithium initially is, and remains, at a pressure higher than its vapor pressure, and when its pressure is equal to or lower than its vapor pressure. In the first case, an analytic solution can

accurately describe the wave motion; in the second case, the solution cannot be approximated with analytic expressions, and numerical computations that include phase transitions are required.

Analytic Solutions

A layer of liquid lithium between two concentric spherical surfaces is shown in Fig. IX-1. The outer surface at R_2 is a rigid wall on which the normal component of the velocity vanishes at all times. The inner surface at R_1 is either a rigid structural shell on which the normal component of the velocity vanishes or a free surface on which the pressure perturbation vanishes. The symbol Δ denotes the thickness of the liquid layer, $R_2 - R_1$, and δ the depth of the layer into which energy is deposited. For neutron energy deposition, $\delta = \Delta$; in general for x-ray and debris energy deposition, $\delta/\Delta \ll 1$.

The contemplated convective velocities parallel to the ICF reactor vessel walls are much smaller than the sound speed in the liquid lithium and can be neglected. Also, we expect the ratio Δ/R_1 to be significantly less than unity; therefore, the plane wave approximation describes the motion with adequate accuracy. With these approximations, the linearized equations that govern the propagation of pressure p and transverse-velocity perturbations u across an incompressible liquid can be solved by using the Fourier-series expansions. The details of the analysis have been published;[4] here we present typical results for a liquid blanket between two structural shells and for a free layer on the inside surface of a spherical vessel.

Figure IX-2 shows the calculated dependence of the ratio of the amplitude of the first harmonic component to

Fig. IX-2. Relative amplitude of first harmonic component of pressure wave in the blanket.

the mean pressure rise (the value that would obtain if the energy was deposited uniformly and so slowly that the waves did not develop) on the nondimensional blanket thickness Δ/λ. (λ is the scale depth of neutron energy deposition.) The values of Δ/λ for current conceptual ICF reactor designs range between 1.0 and 2.0; therefore, the amplitude of the pressure wave for these designs increases steeply and approximately linearly with the blanket thickness. This trend indicates that blankets should be designed to be as thin as possible consistent with energy-extraction and tritium-breeding needs.

Figure IX-3 shows sample results for neutron energy deposition in a 5-cm-thick free-surface layer. The solid curve represents the pressure $p(R_2,t)$ at the wall, and the dashed curve represents the velocity $u(R_1,t)$ at the free surface. These curves indicate a square wave traveling back and forth between the wall and the free surface; this result was expected because neutron energy deposition is nearly uniform in a layer that is thin relative to the e-folding distance.

The small amplitude of the velocity perturbation is significant; it is less than 0.5 m/s even for an amplitude of the pressure perturbation as high as 10^7 dyn/cm^2 (10 atm). With a calculated velocity of 41.5 cm/s, the free surface travels only 8.3×10^{-4} cm before the pressure perturbation reverses its sign.

Numerical Solutions

Anticipated requirements for transmission of driver pulses to the fuel pellet are such that the residual interpulse pressure in an ICF reactor cavity protected by

Fig. IX-1. Configuration of lithium layer.

Fig. IX-3. Velocity at the free surface and pressure at the wall for a 5-cm-thick layer of lithium.

We consider a 5-cm-thick layer of liquid lithium on the inside of a spherical vessel (radius $R_2 = 170$ cm). Neutron transport calculations indicate that energy deposition by 14-MeV neutrons in liquid lithium is well approximated by a source $\dot{S}$ given by

$$\dot{S} = \frac{S_0}{\rho} \exp\left[-(r - R_1)/\lambda\right] \ ,$$

where ρ is the density, $\lambda = 53$ cm, and $S_0 = 0.71 \times 10^{17}$ erg/cm³·s for a 150-MJ pellet and an energy deposition time of 1 ns (10^{-9} s). The initial conditions were cell size $= 0.1$ cm (1 mm), temperature $T_0 = 769.41$ K (0.0663 eV), and density $\rho_0 = 0.48$ g/cm³.

Calculated results show no perceptible effects except for a temperature increase of 3.77 K and a pressure increase of 1 dyn/cm². There is no indication of perceptible motion even when the energy deposition rate is increased tenfold to $S_0 = 0.71 \times 10^{18}$ erg/cm³·s and the temperature increase becomes 38 K. Significant wave and particle velocities appear only when the energy deposition rate is increased another factor of 10 to $S_0 = 0.71 \times 10^{19}$ erg/cm³·s.

The energy of the x rays (and of the debris ions) emitted by ICF pellets may range from 100 eV to 100 keV; the corresponding opacities of cold lithium[11,13,14] are such that the characteristic depth of energy deposition may vary from tens of centimeters to a fraction of a millimeter. When the penetration depth is much larger than the layer thickness Δ, the effect of x rays is indistinguishable (except for the source strength) from the effect of neutron energy deposition discussed above. The effect of x rays whose depth of penetration is small (less than a millimeter) or comparable (a few centimeters) to the thickness of the lithium layer is discussed below.

The characteristic heat conduction time τ_c ($\tau_c = \delta^2/\kappa$, where κ is heat diffusivity) for a 1-mm-thick lithium layer is 3.4×10^{-2} s, and a representative x-ray pulse length is 10^{-8} s. Therefore, the initial imbalance caused by the temperature discontinuity will be resolved with pressure waves (Ref. 1, Sec. V).

For ~8% of a 150-MJ (certainly an upper bound) pellet emitted as x rays and deposited in a 1-mm-thick layer of liquid lithium at a distance of 165 cm during 10^{-8} s, the source strength is $S_0 = 3.5 \times 10^{17}$ erg/cm³·s, and the exponential function can be replaced with unity. Figure IX-4 shows the temperature rise during the pulse in the 1-mm layer adjacent to the free surface. The total temperature increase of 193 K is 8% lower than the

a lithium layer will be close to the vapor pressure of the lithium.[3] Calculating the response of the layer to energy deposition at these conditions requires including transitions between liquid and vapor phases. This inclusion implies a nonunique relationship between the pressure and density (specific volume) and requires numerical computations for an accurate analysis of the phenomena. The results reported here have been obtained with the CHART-D code developed at Sandia National Laboratories (SNL); because the code is well known and adequately documented,[10-13] we will not describe it in detail. The code numerically solves the equations of hydrodynamics in Lagrangian coordinates and uses the most accurate available equation of state of the medium, including phase transitions. We limit the study to the layer of liquid lithium on the inside of a spherical vessel and investigate responses to neutron and x-ray energy depositions.

Fig. IX-4. Temperature rise in the 1-mm-thick layer adjacent to the free surface induced by x-ray energy deposition ($S_0 = 3.5 \times 10^{17}$ erg/cm³·s).

value obtained by using a constant heat capacity $c_p = 3.55$ J/g·K;[15] the discrepancy indicates the amount of heat associated with phase transition and conversion into kinetic energy.

The result (Fig. IX-4) does not indicate unexpected or unusual behavior; however, the plot of the pressure (Fig. IX-5) illustrates the violent transition leading to the development of wave motion. The pressure histories plotted in Fig. IX-5 are for different energy deposition rates obtained by changing the amount of energy deposited and the pulse length. The results illustrate the instantaneous pressure increases associated with transitions to pure liquid state and the threshold rate below which the transition to pure liquid does not occur. The abrupt pressure drop is associated with the reappearance of the vapor in the layer; it occurs at the time when the expansion velocity induced by the transient pressure imbalance attains a quasi-steady value (Fig. IX-6).

Computed results indicate that the transient pressure pulse shown in Fig. IX-5 dissipates in a few millimeters of the two-phase mixture and that its effect never reaches the wall. Therefore, it can be disregarded, and the state of the medium attained at $t = 2 \times 10^{-7}$ s can be taken as the initial condition for the development of subsequent
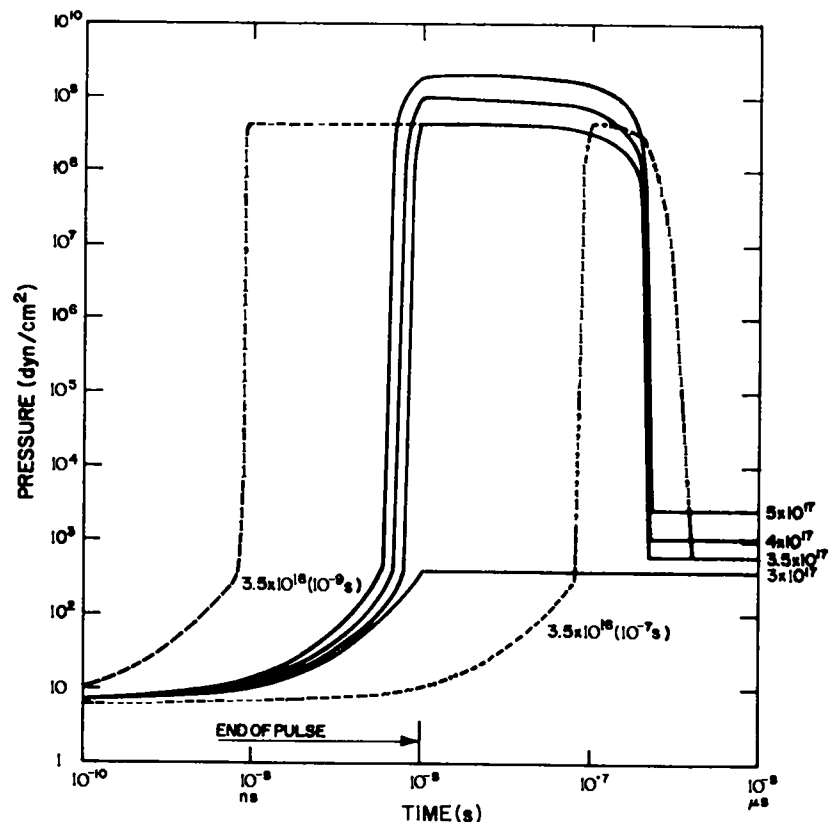

Fig. IX-5. Pressure increase in the 1-mm-thick layer adjacent to the free surface induced by x-ray energy deposition (source strengths in erg/cm³·s).

127
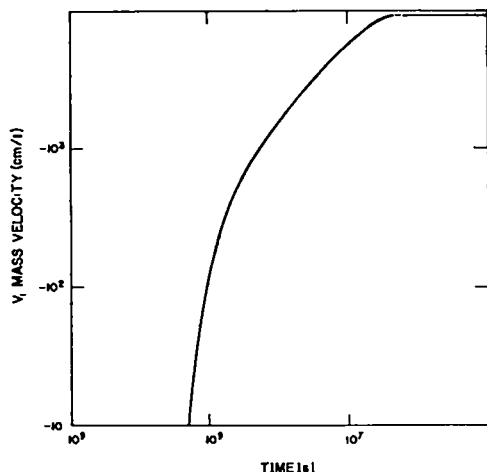
Fig. IX-6. The development of mass velocity associated with x-ray energy deposition ($S_0 = 5 \times 10^{17}$ erg/cm³·s).

phenomena. This result illustrates a previously unanticipated advantage of using a protective liquid-vapor lithium layer >1 cm thick[3] and containing a small amount of vapor. Reference 4 discusses the details of the dissipation of the pressure wave propagating in a two-phase medium.

Summary and Conclusions

The analytic and numerical solutions obtained describe pressure pulse generation and wave propagation in liquid lithium blankets and protective layers; they lead to the following observations and conclusions.

Effects of neutron energy deposition in liquid blankets contained between structural shells can be determined analytically; results show that the mean pressure rise, combined with the first harmonic component of the pressure wave, accounts for nearly 90% of the deposited energy and therefore provides an approximate description of the phenomena that is adequate for many purposes. The ratio of the amplitude of the first harmonic to the mean pressure rise increases nearly linearly with the nondimensional blanket thickness Δ/λ for values of $\Delta/\lambda < 4$; it is ~0.50 for a representative value of the blanket thickness $\Delta/\lambda \approx 1.60$. Therefore, in preliminary calculations, it is sufficient to multiply the estimate of the mean pressure increase by a factor of 1.50 to account for the transient overpressure.

The neutron and x-ray pulses in ICF applications are much shorter than the hydrodynamic and thermal response times of the liquid lithium; therefore, they

deposit energy at constant specific volume, that is, isochorically. The effect of such processes in a liquid-vapor mixture at or near the saturation line is transition to pure liquid accompanied by a sharp and intense pressure increase in the region of energy deposition. However, the pressure pulse generated in this way propagates only a short distance before dissipating because of the low sound speed in two-phase liquid-vapor mixtures. This result is consistent with the use of liquid sprays to suppress intense acoustic oscillations. Computed results indicate that pressure pulses with amplitudes of up to 1000 atm dissipate in a few millimeters of lithium at vapor pressure.

Analysis of the results indicates that the phenomena that develop in lithium layers because of pulsed energy deposition can be assessed accurately only if the validity of the assumptions that enter into the computations is established experimentally.

PLASMA BEHAVIOR IN MAGNETICALLY PROTECTED ICF REACTOR CAVITIES
(I. O. Bohachevsky, J. C. Goldstein, D. O. Dickman)

Introduction

In the ICF process the fusion reaction occurs sufficiently fast (in $<10^{-9}$ s) to resemble a small explosion that produces ions of relatively high energy (1-100 keV). Investigations of the expansion of these ions and their interaction with an externally generated magnetic field embedded in a residual background fluid led to the construction and study of a plasma model consisting of an ionized fluid, relatively energetic ions not in thermodynamic equilibrium with the surrounding fluid, and an electromagnetic field. Discussions of motivation, parameter estimates, and physical assumptions leading to this model have been published previously[5,6] together with the governing equations and the results that illustrate engineering implications for ICF applications.

Here we present (1) a brief description of the plasma model, (2) an outline of the numerical procedure used to calculate the results, and (3) results of a parametric investigation of the ion propagation through electrically conducting fluids with embedded magnetic fields of moderate intensity (several thousand gauss).

Plasma Model

In practical applications, ICF microexplosions will occur inside containment vessels filled with a residual

interpulse fluid.[1] The laser or particle beam transmission requirements to initiate the fusion reaction impose an upper limit on the admissible residual fluid density n. This limit is not known precisely, but it is not expected to exceed a value between 10^{15} or 10^{16} atom/cm³. A representative volume of an ICF containment vessel (4-m-long cylinder with 2-m radius) is 5×10^7 cm³; therefore, the total number of atoms involved may be between 5×10^{22} and 5×10^{23}. If only 0.1% of the nominal pellet energy release of 150 MJ is absorbed by these atoms, the energy per atom will be higher than 1 eV, enough to ionize the medium so that it will be a perfectly conducting plasma.

Under these conditions the collisional cross sections σ for the fluid particles are $\sim 10^{-15}$ cm²; consequently, the mean free path λ ($\lambda \approx 1/\pi n s$) is between 0.30 and 0.03 cm. These estimates show that phenomena with characteristic lengths of several centimeters or more can be modeled with a continuum description.

Fuel pellet debris generated in the microexplosion, however, behaves differently. Calculations[16] based on the Lindhard stopping theory show that even at a density of 1.5×10^{16} atom/cm³ (exceeding the allowable limit), the mean debris ion range in neon is between 2 and 5 m. Ion ranges of that magnitude are comparable to or greater than characteristic dimensions of ICF containment vessels and much greater than the background medium mean free paths. Therefore, the ion motion cannot be approximated within the framework of a fluid model but must be determined from kinetic theory. In our analysis this is accomplished by calculating trajectories for a statistical sample (5 000 to 20 000) of ions.

To prevent the high-energy ions from striking and eroding the wall of the cylinder, an axial magnetic field is impressed that deflects the ion trajectories and guides them into the cylinder ends.[1,6] Preliminary investigations[17] show that a magnetic field intensity of a few thousand gauss is sufficient to accomplish this.

In accord with the estimates made above, the plasma model for the analysis of cavity phenomena consists of three parts: background fluid; discrete, relatively high-energy ions; and an electromagnetic field. We assume that the flash of x rays emitted by the reacting fuel ionizes the single-component background fluid to a degree that makes it a perfectly conducting plasma. Its behavior is described by modified Lundquist equations supplemented with an appropriate equation of state and a rate equation that determines changes in the degree of ionization. We model the expansion of debris ions using a representative sample of ion trajectories calculated by integrating the equation of motion for each simulation ion with the Lorentz force contributing to the acceleration. The model also includes phenomenological terms that describe momentum and energy transfer between the fluid and the discrete ions and a rate equation that determines the average ion charge.

We describe the electromagnetic field with Maxwell's equations, neglecting the displacement current. We replace Ohm's law with postulates that the electric field be always and everywhere perpendicular to the magnetic field, that local charge neutrality prevail, and that the electrons be massless and drift without inertia in the direction perpendicular to electric and magnetic fields. Thus, the model constitutes a generalization and extension of considerations introduced by Dickman, Morse, and Nielson.[18]

Solution

Solutions describing the evolution of plasma conditions inside reactor cavities are obtained by numerical integration of the governing equations. Toward this end, the differential equations are replaced with finite-difference approximations using the Lax-Friedrichs scheme introduced by Lax[19] and applied effectively by Bohachevsky et al.[20-22] to calculate multidimensional flows with shock waves and radiation effects.

The integration is initialized by (1) determining the desired magnetic-field distribution (either by placing coils at appropriate locations or by solving the boundary value problems for the magnetic vector potential); (2) placing simulation particles into desired locations with desired velocities (energies); and (3) prescribing initial distributions for the density, velocity, and temperature of the background fluid.

After initialization the variables are advanced in discrete time steps in the following order: (1) the simulation particles are moved; (2) the values of density, velocity, and internal energy of the fluid are advanced; (3) the auxiliary thermodynamic quantities (including ionization fraction) are determined; (4) the current is calculated; (5) the electric field is calculated; and (6) the magnetic field is advanced, completing the cycle.

The computations are continued until all simulation particles disappear into containment walls or a quasi-steady state has been reached. We record the time, position, and ion energy at the time of impact into the wall to help analyze first-wall heating and erosion.[23]

TIME = 2.4E-05

$\rho_o = 3.44 \times 10^{-8} g/cm^3$

WALL   RMAX =   250.00

AXIS   ZMAX =   625.00

Fig. IX-7. Ion cloud in fluid density of n = 10^{15} atom/cm^3.

$\rho_o = 3.44 \times 10^{-8} g/cm^3$
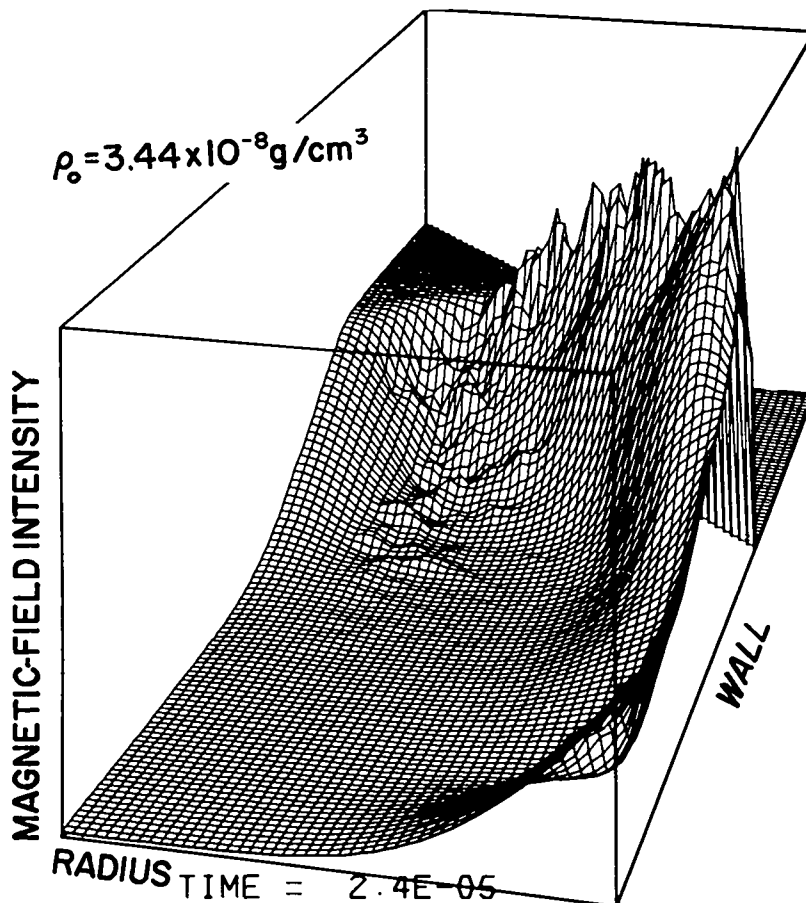
Fig. IX-8. Magnetic-field intensity in fluid density of 10^{15} atom/cm^3.

Results

Figures IX-7 and IX-8 illustrate the expansion of ions through tenuous (10^{14}-10^{15} atom/cm^3) media. The relatively extensive dispersion of ions and the smooth variation of the magnetic-field intensity are significant. Figures IX-9 and IX-10 illustrate the ion expansion through relatively dense (10^{16}-10^{17} atom/cm^3) media. Here the concentration of ions in a thin sheet and the associated discontinuity in the slope of the magnetic-field intensity are significant. The lines in Fig. IX-7 and IX-9 are contours of constant magnetic flux.

Figures IX-11 and IX-12 illustrate the pressure and the axial fluid velocity distributions for an ambient density of 3.44×10^{-8} g/cm^3 (10^{15} atom/cm^3). The maximum values of these variables at the times of the plots were 7×10^4 dyn/cm^2 and 1.6×10^7 cm/s. These results show that the ions impart such a high velocity to the background fluid that despite large energy deposition, the temperature and density in the region interior to the expanding ions decrease to very low values. (This result is predicated on the assumption that radiative energy transport is negligible.) Thus, the individual ions act like jet ejectors, and the effect reduces the density inside the shell of expanding ions to a value less than one-thousandth of the initial ambient density.

Our general investigation did not uncover any fundamental physical reason that would eliminate the possibility of magnetically protecting the reactor cavity wall.

CYCLIC TEMPERATURE AND THERMAL-STRESS FLUCTUATIONS IN FUSION REACTORS
(I. O. Bohachevsky; R. N. Kostoff, DOE/ER)

Introduction

Early commercial fusion reactors, whether they operate as pure fusion

130

electricity generators or as fusion-fission fuel factories, will use the D-T fuel cycle. The D-T fusion reactor produces predominantly 14-MeV neutrons, which interact with an absorbing blanket, and charged particles and radiation, which are absorbed in the wall facing the reacting plasma. The resulting energy deposition in the blanket and in the wall raises the temperature nonuniformly and induces thermal stresses. In general, the fusion plasma core is not expected to burn continuously but intermittently; consequently, the induced thermal stresses will be cyclic. The cycle time, or period, may range from tens of minutes to small fractions of a second, and the fraction of a cycle during which fusion energy is released may range from nearly unity to 10^{-6}. Thus, the characteristics of cyclic thermal and mechanical loads in fusion reactors will span a wide range of parameter values.

We have modeled and analyzed cyclic thermal loads and stresses in the complete potential range of operating conditions. We have examined the two critical components of fusion reactors, namely, the solid wall adjacent to the fusion plasma (first wall) and the fuel elements in the high-power-density region of the blanket. These two components exemplify two limiting cases of thermal loading: the first-wall loads are generated by predominantly shallow energy deposition that may be approximated with a flux across the surface, and the fuel-element loads are generated by predominantly volume-energy deposition of volumetric heating. For these two types of loading, we have derived simple closed-form expressions for temperature excursions and thermal stresses that may be evaluated conveniently and rapidly to compare values for different systems.

The explicit expressions for the parametric dependencies of thermal stresses may be used to identify critical stress areas, to derive comparisons between the

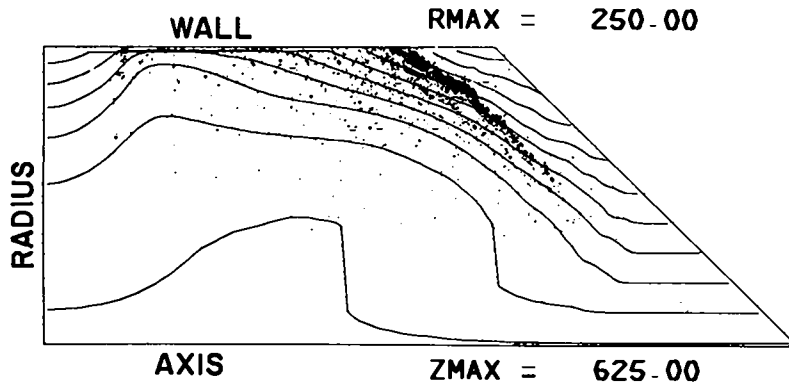TIME = 2.4E-05

$$\rho_0 = 3.44 \times 10^{-6} \, g/cm^3$$
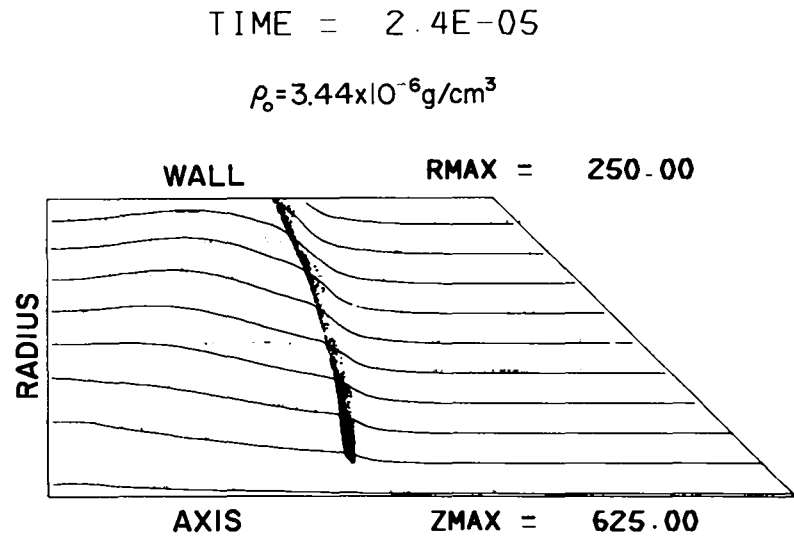
Fig. IX-9. Ion sheet in fluid density of 10^{17} atom/cm^3.
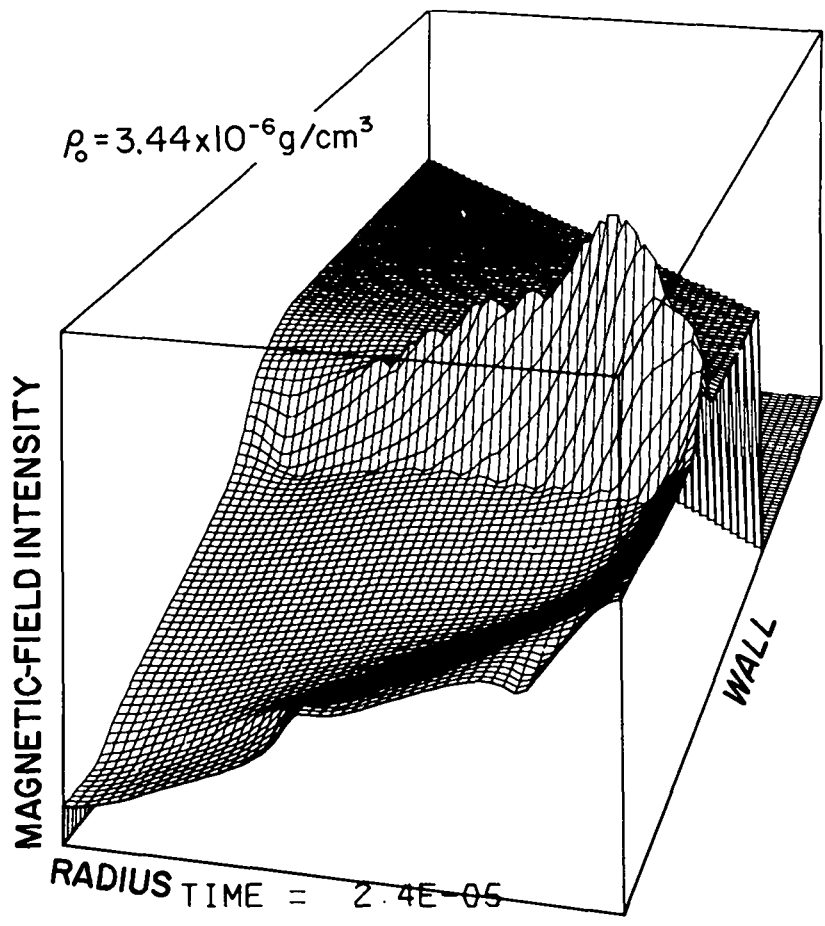
Fig. IX-10. Magnetic-field intensity in fluid density of $n = 10^{17}$ atom/cm^3.
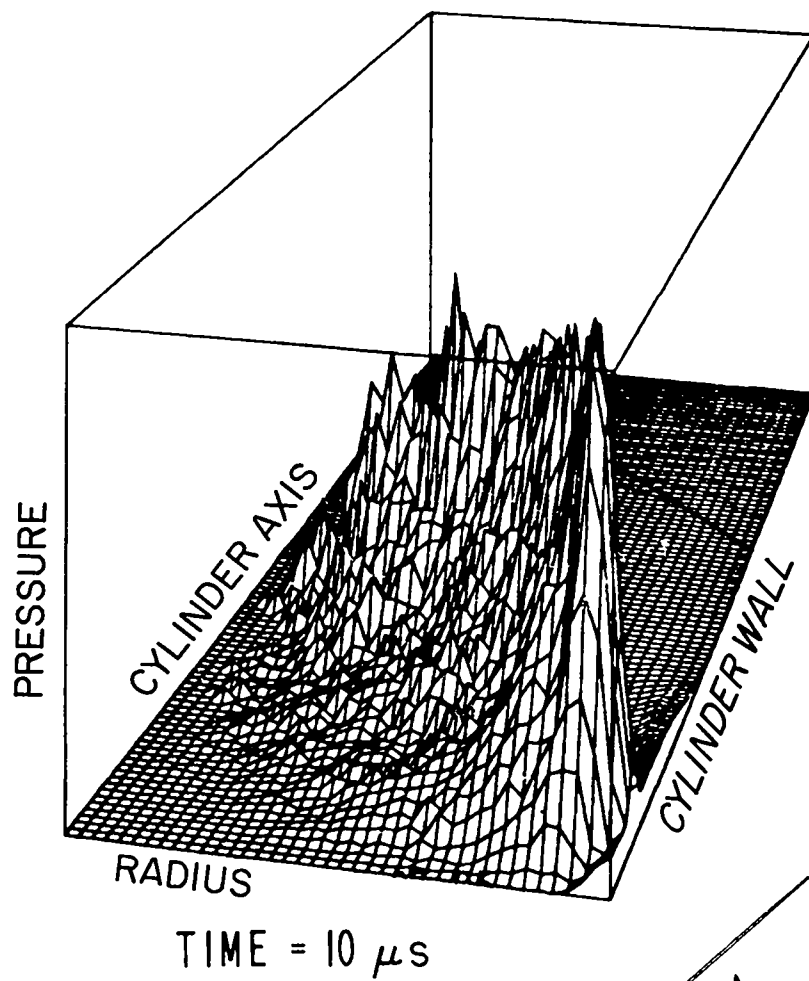
Fig. IX-11. The pressure wave and the low-temperature region inside reactor cavity.
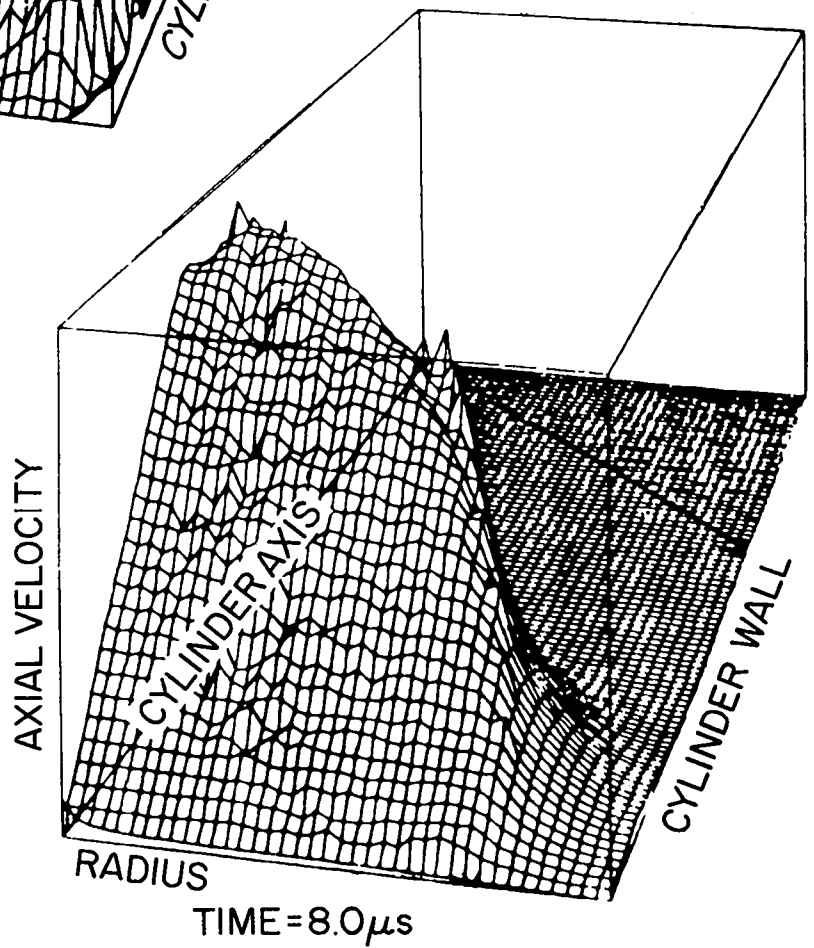
Fig. IX-12. Axial velocity distribution of background fluid.

relative merits of fusion reactor operation in different parameter regimes, and to estimate benefits that may obtain from changes in operating characteristics. The results also provide a quantitative basis for tradeoff studies.

Assumptions

To ensure that the results are simple and accurate enough for practical applications, we assume that energy is released during fuel fusion in pulses that have the shape of a square wave with constant intensity for a specified pulse duration. We also assume that the faces of the structural elements in contact with fluid coolants are at the bulk coolant temperature, which remains constant. This second assumption is a good approximation when the coolant mass flow rate and conductivity are so high that the coolant behaves as an isothermal sink.

We assume further that the fuel elements are enclosed in a thin metallic cladding whose thermal expansion coefficient and heat capacity (but not necessarily the tensile or yield strength) are the same as those of the fuel-element material and that the cladding and the fuel-element materials remain in intimate contact. These assumptions may result in absolute differences between the model predictions and actual fuel-element stresses because of gaps provided between fuel and cladding to accommodate differential expansion. However, relative differences predicted in fuel elements under different fusion pulsing scenarios should be predictable.

Analysis

We used two approaches to solve the heat conduction equation and to calculate stresses in terms of system parameters. The first is expansion into Fourier series and determination of periodic solutions. In the second we obtain a solution for a single pulse and sum the contributions of individual pulses weighted with appropriate time delays and time decays to obtain both the transient and the long-term solutions. The first approach is more accurate when the temperature during a given pulse depends strongly on the temperature profile of the preceding pulse. On the other hand, the second approach is more accurate when the temperature during a given pulse is independent of the temperature profile of the preceding pulse (for example, when the time between pulses is so long that the component cools to bulk coolant temperature before the start of the next pulse).

Results

Figure IX-13, a summary of the results, shows the variation in the ratio of the amplitude of the fluctuating stress component to the mean steady-state stress. This ratio is plotted as a function of the pulse length
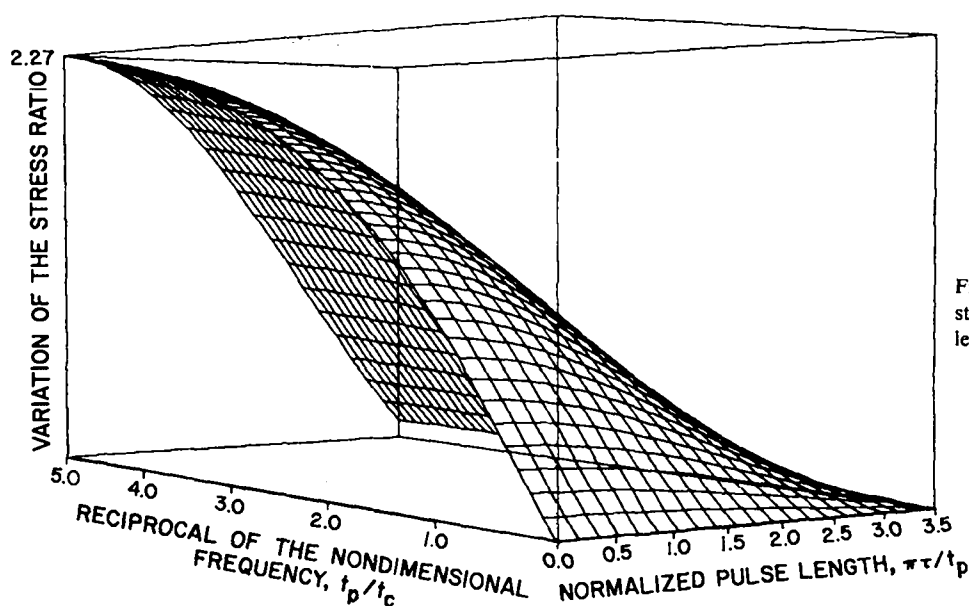
Fig. IX-13. Combined dependence of stress ratio on frequency and pulse length.

normalized with the cycle period t_p and the non-dimensional frequency expressed in cycles per characteristic thermal response time t_c of the structural element. The scale on the axis represents the reciprocal of the nondimensional frequency t_p/t_c to ensure accuracy at high frequencies. These results were derived by using the Fourier-series expansion of the solution; the details of the analysis and results were presented at the 3rd IAEA Committee Meeting and Workshop on Fusion Reactor Design and Technology.[8]

When the pulse duration equals the cycle period, which occurs for steady-state fusion systems such as stellarators, the ratio of stress components vanishes, implying the presence of only steady-state thermal stress. When the pulse length is about 0.85 to 0.90 of the cycle period, as it would be for nominal tokamak operation, the amplitude of the fluctuating stress component equals about 0.10 to 0.15 of the steady-state stress for reasonable values of the frequency; the presence of the fluctuating stress component is considered detrimental. For very short pulses, like those in ICF reactors and magnetic pinches, the amplitude of the fluctuating stress component is a strong function of the frequency, which is the ratio of the characteristic thermal diffusion time to cycle time. For small values of τ and high frequencies, which represent nominal 10-Hz operation of ICF reactors with characteristic thermal diffusion times exceeding 1 s, the fluctuating stress component is nearly negligible and in effect the system is in steady-state stress. For short pulses and low frequency, the amplitude of the fluctuating stress reaches the maximum value of 1.16 times the steady-state value of the stress for the first wall and 0.92 times the steady-state value for the fuel element in the fusion-fission hybrid. This result may not be exact because the accuracy of the Fourier-series representation deteriorates as the cycle time increases significantly above the characteristic thermal diffusion time.

When the single-pulse approach is used to analyze the low-frequency case, the results show that for short pulses, the ratio of the fluctuating stress component to the value of the stress that would obtain in the case of high-frequency (equivalent to steady-state) operation equals the ratio of the cycle time to the pulse length, which may be very large. In this case one can reduce the fluctuating stress amplitude by reducing the component size and thus its characteristic thermal diffusion time; this effectively increases the nondimensional frequency of operation. Reduction of component sizes appears practical for magnetic-pinch systems but difficult for slow-pulsed, large ICF systems.

Both the Fourier-series and the single-pulse analyses predict the same value of the steady-state stress limit as the pulse length τ approaches the cycle period t_p.

REFERENCES

1. I. O. Bohachevsky, "Models and Analyses for Inertial Confinement Fusion Reactor Studies," Los Alamos National Laboratory report LA-8557 (May 1981).

2. Roger B. Perkins and the Inertial Fusion Program Staff, "Inertial Fusion Program, July 1—December 31, 1979," Los Alamos National Laboratory report LA-8511-PR (October 1981).

3. J. H. Pendergrass, T. G. Frank, and I. O. Bohachevsky, "A Modified Wetted Wall Inertial Fusion Reactor Concept," Proc. Top. Meet. Technol. Controlled Fusion, ANS, 4th, King of Prussia, Pennsylvania, October 14-17, 1980, DOE/Conf. 8010, July 1981, Vol. II, p. 1131.

4. I. O. Bohachevsky, Nucl. Technol./Fusion 1, 110-119 (1982).

5. I. O. Bohachevsky, J. C. Goldstein, and D. O. Dickman, "A Plasma Model for ICF Reactor Studies, Proc. Int. Conf. on Plasma Phys., Nagoya, Japan, April 7-11, 1980 (Fusion Research Association of Japan), Vol. 1, p. 384.

6. I. O. Bohachevsky, J. C. Goldstein, and D. O. Dickman, Nucl. Technol./Fusion 1, 390-401 (1981).

7. I. O. Bohachevsky, J. C. Goldstein, and D. O. Dickman, "Expansion of Ions in Conducting Fluids with Imbedded Magnetic Fields," Los Alamos National Laboratory report LA-9165-MS (January 1982).

8. I. O. Bohachevsky and R. N. Kostoff, "Cyclic Thermal Stresses in Fusion Reactors," Proc. 3rd Int. At. Energy Agency Comm. Meet. Workshop Fusion React. Des. Technol., Tokyo, Japan, October 5-16, 1981 (to be published in Nuclear Technology/Fusion).

9. I. O. Bohachevsky and R. N. Kostoff, "First Wall and Blanket Stresses Induced by Cyclic Fusion Core Operations," Proc. 9th Symp. Eng. Probl. Fusion Res., Chicago, Illinois, October 26-29, 1981 (IEEE, New York, 1981), Publication No. 81CH1715-2 NPS.

10. S. L. Thompson and H. S. Lauson, "Improvements in the CHART D Radiation-Hydrodynamic Code II: A Revised Program," Sandia Laboratories report SC-RR-71 0713 (February 1972).

11. S. L. Thompson and H. S. Lauson, "Improvements in the CHART D Radiation-Hydrodynamic Code III: Revised Analytic Equation of State," Sandia Laboratories report SC-RR-71 0714 (March 1972).

12. S. L. Thompson and H. S. Lauson, "Improvements in the CHART D Radiation-Hydrodynamic Code IV: User Aid Programs," Sandia Laboratories report SC-71-0715 (March 1973).

13. S. L. Thompson and H. S. Lauson, "Improvements in the CHART D Radiation-Hydrodynamic Code V: 1972-1973 Modifications," Sandia Laboratories report SLA-73-0477 (October 1973).

14. Ellery Storm and Harvey I. Israel, "Photon Cross Sections from 0.001 to 100 MeV for Elements 1 Through 100," Los Alamos Scientific Laboratory report LA-3753 (November 1967).

15. J. O. Cowles and A. D. Pasternak, "Lithium Properties Related to Use as a Nuclear Reactor Coolant," Lawrence Radiation Laboratory report UCRL-50647 (April 1969).

16. R. W. Conn, S. I. Abdel-Khalik, G. A. Moses, F. Beranek, E. T. Cheng, G. W. Cooper, R. B. Droll, T. Henderson, J. Howard, T. O. Hunter, E. Maynard, K. R. Okula, M. Ortman, M. M. H. Ragheb, W. B. Rensel, D. Solomon, R. L. Spencer, I. N. Sviatoslavsky, W. F. Vogelsang, R. D. Watson, and W. G. Wolfer, "SOLASE A Conceptual Laser Fusion Reactor Design," University of Wisconsin Fusion Research Program report UWFDM-220 (December 1977).

17. J. C. Goldstein, I. O. Bohachevsky, and D. O. Dickman, APS Bull. 24, No. 8, 1071 (October 1979), paper 7X4.

18. D. O. Dickman, R. L. Morse, and C. W. Nielson, Phys. Fluids 12, 1708-1716 (1969).

19. P. D. Lax, Comm. Pure Appl. Math. VII, 159-193 (1954).

20. I. O. Bohachevsky and E. L. Rubin, AIAA J. 4, 600-607 (1966).

21. I. O. Bohachevsky and R. E. Mates, AIAA J. 4, 776-782 (1966).

22. I. O. Bohachevsky and R. N. Kostoff, AIAA J. 8, 1024-1031 (1972).

23. I. O. Bohachevsky and J. F. Hafer, Nucl. Technol. 41, 229-311 (1978).

X. RESOURCES, FACILITIES, AND OPERATIONAL SAFETY
(F. P. Durham)

All buildings for HEGLF (Antares) have been constructed. Operational safety policies and procedures continued to be applied successfully to minimize the hazards of operating high-power lasers.

MANPOWER DISTRIBUTION

The distribution of employees assigned to the various categories of the DOE-supported Inertial Fusion Research Program is shown in Table X-I.

FACILITIES

High Energy Gas Laser Facility (HEGLF)

Construction Package I, which includes the Laser Hall, the mechanical building, the office building, and a warehouse, and Construction Package II, which includes the Target Building, the power-transmission system, and miscellaneous construction, have been completed.

Target Fabrication Facility

Construction of the Inertial Fusion Target Fabrication Facility began early in July and is 15% complete. Bids were opened on June 9 and a contract was awarded by DOE to Davis and Associates of Santa Fe, New Mexico, for $9 347 000. The work, which will take about 2 years, has two phases. Phase I consists of site preparation, utilities preparation, and construction of the building structure. Phase II, authorized in December 1981, comprises completion of interior laboratory construction, including the mechanical and electrical systems and installation of laboratory equipment. The facility was designed by Black and Veatch, Consulting Engineers, Kansas City, Missouri; an artist's sketch is shown in Fig. X-1.

The facility will provide a centralized target fabrication laboratory and office space to support the expanded needs of the Helios and Antares laser systems, SNL's pulsed-power fusion program, and related inertial fusion programs. The facility is dedicated to the development of target fabrication techniques, materials, processes, and characterization methods, and to the production, assembly, and characterization of targets for the above programs.

Davis and Associates will build a two-story building (Fig. X-1) with ~50 000 ft^2 of laboratory space divided among 60 individual laboratories and 12 000 ft^2 of office space. It will be located at Los Alamos Technical Area 35 near the Antares and Helios laser facilities. A large penthouse enclosure will house 13 air-handling units, with a total capacity of 205 000 cfm, and 10 exhaust systems for more than 50 fume hoods, with a capacity of 125 000 cfm.

Special features of the facility are large clean areas required for target preparation and assembly operations, as well as for process development and characterization; a tritium-handling laboratory for filling targets with DT gas; target coating laboratories equipped for electroplating, PVD, and CVD; plastic foam development and production laboratories; a laser welding and solid-state joining laboratory; and a precision machining and measurements laboratory.

OPERATIONAL SAFETY

The excellent lost-time injury rate continued during this period with no serious accidents reported.

TABLE X-I. Approximate Staffing Level of Laser Program, 1981.

Laser development	45
Target experiments	140
Target design	40
Target fabrication	52
Diagnostics development	48
Systems studies	5
	330
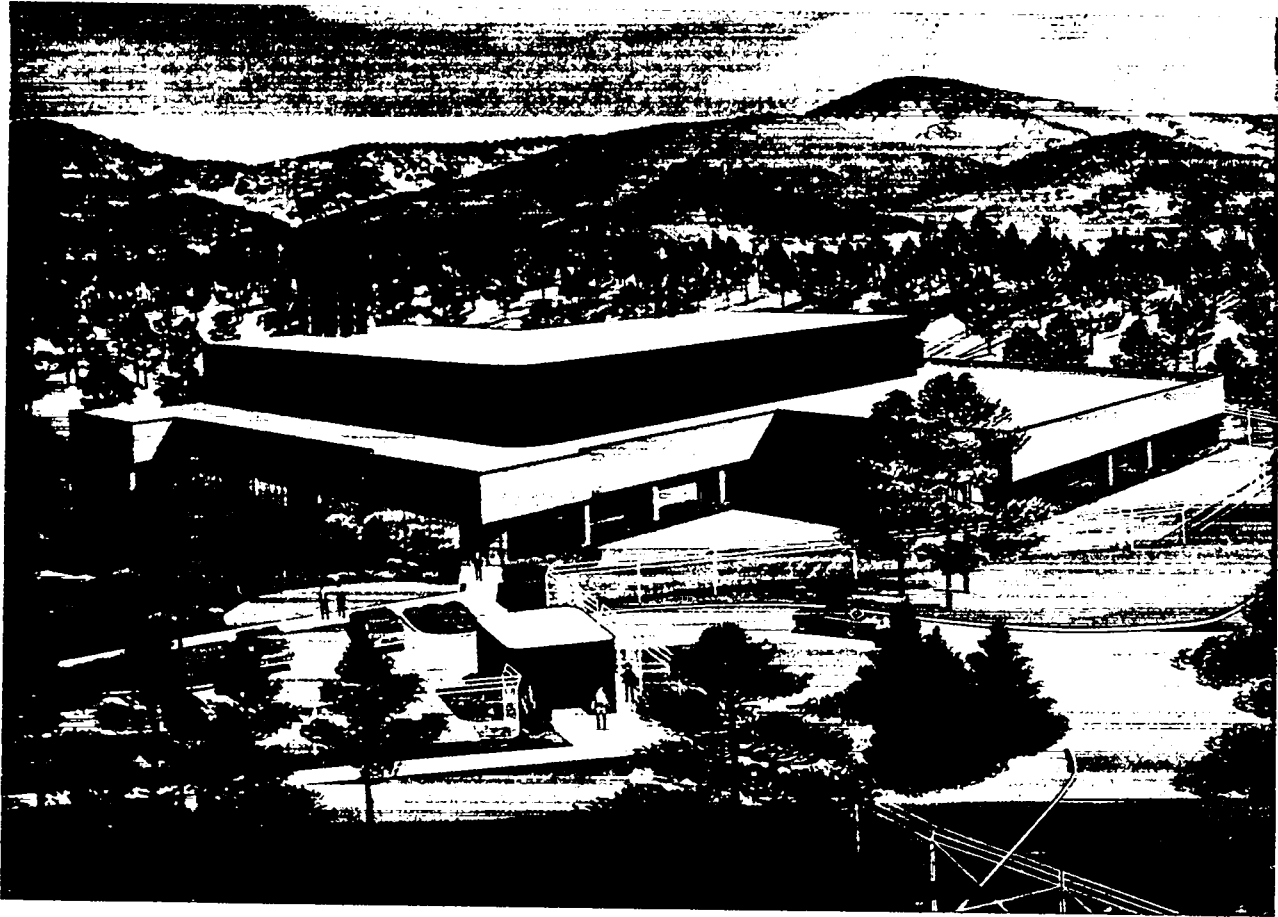
Fig. X-1. Artist's sketch of Target Fabrication Facility.

XI. PATENTS, PUBLICATIONS, AND PRESENTATIONS

PATENTS

Serial numbers, filing dates, patent numbers, and issue dates may not be known for several months after they are assigned. Therefore, for any given period, cases may be missing from these listings if patent activity occurred later in the reporting period.

The following applications were filed in the U.S. Patent Office.

S.N. 226,575 — "Segmented Pyroelectric Detector," Suzanne C. Stotlar and Edward J. McLellan.

S.N. 233,530 — "Single Electron Beam RF Feedback Free Electron Laser," Charles A. Brau, Stephen D. Rockwood, and William E. Stein.

S.N. 242,807 — "Method of Forming Metallic Coatings on Polymeric Substrates and of Forming Graded Polymeric Coatings or Films," Raimond Liepins.

S.N. 271,141 — "Combination Free Electron and Gaseous Laser," Charles A. Brau, Stephen D. Rockwood, and William E. Stein.

S.N. 274,917 — "Method and Apparatus for Fast Linear Pulse Detection Using Gaseous Plasmas," Edward J. McLellan and John A. Webb.

S.N. 275,478 — "Free Electron Laser Using RF Coupled Accelerating and Decelerating Structures," Charles A. Brau, Donald A. Swenson, and Thomas J. Boyd, Jr.

S.N. 284,151 — "Plasma Channel Optical Pumping Device and Method," O'Dean P. Judd.

S.N. 293,910 — "Intense Transient Magnetic Field Generation by Laser-Plasma," Robert F. Benjamin.

S.N. 293,912 — "Microscope and Method of Use," Wayne L. Bongianni.

S.N. 294,601 — "Reinjection Laser Oscillator and Method," Edward J. McLellan.

S.N. 297,477 — "Method and Use for Producing Cryogenic Targets," James T. Murphy and John Miller.

The following patents were issued by the U.S. Patent Office.

U.S. Pat. 4,243,888 — "Laser Beam Alignment Apparatus and Method," Charles R. Gruhn and Robert B. Hammond.

U.S. Pat. 4,264,868 — "High Power Gas Laser Amplifier," Wallace T. Leland and Thomas F. Stratton.

U.S. Pat. 4,265,982 — "Coated Woven Materials and Method of Preparation," William J. McCreary and David W. Carroll.

U.S. Pat. 4,266,506 — "Apparatus for Producing Cryogenic Inertially Driven Fusion Targets," John R. Miller.

U.S. Pat. 4,277,305 — "Beam Heated Linear Theta-Pinch Device for Producing Hot Plasmas," Ihor O. Bohachevsky.

PUBLICATIONS

This list of publications is prepared from a stored computer data base.

Target Fabrication

A. Young and D. Moreno, "Low Density Microcellular Plastic Foams," in "Particle Beam Fusion Progress Report, January—June, 1980," Sandia National Laboratories report SAND-80-2500 (May 1981).

S. M. Butler and M. H. Thomas, "Glass-Sealed Laser Fusion Targets Containing Gas Not Permeable Through the Wall," J. Vac. Technol. 18, 1291 (1981).

R. Liepins, M. Campbell, J. S. Clements, J. Hammond, and R. Jay Fries, "Plastic Coating of Microsphere Substrates," J. Vac. Technol. 18, 1218 (1981).

W. L. Bongianni, "Acoustic Microscopy for ICF Target Analysis," J. Vac. Technol. 18, 1214 (1981).

J. V. Milewski and R. G. Marsters, "Tensile Testing of Glass Microshells," J. Vac. Technol. 18, 1279 (1981).

J. K. Feuerherd and E. J. Farnum, "Micromachining of Laser Fusion Target Parts," J. Vac. Technol. 18, 1284 (1981).

J. T. Murphy and J. R. Miller, "Improved IF Cryogenic-Target Production Technique," J. Vac. Technol. 18, 1286 (1981).

E. H. Farnum, A. H. Gutacker, and R. Mulford, "A Cleaning Procedure for Inertial Fusion Targets," J. Vac. Technol. 18, 1195 (1981).

Theory

J. R. Ackerhalt, H. W. Galbraith, and J. C. Goldstein, "Self-Focusing in Sulfur Hexafluoride," Opt. Lett. 6, 377 (1981).

I. O. Bohachevsky, J. C. Goldstein, and D. O. Dickman, "Plasma Behavior in Magnetically Protected Inertial Confinement Fusion Reaction Cavities," Nucl. Technol. 1, 390-401 (1981).

J. C. Comly, Jr., W. T. Leland, C. J. Elliott, M. J. Kircher, and E. T. Salesky, "Discharge and Kinetics Modeling in Electron-Beam-Controlled CO_2 Laser Amplifiers," IEEE J. Quantum Electron. QE-17, 1786-1799 (1981).

R. A. Fisher, B. R. Suydam, and B. J. Feldman, "Transient Analysis of Kerr-Like Phase Conjugators Using Frequency-Domain Techniques," Phys. Rev. A 23, 3071 (1981).

J. C. Goldstein, S. J. Czuchlewski, and A. V. Nowak, "Saturation of Hot CO_2 by Short 10.6 μm Laser Pulses," IEEE J. Quantum Electron. QE-17, 1299-1302 (1981).

A. M. Hunter and R. O. Hunter, "Bi-Directional Amplification with Nonsaturable Absorption and Amplified Spontaneous Emission," IEEE J. Quantum Electron. QE-17, 1879-87 (1981).

J. M. Kindel and E. L. Lindman, Jr., "Target Designs for Energetic Ions," Nucl. Fusion 19, 597 (1979).

R. J. Mason, "Apparent and Real Thermal Inhibition in Laser Produced Plasmas," Phys. Rev. Lett. 47, 652-656 (1981).

B. E. Newnam, K. L. Hohla, R. W. Warren, and J. C. Goldstein, "Optical Diagnostics for the Los Alamos Free-Electron Laser Amplifier Experiment," IEEE J. Quantum Electron. QE-17, 1480-7 (1981).

A. J. Scannapieco, "ORBEOS - A Spherical, Fully Multi-Dimensional Flux-Corrected Transport Hydrodynamics Code," Los Alamos National Laboratory report LA-8908-MS (July 1981).

Experiments and Diagnostics

L. A. Jones and B. A. Hammel, "Radiation from a High Temperature Plasma Seeded with High-Z Elements," in *FY 81 Chemical Sciences Summary Book* (US Department of Energy, Washington, D.C., 1981).

D. E. Casperson and D. W. Forslund, "Stimulated Backscatter Measurements on Helios Using a Double-Pulse Technique," Proc. Los Alamos Conf. on Optics '81, Santa Fe, New Mexico, April 6-10, 1981, D. L. Liebenberg, Ed., SPIE Vol. 288 (1981).

L. A. Jones, B. A. Hammel, and S. Singer, "Radiation from a High Temperature Plasma Seeded with High-Z Elements," Proc. Atomic Physics Program Contractor's Workshop, Argonne National Laboratory, Argonne, Illinois, April 1-2, 1981 (US Department of Energy, Washington, D.C., 1981).

D. E. Casperson, "Optical Diagnostics of CO_2 Laser Fusion Targets Using Backscattered Light," Proc. Los Alamos Conf. Opt. '81, Santa Fe, New Mexico, April 6-10, 1981, D. H. Liebenberg, Ed., SPIE Vol. 288 (1981).

J. D. Seagrave, C. W. Woods, and L. A. Jones, "Position Diagnostics for a Magnetic-Pinch Imploding-Cylinder X-Ray Generator," Proc. Los Alamos Conf. Opt. '81, Santa Fe, New Mexico, April 6-10, 1981, D. H. Liebenberg, Ed., SPIE Vol. 288 (1981).

L. A. Jones, K. H. Finken, A. Dangor, E. Kallne, S. Singer, I. Lindemuth, J. Brownell, and T. Oliphant, "A Laser Initiated, Gas Embedded Z-Pinch: Experiment and Computation," Appl. Phys. Lett. 38 (7), 522 (1981).

M. D. Montgomery, J. V. Parker, K. B. Riepe, and R. L. Sheffield, "Heating of a Dense Plasma Using an Intense, Relativistic Electron Beam," Appl. Phys. Lett. 39, 217-219 (1981).

A. V. Nowak and D. O. Ham, "Self-Focusing of 10 μm Laser Pulses in SF_6," Opt. Lett. 6, 186-187 (1981).

R. F. Haglund, A. V. Nowak, and S. J. Czuchlewski, "Gaseous Saturable Absorbers for the Helios CO_2 Laser System," IEEE J. Quantum Electron. QE-17, 1799-1808 (1981).

L. H. Greene, A. J. Sievers, and J. F. Figueira, "Nonlinear Optical Properties of Matrix Isolated SF_6," IEEE J. Quantum Electron. QE-17, 446 (1981).

R. L. Carman, D. W. Forslund, and J. M. Kindel, "Visible Harmonic Emission as a Way of Measuring Profile Steepening," Phys. Rev. Lett. 46, 29-32 (1981).

R. P. Godwin, "Experiments Fundamental to Laser-Initiated Fusion," Electro-Opt. Syst. Des. 13, 25 (1981).

P. Lee, D. B. van Hulsteyn, A. Hauer, and S. Whitehill, "Low-Energy X-ray Imaging of Laser Plasmas," Opt. Lett. 6, 196-197 (1981).

T. H. Tan, G. H. McCall, R. Kopp, T. Ganley, D. van Hulsteyn, A. Hauer, A. Williams, K. Mitchell, J. S. Ladish, D. Giovanielli, E. Linnebur, and R. J. Fries, "CO_2 Laser-Driven High-Density Implosion Experiments," Phys. Fluids 24, 754-758 (1981).

A. Hauer, W. Priedhorsky, and D. B. van Hulsteyn, "Shell Satellite Lines in CO_2 Laser-Produced Plasmas," Appl. Opt. 20, 3477 (1981).

M. A. Yates, "Development of a Radiochemical Target Density Diagnostic for the Los Alamos Inertial Fusion Program," Los Alamos National Laboratory report LA-9097-MS (December 1981).

W. A. Reupke and H. S. Cullingford, "A Comparison of Wetted Wall and Magnetically Protected Wall ICF Hybrid Concepts," Proc. Topical Meet. Technol. Controlled Nucl. Fusion, ANS, 4th, CONF-801011, Vol. II (US Department of Energy, Washington, D.C., 1981), pp. 1555-1568.

J. G. Freiwald, J. H. Pendergrass, and T. G. Frank, "Environmental and Safety Envelope Analysis for Inertial Fusion Applications," Proc. Topical Meet. Technol. Controlled Nucl. Fusion, ANS, 4th, CONF-801011, Vol. II (U.S. Department of Energy, Washington, D.C., 1981), pp. 1257-1264.

T. G. Frank and C. E. Rossi, "Technology Requirements for Commercial Applications of Inertial Fusion," Nucl. Technol. Fusion 1, 359-376 (1981).

M. J. Monsler, J. Hovingh, D. L. Cook, T. G. Frank, and G. A. Moses, "An Overview of Inertial Fusion Reactor Design," Nucl. Technol. Fusion 1, 302-358 (1981).

I. O. Bohachevsky, "Models and Analyses for ICF Reactor Studies," Los Alamos National Laboratory report LA-8557 (May 1981).

J. H. Pendergrass, T. G. Frank, and I. O. Bohachevsky, "A Modified Wetted-Wall Inertial Fusion Reactor Concept," Proc. Topical Meet. Technol. Controlled Nucl. Fusion, ANS, 4th, CONF-801011, Vol. II (US Department of Energy, Washington, D.C., 1981), p. 1131.

S. Singer, C. James Elliott, J. F. Figueira, I. Liberman, J. V. Parker, and G. T. Schappert, "High Power, Short Pulse CO_2 Laser Systems for Inertial-Confinement Fusion," in Developments in High-Power Lasers and Their Applications (LXXIV Corso Soc. Ital. Fis., Bologna, Italy, 1981).

Laser Development

S. J. Czuchlewski, "Pulse Propagation in a One-Atmosphere CO_2 Laser Amplifier," Proc. 1980 Int. Laser Conf., New Orleans, Louisiana, December 14-18, 1980, C. B. Collins, Ed. (STS Press, McLean, Virginia, 1981), pp. 496-502.

J. C. Goldstein, S. J. Czuchlewski, and A. V. Nowak, "Saturation of Hot CO_2 at 10.6 μm," Proc. 1980 Int. Laser Conf., New Orleans, Louisiana, December 14-18, 1980, C. B. Collins, Ed. (STS Press, McLean, Virginia, 1981), pp. 623-626.

J. C. Goldstein, R. F. Haglund, Jr., and J. C. Comly, Jr., "Small Signal Gain Spectrum of an 1800 Torr CO_2 Amplifier," Proc. Los Alamos Conf. Opt. '81, Santa Fe, New Mexico, April 6-10, 1981, D. H. Liebenberg, Ed., SPIE Vol. 288 (1981).

R. F. Haglund, Jr., "Temporal Shaping of Nanosecond CO_2 Laser Pulses in Multiphoton Saturable Absorbers," Proc. Los Alamos Conf. Opt. '81, Santa Fe, New Mexico, April 6-10, 1981, D. H. Liebenberg, Ed., SPIE Vol. 288 (1981).

G. A. Kyrala, "Out-of-Focus Intensity Distribution: Effects of Focal Number and Aberration," Proc. Los Alamos Conf. Opt. '81, Santa Fe, New Mexico, April 6-10, 1981, D. H. Liebenberg, Ed., SPIE Vol. 288 (1981).

P. B. Lyons, "Time Resolved X-Ray Diagnostics," AIP Conf. Proc. (American Institute of Physics, New York, 1981), No. 75, pp. 59-65.

R. H. Day, "Photoemission Measurements for Low Energy X-Ray Detector Applications," AIP Conf. Proc. (American Institute of Physics, New York, 1981), No. 75, pp. 44-58.

W. Priedhorsky, "Epoxy Replication for Wolter X-Ray Microscope Fabrication," AIP Conf. Proc. (American Institute of Physics, New York, 1981), pp. 332-333.

R. H. Day, P. Lee, E. Saloman, and D. Nagel, "Photoelectric Quantum Efficiencies and Filter Window Absorption Coefficients From 20 eV to 10 keV," J. Appl. Phys. 52, 6965 (1981).

P. Rockett, D. van Hulsteyn, and W. Priedhorsky, "Hard X-Ray Imaging of Laser-Plasmas Using Medical Technology," Appl. Opt. 20, No. 21, 3704 (1981).

W. Priedhorsky, D. Lier, R. Day, and D. Gerke, "Hard X-Ray Measurements of 10.6 μm Laser Irradiated Targets," Phys. Rev. C 47, No. 23, 1661 (1981).

P. Lee, "X-Ray Diffraction in Multilayers," Opt. Commun. 37, No. 3, 159 (1981).

J. V. Parker, "Passive Retropulse Protection Through Enhanced Optical Breakdown," Proc. Los Alamos Conf. Opt. '81, Santa Fe, New Mexico, April 6-10, 1981, D. H. Liebenberg, Ed., SPIE Vol. 288 (1981).

C. W. Woods, R. F. Alexander, and C. R. Collins, "Design and Construction of a Short Pulse Front End for a Large CO_2 Laser," Proc. Los Alamos Conf. Opt. '81, Santa Fe, New Mexico, April 6-10, 1981, D. H. Liebenberg, Ed., SPIE Vol. 288 (1981).

J. F. Figueira, S. J. Czuchlewski, C. R. Phipps, and S. J. Thomas, "Plasma-Breakdown Retropulse Isolators for the Infrared," Appl. Opt. 20, 838-841 (1981).

S. J. Czuchlewski and J. F. Figueira, "Threshold Conditions for Laser-Initiated Plasma Shutters," Appl. Phys. Lett. 38, 325-327 (1981).

R. L. Carlson, J. P. Carpenter, D. E. Casperson, R. B. Gibson, R. P. Godwin, R. F. Haglund, Jr., J. A. Hanlon, E. L. Jolly, and T. F. Stratton, "Helios: A 15 TW Carbon Dioxide Laser-Fusion Facility," IEEE J. Quantum Electron. QE-17, 1662-1678 (1981).

R. B. Gibson, M. J. Kircher, C. E. Knapp, W. T. Leland, R. Sierra, and G. W. York, "Inversion Recovery Following Saturated Extraction in E-Beam-Controlled CO_2 Amplifiers," IEEE J. Quantum Electron. QE-17, 32 (1981).

K. B. Riepe, L. L. Barrone, K. J. Bickford, and G. H. Livermore, "Antares Prototype 300-kJ, 250-kA Marx Generator-Final Report," Los Alamos National Laboratory report LA-8491 (January 1981).

A. W. Ehler, J. Kephart, S. Gitomer, R. Goldman, F. Begay, T. H. Tan, A. Williams, D. van Hulsteyn, S. Pederson, J. Hayden, and J. Sollid, "Measurement of Fast Ion Energy from CO_2 Laser Heated Targets," Bull. Am. Phys. Soc. 26, 935 (1981).

J. Kephart, A. W. Ehler, S. Gitomer, R. Goldman, F. Begay, T. Tan, A. Williams, D. van Hulsteyn, S. Pederson, J. Hayden, and J. Sollid, "Comparison of the Angular Distribution of Ions Emitted from Laser Heated Targets," Bull. Am. Phys. Soc. 26, 934 (1981).

A. J. Kozubal, "Decision Graphs: A Tool for Developing Real-Time Software," in *Engineering Software II*, R. A. Adey, Ed., Proc. 2nd Int. Conf. Eng. Software, Imperial College of Science and Technology, London, England, March 24-26, 1981 (CML Publications Ltd., Southhampton, Great Britian, 1981), pp. 91-96.

J. E. Sollid and C. W. Bjork, "Calorimetry at 10.6 μm Using Organic Volume Absorbers," Proc. Soc. Phot-Opt. Instrum. Eng. 288, 476-483 (1981).

J. E. Sollid, C. W. Bjork, and S. Levings, "Calorimetry at 10.6 μm Using BeO as an Absorber," Opt. News 7, 73 (1981).

B. J. Feldman, R. A. Fisher, and S. L. Shapiro, "Ultraviolet Phase Conjugation," Opt. Lett. 6, 84 (1981).

I. J. Bigio and M. Slatkine, "Attainment of the Theoretical Minimum Input Power for Injection-Locking of an Unstable Resonator KrF Laser," Opt. Lett. 6, 336 (1981).

I. J. Bigio, B. J. Feldman, R. A. Fisher, and M. Slatkine, "Phase Conjugation and Image-Retaining Reflection of KrF Laser Radiation at 2486 Å," IEEE J. Quantum Electron. QE-17, 220 (1981).

M. Slatkine and I. J. Bigio, "Demonstration of Ultra-Low Injected Power for Locking a High Power Unstable KrF Resonator," IEEE J. Quantum Electron. QE-17, 228 (1981).

PRESENTATIONS

Target Fabrication

The following presentations were made at the American Vacuum Society 28th Annual Symposium, Anaheim, California, November 2-6, 1981.

N. Elliott, W. Anderson, T. Archuleta, and D. Stupin, "Thin Film Measurement Using X-Ray Peak Ratioing."

W. L. Bongianni, "Beam Profile Measurements on the Magnetoelastic Microscope."

D. E. Cooper, "Phase Modulation Interferometer for ICF Target Characteristics."

B. Jorgensen, "A Technique for Calculating DT Content in Glass Microballoons From X-Ray Counts."

D. M. Stupin, K. R. Moore, G. D. Thomas, and R. Whitman, "Automated Computer Analysis of X-Ray Radiographs Greatly Facilitates Measurements of Coating Thickness."

A. T. Young, D. K. Moreno, R. G. Marsters, "Preparation of Multishell Target Plastic Foam Cushion Material by Thermally Induced Phase Inversion Processes."

J. T. Murphy, "Experimental Evidence in Support of David A. Glocker's Multi-Shell Cryogenic Laser Fusion Target Using Superconducting Levitation."

L. R. Foreman, "Novel Cryogenic Target for Laser Fusion."

D. M. Stupin and G. H. Stokes, "It May Be Possible to Detect Coating Thickness Variations as Small as 0.1% in Laser Fusion Targets."

In addition, the following presentations were given at various institutions.

A. T. Young, "New, Low Density, Microcellular Foams for ICF Target Cushions," Lawrence Livermore National Laboratory, Livermore, California, February 20, 1981.

E. H. Farnum, "Fabrication Techniques for Laser Fusion Targets," Colloquium on ICF Target Fabrication, Argonne National Laboratory, Argonne, Illinois, March 20, 1981.

A. T. Young, "A Phase Inversion Process for the Preparation of Plastic Foams for ICF Targets," KMS Fusion Corporation, Ann Arbor, Michigan, April 3, 1981.

E. H. Farnum, classified talk, Las Vegas, Nevada, May 7, 1981.

R. Jay Fries, "The Use of Low-Pressure-Plasma Polymerization in the Fabrication of Targets for Inertial Confinement Fusion," 11th Symposium on Plasma Chemistry, Osaka, Japan, June 12, 1981.

E. H. Farnum, J. K. Feuerherd, S. Pederson, M. H. Thomas, and P. Gobby, "Materials in ICF Targets; How Materials Choice Affects Target Assembly Technique," ICF Topical Conference in Seattle, Washington, August 11-13, 1981.

A. T. Young, M. C. Lee, I-An Feng, D. D. Elleman, and T. Wang, "Polymer Coating of Glass Microballoons Levitated in a Focused Acoustic Field," Materials Research Society Symposium, Boston, Massachusetts, November 16, 1981.

Theory

The following presentations were made at the American Physics Society Annual Meeting of the Plasma Physics Division, New York, New York, October 12-16, 1981.

R. F. Benjamin and E. L. Lindman, "Magnetic Control of Laser-Produced Hot Electrons."

J. U. Brackbill, "New Developments in Modeling Nonlinear, Low Frequency Plasma Physics Phenomena."

J. U. Brackbill and D. W. Forslund, "Nonlinear Evolution of Low Frequency Plasma Instabilities."

C. W. Cranfill, C. H. Aldrich, and D. W. Forslund, "General Self-similar Description of Fast-ion Blowoff from Laser-heated Targets."

C. J. Elliott, "Optical Mode Quality in a Free-electron Laser."

D. W. Forslund and J. U. Brackbill, "Magnetic Field Enhanced Lateral Transport."

S. R. Goldman, D. C. Wilson, R. H. Day, A. Hauer, W. C. Priedhorsky, and P. D. Rockett, "Computer Simulation of Laser-irradiated Microballoons with Thicknesses both Large and Small Compared to the Superthermal Range."

W. P. Gula, "A Study of the Effects of Non-spherically Symmetric Ion Beam Deposition on Spherically Symmetric Targets."

K. Lee, J. U. Brackbill, D. W. Forslund, and K. B. Quest, "Dissipation of Reflected Ion Beams from Quasi-Perpendicular Shocks Due to Electromagnetic Ion-cyclotron Instability."

R. D. Jones, "Heating and Transport of a High Z Plasma in the Presence of an Intense Laser Field."

J. M. Kindel, "Implications of Current CO_2 Experiments for Target Design."

K. B. Quest, J. U. Brackbill, D. W. Forslund, and K. Lee, "Anisotropy Driven Instabilities Downstream of a Parallel Shock."

R. J. Mason, "Suprathermal Electron Coupling For Thin Foils."

H. M. Ruppel and J. U. Brackbill, "An Adaptively Zoned Particle in Cell Method for Multi-Material Problems."

E. K. Stover, D. C. Wilson, J. Mack, D. van Hulsteyn, G. McCall, and A. Hauer, "Enhanced Energy Deposition Symmetry by Suprathermal Electron Transport."

T. H. Tan, C. Barnes, R. Benjamin, A. W. Ehler, G. Schappert, A. Williams, and D. van Hulsteyn, "Vacuum Insulation Experiments From CO_2 Laser Irradiated Targets."

D. C. Wilson, S. R. Goldman, R. H. Day, W. C. Priedhorsky, P. D. Rockett, and A. Hauer, "Numerical Modeling of X-ray Emission from 10.6 Micron Laser-Irradiated High Z Shells."

M. A. Yates, J. Kephart, R. Robertson, F. Begay, T. H. Tan, A. W. Ehler, A. Williams, K. Wilson, D. van Hulsteyn, R. Benjamin, S. Pederson, J. Hayden, and C. Barnes, "Ion Emission From CO_2 Laser Irradiated Vacuum Insulation Targets."

The following presentations were made at the American Geophysical Union Spring Meeting, Baltimore, Maryland, May 25-29, 1981.

C. Barnes, "Double Layers and Ion-cyclotron Waves."

D. W. Forslund and J. U. Brackbill, "Lower Hybrid Drift Instability in Self-consistent Density Gradients."

K. Lee, J. U. Brackbill, D. W. Forslund, and K. B. Quest, "Dissipation of Reflected Ion Beams From Quasi-perpendicular Shocks Due to Electromagnetic Ion-cyclotron Instability."

K. B. Quest, K. Lee, D. W. Forslund, and J. U. Brackbill, "Angular Wavenumber Spectrum of the Finite-Larmor-Radius Firehose Instability."

The following presentations were made at the 1981 IEEE International Conference on Plasma Science, Santa Fe, New Mexico, May 18-20, 1981.

D. E. Casperson and D. W. Forslund, "Stimulated Backscatter Measurements on Helios Using a Double-pulse Technique."

C. J. Elliott, "Ergodic Behavior of Pendulum Motion as in a Free Electron Laser."

D. W. Forslund and J. C. Comly, Jr., "Analytic Formulae for Stopping Power of One Dimensional Electron Distributions in High Z Material."

R. J. Mason, "Apparent and Real Thermal Inhibition in Laser Produced Plasmas."

A. J. Scannapieco, "The Stability of Planetary Type Waves in Laser Fusion Targets."

The following presentations were made at the 11th Annual Anomalous Absorption Conference, Université du Quebec, Montreal, Quebec, Canada, June 2-5, 1981.

R. J. Mason, "Thermal Transport Inhibition in Laser Produced Plasmas."

F. Begay, D. W. Forslund, and D. E. Casperson, "Observation of a Two Component High Energy Electron Distribution in Double-pulsed CO_2 Laser-induced Plasmas."

The following presentations were made at the Topical Conference on Symmetry Aspects of Inertial Fusion Implosions, Naval Research Laboratory, Washington, D.C., May 27-28, 1981.

D. C. Wilson, J. M. Mack, E. K. Stover, D. van Hulsteyn, G. H. McCall, and A. Hauer, "Enhanced Energy Deposition Symmetry by Hot Electron Transport."

G. S. Fraley, "Rayleigh-Taylor Stability for a Shock Wave-Density Discontinuity Interaction."

The following presentations were made at the Conference on Lasers and Electro-Optics '81, Washington, D.C., June 10-12, 1981.

J. R. Ackerhalt, H. W. Galbraith, and J. C. Goldstein, "Self-Focusing in SF_6."

I. J. Bigio, J. C. Goldstein, and M. Slatkine, "Mode Development in Injection-locked Unstable Resonators with Short-gain Duration Excimer Media."

J. C. Goldstein, R. F. Haglund, Jr., and J. C. Comly, Jr., "Small-signal Gain Spectrum of an 1800 Torr CO_2 Amplifier."

In addition, the following presentations were made at various institutions.

C. J. Elliott, R. G. Bjurstrom, J. P. Carpenter, E. L. Coffelt, J. J. Hayden, D. E. Hebron, J. McLeod, and V. Romero, "In-situ Optical Breakdown - Studies for a Large CO_2 Laser Amplifier," Proc. Los Alamos Conf. Optics, Santa Fe, New Mexico, April 6-10, 1981, D. H. Liebenberg, Ed., SPIE Vol. 288 (1981).

D. W. Forslund, "Large Scale Simulation Requirements for Inertial Fusion," 1981 Workshop on High-Speed Computing Architecture and Large Scale Calculations, Gleneden Beach, Oregon, March 30-April 2, 1981.

D. W. Forslund and J. U. Brackbill, "New Multi-dimensional Electromagnetic Plasma Simulation Methods and Applications," 20th General Assembly of the International Union of Radio Science, Washington, D.C., August 10-18, 1981.

J. C. Goldstein and W. B. Colson, "Pulse Propagation in Tapered Wiggler Free Electron Lasers," International Conference on Lasers, New Orleans, Louisiana, December 14-18, 1981.

J. C. Goldstein, "Chirped Pulses in Tapered - Wiggler Free Electron Laser Oscillators," 1981 IEEE International Conference on Infrared and Millimeter Waves, Miami, Florida, December 7-12, 1981.

W. P. Gula and G. R. Magelssen, "Scaling Laws for Simple Heavy Ion Targets," Fourth International Topical Conference on High Power Electron and Ion Beam Research and Technology, École Polytechnique, Palaiseau, France, June 23-July 3, 1981.

J. M. Kindel, B. Bezzerides, D. W. Forslund, R. S. Goldman, R. D. Jones, E. K. Stover, and D. C. Wilson, "Theoretical Understanding of Carbon Dioxide Interaction Experiments," 10th European Conference on Controlled Fusion and Plasma Physics, Moscow, USSR, September 14-19, 1981.

R. J. Mason, "Suprathermal Electron Transport in Laser Produced Plasmas," Proc. ANS/ENS International Topical Meeting on Advances in Mathematical Methods for Nuclear Engineering Problems, Munich, West Germany, April 27-29, 1981; presented colloquia on same subject at École Polytechnique and at Centre d' Etudes de Limeil, France, June 23-July 3, 1981; Max Planck Institut für Plasma Physik, Munich, and GSI, Darmstadt, in West Germany, and the Rutherford Laboratory and AWRE in Great Britian, May 6-9, 1981.

R. J. Mason, "Electron Transport in Laser Produced Plasmas," National Research Council of Canada, Ottawa, Canada, September 4, 1981.

R. J. Mason, "Prospects for Implicit Moment Simulation of Plasmas," Colloquium at Princeton University and Rutger's Statistical Mechanics Meeting, Princeton, New Jersey, December 17-18, 1981.

J. S. Saltzman and J. U. Brackbill, "Applications and Generalizations of Variational Methods for Generating Adaptive Meshes," Symposium on the Numerical Generation of Curvilinear Coordinate Systems and Use in the Numerical Solution of Partial Differential Equations, Nashville, Tennessee, April 13-16, 1981.

B. R. Suydam, R. A. Fisher, and B. J. Feldman, "Transient Phase Conjugation in a Sluggish Kerr Medium," Optical Society of America Annual Meeting, Orlando, Florida, October 26-30, 1981.

Experiments and Diagnostics

The following presentations were made at the American Physics Society Annual Meeting of the Plasma Physics Division, New York, New York, October 12-16, 1981.

A. Hauer, "Spectrograph Measurements of 50-1000 eV X-Radiation from Spherical Targets at Helios."

S. K. Wilson and F. Begay, "Analysis of Charged Particles Recorded in Dielectric Plastic Detectors."

M. M. Mueller, "Calculation of Electron Transmission Spectra for an Incident Continuum by Means of Fitting Data in Four Variables."

A. W. Ehler, J. Kephart, F. Begay, T. H. Tan, and A. Williams, "Measurements of Fast Ion Energy From CO_2 Laser Heated Targets."

A. W. Ehler, F. Begay, T. H. Tan, and A. Williams, "Comparison of the Angular Distribution of Ions Emitted from Laser Heated Targets."

B. A. Hammel, L. A. Jones, and K. C. Chambers, "The Z-Pinch of an Annular Gas Jet."

D. Kania, "Laser Heating of Aluminum Exploding Wire Plasma."

R. L. Sheffield and M. D. Montgomery, "Dense Plasma Heating Using an Intense Relativistic Electron Beam."

The following presentations were made at the IEEE International Conference on Plasma Physics, Santa Fe, New Mexico, May 18-20, 1981.

J. V. Parker, K. B. Riepe, M. D. Montgomery, and R. L. Sheffield, "Heating of a Dense Plasma by an Intense Relativistic Electron Beam."

C. W. Woods, J. D. Seagrave, and L. A. Jones, "Nitrogen Laser Arrays for Schlieren and Shadow Diagnostics of a Magnetic-Pinch Imploding-Cylinder X-Ray Generator."

B. A. Hammel, L. A. Jones, and M. Hamm, "The Z-Pinch of a Gas Jet."

In addition, the following presentations were made at various institutions.

R. L. Carman, "Influences on Target Irradiation Symmetry in CO_2 Laser-Fusion Experiments," Topical Conference on Symmetry Aspects of Inertial Fusion Implosions, Naval Research Laboratory, Washington, D.C., May 27-28, 1981.

A. Hauer, "Survey of Atomic Physics Issues in Experimental Inertial Confinement," International Conference on Physics Electron and Atomic Collisions, Gatlinburg, Tennessee, July 19-21, 1981.

R. L. Carman, "Nonlinear Optical Phenomena Occurring in CO_2 Laser Produced Plasmas," Gordon Conference on Nonlinear Optics and Lasers, Wolfeboro, New Hampshire, August 3-5, 1981.

T. H. Tan and A. H. Williams, "Use of Fiber Optics in the CO_2 Laser Fusion Environment," SPIE 25th International Symposium, San Diego, California, August 24-28, 1981.

J. F. Figueira and S. J. Thomas, "Generation of Surface Microstructure in Metals and Semiconductors by Short-Pulse CO_2 Lasers," XIIth International Quantum Electronics Conference, Munich, Germany, June 22-25, 1981.

J. F. Figueira, S. J. Thomas, P. B. Mumola, and D. C. Jordan, "Grazing Incidence Damage Thresholds of Metal Mirrors at 10 Micrometers," Conference on Lasers and Electro-Optics 1981, Washington, D.C., June 10-12, 1981.

J. F. Figueira, S. J. Thomas, and R. F. Harrison, "Damage Thresholds to Metal Mirrors by Short Pulse CO_2 Laser Radiation," Laser Damage in Optical Materials—1981, National Bureau of Standards, Boulder, Colorado, November 17-18, 1981.

R. L. Carman and R. F. Benjamin, "Self-Focusing and High Harmonics Production in CO_2 Laser-Produced Plasmas," 11th Annual Anomalous Absorption Conference, Université du Quebec, Montreal, Quebec, Canada, June 2-5, 1981.

J. F. Figueira, S. J. Thomas, and R. F. Harrison, "Generation of Microstructure with Short-Pulse CO_2 Lasers," Optical Society of America 1981 Annual Meeting, Orlando, Florida, October 26-30, 1981.

System Studies

The following presentations were made at various institutions.

M. D. Thomason and B. J. Feldman, "Laser Double Resonance Determination of Rapid Vibrational and Rotational Energy Transfer Rates in CO_2," 34th Gaseous Electronics Conference, Boston, Massachusetts, October 20-23, 1981.

I. O. Bohachevsky and R. N. Kostoff, "First Wall and Blanket Stresses Induced by Cyclic Fusion Core Operations," 9th Symposium on Engineering Problems of Fusion Research, Chicago, Illinois, October 26-29, 1981.

T. G. Frank, J. H. Pendergrass, D. L. Cook, and J. H. Pitts, "Power Plant Design for Inertial Confinement Fusion—Implications for Pellets," American Vacuum Society 28th National Symposium, Anaheim, California, November 2-6, 1981.

J. H. Pendergrass and T. G. Frank, "Inertial Fusion Commercial Applications Economic Studies," American Nuclear Society 1981 Annual Meeting, Miami, Florida, June 7-11, 1981, Trans. Am. Nucl. Soc. 38, 228 (1981).

I. O. Bohachevsky and R. N. Kostoff, "Cyclic Thermal Stresses in Fusion Reactors," 3rd International Atomic Energy Agency Committee Meeting and Workshop on Fusion Reactor Design and Technology, Tokyo, Japan, October 5-16, 1981.

Laser Development

The following presentations were made at the Los Alamos Conference on Optics '81, Santa Fe, New Mexico, April 6-10, 1981.

W. Bauke, A. C. Saxman, and N. O'Kay, "Optical Tooling for Antares."

J. P. Carpenter, R. G. Bjurstrom, E. L. Coffelt, C. J. Elliott, and J. J. Hayden, "In Situ Optical Breakdown Studies of a Large CO_2 Laser Amplifier."

R. Day, V. K. Viswanathan, A. C. Saxman, R. E. Lujan, G. Woodfin, and W. C. Sweatt, "Antares Alignment Gimbal Positioner."

B. J. Feldman, R. A. Fisher, and S. L. Shapiro, "Ultraviolet Phase Conjugation."

T. Swann, C. Combs, and J. Witt, "Opto-Mechanical Devices for the Antares Automatic Beam Alignment System."

V. K. Viswanathan, I. Liberman, A. Gibbs, P. S. Bolen, and B. D. Seery, "High-Power Infrared Smartt Interferometer."

R. C. Smith, E. K. Hodson, and R. L. Carlson, "Multigigahertz Beam Diagnostics for Laser Fusion."

The following presentations were made at the Conference on Lasers and Electro-Optics, Washington, D.C., June 10-12, 1981.

R. Gibson, R. Sierra, and G. York, "Double-Pulse Energy Extraction in an Electron-Beam Sustained Carbon Dioxide Laser Amplifier."

R. B. Gibson, M. J. Kircher, C. E. Knapp, W. T. Leland, R. Sierra, and G. W. York, "Inversion Recovery Following Saturated Extraction in E-Beam-Controlled CO_2 Amplifiers."

A. C. Saxman, "Analysis of a Multiplex Laser System Design Based Upon the Antares System."

I. J. Bigio, B. J. Feldman, R. A. Fisher, and M. Slatkine, "Phase Conjugation and Image-Retaining Reflection of KrF Laser Radiation at 2486 Å."

M. Slatkine and I. J. Bigio, "Demonstration of the Use of Ultra-low Injected Power for Locking a High-Power Unstable KrF Resonator."

The following presentations were made at the Gordon Conference on Nonlinear Optics and Lasers, Wolfeboro, New Hampshire, August 3-5, 1981.

I. J. Bigio and M. Slatkine, "Injection Locking of Excimer Lasers."

B. J. Feldman, R. A. Fisher, S. L. Shapiro, I. J. Bigio, and M. Slatkine, "Ultraviolet Phase Conjugation."

B. J. Feldman, M. Slatkine, and I. J. Bigio, "Ultraviolet Phase Conjugation."

B. J. Feldman, "Stimulated Scattering Processes in the Ultraviolet and Implications in Phase Conjugation."

The following presentations were made at the American Vacuum Society 28th National Symposium, Anaheim, California, November 2-6, 1981.

N. G. Wilson, R. H. Swinderman, J. W. Allen, and C. R. Winkelman, "Vacuum System and Target Chamber for the Antares High-Energy Gas Laser Facility."

N. G. Wilson and C. R. Winkelman, "Vacuum and Gas Systems for the Antares High-Energy Laser Facility CO_2 Power Amplifier."

C. R. Winkelman and P. J. Flemming, "The Antares Laser Fusion Vacuum System."

The following presentations were made at the National Bureau of Standards Workshop on Measurement of Electrical Quantities in Pulse Power Systems, Boulder, Colorado, March 2-4, 1981.

W. R. Scarlett, "Measurement of Electrical Quantities in Pulse Power Systems."

M. E. Thuot and W. R. Scarlett, "A Fiber Optic Monitoring System for Antares Pulse Power System."

The following presentations were made at the American Physics Society Annual Meeting of the Plasma Physics Division, New York, New York, October 12-16, 1981.

F. Begay, W. Priedhorsky, A. Hauer, and P. Rockett, "Observation of High Energy Electron Distribution in CO_2 Laser-Produced Plasmas."

S. J. Czuchlewski, T. Sheheen, J. Hyde, and R. Ainsworth, "Vacuum Plasma Isolator for High-Power 10-μm Lasers."

P. Lee and K. Mitchell, "Soft X-Ray Emission From Laser Produced Plasmas."

W. Priedhorsky and E. Stover, "Bremsstrahlung Measurements of Hot Electron Penetration into CO_2 Laser Targets."

The following presentations were made at the 1981 International Conference on Lasers, New Orleans, Louisiana, December 14-18, 1981.

I. J. Bigio and M. Slatkine, "Injection Locking of Excimer Lasers."

I. J. Bigio, B. J. Feldman, R. A. Fisher, S. L. Shapiro, and M. Slatkine, "Ultraviolet Phase Conjugation."

The following presentations were given at the SPIE 25th International Symposium, San Diego, California, August 24-28, 1981.

B. J. Feldman, R. A. Fisher, and C. R. Phipps, "Optical Phase Conjugation at Los Alamos."

J. L. Longmire and M. E. Thuot, "A Fiber Optic Analog and Timing Monitoring System for the Antares Laser Fusion Program."

V. K. Viswanathan, "Phase Aberrations and Beam Cleanup Techniques in Carbon-Dioxide Laser Fusion Systems."

V. K. Viswanathan, "Use of Zernike Polynomials and Interferometry in the Optical Design and Assembly of Large Carbon-Dioxide Laser Systems."

In addition, the following presentations were made at various institutions.

L. Burczyk, "A Simplified Extension of the Q-Bus for a High-Energy Laser Control Application," IEEE and University of New Mexico Conference on Systems and Circuits, Mini and Microcomputer Session, Albuquerque, New Mexico, February 25, 1981.

L. Burczyk, "A Simplified Extension of the LSI-11 Q-Bus for a High-Energy Laser Control Application," IEEE Conference, Circuits and Systems Proceedings, Albuquerque, New Mexico, June 30, 1981.

L. Burczyk, D. Call, R. Dingler, A. J. Kozubal, M. E. Thuot, and S. White, "The Antares Control Network," US Department of Energy Mini/Microcomputer Information Interchange Meeting, Sandia National Laboratories, Albuquerque, New Mexico, March 10-12, 1981.

R. Cutler, "An Alternative Way for Non Contacting Measurements of Long Radii Elements," Conference on Conical Element Metrology, Albuquerque, New Mexico, June 24-25, 1981.

R. Hammond, N. Paulter, A. Iverson, and R. Smith, "Sub-100 ps Bulk-Recombination-Limited InP:Fe Photoconductive Detector," International Electron Devices Meeting, Washington, D.C., December 8-10, 1981.

J. P. Hong and R. L. King, "Implementation of NCAR Graphics on UNIX using Pipes," 14th Hawaii International Conference on System Sciences, University of Hawaii, Honolulu, Hawaii, January 8-9, 1981.

C. R. Phipps, "Modern Applications of Nonlinear Optics," Department of Physics Seminar, University of Washington, Seattle, Washington (1981).

W. Priedhorsky, "Lead Stearate as a High Reflectivity Coating for X-Ray Optics," SPIE Program Committee on Soft X-Ray Optics, Brookhaven National Laboratory, Upton, New York, November 18-20, 1981.

M. Slatkine and I. J. Bigio, "Injection Locking an Unstable XeF Resonator with an Ar-ion Laser at 3511 Å," Optical Society of America Annual Meeting, Orlando, Florida, October 26-30, 1981.
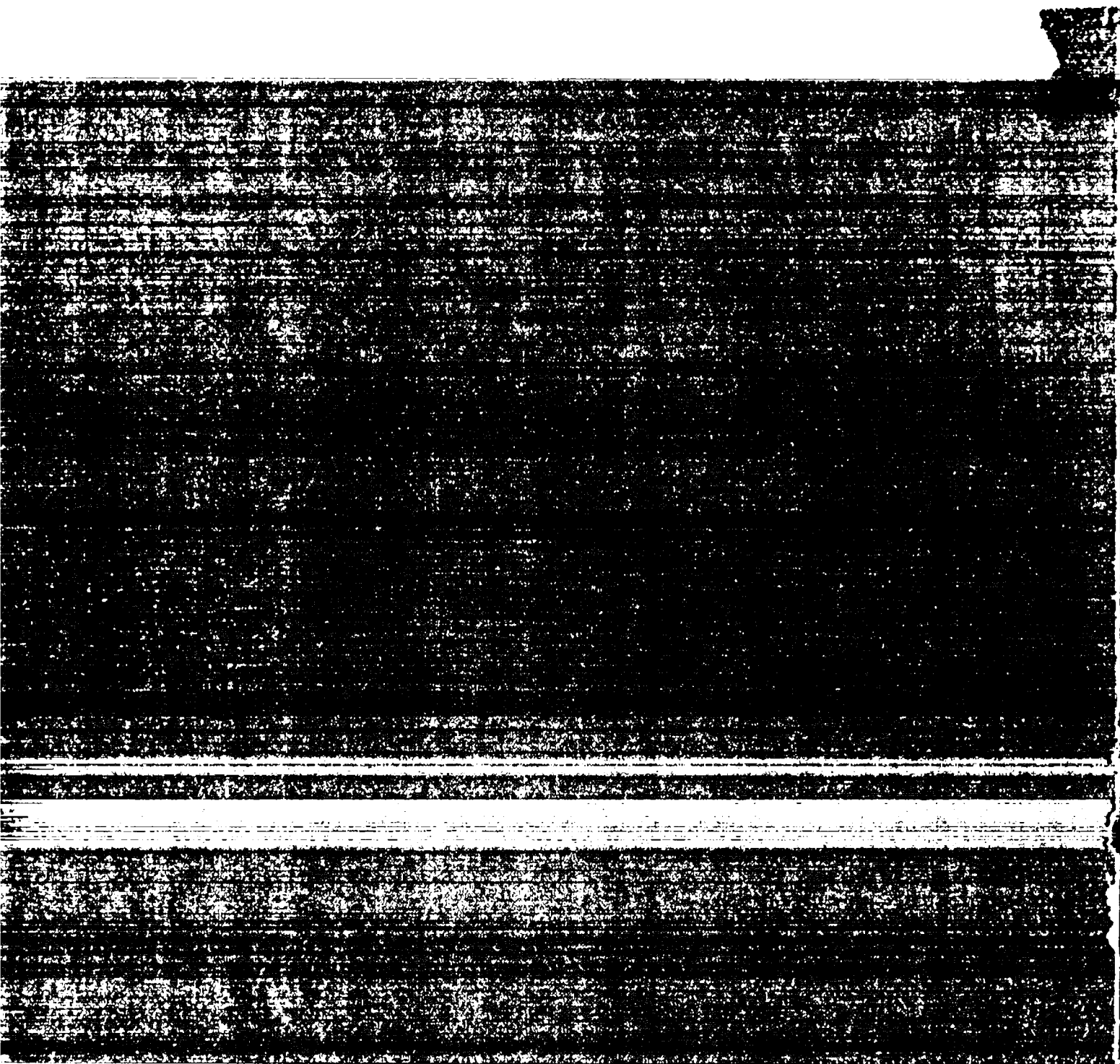
R. Wright, "Automatic Generation of C-Code for the Antares Control System," 1981 IEEE International Conference on Plasma Science, Santa Fe, New Mexico, May 18-20, 1981.

Page Range	NTIS Price Code	Page Range	NTIS Price Code	Page Range	NTIS Price Code	Page Range	NTIS Price Code
001-025	A02	151-175	A08	301-325	A14	451-475	A20
026-050	A03	176-200	A09	326-350	A15	476-500	A21
051-075	A04	201-225	A10	351-375	A16	501-525	A22
076-100	A05	226-250	A11	376-400	A17	526-550	A23
101-125	A06	251-275	A12	401-425	A18	551-575	A24
126-150	A07	276-300	A13	426-450	A19	576-600	A25
						601-up*	A99

*Contact NTIS for a price quote.

Los Alamos